



POLITECNICO DI MILANO
DEPARTMENT OF ARCHITECTURE, BUILT ENVIRONMENT AND
CONSTRUCTION ENGINEERING
DOCTORAL PROGRAM IN STRUCTURAL MECHANICS

In- and Out-of-Plane Homogenized Limit Analysis of Non-Periodic Masonry Walls Based on a Novel Pixel/Voxel Strategy

Doctoral Dissertation of:
Simone Tiberti

Supervisor:
Prof. Gabriele Milani

Tutor:
Prof. Tommaso D'Antino

The Chair of the Doctoral Program:
Prof. Marco Scaioni

2019 – Cycle XXXII

Acknowledgements

It is a common feature in the acknowledgements to leave the most important people to thank at the very end of the section. Therefore, I would like to start with the two individuals without whom none of this would have happen.

I will be eternally grateful to Professor Gabriele Milani for inviting me to join this PhD program. I thank him for his guidance, his limitless knowledge of the topics we dealt with, his helpfulness. I have learnt many things during these three-and-a-half years, and he taught me the greatest part of them.

My beloved mother Cristina is the driving force behind many of the good things in my life, and I would have not reached the end without her constant support, her hugs, her meals, and her good-heartedness. I love you, mamma.

I need to thank my personal Dream Team: Fede, Feva, Gio, Marti, Quaglio, Teo. The quality time we have spent together all these years, their affection and support have been (and are) invaluable to me.

I wish to express my gratitude to Marco, Ilaria, Ester, Ale, Salvo, the people of Bastian Contrario Parma - my safe haven. They have nurtured me and hosted me during many mornings, afternoons, evenings, and nights of work and play, and I am thankful for that.

I am indebted to all the colleagues I have met during these years, for their support and help in troubled times. Special thanks to Jacopo, Gabriel, Nicola, Ahmad, Roberto, and Matteo.

Lastly, I would like to thank my favorite football team, Parma Calcio 1913, for the many moments of joy and relief (and anger and despair) it has given me in these three-and-a-half years. I will never forget what happened May 18th, 2018. Never. Forza Magico Parma!

Abstract

HOMOGENIZATION is a meso-scale averaging procedure that has

been widely used over the past decades to derive the macroscale mechanical characteristics of periodic masonry starting from those of its constitutive materials. Both the in- and out-of-plane behaviors have been reliably assessed, in either the linear or nonlinear range but also through the use of limit analysis. The application of homogenization techniques to old masonry structures was early recognized as interesting and promising. However, historical masonry buildings sometimes display a quasi-periodic, if not wholly random, arrangement of units which is sometimes also coupled with the presence of multi-leaf walls. This is apparently in disagreement with the very idea behind homogenization, i.e. the identification of a Representative Element of Volume (REV) able to generate a periodic pattern when translated. Nonetheless, few past works have attempted and eventually succeeded to overcome this issue. Still, the lack of a comprehensive model for non-periodic masonry is rather evident. This PhD thesis presents an innovative approach that comes from the combination of homogenization and limit analysis. This aims at investigating the in- and out-of-plane collapse behavior of non-periodic masonry walls through the derivation of homogenized failure surfaces, which represent homogenized macroscopic failure criteria for the considered wall. The deformed shapes at collapse for selected in- and out-of-plane load conditions can also be extracted. Moreover, an automated procedure is introduced in this PhD thesis that enables the creation of a finite element mesh directly from the image file representing the rasterized sketch of a generic masonry element. This procedure goes under the name “pixel strategy” if a 2D finite element mesh is needed, where the elements are planar and rectangular; conversely, its extension in the 3D case is named “voxel strategy”, and there the resulting finite elements are solid bricks. The finite element meshes so obtained represent the bases for the extraction of the homogenized failure surfaces. Six real case studies are extensively investigated in terms of both in- and out-of-plane collapse behavior; the influence of the rate of non-periodicity on such behaviors is also

investigated and critically discussed. Eventually, the proposed procedure is extended for application on multi-leaf walls, which represent a common construction technique in several European countries, especially in Italy. In this regard, two three-leaf case studies are investigated in terms of out-of-plane collapse behavior, also considering the role played by the presence of transversal interconnection between the external layers.

Table of Contents

ACKNOWLEDGEMENTS	i
ABSTRACT	iii
LIST OF TABLES	ix
LIST OF FIGURES.....	x
INTRODUCTION	1
1.1 OBJECTIVES AND SCOPES OF THE THESIS	1
1.2 STRUCTURE OF THE THESIS.....	3
LITERATURE REVIEW	7
2.1 NUMERICAL STRATEGIES FOR MODELLING MASONRY	7
2.1.1 <i>Macro-Modelling</i>	8
2.1.2 <i>Micro-Modelling</i>	10
2.1.3 <i>Homogenization</i>	13
2.2 HOMOGENIZATION APPLIED TO PERIODIC MASONRY	14
2.2.1 <i>Homogenization for Elastic Characteristics of Masonry</i>	14
2.2.2 <i>Homogenization for Non-Linear Analysis of Masonry</i>	16
2.2.3 <i>Homogenization for Modelling Damage in Masonry</i>	18
2.3 HOMOGENIZATION AND LIMIT ANALYSIS	19
2.3.1 <i>In-Plane Collapse Behavior</i>	20
2.3.2 <i>Out-of-Plane Collapse Behavior</i>	25
2.4 HOMOGENIZATION APPLIED TO NON-PERIODIC MASONRY	30
2.4.1 <i>Homogenization Applied to Non-Periodic Multi-Leaf Walls</i>	33
2.5 CONCLUSIONS	33
2.6 REFERENCES.....	36
MESH GENERATOR FOR MASONRY PANELS	42
3.1 2D MESH GENERATOR	43
3.2 3D MESH GENERATOR	45
3.3 COARSING STRATEGY	50
3.4 3D MESH GENERATOR FOR MULTI-LEAF MASONRY WALLS.....	52
3.5 REFERENCES.....	53
2D HOMOGENIZED LIMIT ANALYSIS OF NON-PERIODIC MASONRY	54
4.1 PROBLEM FORMULATION	55
4.1.1 <i>Velocity Jumps and Plastic Flow Constraints</i>	55
4.1.2 <i>Periodicity Boundary Conditions</i>	59
4.1.3 <i>Normalization of Dissipated External Power</i>	60
4.1.4 <i>Power Dissipation in Velocity Discontinuities</i>	62

4.1.5	<i>Assembly and Solution of the Linear Programming Problem</i>	62
4.1.6	<i>Master-Slave Approach</i>	65
4.1.7	<i>Construction of the Homogenized Failure Surfaces</i>	66
4.2	CASE STUDIES.....	68
4.2.1	<i>Strategy for the Identification of the Statistical REV</i>	68
4.2.2	<i>Case Study 1: Rubble Masonry Building in Casola in Lunigiana, Tuscany</i>	70
4.2.3	<i>Case Study 2: Quasi-Periodic Masonry Ruin in Codiponte, Tuscany</i>	79
4.2.4	<i>Case Study 3: Quasi-Periodic Masonry Parish Church in Filattiera, Tuscany</i>	88
4.2.5	<i>Case Study 4: Quasi-Periodic Masonry Tower Ruins in Mulazzo, Tuscany</i>	97
4.2.6	<i>Case Study 5: Quasi-Regular Masonry Parish Church in San Secondo Parmense, Emilia Romagna</i>	105
4.2.7	<i>Case Study 6: Quasi-Regular Masonry Grand Corridor in Sabbioneta, Lombardy</i>	112
4.3	CONCLUSIONS	119
4.4	REFERENCES.....	121

3D HOMOGENIZED LIMIT ANALYSIS OF SINGLE-LEAF NON-PERIODIC MASONRY
..... **123**

5.1	PROBLEM FORMULATION	124
5.1.1	<i>Velocity Jumps and Plastic Flow Constraints</i>	125
5.1.2	<i>Master-Slave Relations for Unit Elements</i>	129
5.1.3	<i>Periodicity Boundary Conditions</i>	131
5.1.4	<i>Normalization of Dissipated External Power</i>	131
5.1.5	<i>Power Dissipation in Velocity Discontinuities</i>	133
5.1.6	<i>Assembly and Solution of the Linear Programming Problem</i>	133
5.1.7	<i>Construction of the Out-of-Plane Homogenized Failure Surfaces</i>	135
5.2	NUMERICAL VALIDATION	137
5.2.1	<i>Running Bond Masonry REV</i>	137
5.2.2	<i>English Bond Masonry REV</i>	143
5.3	CASE STUDIES.....	149
5.3.1	<i>Case Study 1: Rubble Masonry Building in Casola in Lunigiana, Tuscany</i>	150
5.3.2	<i>Case Study 2: Quasi-Periodic Masonry Ruin in Codiponte, Tuscany</i>	154
5.3.3	<i>Case Study 3: Quasi-Periodic Masonry Parish Church in Filattiera, Tuscany</i>	157
5.3.4	<i>Case Study 4: Quasi-Periodic Masonry Tower Ruins in Mulazzo, Tuscany</i>	160
5.3.5	<i>Case Study 5: Quasi-Regular Masonry Parish Church in San Secondo Parmense, Emilia Romagna</i>	163

5.3.6	<i>Case Study 6: Quasi-Regular Masonry Grand Corridor in Sabbioneta, Lombardy</i>	166
5.4	CONCLUSIONS	169
5.5	REFERENCES.....	171
3D HOMOGENIZED LIMIT ANALYSIS OF THREE-LEAF NON-PERIODIC MASONRY		
.....		173
6.1	PROBLEM FORMULATION	175
6.2	CASE STUDIES	179
6.2.1	<i>Case Study 1: Three-Leaf Rubble Masonry Wall</i>	180
6.2.2	<i>Case Study 2: Three-Leaf Quasi-Regular Masonry Wall</i>	185
6.3	CONCLUSIONS	195
6.4	REFERENCES.....	195
CONCLUSIONS		196
7.1	COMPREHENSIVE STUDY OF THE COLLAPSE BEHAVIOR OF MULTI-LEAF WALLS..	197
7.2	DEVELOPMENT OF GUI-BASED MATLAB APP FOR HOMOGENIZED LIMIT ANALYSIS OF NON-PERIODIC MASONRY	199
7.3	REFERENCES.....	202

List of Tables

Table 4.1	68
Table 4.2	69
Table 4.3	69
Table 4.4	76
Table 4.5	78
Table 4.6	87
Table 4.7	95
Table 4.8	104
Table 4.9	110
Table 4.10	118
Table 5.1	138
Table 5.2	144
Table 5.3	150
Table 6.1	180

List of Figures

Fig. 2.1. Visual representation of the macro-modelling strategy.....	8
Fig. 2.2. Visual representation of the classic micro-modelling strategy.....	10
Fig. 2.3. Visual representation of the micro-modelling strategy with mortar joints reduced to interfaces.....	11
Fig. 2.4. Visual representation of the homogenization strategy applied to masonry.	13
Fig. 2.5. (a) Division of one quarter of the REV in 9 sub-domains; (b) division of the whole REV in 36 sub-domains by Milani and co-workers [43].	20
Fig. 2.6. Comparison of the results obtained by Milani and co-workers for different polynomial expansions by Milani and co-workers [43]; the results are also compared to those derived by de Buhan and de Felice.....	21
Fig. 2.7. Comparison between the lower- and upper-bound approaches by Milani and co-workers [43].....	21
Fig. 2.8. (a) Sub-division of the REV into rectangular cells; (b) strain-periodic kinematically admissible velocity field under macroscopic normal stresses; (c) strain-periodic kinematically admissible velocity field under macroscopic shear stresses by Milani & Taliercio [46].	23
Fig. 2.9. (a) Homogenized failure surfaces obtained with the proposed method in the tension-tension range; (b) homogenized failure surfaces obtained with the proposed method in the compression-compression range by Milani & Taliercio [46].	24
Fig. 2.10. 3D system of blocks for the kinematic identification by Cecchi & Sab [30] and by Cecchi and co-workers [51].	26
Fig. 2.11. Out-of-plane homogenized failure surface in the M_{11} - M_{22} plane, for different values of the macroscopic shear force T_{13} by Cecchi and co-workers [51].	27
Fig. 2.12. Out-of-plane homogenized failure surface in the M_{11} - M_{12} plane, for different values of the macroscopic shear force T_{13} by Cecchi and co-workers [51].	27

Fig. 2.13. Definition of horizontal bending moment (M_{xx}), vertical bending moment (M_{yy}), and torsional moment (M_{xy}) by Milani & Taliercio [53].	28
Fig. 2.14. Comparison of out-of-plane homogenized failure surfaces obtained with different approaches in the M_{xx} - M_{yy} plane by Milani & Taliercio [53].	29
Fig. 2.15. Comparison of out-of-plane homogenized failure surfaces obtained with different approaches in the M_{xx} - M_{xy} plane by Milani & Taliercio [53].	29
Fig. 2.16. (a) Brick masonry tower (“Castello delle Rocche” in Finale Emilia, Modena, Italy); (b) rubble masonry tower (outer city walls in Norcia, Perugia, Italy); (c) residential rubble masonry building in Pretare, Ascoli Piceno, Italy; (d) rubble masonry used as infills (outside wall of the Baths of Caracalla, Rome, Italy).	31
Fig. 3.1. Pixel strategy for the creation of finite elements	44
Fig. 3.2. (a) Black-and-white rasterized sketch of a sample masonry element; (b) 2D discretization.....	45
Fig. 3.3. (a) Sample image of a stone embedded in mortar; (b) mid-plane of the 3D FE mesh; (c) 3D FE mesh with extruded stone; (d) aerial view of the 3D FE mesh with ellipsoidal stone; (e) 3D FE mesh with ellipsoidal stone; (f) section of 3D FE mesh with ellipsoidal stone.....	46
Fig. 3.4. Voxel strategy for creating the 3D finite element mesh.....	48
Fig. 3.5. (a) Black-and-white rasterized sketch of the sample masonry element; (b) 3D discretization with extruded transversal configuration; (c) 3D discretization with ellipsoidal units.....	49
Fig. 3.6. Coarsing strategy for reducing the mesh size.....	50
Fig. 3.7. (a) Black-and-white rasterized sketch of the sample masonry element; (b) 2D discretization with a 2×2 coarsing strategy; (c) 2D discretization with a 3×3 coarsing strategy; (d) 2D discretization with a 4×4 coarsing strategy; (e) 2D discretization with a 5×5 coarsing strategy.....	51
Fig. 3.8. 3D finite element mesh for a three-leaf wall.....	52
Fig. 4.1. Velocity jumps for a generic horizontal interface.	56
Fig. 4.2. Velocity jumps for a generic vertical interface.	56
Fig. 4.3. Mohr-Coulomb criterion + tension cut-off.....	57
Fig. 4.4. Periodicity boundary conditions.....	59

Fig. 4.5. Angles defining the tensile in-plane load condition.....	60
Fig. 4.6. Crack patterns within mortar joints in a stone masonry church (Arquata del Tronto, Ascoli Piceno, Italy).	65
Fig. 4.7. (a) Masonry type for case study 1 [12]; (b) sketch of one of its masonry panels; (c) black-and-white rasterization of the sketch.....	70
Fig. 4.8. Test-windows extracted for case study 1: (a) small size; (b) medium size; (c) large size; (d) huge size.....	71
Fig. 4.9. Homogenized failure surfaces, means and envelopes for the small test-window size of case study 1.	73
Fig. 4.10. Homogenized failure surfaces, means and envelopes for the medium test-window size of case study 1.	74
Fig. 4.11. Homogenized failure surfaces, means and envelopes for the large test-window size of case study 1.	75
Fig. 4.12. Failure modes for the large test-window size of case study 1 when $\theta = 0^\circ$	77
Fig. 4.13. (a) Masonry type for case study 2 [12]; (b) sketch of the considered masonry panel; (c) black-and-white rasterization of the sketch.	80
Fig. 4.14. Test-windows extracted for case study 2: (a) small size; (b) medium size; (c) large size; (d) huge size.....	81
Fig. 4.15. Homogenized failure surfaces, means and envelopes for the small test-window size of case study 2.	83
Fig. 4.16. Homogenized failure surfaces, means and envelopes for the medium test-window size of case study 2.	84
Fig. 4.17. Homogenized failure surfaces, means and envelopes for the large test-window size of case study 2.	85
Fig. 4.18. Homogenized failure surfaces, means and envelopes for the huge test-window size of case study 2.	86
Fig. 4.19. (a) Masonry type for case study 3; (b) sketch of the considered masonry panel; (c) black-and-white rasterization of the sketch.	88
Fig. 4.20. Test-windows extracted for case study 3: (a) small size; (b) medium size; (c) large size; (d) huge size.....	89

Fig. 4.21. Homogenized failure surfaces, means and envelopes for the small test-window size of case study 3.	91
Fig. 4.22. Homogenized failure surfaces, means and envelopes for the medium test-window size of case study 3.	92
Fig. 4.23. Homogenized failure surfaces, means and envelopes for the large test-window size of case study 3.	93
Fig. 4.24. Homogenized failure surfaces, means and envelopes for the huge test-window size of case study 3.	94
Fig. 4.25. Failure modes for the huge test-window size of case study 3 when $\theta = 0^\circ$	96
Fig. 4.26. (a) Masonry type for case study 4; (b) sketch of the considered masonry panel; (c) black-and-white rasterization of the sketch.	97
Fig. 4.27. Test-windows extracted for case study 4: (a) small size; (b) medium size; (c) large size; (d) huge size.	98
Fig. 4.28. Homogenized failure surfaces, means and envelopes for the small test-window size of case study 4.	100
Fig. 4.29. Homogenized failure surfaces, means and envelopes for the medium test-window size of case study 4.	101
Fig. 4.30. Homogenized failure surfaces, means and envelopes for the large test-window size of case study 4.	102
Fig. 4.31. Homogenized failure surfaces, means and envelopes for the huge test-window size of case study 4.	103
Fig. 4.32. (a) Masonry type for case study 5; (b) sketch of one of its masonry panels; (c) black-and-white rasterization of the sketch.	105
Fig. 4.33. Test-windows extracted for case study 5: (a) small size; (b) medium size; (c) large size; (d) huge size.	106
Fig. 4.34. Homogenized failure surfaces, means and envelopes for the small test-window size of case study 5.	108
Fig. 4.35. Homogenized failure surfaces, means and envelopes for the medium test-window size of case study 5.	109
Fig. 4.36. Failure modes for the medium test-window size of case study 5 when $\theta = 0^\circ$	111

Fig. 4.37. (a) Masonry type for case study 6; (b) sketch of the considered masonry panel; (c) black-and-white rasterization of the sketch.	112
Fig. 4.38. Test-windows extracted for case study 6: (a) small size; (b) medium size; (c) large size; (d) huge size.	113
Fig. 4.39. Homogenized failure surfaces, means and envelopes for the small test-window size of case study 6.	115
Fig. 4.40. Homogenized failure surfaces, means and envelopes for the medium test-window size of case study 6.	116
Fig. 4.41. Homogenized failure surfaces, means and envelopes for the large test-window size of case study 6.	117
Fig. 4.42. Comparison of the mean homogenized failure surfaces among the six case studies: (a) $\theta = 0^\circ$; (b) $\theta = 22.5^\circ$; (c) $\theta = 45^\circ$	120
Fig. 5.1. Velocity jumps for a generic interface normal to axis X.....	125
Fig. 5.2. Velocity jumps for a generic interface normal to axis Y.....	126
Fig. 5.3. Mohr-Coulomb failure criterion with tension and compression cutoffs.	127
Fig. 5.4. Graphical representation of a masonry unit (M) and a unit finite element (S).	130
Fig. 5.5. Periodicity boundary conditions.	131
Fig. 5.6. Angles defining the out-of-plane load condition.....	132
Fig. 5.7. (a) In-plane layout of the running bond masonry REV; (b) Mesh 1; (c) Mesh 2.	138
Fig. 5.8. Comparison of in-plane homogenized failure surfaces in the tension-tension range, for different values of angle θ	139
Fig. 5.9. Comparison of in-plane homogenized failure surfaces in the compression-compression range, for different values of angle θ	140
Fig. 5.10. Failure modes for in-plane load conditions on Mesh 1: (a) uniaxial horizontal tension; (b) uniaxial vertical tension; (c) uniaxial horizontal compression; (d) uniaxial vertical compression.	141

Fig. 5.11. Comparison of out-of-plane homogenized failure surfaces with Milani-Taliercio: (a) M_{xx} - M_{yy} plane; (b) M_{xx} - M_{xy} plane.....	142
Fig. 5.12. Failure modes for out-of-plane load conditions on Mesh 1: (a) M_{xx} ; (b) M_{yy} ; (c) M_{xy}	143
Fig. 5.13. English bond masonry REV used for validation against data from Cecchi-Milani.	144
Fig. 5.14. Comparison of out-of-plane homogenized failure surfaces with Cecchi-Milani: (a) M_{xx} - M_{yy} plane; (b) M_{xx} - M_{xy} plane.	145
Fig. 5.15. (a) Finer mesh for the English bond masonry REV; (b) piecewise linear approximation for the 3D Mohr-Coulomb failure criterion used by Cecchi-Milani; (c) Model A, box-shaped approximation in the τ_1 - τ_2 plane; (d) Model B, circumscribing approximation in the τ_1 - τ_2 plane.	147
Fig. 5.16. Comparison of different out-of-plane homogenized failure surfaces in the M_{xx} - M_{xy} plane: (a) Model A; (b) Model B.	148
Fig. 5.17. Failure modes for out-of-plane load conditions on English bond masonry REV: (a) M_{xx} ; (b) M_{yy} ; (c) M_{xy}	149
Fig. 5.18. (a) case study 1; (b) case study 2; (c) case study 3; (d) case study 4; (e) case study 5; (f) case study 6.	150
Fig. 5.19. Out-of-plane homogenized failure surfaces for case study 1.	152
Fig. 5.20. Failure modes under M_{xx} , M_{yy} , and M_{xy} for the four test-windows of case study 1.....	153
Fig. 5.21. Out-of-plane homogenized failure surfaces for case study 2.	155
Fig. 5.22. Failure modes under M_{xx} , M_{yy} , and M_{xy} for the four test-windows of case study 2.....	156
Fig. 5.23. Out-of-plane homogenized failure surfaces for case study 3.	158
Fig. 5.24. Failure modes under M_{xx} , M_{yy} , and M_{xy} for the four test-windows of case study 3.....	159
Fig. 5.25. Out-of-plane homogenized failure surfaces for case study 4.	161
Fig. 5.26. Failure modes under M_{xx} , M_{yy} , and M_{xy} for the four test-windows of case study 4.....	162

Fig. 5.27. Out-of-plane homogenized failure surfaces for case study 5.	164
Fig. 5.28. Failure modes under M_{xx} , M_{yy} , and M_{xy} for the four test-windows of case study 5.	165
Fig. 5.29. Out-of-plane homogenized failure surfaces for case study 6.	167
Fig. 5.30. Failure modes under M_{xx} , M_{yy} , and M_{xy} for the four test-windows of case study 6.	168
Fig. 5.31. Comparison of the flexural and torsional out-of-plane mean homogenized failure surfaces among the six case studies.	170
Fig. 6.1. Difference in terms of macroscopic quantities between the single-leaf (left) and multi-leaf case (right).....	175
Fig. 6.2. (a) Test-window C of case study 1; (b) test-window B of case study 1; (c) in-plane configuration of both the outer wythes for Instance 1, and of one wythe of Instance 2; (d) in-plane configuration of the other outer wythe of Instance 2.	181
Fig. 6.3. First case study: (a) 3D finite element mesh for Instance 1; (b) exploded view of the 3D finite element mesh for Instance 1; (c) 3D finite element mesh for Instance 2; (d) exploded view of the 3D finite element mesh for Instance 2.....	182
Fig. 6.4. Flexural and torsional out-of-plane homogenized failure surfaces for the two instances of the first case study.	183
Fig. 6.5. Failure modes under M_{xx} , M_{yy} , and M_{xy} for the two instances of the first case study.	184
Fig. 6.6. (a) Test-window C of case study 6; (b) test-window B of case study 6; (c) in-plane configuration of both the outer wythes for Instance 1, and of one wythe of Instance 2; (d) in-plane configuration of the other outer wythe of Instance 2.	186
Fig. 6.7. Second case study, first numerical application: (a) 3D finite element mesh for Instance 1; (b) exploded view of the 3D finite element mesh for Instance 1; (c) 3D finite element mesh for Instance 2; (d) exploded view of the 3D finite element mesh for Instance 2.....	187
Fig. 6.8. Flexural and torsional out-of-plane homogenized failure surfaces for the two instances of the first numerical application of the second case study.....	189
Fig. 6.9. Failure modes under M_{xx} , M_{yy} , and M_{xy} for the two instances of the first numerical application of the second case study.....	190

Fig. 6.10. (a) 3D finite element mesh for Instance 3; (b) exploded view of the 3D finite element mesh for Instance 3.....	191
Fig. 6.11. Flexural and torsional out-of-plane homogenized failure surfaces for the two instances of the second numerical application of the second case study. ...	193
Fig. 6.12. Failure modes under M_{xx} , M_{yy} , and M_{xy} for the two instances of the second numerical application of the second case study.....	194
Fig. 7.1. Multi-leaf walls in two buildings located in Accumoli (RI), revealed after the collapse of the façade due to the 2016 Central Italy earthquake.....	197
Fig. 7.2. Conceptual workflow of the procedure to develop in the MATLAB app.	200

INTRODUCTION

1.1 Objectives and Scopes of the Thesis

This PhD thesis presents an innovative approach aiming at the assessment of the in- and out-of-plane collapse behavior of non-periodic masonry. Specifically, this work introduces an automated procedure that takes the rasterized sketch of a non-periodic masonry structural element as input, and gives its in- and out-of-plane homogenized failure surfaces as outputs – the latter acting as macroscopic strength criteria for the considered structural element.

The scopes of this PhD thesis can be summarized in the following points:

- a. Devising an automated procedure for the generation of a 2D finite element mesh from the rasterized sketch of a generic masonry element, based on a “pixel strategy” that transforms each pixel of the sketch into a single, planar finite element;
- b. Conceiving an analogous automated procedure that allows the generation of a 3D finite element mesh from the rasterized sketch of a generic masonry element, based on a more refined “voxel strategy” where each pixel of the sketch is first converted into a voxel (its 3D counterpart), which is in turn transformed into solid finite elements;
- c. Elaborating a numerical strategy for obtaining a coarser finite element mesh when the number of pixels in the original sketch is too high;
- d. Elaborating a numerical strategy for correctly representing the tridimensional shape of the units when a 3D finite element mesh is created;

-
- e. Devising an automated procedure for generating the 3D finite element mesh of a multi-leaf walls;
 - f. Developing an original method for assessing the in-plane collapse behavior of non-periodic masonry, based on both the upper bound theorem of limit analysis and the meso-scale technique known as homogenization. The collapse behavior is addressed by extracting in-plane homogenized failure surfaces of non-periodic masonry structural elements: these serve as macroscopic strength criteria capable of identifying the collapse value of different in-plane load conditions. The 2D finite element mesh created with the aforementioned “pixel strategy” is used as input, and the method is written into a standard-form linear programming problem (subjected to a set of equality constraints) that gives the in-plane homogenized failure surfaces as outputs. The method also allows the extraction of deformed shapes at collapse for the selected structural element.
 - g. Investigating the in-plane collapse behavior of six real case studies, all concerning buildings consisting of non-periodic masonry with different rates of randomness in the units’ arrangement. A suitable, general strategy is conceived for the identification of the Statistically Equivalent Periodic Unit Cell in each case study, based on the so-called “test-window method”. In-plane homogenized failure surfaces and some relevant deformed shapes at collapse are extracted and critically commented for the six case studies.
 - h. Developing an original method for assessing the out-of-plane collapse behavior of non-periodic masonry, again based on the upper bound theorem of limit analysis and on homogenization. Similarly to the in-plane case, this collapse behavior is addressed by extracting out-of-plane homogenized failure surfaces of non-periodic masonry structural elements: here, they identify the collapse value of different out-of-plane load conditions, enforced in terms of a combination of different flexural/torsional moments. The 3D finite element mesh created with the aforementioned “voxel strategy” is used as input, and the out-of-plane kinematics of the elements is governed by a Kirchhoff-Love plate model. The method is written again into a standard-form linear programming problem (subjected to a set of equality constraints) that gives the out-of-plane homogenized failure surfaces as outputs. Once more, the method

allows the extraction of deformed shapes at collapse for the selected structural element.

- i. Validating the method for the out-of-plane collapse behavior against data available in literature for periodic masonry elements. Specifically, the out-of-plane homogenized failure surfaces extracted from the present method are compared to those previously derived by other authors that used different methods.
- j. Investigating the out-of-plane collapse behavior of the six real case studies previously discussed in terms of their in-plane behavior. These case studies are considered as single-leaf walls. Out-of-plane homogenized failure surfaces and relevant deformed shapes at collapse are extracted and critically commented for all the six case studies.
- k. Investigating the out-of-plane collapse behavior of multi-leaf walls. To achieve this goal, two of the previously investigated six case studies are considered as three-leaf walls, displaying an inner mortar layer enclosed by two outer masonry layers. The method for assessing the out-of-plane collapse behavior is then modified to account for the presence of multiple layers in the wall – namely, the kinematics is suitably modified. The influence of transversal interconnection (represented by units extending along the whole thickness) is also investigated.

1.2 Structure of the Thesis

This PhD thesis consists of seven Chapters, the first two representing a wide introduction that defines the motivation behind this work and its goals, and explores the engineering field in which this work is grounded. In particular,

- The current chapter (*Chapter 1*) serves as the proper introduction of this PhD thesis, describing its motivation and detailing its scopes.
- *Chapter 2* offers a deep insight into the state of the art concerning the numerical strategies for modelling masonry. An extensive literature review is here presented, focusing on homogenization applied to masonry and with special attention given to its pairing with limit analysis. Several classic works in this field are recapped and summarily described.

The next four chapters of this PhD thesis extensively discuss the original tools and methods here developed for the assessment of the in- and out-of-plane collapse behavior of non-periodic masonry. In particular,

- *Chapter 3* offers a detailed description of the strategies adopted for creating a finite element mesh from the rasterized sketch of a generic masonry element. The first part of this chapter is devoted to presenting the “pixel strategy” conceived for generating a 2D finite element mesh. The basic idea behind this strategy is the transformation of a pixel into a planar finite element, so that the mesh is automatically created from the source image in very few steps. These are listed in a logical fashion and are eventually transcribed into a MATLAB script. Similarly, the second part of this chapter is devoted to presenting the “voxel strategy” conceived for generating a 3D finite element mesh. Here, the basic idea is the transformation of a voxel (the 3D equivalent of a pixel) into a solid finite element. Again, the logical steps that allow the creation of the 3D mesh are eventually transcribed into a MATLAB script. The third part of this chapter describes the so-called “coarsening strategy”, which enables the reduction of the number of finite elements in the mesh when the source image contains a huge number of pixels. The fourth and final part of this chapter briefly describes the strategy adopted for the creation of a 3D finite element mesh of a multi-leaf wall.
- *Chapter 4* is devoted to the full description of the procedure developed for assessing the in-plane collapse behavior of non-periodic masonry walls. The first part of this chapter broadly describes the approach on which this procedure is based, which combines the upper bound theorem of limit analysis and homogenization. This is then synthesized into a standard-form linear programming problem, subjected to equality constraints that directly come from the very mathematical formulation of this problem. Eventually, this problem is implemented into a MATLAB script that also contains the 2D mesh generating tool. This part also describes the method for constructing the in-plane homogenized failure surfaces and the deformed shapes at collapse extracted for in-plane load conditions. The second part of this chapter presents the numerical application of the procedure previously described. This application is represented by an extensive investigation on six case studies, which actually are six non-periodic masonry walls that are part of existing buildings located in Tuscany and Emilia-Romagna. The resulting in-

plane homogenized failure surfaces and deformed shapes at collapse for each case study are critically commented and compared.

- *Chapter 5* is devoted to the full description of the procedure developed for assessing the out-plane collapse behavior of non-periodic masonry walls. The first part of this chapter broadly describes the approach on which this procedure is based, which employs a Kirchhoff-Love plate model for the out-of-plane kinematics, and which again combines the upper bound theorem of limit analysis and homogenization. This is then synthesized into a standard-form linear programming problem, subjected to equality constraints that directly come from the very mathematical formulation of this problem. Eventually, this problem is implemented into a MATLAB script that also contains the 3D mesh generating tool. This part also describes the method for constructing the out-of-plane homogenized failure surfaces and the deformed shapes at collapse extracted for out-of-plane load conditions (set as flexural/torsional moments). The second part of this chapter presents the numerical validation of the procedure previously described: here, the out-of-plane homogenized failure surfaces are extracted for two periodic masonry bonds (namely, running bond masonry and English bond masonry), which are then compared to those available in literature for the same masonry bonds, obtained with the use of two different methods. The third and final part of this chapter presents the numerical application of the procedure here described. This application is represented by an extensive investigation on the six non-periodic real case studies already inquired in the previous chapter. Once more, the resulting out-of-plane homogenized failure surfaces and deformed shapes at collapse for each case study are critically commented and compared.
- *Chapter 6* is devoted to the study of the out-of-plane collapse behavior of multi-leaf walls, using a modified version of the procedure developed in the previous chapter for single-leaf walls. The first part of this chapter describes the modifications needed in the mathematical formulation of the linear programming problem to account for the presence of several layers in the wall thickness. The second part of this chapter presents the numerical application of the modified procedure. This application is represented by two custom-built case studies, consisting of three-leaf walls that are created starting from two of the six real case studies previously investigated. Specifically, a rubble three-leaf masonry wall and a quasi-regular masonry wall are created and inquired in terms of

their out-of-plane collapse behavior. In the latter case, the influence of the transversal interconnection (simulated by the presence of bricks that spread throughout the whole thickness of the wall) is also investigated. Again, the resulting out-of-plane homogenized failure surfaces and deformed shapes at collapse for each case study are critically commented.

The final chapter of this PhD thesis (*Chapter 7*) offers a brief recap of the contents, and is mainly devoted to discussing the future developments that may possibly be originated by this work – i.e. an original study solely focused on the collapse behavior of non-periodic multi-leaf walls, and the development of GUI-based MATLAB app that performs all the tasks and procedures described in this PhD thesis, with the aim of providing researchers and practitioners with a useful tool for quickly assessing the collapse behavior of a non-periodic masonry wall.

CHAPTER 2

LITERATURE REVIEW

This chapter is meant to present an extensive literature review concerning the state of the art of the available numerical strategies for modelling masonry. Section 2.1 recalls the two strategies commonly adopted, which are macro- and micro-modelling, and concludes by introducing a third, more recent strategy that is also the one employed in this PhD thesis: homogenization. The latter's application to periodic masonry is thoroughly discussed in Section 2.2, where many classical works in this regard are examined covering a wide range of applications for the description of masonry's elastic and inelastic behavior. Section 2.3 is entirely devoted to offering a deep insight on the pairing of homogenization and the theorems of limit analysis: several works in this field are recapped and summarily described. Finally, Section 2.4 is dedicated to the available statistical procedures that allow the application of homogenization to non-periodic masonry, with a coda focusing on multi-leaf walls.

2.1 Numerical Strategies for Modelling Masonry

When it comes to defining a mechanical model for construction materials, masonry stands out for being the trickiest one. This is due to its inherent nature, being it composed by two fragile materials (units and mortar) both exhibiting softening in tension and compression. The mutual interaction between these two materials must also be properly addressed. Further issues arise when dealing with historical masonry buildings, where both units and mortar may vary in nature within a wide range of different materials with their own mechanical properties. Moreover, the dimension of the units and the way they are assembled into masonry are something that cannot be ignored. All this leads to stating that, in general, masonry needs to be at least regarded as an orthotropic material.

For practical applications, and for sake of simplicity, it is widely accepted to use a simplified isotropic model for masonry, whose properties at the macro-level

are directly drawn from the characteristics of units and mortar at the micro-level. This is achieved by using empirical formulae, which can also be found in relevant European building codes [1], but with an unwelcome side effect in the guise of high safety factors. Nonetheless, this kind of model represents a huge approximation of the actual behavior, especially when considering the material behavior at failure.

Several rather advanced material models for masonry – including elastoplasticity and orthotropic damage – have been proposed in the last few decades by different researchers. Generally, three different modelling strategies are adopted, known in the technical literature as macro-modelling, micro-modelling and homogenization.

2.1.1 Macro-Modelling

A numerical strategy frequently adopted for modelling masonry is the so-called “macro-modelling”: the heterogeneous composite consisting of units and mortar is substituted with an equivalent homogeneous material (Fig. 2.1). In computational terms, this removes the need of separately meshing units and mortar. Therefore, this strategy is particularly convenient for tackling complex numerical analyses of large-scale structures, which require swift and efficient computations.

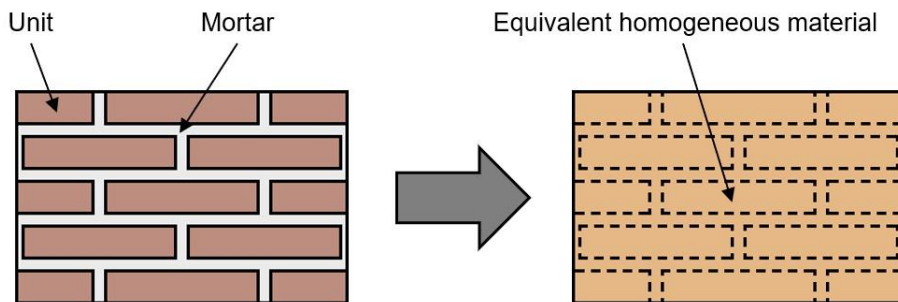


Fig. 2.1. Visual representation of the macro-modelling strategy.

This strategy has been extensively exploited in several works for describing masonry as a monolithic material. In one classic paper, Di Pasquale [2] develops a full constitutive model that considers masonry as a “no-tension” material. Conversely, a series of papers authored by Lourenço and co-workers [3][4] elaborates a complex plane-stress model for masonry as a quasi-brittle, orthotropic material; this model features distinct fracture energies in tension and compression, and independent behaviors along each material axis. Eventually,

the model is validated against experimental results obtained for masonry shear walls.

Masonry is well-known for being highly vulnerable to seismic actions; unreinforced masonry buildings hit by an earthquake usually display a severe state of damage, which is represented by widespread crack patterns in the walls. Therefore, a special attention has been given to developing macro-scale models for masonry that are also able to simulate the formation of cracks. For instance, Pelà and co-workers [5] develop a localized mapped damage model that is in general applicable to orthotropic materials, including masonry. This methodology employs an orthotropic failure criterion that is linked to an isotropic one in a mapped space. This model is successfully validated for masonry against experimental data on masonry wallets and beams. Instead, Toti and co-workers [6] envision a non-local, isotropic damage-plastic model specifically aimed at the dynamic analysis of large-scale structures. The non-local approach is here employed to avoid experiencing strain localization and mesh sensitivity. This model is successfully applied to simulate the damaged state of a masonry pillar located in the Basilica of S. Maria di Collemaggio, hit by the disastrous 2009 L'Aquila earthquake. A different non-local damage-plastic model is introduced by Gatta and co-workers [7], which is conversely focused on mirroring the cyclic behavior of masonry structures under static and dynamic loading. The validation of the proposed model is carried out against experimentally tested walls under cyclic actions. Furthermore, Saloustros and co-workers [8] present an algorithm to track multi-directional intersecting cracks that form within masonry shear walls under in-plane cyclic loads. Analogously to [6], this algorithm is conceived to remove localization of damage due to mesh-dependency and the orientation of finite elements; it also employs an orthotropic damage model. The validation is performed against experimental data obtained from the in-plane cyclic loading of a real masonry shear wall. Eventually, a recent paper by Clementi and co-workers [9] makes use of the non-smooth contact dynamics (NSCD) method to simulate the damage formation in historical masonry buildings. The “non-smooth” part of the NSCD method employs a peculiar formulation of the motion laws for modelling mechanical systems with unilateral contacts and friction. The NSCD method is here validated against the real damage state of five masonry churches located in the Italian Apennines and heavily affected by the 2016 Central Italy seismic sequence.

The major drawback of macro-modelling is represented by the actual calibration of material parameters. In fact, they may be extracted arbitrarily from ranges of values recommended by codes and standards, derived through empirical

formulae based on the constituents' material parameters, or determined as the mean values resulting from experimental campaigns. The limitations are rather evident: in the first and second case, the parameters eventually adopted may questionably represent the true mechanical properties of the material; in the third case, it must be noted that when the level of sophistication of the model increases, the number of inelastic parameters grows and the experimental characterization may become costly and cumbersome. Moreover, as shown by Miccoli and co-workers in [10], simple macro-models may be unable to fully grasp either the non-linear behavior or the crack patterns observed in experimental specimens, thus resulting in an unsatisfactory reliability of the adopted macro-models.

2.1.2 Micro-Modelling

The numerical strategy opposite to macro-modelling is the so-called “micro-modelling”: it is simply characterized by the distinct modelling of mortar joints and units at a structural level, with the possibility to employ a separate model also for the unit/mortar interfaces (Fig. 2.2). A common method to simplify the overall problem is represented by the reduction of mortar joints to interfaces between units (Fig. 2.3). Considering the heterogeneity of masonry, micro-modelling seems the most suitable strategy to properly simulate its mechanical behavior in all its aspects.

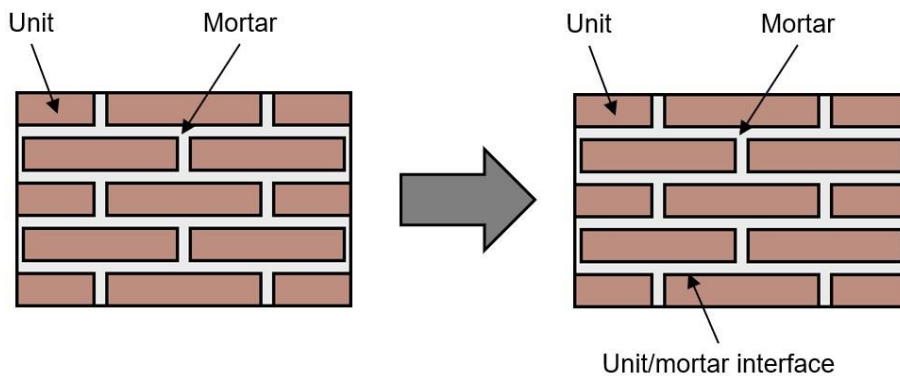


Fig. 2.2. Visual representation of the classic micro-modelling strategy.

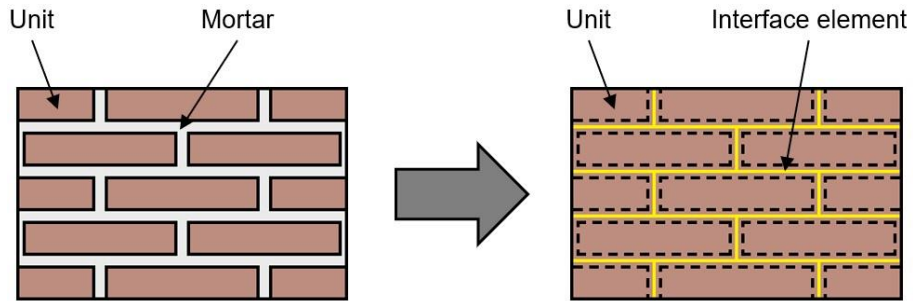


Fig. 2.3. Visual representation of the micro-modelling strategy with mortar joints reduced to interfaces.

The effectiveness of micro-modelling in simulating masonry-like materials is inquired by Baraldi and co-workers [11]. Here, a critical comparative review is presented among several strategies: one uses the Discrete Element Model (DEM), in which the units are rigid and the mortar joints are reduced to interfaces, another uses an heterogeneous Finite Element Model (FEM), and the last uses an equivalent homogeneous FEM. For the latter, the difference between Cauchy and micropolar continua is also investigated. The numerical applications involve masonry panels subjected to different constraints and loading conditions. The authors conclude that the heterogeneous FEM (corresponding to a micro-modelling strategy) is not the best performing model from both a mechanical and computational points of view. The effectiveness of DEM is further inquired in a separate, more recent work by Baraldi and co-workers [12]. Here, two numerical models are compared: a discrete model conceived by the authors, and a mixed discrete/finite element model that is usually adopted in rock mechanics. The numerical applications involve masonry panels of two distinct shapes (rectangular or square), presenting different slenderness, unit dimensions, and constraints. The results show how the discrete model necessitates a minor computational effort but is in general less accurate than the mixed discrete/finite element method. Nonetheless, both methods are suitable for investigating the non-linear response of masonry. Sarhosis & Lemos [13] instead present a detailed micro-modelling approach that considers units and mortar as consisting of irregular particles. This enables all types of failure in masonry: within units, within mortar, and at their interfaces. The numerical validation is successfully performed against the results obtained for small-scale experiments. The authors deem this approach as being a useful tool for reliably predicting the mechanical properties of masonry without resorting to pricey experimental campaigns or empirical formulae. A different, detailed micro-modelling approach is proposed by Zheng and co-workers [14], which employs extrinsic cohesive elements. The numerical validation is performed on

diagonally compressed stone masonry panels. Eventually, Petracca and co-workers [15] devise a continuous micro-model based on damage mechanics and used for representing both units and mortar. For the latter, a bi-dissipative damage model is employed to account for dilatancy. This model is directly compared and validated against two available discrete micro-models.

Several micro-modelling approaches where mortar joints are reduced to interfaces have been suggested over the years. For instance, Lotfi & Shing [16] conceive an interface constitutive model that simulates the initiation and propagation of cracks under a combination of normal and shear stresses; dilatancy is simulated as well. The proposed model is successfully validated for predicting the load-carrying capacity of a concrete masonry panel. Conversely, Lourenço & Rots [17] develop an elastoplastic interface constitutive model that is formulated in terms of softening plasticity for tension, shear, and also compression. The model is successfully validated for predicting the experimental collapse load of a masonry shear wall. Furthermore, Macorini & Izzuddin [18] present a 2D non-linear interface element that is used for modelling mortar and unit-mortar interfaces – while units are modelled through a 3D solid elements. The interface element accounts for non-linearities in both geometry (large displacements) and mechanics (work-softening non-associated plasticity). The interface element is successfully employed in a numerical validation that involves experimental in- and out-of-plane loaded walls. Analogously, Nazir & Dhanasekar [19] propose a non-linear interface element aiming at modelling thin layer mortared masonry. The element employs different failure criteria in the shear-tension and shear-compression regimes; its plastic flow vectors are analytically integrated within the implicit finite element framework. This interface element is calibrated through experimental results coming from compression, flexural and shear tests; it is then successfully validated for predicting the biaxial behavior of thin layer mortared masonry as well as the response of a shear wall consisting of the same masonry type.

The major drawback of micro-modelling is represented by its onerous computational requirements; even if the joints are reduced to interfaces (thus limiting variables, especially in the non-linear range) this approach remains very demanding, because units and mortar are meshed separately. In order to obtain sufficiently reliable solutions in terms of displacements and stresses, the constitutive materials should be meshed with more than one element, with the consequent growth in number of non-linear equations to deal with, even for small masonry panels. Partitioning methods have been recently proposed to overcome such computational limitations and speed up structural analyses (see

for instance Macorini & Izzuddin [20]), but it is safe to say that micro-modelling is at times an unfeasible numerical strategy due to its high computational costs.

2.1.3 Homogenization

Homogenization (Fig. 2.4) is a meso-scale averaging procedure that is performed on a basic cell called Representative Element of Volume (in short, REV). For periodic media, this is the smallest portion encompassing all the physical and geometrical characteristics needed for a complete description of the material. In fact, it must be capable of recreating the original periodic pattern by repetition, i.e. by translation in the 2D or 3D space. Homogenization represents a fair compromise between micro- and macro-modelling: in fact, it requires the accurate modelling of the material at the microscale – as in the former approach – but restricted only to the identified REV, thus greatly reducing the computational effort. On the other hand, homogenization aims at deriving macroscale properties for the considered material – as in the latter approach – but starting from a limited portion of the material itself (i.e. the REV), so that no lengthy and costly experimental campaigns are required.

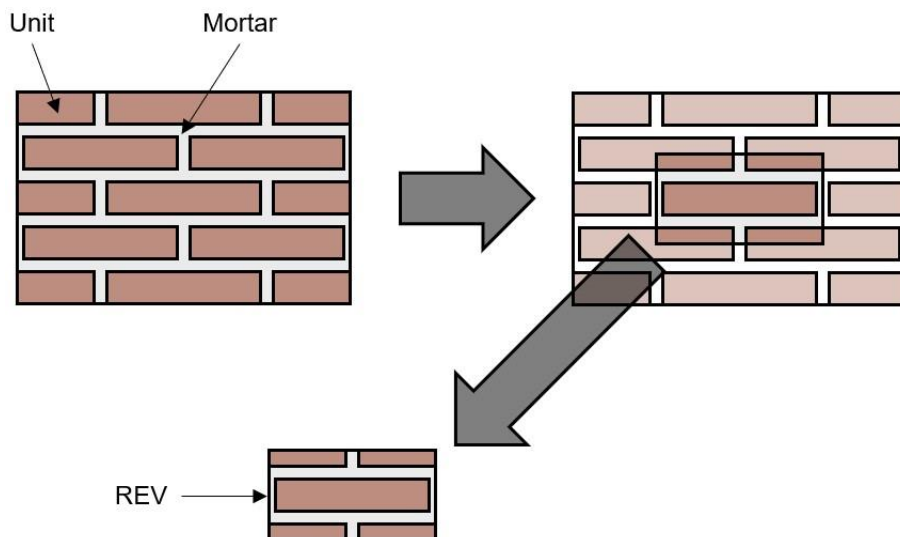


Fig. 2.4. Visual representation of the homogenization strategy applied to masonry.

Generally, masonry consists of bricks and/or stones - the units - joined by mortar and often assembled with a periodic arrangement (e.g. English, Flemish, stretcher bond), thus allowing for a successful application of homogenization.

2.2 Homogenization Applied to Periodic Masonry

2.2.1 Homogenization for Elastic Characteristics of Masonry

One of the earliest attempts to employ a homogenization technique in the assessment of masonry's mechanical characteristics is found in Pande and co-workers [21]. This application is devoted to evaluating the equivalent elastic moduli of brick masonry, albeit in an approximate way. Here, masonry is considered at the macro-scale as a homogenous orthorhombic elastic material (borrowing the concept of orthorhombic structure from crystallography).

A first, complete overview on the application of homogenization to periodic masonry is presented by Anthoine [22]. This work is remarkable because it offers a rigorous formulation of the homogenization problem, including the concept of periodic and anti-periodic fields; the strain-periodic displacement field is defined for both 2D and 3D periodic media. Here, the focus is on the application of homogenization in linear elasticity, aiming at evaluating the in-plane elastic characteristics; both units and mortar are considered as linear elastic materials. The numerical application employs the finite element method for both 2D and 3D periodic masonry, and in the former case is performed under the hypothesis of plane stress. Two types of periodic masonry are here studied: stack bond masonry and running bond masonry. The resulting elastic constants of the homogenized material are very similar for both masonry bonds in the 2D and 3D periodic cases; the homogenized material is also found to be orthotropic, as expected. Eventually, some issues that have proved to be relevant in later applications are here pointed out, for instance the errors possibly arising in the non-linear range from the plane stress assumption and the role played by masonry bond.

In an indirect follow-up of the previous work, Anthoine [23] presents an investigation on the proper assumption to be used in the homogenization of periodic masonry. Namely, three hypotheses are here compared: plane stress, generalized plane strain, and full 3D homogenization. The results show that the plane stress hypothesis is fairly suitable in the linear range (elasticity), whereas it leads to plain errors if used in the non-linear range (i.e. when introducing damage). Its use must also be limited if the considered periodic masonry is very thin. Conversely, generalized plane strain is deemed suitable for both the elastic linear and non-linear ranges. Eventually, it is stated that a full 3D homogenization should always be used in cases where the geometrical characteristics of masonry vary along the wall thickness. A subsequent effort

presented by Mistler and co-workers [24] deals with the generalization of homogenization for assessing also the out-of-plane behavior of periodic masonry, again limiting the scope to the linear range – i.e. extracting only the elastic in- and out-of-plane characteristics. In a more recent work, Addessi & Sacco [25] seek to overcome the limitations brought by the plane stress and generalized plane strain hypotheses. To do so, an enriched kinematic formulation is proposed, labelled Enriched Plate State (EPS), which introduces the out-of-plane strain components with non-null transversal displacements. Both units and mortar are considered as elastic isotropic materials. The results show that the proposed EPS formulation gives results that are more accurate than those obtained with plane stress, plane strain, and generalized plane strain; they are ultimately closer to those coming from a full 3D homogenization. The elastic domain of running bond masonry is eventually calculated.

Drougkas and co-workers [26] propose a model for the analysis of periodic masonry REV that is based on detailed micro-modelling principles. The model aims at evaluating the orthotropic elastic characteristics of periodic masonry; along with the usual stack and running bond masonry, it is applied also to the less common Flemish bond masonry. The numerical validation of the model is successfully carried out through comparisons with values experimentally obtained in compression for stack, running, and Flemish bond masonry, which are available in literature. Eventually, Di Nino & Luongo [27] conceive a homogenization procedure that enables the derivation of closed-form expression for the elastic characteristics of in-plane loaded running bond masonry. Here, the REV is modelled through several springs that are combined in series and parallel. The proposed procedure is successfully validated against results obtained with finite element analyses and with other approximated closed-form expressions.

Further elaborations on homogenization are discussed by Lourenço in a seminal work that extensively deals with this technique [28]. First, a novel 3D formulation for layered composites is proposed, not only in elasticity but also in elastoplasticity (namely, J_2 -plasticity). Then, this novel formulation is validated through three examples in which the results coming from the proposed 3D layered model are compared against those obtained with a 2D homogenization. Furthermore, the adequacy of two-step homogenization procedures – previously developed by other authors – is investigated for different stiffness ratios of the masonry constituents. Considerable errors are observed when the stiffness ratio is higher than 10 (which means being in presence of nonlinear behavior). Eventually, the behavior of masonry under tension parallel to the bed joints is

studied, which is used as an example of the application of a nonlinear homogenization technique.

Cecchi & Di Marco [29] perform an investigation regarding the influence of certain geometrical and mechanical parameters on the elastic characteristics of periodic masonry. Namely, they inquire the effect produced by two perturbative parameters: the variations of mortar joints' thickness with respect to that of the units, and the variations in stiffness of the units with respect to that of mortar joints. This investigation is performed for the two classical periodic masonry types, i.e. stack and running bond masonry. Among the results obtained from the investigation, running bond masonry displays greater stiffness with respect to stack bond masonry. Moreover, if the stiffness of only the head joints is increased, this has a relevant effect only on stack bond masonry.

Cecchi & Sab [30] propose an identification procedure that enables the formulation of two homogenized plate models, both referring to a numerical discrete 3D model. This consists of blocks (considered as infinitely rigid elements) that are connected through thin mortar joints (considered as elastic interfaces). The 3D model is then compared to both a homogenized Kirchhoff-Love plate model and a more refined Reissner-Mindlin plate model. While both plate models share the same bending constants, the shear parameters in the latter plate model are evaluated through a compatible identification procedure that occurs between the original discrete 3D model and the homogenized Reissner-Mindlin one. A case study is then considered to draw comparisons between the results obtained with the discrete 3D model and the two homogenized plate models. Namely, a series of numerical analyses is performed on the case study in which several parameters denoting the physical characteristics of the case study itself are varied. The results show that both the homogenized plate models ultimately coincide in an asymptotic fashion with the discrete 3D model, although the Reissner-Mindlin model shows a better convergence.

2.2.2 Homogenization for Non-Linear Analysis of Masonry

Homogenization is also extensively employed as a useful and reliable technique for applications that involve non-linear analyses of masonry. For instance, Reccia and co-workers [31] envision a full 3D homogenization procedure to perform non-linear finite element analyses of bridges. Focusing on the Venice trans-lagoon railway bridge as a final application, each of its components is modelled with rigid parallelepiped elements and quadrilateral interfaces. These

employ an orthotropic constitutive law with softening. The considered bridge is investigated both under service loads and up to failure due to the crossing of a train. The results are then compared with collapse loads and failure mechanisms predicted by limit analysis. Milani & Bertolesi [32] propose a quasi-analytical homogenization approach aiming at performing non-linear analysis on in-plane loaded running bond masonry walls. This approach uses a model for mortar joints that considers their softening behavior. The REV is discretized with triangular elastic finite elements and non-linear joints that are reduced to interfaces, the latter displaying a holonomic behavior. The homogenized stress-strain diagrams are evaluated through the proposed quasi-analytical method, and they can be either implemented in a finite element code or a rigid element approach. The numerical validation is successfully performed on an experimentally tested windowed masonry panel.

Milani & Bruggi [33] present a two-step procedure based on topology optimization and homogenization devoted to carrying out 2D pushover analyses in a steadfast way. The overall model employs triangular rigid finite elements and non-linear interfaces. The first step (topology optimization) determines the optimal shape of the mesh and position of the interfaces, whose mechanical properties are evaluated through homogenization in the non-linear range. The second step occurs at a structural level, where the pushover analyses are carried out. The validation is successfully performed on a multi-story windowed masonry wall. Another application aiming at performing pushover analyses is introduced by Casolo & Milani [34]. Here, homogenization is exploited to derive out-of-plane moment-curvature diagrams for masonry – two in bending and one in torsion – later used as constitutive models for the springs in a discrete model called Rigid Body and Spring Model (RBSM). This is introduced in an earlier solo work by Casolo [35] and is conceived for modelling the in-plane behavior of masonry walls. These are discretized with plane rigid elements connected through a system of normal and shear springs. The main advantage of RBSM is that the nonlinearities (of any kind) can be concentrated in the springs which are discrete elements and not continuous, thus simplifying the problem. The numerical application in [34] focuses on the pushover analysis of out-of-plane loaded masonry walls. Furthermore, Petracca and co-workers [36] propose a homogenization method grounded on the thick shell theory aiming at tackling the analysis of out-of-plane loaded masonry walls. The main innovation here is that both units and mortar are modelled with a non-linear behavior; namely, tension/compression continuum damage constitutive laws are employed. The method here presented is successfully assessed through comparisons with

results coming from a running bond masonry wall that is experimentally tested under out-of-plane actions.

2.2.3 Homogenization for Modelling Damage in Masonry

As already pointed out in Section 2.1.1, finding effective ways to model the evolution of damage for masonry is paramount to fully grasp its mechanical behavior in the non-linear range. Hence, several works deal with formulations of the homogenization approach that include or produce damage models for simulating the formation of cracks in masonry. An early example is provided by Pegon & Anthoine [37] containing a detailed discussion on how to formulate the homogenization problem when units and mortar are endowed with a continuum damage model. Plane stress and generalized plane strain are assumed as the two main working hypotheses. Also, suitable numerical strategies to solve this problem are presented, along with a numerical application on a running bond masonry REV.

Luciano & Sacco [38] seek to use homogenization for developing a damage model that is specifically applicable to historical masonry. Here, homogenization is actually employed for deriving the elastic moduli of uncracked and cracked masonry. From this, a damage evolution law is obtained for masonry that considers the correct geometry and the mechanical properties of the two constitutive materials. Finally, two damage constitutive laws are defined for the homogenized material based on the strength of mortar: one uses an energy criterion, the other a cohesive Coulomb criterion. The numerical applications involve a running bond masonry REV and a full masonry wall. Similarly, Zucchini & Lourenço [39] propose a problem formulation that combines a micro-mechanical homogenization model and an isotropic damage model for units and mortar. The definition of a crack opening width for the REV's head joint is also provided. An iterative procedure is used to solve the problem and to evaluate the damage parameters. The numerical application again focuses on running bond masonry.

Rekik & Lebon [40] devise a procedure that exploits homogenization for modelling interface damage in masonry. Here, the material is thought as consisting of three different constituents: units, mortar, and their mutual interfaces. The latter display small thickness, low stiffness, and a predetermined damage ratio. The procedure enables to extract the properties of the interface material, and follows three steps: in the first one, homogenization is applied to the undamaged unit/mortar material, obtaining a first homogeneous equivalent

material. In the second step, this resulting material is supposed to be damaged, and the assessment of its global behavior leads to defining a second homogeneous equivalent material. In the third and last step, an asymptotic analysis is carried out to this second material as an interface, thus deducing the properties of the interface material from those of the second material. From a computational point of view, the interfaces are modelled as connector finite elements. The procedure is successfully validating against experimental data in two applications: one involves a triplet of solid bricks, the other a triplet of hollow bricks. A different procedure is presented by Sacco & Lebon [41] aiming at deriving a damage-friction constitutive law for the unit/mortar interface. The chosen model for such interface takes several features into account: the evolution of cracks, the unilateral contact originating by crack closure, and the effect of friction. A non-linear micro-mechanical problem is then formulated; its solution consists in the formulation of three linear subproblems, whose solutions are then aptly combined to provide the solution of the original non-linear problem. Eventually, the procedure is applied to an analytical REV consisting of two layers (unit and mortar) and a micro-crack between them; the reliability of the interface model is investigated under mode I, mode II, and mixed mode numerical fracture tests.

2.3 Homogenization and Limit Analysis

Despite its inability to address the post-peak behavior of structures, limit analysis remains a quick and simple approach for assessing their structural response at collapse (e.g. in terms of load multiplier and failure mechanisms). Indeed, the combination of limit analysis and homogenization for modelling the collapse behavior of masonry has been explored in literature over the last twenty years. An early application in this regard is presented by de Buhan & de Felice [42], showing how the implementation of homogenization within a limit analysis approach is capable of providing a macroscopic strength criterion of the homogenized masonry. Namely, an upper-bound approach is used here on the limit analysis side of the problem. As a numerical application, the results obtained from the theoretical formulation of the combined homogenization-limit analysis problem are utilized to evaluate the stability of laterally loaded wall specimens.

2.3.1 In-Plane Collapse Behavior

Comprehensibly, the combination of homogenization and limit analysis is exploited by some scholars to assess the in-plane collapse behavior of masonry. The first part of a seminal work by Milani and co-workers [43] presents a micro-mechanical approach for the homogenized limit analysis of masonry walls subjected to in-plane loads. The REV is divided into 36 sub-domains (reduced to 9 if only one quarter is considered, see Fig. 2.5); the homogenization problem is formulated as a linear optimization problem for the rigid-plastic case, in which units and mortar joints are rigid, therefore discontinuities can only occur at their mutual interfaces. Mortar joints can also be reduced to interfaces for sake of simplicity.

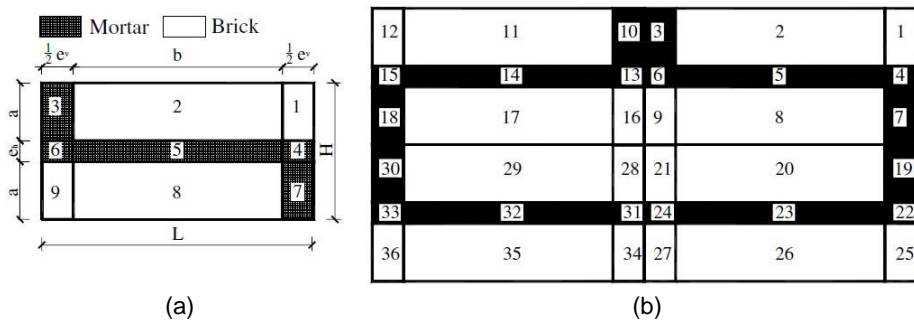


Fig. 2.5. (a) Division of one quarter of the REV in 9 sub-domains; (b) division of the whole REV in 36 sub-domains by Milani and co-workers [43].

The problem is also formulated under the hypothesis of plane stress; the expression for the 2D stress field adopts a polynomial expansion (which means that the limit analysis part of the problem uses a lower-bound approach). First, a preliminary investigation on the elastic characteristics is carried out, comparing the results to those obtained by Anthoine in [22]. Then, the overall problem is applied to the derivation of homogenized failure surfaces, which here represent the macroscopic strength criteria for masonry previously discussed. The reliability of the proposed model is tested against the results presented by de Buhan & de Felice [42] (see Fig. 2.6) in the tensile-tensile range, with the aim of draw comparisons with a closed-form solution coming from an upper-bound approach. Other numerical applications involve the results obtained experimentally by other authors. In one case, the present problem is reformulated using an upper-bound approach – the units are infinitely resistant, and the joints are reduced to interfaces are endowed with a frictional failure surface and a compression cut-off. Eventually, a comparison is drawn between

the lower- and upper-bound approaches, as shown in Fig. 2.7 for a particular case.

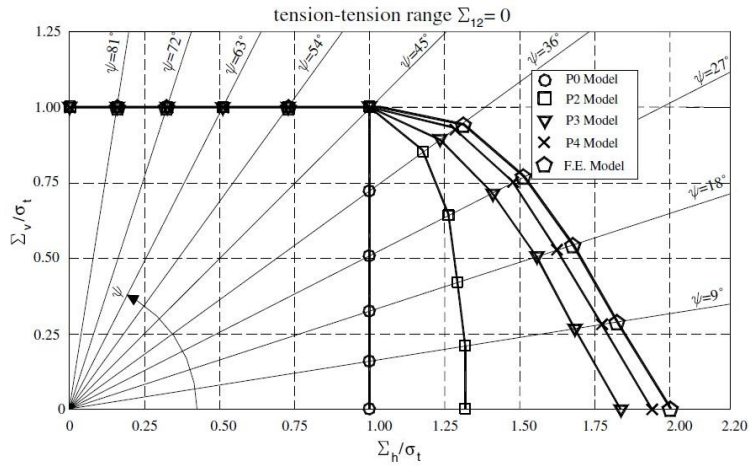


Fig. 2.6. Comparison of the results obtained by Milani and co-workers for different polynomial expansions by Milani and co-workers [43]; the results are also compared to those derived by de Buhan and de Felice.

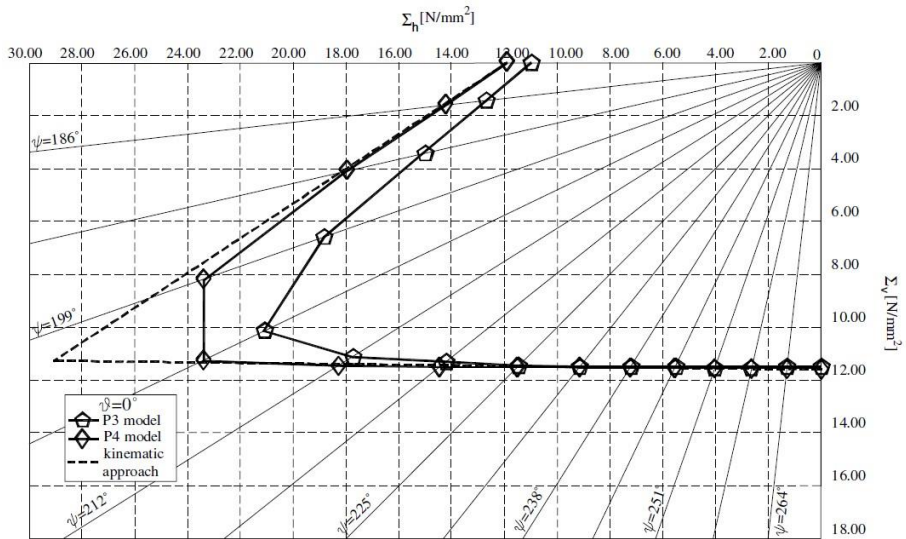


Fig. 2.7. Comparison between the lower- and upper-bound approaches by Milani and co-workers [43].

The second part, which is the direct follow-up of the first one and is also authored by Milani and co-workers [44], presents a few structural applications of the micro-

mechanical approach for the homogenized limit analysis described in the first part. First, the lower- and upper-bound formulations of the approach are recalled; then, three case studies are considered for numerical applications, comparing the analytical results to experimental data previously obtained for the same cases. Namely, the three considered applications are a masonry panel acting as a deep beam, a masonry shear wall, and one inner wall of a five-story building located in Catania, Italy. All the three case studies are investigated employing both the lower- and upper-bound approaches, and give satisfactory results – especially for the upper-bound approach.

A further solo work by Milani [45] introduces a different homogenized model that considers the softening behavior of in-plane loaded masonry, aiming at performing non-linear analyses. The overall procedure consists of two steps; in the first, the considered REV is discretized into triangular elastic finite elements and non-linear interfaces in place of mortar joints. A standard non-linear finite element approach is enforced on the REV, which results in homogenized stress-strain diagrams. In the second step (taking place at a structural level) the sought-after non-linear analyses are performed using triangular rigid elements joined by non-linear interfaces to which the previously obtained homogenized diagrams are assigned. This discretized non-linear problem is solved through a standard quadratic programming algorithm. The numerical applications involve a masonry panel acting as a deep beam and a windowed masonry shear walls, for both of which the analytical results are compared to available experimental data.

A different approach for deriving the macroscopic strength criteria is used in a work by Milani & Taliervo [46] combining the upper bound theorem of limit analysis with homogenization. This approach is analogous to the so-called “Method of Cells”, originally developed for fiber-reinforced unidirectional composites. The REV is sub-divided into rectangular cells (see Fig. 2.8a), in which two strain-rate periodic, piecewise differentiable velocity fields are employed that characterize the deformation mode for macroscopic normal stresses (Fig. 2.8b) and for macroscopic shear stresses (Fig. 2.8c).

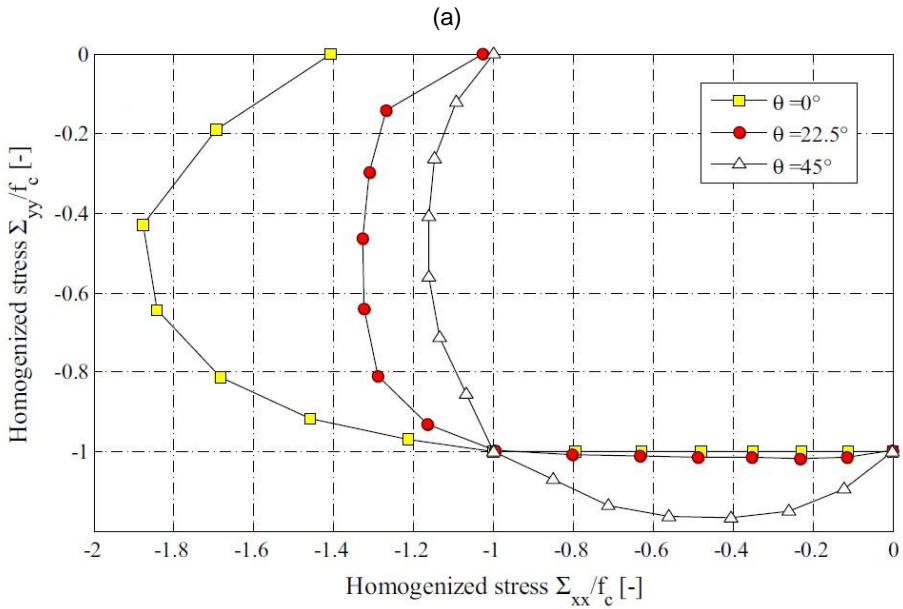
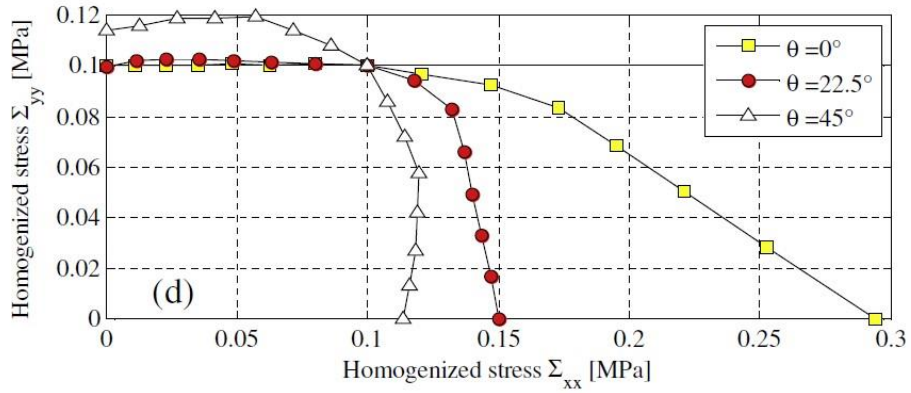


Fig. 2.9. (a) Homogenized failure surfaces obtained with the proposed method in the tension-tension range; (b) homogenized failure surfaces obtained with the proposed method in the compression-compression range by Milani & Taliercio [46].

Other relevant approaches are presented by Stefanou and co-workers [47] and by Godio and co-workers [48]. The former performs a full 3D homogenization and considers separate yield surfaces for the failure of units and mortar; the latter provides a procedure for the assessment of the in-plane strength domain of discrete media, here applied to masonry, which is formulated in the framework of the Cosserat continuum theory.

2.3.2 Out-of-Plane Collapse Behavior

Only a few works available in literature deal with the out-of-plane collapse behavior of masonry. For instance, Milani and co-workers [49] present an approach that expands upon the one presented in [43]; here, the masonry REV is considered as consisting of several layers over the thickness, for which a Kirchhoff-Love plate model is used. An anisotropic failure surface is employed that is grounded on a polynomial representation of the stress tensor components in a predetermined number of sub-domains. This is then combined to triangular finite elements. The linear optimization problem is eventually formulated using both a lower- and an upper-bound approach. In this case, the results consist of the internal forces distribution in critical sections for the lower-bound approach, and of failure loads and collapse modes for the upper-bound approach. The proposed methodology is successfully validated against the results obtained for several experimental tests. First, an assessment of the method's reliability is carried out by considering four-point bending tests performed on hollow concrete masonry wallets, characterized by different orientations of the bed joints. Then, two different sets of experimental tests are utilized for validation: one consists of hollow concrete masonry panels tested under out-of-plane load conditions and displaying different boundary conditions; the other consists of brick masonry walls again tested under out-of-plane load conditions and displaying the presence of different openings.

Sab and co-workers [50] aim at determining the yield strength domain for out-of-plane loaded brick masonry. Their procedure is applicable to either thin or thick periodic brick masonry panels, and is oriented to the usual stack and running bond masonry types. In both cases, units are considered infinitely rigid and are connected through Mohr-Coulomb interfaces. The Kirchhoff-Love plate model is first applied to the considered masonry panel for in- and out-of-plane load conditions; then, a Reissner-Mindlin plate model is also employed to grasp the influence of out-of-plane shear forces. The out-of-plane yield strength domains are eventually extracted for running bond masonry, following an upper-bound approach for the combined homogenization-limit analysis problem.

A similar approach is used by Cecchi and co-workers [51] specifically devised for out-of-plane loaded running bond masonry; also here, an upper-bound limit analysis approach is employed, along with a Reissner-Mindlin plate model. The procedure uses the so-called "kinematic identification" previously described in [30]: first, a 3D system of blocks connected by interfaces is considered (Fig. 2.10), in which the blocks are infinitely resistant and the interfaces (representing

the mortar joints) are provided with an associate flow rule and a Mohr-Coulomb failure criterion with cut-offs in tension and compression. Then, this 3D system of blocks is kinematically identified with a 2D Reissner-Mindlin plate.

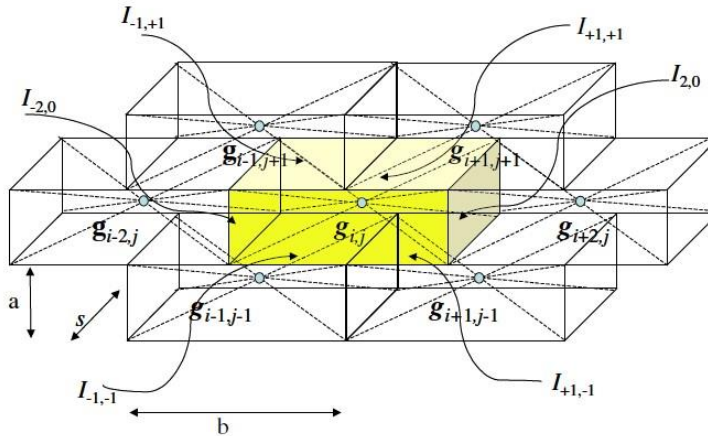


Fig. 2.10. 3D system of blocks for the kinematic identification by Cecchi & Sab [30] and by Cecchi and co-workers [51].

This work does not directly use a rigorous homogenization approach, yet it is still able to derive the out-of-plane homogenized failure surfaces (i.e. the macroscopic strength criteria) as the results of a linear programming problem in which the dissipated internal power is the function to minimize. The out-of-plane homogenized failure surfaces are expressed as functions of macroscopic bending and torsional moments, and are also function of the macroscopic shear forces. For instance, Fig. 2.11 reports the out-of-plane homogenized failure surface in the M_{11} - M_{22} plane for different values of the macroscopic shear force T_{13} , where M_{11} and M_{22} are the macroscopic horizontal and vertical bending moments, respectively; this failure surface is characterized by a parallelogram-like shape. Conversely, Fig. 2.12 reports the out-of-plane homogenized failure surface in the M_{11} - M_{12} plane, again for different values of the macroscopic shear force T_{13} . M_{12} is the macroscopic torsional moment; unlike the previous one, this failure surface is characterized by a hexagonal shape. Eventually, two structural examples are analyzed to compare the proposed Reissner-Mindlin model to a Kirchhoff-Love homogenization-limit analysis approach: one consists of a masonry wall subjected to cylindrical bending, the other of a rectangular masonry plate presenting a central window.

A distinct but related work presented by Cecchi & Milani [52] employs the same approach, here instead applied to English bond masonry.

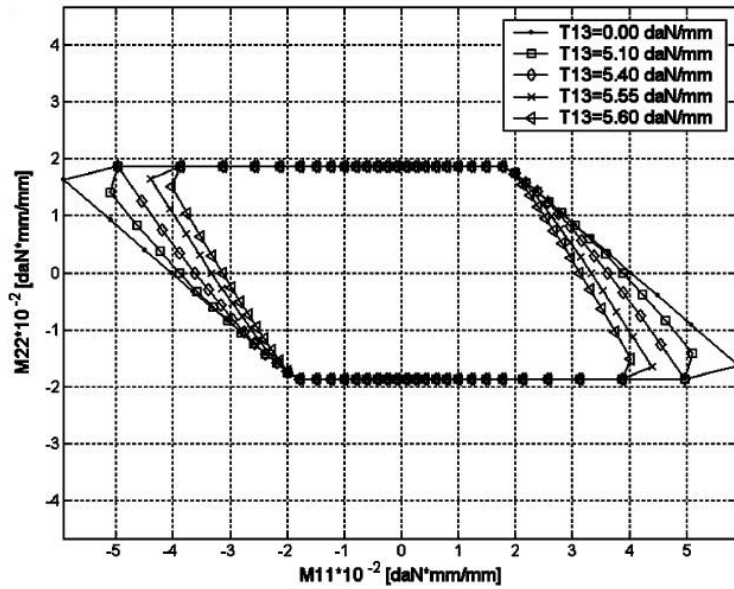


Fig. 2.11. Out-of-plane homogenized failure surface in the M_{11} - M_{22} plane, for different values of the macroscopic shear force T_{13} by Cecchi and co-workers [51].

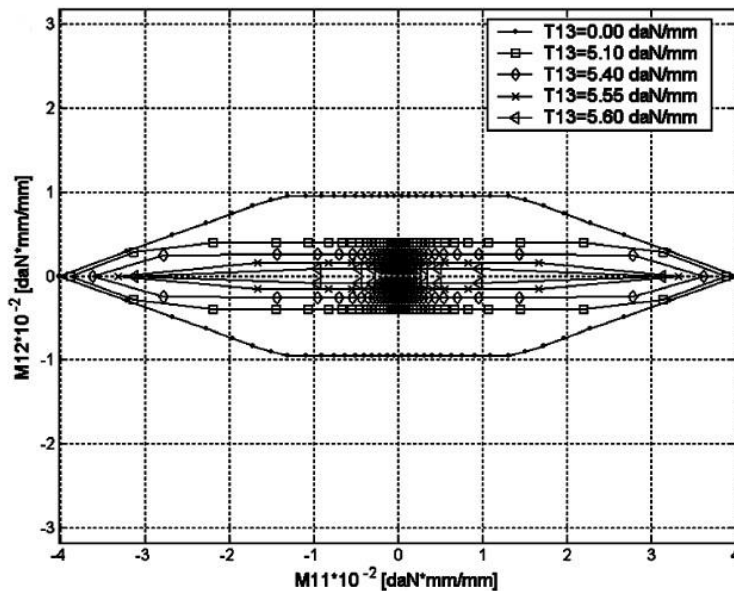


Fig. 2.12. Out-of-plane homogenized failure surface in the M_{11} - M_{12} plane, for different values of the macroscopic shear force T_{13} by Cecchi and co-workers [51].

Finally, Milani & Taliercio [53] propose an extension to the out-of-plane case of the approach based on the Method of Cells previously developed for the in-plane case [46]. In this application, the horizontal and vertical bending moments, as well as the torsional one, are first defined (Fig. 2.13).

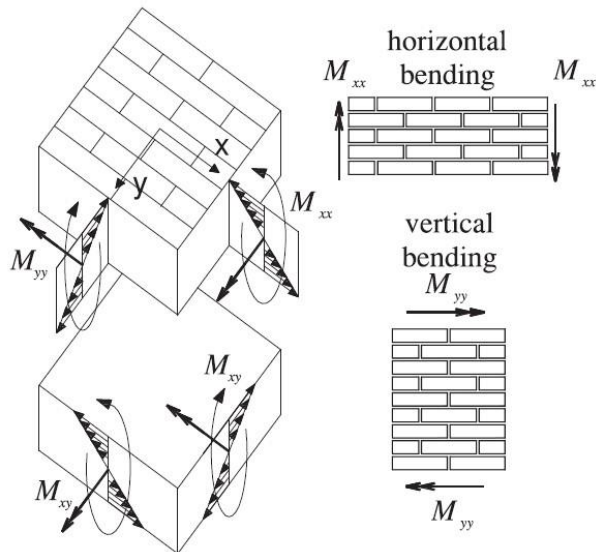


Fig. 2.13. Definition of horizontal bending moment (M_{xx}), vertical bending moment (M_{yy}), and torsional moment (M_{xy}) by Milani & Taliercio [53].

Then, the upper-bound approach for deriving the out-of-plane homogenized failure surfaces is described. Several features are investigated in terms of out-of-plane response: namely, the use of interfaces in lieu of joints with finite thickness (Fig. 2.14 and Fig. 2.15), the 3D effects observed in masonry walls with thick joints, and the influence of joints' thickness on the out-of-plane behavior under vertical pre-compression are each addressed. Two structural examples are eventually considered for the numerical validation of the proposed approach: one involves an orthotropic rectangular masonry wall (considered as a plate), the other involves several windowed masonry panels.

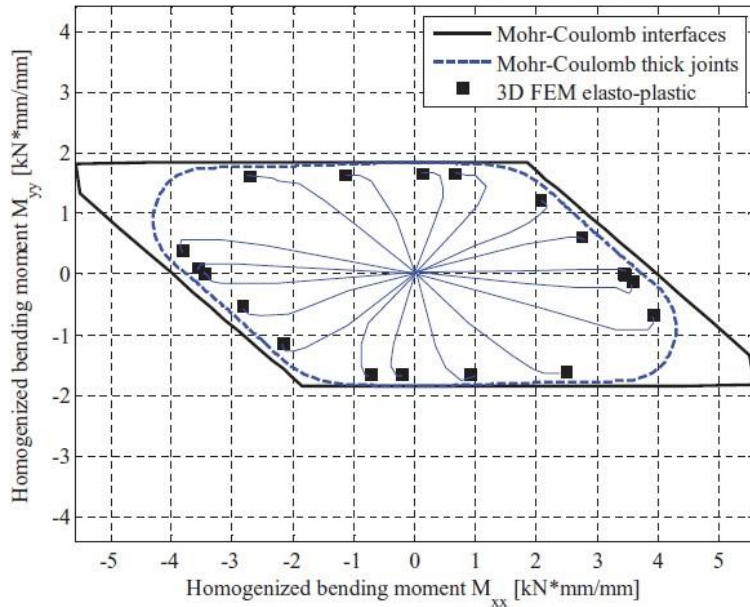


Fig. 2.14. Comparison of out-of-plane homogenized failure surfaces obtained with different approaches in the M_{xx} - M_{yy} plane by Milani & Taliercio [53].

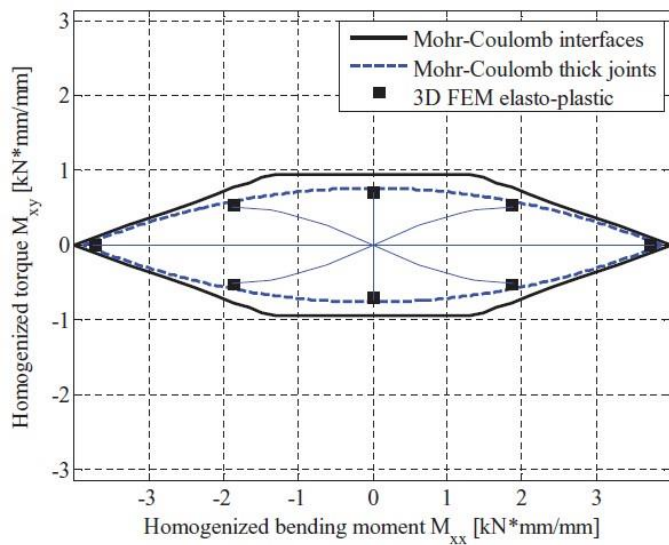


Fig. 2.15. Comparison of out-of-plane homogenized failure surfaces obtained with different approaches in the M_{xx} - M_{xy} plane by Milani & Taliercio [53].

2.4 Homogenization Applied to Non-Periodic Masonry

The application of homogenization techniques to the analysis of historical masonry structures appears natural and capable of producing promising results. For instance, the immediate applicability of homogenization to the representation of old masonry material is recognized by Luciano & Sacco in [38], already recapped in Section 2.2.3; another relevant application of homogenization to a historical structure (namely, the Venice trans-lagoon railway bridge) is the work by Reccia and co-workers cited in Section 2.2.2 [31]. Furthermore, Zeman and co-workers [54] employ a homogenization approach to obtain macro-scale mechanical characteristics for the periodic sandstone masonry that characterizes the vaults of the Charles Bridge in Prague; this represents just one part of a broader work aiming at a multi-scale and multi-physics analysis of that monumental bridge.

However, the founding idea behind homogenization (i.e. the identification of a REV) implies that its use is only limited to those masonry buildings where the units are periodically arranged. On the other hand, several old constructions consist of stone masonry in which the units are assembled randomly, or at least without a clear periodic pattern. Some real instances are shown in Fig. 2.16b-d, taken from both monumental and ordinary masonry buildings located in Italy. Another example is represented by the previously mentioned Charles Bridge in Prague, which is truly significant because it displays several types of masonry bonds [54]. Along with the periodic sandstone masonry of its vaults, the bridge consists of non-periodic sandstone masonry (located in the breast walls) and of irregular quarry masonry (used as infill).

The generic term “non-periodic masonry” is used to describe all those masonry bonds in which the units are not arranged according to a periodic pattern. More specific terms exist to define the various cases: for instance, masonry displaying a wholly random arrangement of the units is called “rubble masonry”; masonry consisting of units with non-uniform geometry but clearly visible mortar bed joints is called “quasi-periodic masonry”; finally, masonry consisting of units with similar (but not equal) geometry and clearly visible mortar bed joints is called “quasi-regular masonry”. Nonetheless, any effective application of homogenization is apparently ruled out in these cases, since the identification of a suitable REV appears cumbersome, if not impossible.



(a)



(b)



(c)



(d)

Fig. 2.16. (a) Brick masonry tower (“Castello delle Rocche” in Finale Emilia, Modena, Italy); (b) rubble masonry tower (outer city walls in Norcia, Perugia, Italy); (c) residential rubble masonry building in Pretare, Ascoli Piceno, Italy; (d) rubble masonry used as infills (outside wall of the Baths of Caracalla, Rome, Italy).

The application of homogenization to non-periodic masonry is first addressed in a work by Cluni & Gusella [55]. Here, the aim is the derivation of homogenized medium stiffness tensor coefficients for a non-periodic masonry panel. The presented approach is based on the concept of “test-window” – a cell of finite size extracted from the considered masonry panel. The stiffness tensor coefficients are derived from averaging those obtained for several test-windows of the same size that are extracted from different locations on the panel. The size of the test-window is then increased, and the procedure is repeated also evaluating the variations in terms of coefficients due to the expansion of the test-window itself. The actual size of the REV is determined when, after a series of iterations, that variation becomes sufficiently small.

Cavalagli and co-workers [56][57] show that it is still possible to identify a REV through the use of statistical tools (here represented by Monte Carlo simulations), provided that the selected cell is a statistically acceptable representation of the considered non-periodic masonry. Therefore, the concept of Representative Element of Volume evolves into that of a Statistically Equivalent Periodic Unit Cell (abbreviated with the acronym SEPUC). This new entity is introduced in a work by Zeman & Šejnoha [58] concerning the derivation of a Representative Element of Volume from a random microstructure. The concept is further explored in a later work by Šejnoha and co-workers [59] devoted to the study of historical masonry, with a specific focus on the non-periodic masonry bonds observed in the aforementioned Charles Bridge in Prague. Finally, it must be noted that the concept of SEPUC is sufficiently general to enable its application to other non-periodic media such as mastic asphalt mixtures [60], plain weave composites [61], and porous materials [62].

A different approach is presented in a series of two works authored by Milani & Lourenço [63][64]. These aim at deriving in- and out-of-plane homogenized failure surfaces for a REV consisting of a central block encircled by several others in a random arrangement, all connected through rigid-plastic interfaces. Here, a series of Monte Carlo simulations is repeated on the REV, assuming the length and height of each block as stochastic variables. This is equivalent to consider a random disposition of the mortar joints, implying that the overall dimensions of the REV vary at each Monte Carlo simulation. An envelope of homogenized failure surfaces is then obtained, and its average is deemed representative of the chosen geometry.

Eventually, Cecchi & Sab use the identification procedure they previously presented in [30] to address the in-plane [65] and out-of-plane [66] elastic response of brickwork displaying a random arrangement of blocks. In both cases, the starting point is a cell consisting of one central block encircled by six other blocks, arranged with a running bond pattern. Therefore, a random perturbation (ultimately expressed as a parameter) is introduced into this discrete model by changing the position of the vertical interfaces between the various blocks, which implies a random variation of their length - their height and width are instead unaffected. The effects of the random perturbation are inquired in terms of the effective elastic moduli of the homogenized plate model for the in-plane case, and in terms of the bending stiffnesses for the out-of-plane case. The extension of this approach to the elastoplastic range is carried out in a work by Baraldi & Cecchi [67], where they add a further perturbation in which also the height of the blocks is changed. The structural application focuses on the

collapse behavior of rectangular masonry panels, expressed in terms of collapse load and failure mechanisms.

2.4.1 Homogenization Applied to Non-Periodic Multi-Leaf Walls

The literature dealing with multi-leaf walls is in general very scarce; works that seek to apply homogenization to such kind of walls are practically nonexistent. One attempt can be found in the work of Drougkas and co-workers [26], where the proposed model for the analysis of periodic masonry is aptly modified to account for a three-leaf running bond masonry wall. An application directly devoted to the study of multi-leaf walls is presented by Casolo & Milani [68]. Here, the investigation involves two three-leaf walls presenting a quasi-periodic arrangement of units: one wall consists of large squat blocks and weak transversal interconnection, whereas the other has longer clay bricks with slightly better transversal interconnection. Three mechanical models are devised for representation at the meso-scale:

- One employing a simplified FE averaging procedure on a sufficiently large REV subject to increasing bending and torsion.
- One making use of a simplified kinematics of the REV in both the outer wythes and the inner filler, which are treated independently.
- One exploiting the RBSM with suitable nonlinear mechanical properties for the springs, considering limited interlocking between core and external layers.

All three models are required to reproduce (1) orthotropy in bending, depending on texture and transversal interlocking, and (2) the influence of vertical in-plane pre-compression, both during pre-peak and post-peak phases. The numerical application employs only the RBSM for the study of a church façade damaged during the Friuli earthquake.

2.5 Conclusions

An exhaustive literature review has been carried out in this chapter, focused on the numerical strategies commonly adopted for modelling masonry and with a special attention to the technique known as homogenization in all its applications. Some considerations can be inferred from the presented literature review:

-
- The macro- and micro-modelling numerical strategies have found and still find extensive use in literature, despite their undeniable drawbacks: this is due to the immediate applicability to large-scale structures in the case of macro-modelling, and to the undeniable accuracy in representing the actual configuration of masonry in the case of micro-modelling.
 - Over the last quarter of century, homogenization has emerged as a viable and reliable numerical strategy for the mechanical modelling of periodic masonry, representing a satisfying compromise between the macro- and micro-modelling.
 - Since the beginning of its popularity and until nowadays, the main application of homogenization is oriented to deriving the elastic characteristics of masonry, which is most commonly (and rightfully) modelled as an orthotropic material.
 - Homogenization has proved its usefulness also for non-linear applications, either devoted to performing non-linear analyses or to defining damage models.
 - The pairing of homogenization and the lower and upper bound theorem of limit analysis has been explored by some authors, giving interesting results in terms of in- and out-of-plane collapse behavior of masonry.
 - Despite an apparent contradiction to its founding concept (the identification of a Representative Element of Volume), some methods have been developed that enable the application of homogenization also to non-periodic masonry.
 - The study of multi-leaf walls is seldom addressed by the technical literature, let alone the application of homogenization for assessing their macroscopic behavior.

From the literature review, it clearly emerges the lack of a comprehensive model for non-periodic masonry that combines homogenization and limit analysis. This model must be capable of considering the actual bond of real non-periodic masonry panels, therefore it requires also the implementation of a procedure devoted to the creation of a 2D or 3D finite element mesh from the image (or simply the sketch) of the real non-periodic masonry panel under consideration. The model must also be capable of addressing both the in- and out-of-plane

collapse behavior of non-periodic masonry, with the possibility to extract the deformed shapes at collapse for selected in- and out-of-plane load conditions. Eventually, the formulation of the model must be general enough to be extended to multi-leaf non-periodic masonry walls, for which the lack of dedicated literature is most evident.

2.6 References

- [1] European Committee for Standardization. (2005). Eurocode 6: Design of masonry structures - Part 1-1: General rules for reinforced and unreinforced masonry structures (EN 1996-1-1). Central Secretariat, CEN.
- [2] Di Pasquale, S. (1992). New trends in the analysis of masonry structures. *Meccanica*, 27(3), 173-184.
- [3] Lourenço, P. B., de Borst, R., & Rots, J. G. (1997). A plane stress softening plasticity model for orthotropic materials. *International Journal for Numerical Methods in Engineering*, 40(21), 4033-4057.
- [4] Lourenço, P. B., Rots, J. G., & Blaauwendraad, J. (1998). Continuum model for masonry: parameter estimation and validation. *Journal of Structural Engineering*, 124(6), 642-652.
- [5] Pelà, L., Cervera, M., Oller, S., & Chiumenti, M. (2014). A localized mapped damage model for orthotropic materials. *Engineering Fracture Mechanics*, 124, 196-216.
- [6] Toti, J., Gattulli, V., & Sacco, E. (2015). Nonlocal damage propagation in the dynamics of masonry elements. *Computers & Structures*, 152, 215-227.
- [7] Gatta, C., Addessi, D., & Vestroni, F. (2018). Static and dynamic nonlinear response of masonry walls. *International Journal of Solids and Structures*, 155, 291-303.
- [8] Saloustros, S., Cervera, M., & Pelà, L. (2018). Tracking multi-directional intersecting cracks in numerical modelling of masonry shear walls under cyclic loading. *Meccanica*, 53(7), 1757-1776.
- [9] Clementi, F., Ferrante, A., Giordano, E., Dubois, F., & Lenci, S. (2019). Damage assessment of ancient masonry churches stroked by the Central Italy earthquakes of 2016 by the non-smooth contact dynamics method. *Bulletin of Earthquake Engineering*, 1-32.
- [10] Miccoli, L., Garofano, A., Fontana, P., & Müller, U. (2015). Experimental testing and finite element modelling of earth block masonry. *Engineering Structures*, 104, 80-94.
- [11] Baraldi, D., Cecchi, A., & Tralli, A. (2015). Continuous and discrete models for masonry like material: A critical comparative study. *European Journal of Mechanics-A/Solids*, 50, 39-58.
- [12] Baraldi, D., Reccia, E., & Cecchi, A. (2018). In plane loaded masonry walls: DEM and FEM/DEM models. A critical review. *Meccanica*, 53(7), 1613-1628.

-
- [13] Sarhosis, V., & Lemos, J. V. (2018). A detailed micro-modelling approach for the structural analysis of masonry assemblages. *Computers & Structures*, 206, 66-81.
- [14] Zhang, S., Mousavi, S. M. T., Richart, N., Molinari, J. F., & Beyer, K. (2017). Micro-mechanical finite element modeling of diagonal compression test for historical stone masonry structure. *International Journal of Solids and Structures*, 112, 122-132.
- [15] Petracca, M., Pelà, L., Rossi, R., Zaghi, S., Camata, G., & Spacone, E. (2017). Micro-scale continuous and discrete numerical models for nonlinear analysis of masonry shear walls. *Construction and Building Materials*, 149, 296-314.
- [16] Lotfi, H. R., & Shing, P. B. (1994). Interface model applied to fracture of masonry structures. *Journal of Structural Engineering*, 120(1), 63-80.
- [17] Lourenço, P. B., & Rots, J. G. (1997). Multisurface interface model for analysis of masonry structures. *Journal of Engineering Mechanics*, 123(7), 660-668.
- [18] Macorini, L., & Izzuddin, B. A. (2011). A non-linear interface element for 3D mesoscale analysis of brick-masonry structures. *International Journal for Numerical Methods in Engineering*, 85(12), 1584-1608.
- [19] Nazir, S., & Dhanasekar, M. (2014). A non-linear interface element model for thin layer high adhesive mortared masonry. *Computers & Structures*, 144, 23-39.
- [20] Macorini, L., & Izzuddin, B. A. (2013). Nonlinear analysis of masonry structures using mesoscale partitioned modelling. *Advances in Engineering Software*, 60, 58-69.
- [21] Pande, G. N., Liang, J. X., & Middleton, J. (1989). Equivalent elastic moduli for brick masonry. *Computers and Geotechnics*, 8(3), 243-265.
- [22] Anthoine, A. (1995). Derivation of the in-plane elastic characteristics of masonry through homogenization theory. *International Journal of Solids and Structures*, 32(2), 137-163.
- [23] Anthoine, A. (1997). Homogenization of periodic masonry: plane stress, generalized plane strain or 3D modelling? *Communications in Numerical Methods in Engineering*, 13(5), 319-326.
- [24] Mistler, M., Anthoine, A., & Butenweg, C. (2007). In-plane and out-of-plane homogenisation of masonry. *Computers & Structures*, 85(17-18), 1321-1330.
-

-
- [25] Addessi, D., & Sacco, E. (2014). A kinematic enriched plane state formulation for the analysis of masonry panels. *European Journal of Mechanics-A/Solids*, 44, 188-200.
- [26] Drougkas, A., Roca, P., & Molins, C. (2015). Analytical micro-modeling of masonry periodic unit cells – Elastic properties. *International Journal of Solids and Structures*, 69, 169-188.
- [27] Di Nino, S., & Luongo, A. (2019). A simple homogenized orthotropic model for in-plane analysis of regular masonry walls. *International Journal of Solids and Structures*, 167, 156-169.
- [28] Lourenco, P. B. (1996). Computational strategies for masonry structures [Ph. D. thesis]. *Delft University, The Netherlands*.
- [29] Cecchi, A., & Di Marco, R. (2002). Homogenized strategy toward constitutive identification of masonry. *Journal of Engineering Mechanics*, 128(6), 688-697.
- [30] Cecchi, A., & Sab, K. (2004). A comparison between a 3D discrete model and two homogenised plate models for periodic elastic brickwork. *International Journal of Solids and Structures*, 41, 2259-2276.
- [31] Reccia, E., Milani, G., Cecchi, A., & Tralli, A. (2014). Full 3D homogenization approach to investigate the behavior of masonry arch bridges: The Venice trans-lagoon railway bridge. *Construction and Building Materials*, 66, 567-586.
- [32] Milani, G., & Bertolesi, E. (2017). Quasi-analytical homogenization approach for the non-linear analysis of in-plane loaded masonry panels. *Construction and Building Materials*, 146, 723-743.
- [33] Milani, G., & Bruggi, M. (2018). Simple homogenization-topology optimization approach for the pushover analysis of masonry walls. *International Journal of Architectural Heritage*, 12(3), 395-408.
- [34] Casolo, S., & Milani, G. (2010). A simplified homogenization-discrete element model for the non-linear static analysis of masonry walls out-of-plane loaded. *Engineering Structures*, 32(8), 2352-2366.
- [35] Casolo, S. (2004). Modelling in-plane micro-structure of masonry walls by rigid elements. *International Journal of Solids and Structures*, 41(13), 3625-3641.
- [36] Petracca, M., Pelà, L., Rossi, R., Oller, S., Camata, G., & Spacone, E. (2017). Multiscale computational first order homogenization of thick shells for the analysis of out-of-plane loaded masonry walls. *Computer Methods in Applied Mechanics and Engineering*, 315, 273-301.
-

-
- [37] Pegon, P., & Anthoine, A. (1997). Numerical strategies for solving continuum damage problems with softening: application to the homogenization of masonry. *Computers & Structures*, 64(1-4), 623-642.
- [38] Luciano, R., & Sacco, E. (1997). Homogenization technique and damage model for old masonry material. *International Journal of Solids and Structures*, 34(24), 3191-3208.
- [39] Zucchini, A., & Lourenço, P. B. (2004). A coupled homogenisation–damage model for masonry cracking. *Computers & Structures*, 82(11-12), 917-929.
- [40] Rekik, A., & Lebon, F. (2012). Homogenization methods for interface modeling in damaged masonry. *Advances in Engineering Software*, 46(1), 35-42.
- [41] Sacco, E., & Lebon, F. (2012). A damage–friction interface model derived from micromechanical approach. *International Journal of Solids and Structures*, 49(26), 3666-3680.
- [42] de Buhan, P., & de Felice, G. (1997). A homogenization approach to the ultimate strength of brick masonry. *Journal of the Mechanics and Physics of Solids*, 45(7), 1085-1104.
- [43] Milani, G., Lourenço, P. B., & Tralli, A. (2006). Homogenised limit analysis of masonry walls, Part I: Failure surfaces. *Computers & Structures*, 84(3-4), 166-180.
- [44] Milani, G., Lourenço, P. B., & Tralli, A. (2006). Homogenised limit analysis of masonry walls, Part II: Structural examples. *Computers & Structures*, 84(3-4), 181-195.
- [45] Milani, G. (2011). Simple homogenization model for the non-linear analysis of in-plane loaded masonry walls. *Computers & Structures*, 89(17-18), 1586-1601.
- [46] Milani, G., & Taliercio, A. (2015). In-plane failure surfaces for masonry with joints of finite thickness estimated by a method of cells-type approach. *Computers & Structures*, 150, 34-51.
- [47] Stefanou, I., Sab, K., & Heck, J. V. (2015). Three dimensional homogenization of masonry structures with building blocks of finite strength: A closed form strength domain. *International Journal of Solids and Structures*, 54, 258-270.
- [48] Godio, M., Stefanou, I., Sab, K., Sulem, J., & Sakji, S. (2017). A limit analysis approach based on Cosserat continuum for the evaluation of the in-plane strength of discrete media: Application to masonry. *European Journal of Mechanics-A/Solids*, 66, 168-192.
-

-
- [49] Milani, G., Lourenço, P., & Tralli, A. (2006). Homogenization approach for the limit analysis of out-of-plane loaded masonry walls. *Journal of Structural Engineering*, 132(10), 1650-1663.
- [50] Sab, K., Dallot, J., & Cecchi, A. (2007). Determination of the overall yield strength domain of out-of-plane loaded brick masonry. *International Journal for Multiscale Computational Engineering*, 5(2), 83-92.
- [51] Cecchi, A., Milani, G., & Tralli, A. (2007). A Reissner–Mindlin limit analysis model for out-of-plane loaded running bond masonry walls. *International Journal of Solids and Structures*, 44(5), 1438-1460.
- [52] Cecchi, A., & Milani, G. (2008). A kinematic FE limit analysis model for thick English bond masonry walls. *International Journal of Solids and Structures*, 45(5), 1302-1331.
- [53] Milani, G., & Taliercio, A. (2016). Limit analysis of transversally loaded masonry walls using an innovative macroscopic strength criterion. *International Journal of Solids and Structures*, 81, 274-293.
- [54] Zeman, J., Novák, J., Šejnoha, M., & Šejnoha, J. (2008). Pragmatic multi-scale and multi-physics analysis of Charles Bridge in Prague. *Engineering Structures*, 30(11), 3365-3376.
- [55] Cluni, F., & Gusella, V. (2004). Homogenization of non-periodic masonry structures. *International Journal of Solids and Structures*, 41(7), 1911-1923.
- [56] Cavalagli, N., Cluni, F., & Gusella, V. (2013). Evaluation of a statistically equivalent periodic unit cell for a quasi-periodic masonry. *International Journal of Solids and Structures*, 50(25-26), 4226-4240.
- [57] Cavalagli, N., Cluni, F., & Gusella, V. (2018). Failure surface of quasi-periodic masonry by means of Statistically Equivalent Periodic Unit Cell approach. *Meccanica*, 53(7), 1719-1736.
- [58] Zeman, J., & Šejnoha, M. (2007). From random microstructures to representative volume elements. *Modelling and Simulation in Materials Science and Engineering*, 15(4), S325.
- [59] Šejnoha, J., Šejnoha, M., Zeman, J., Sýkora, J., & Vorel, J. (2008). Mesoscopic study on historic masonry. *Structural Engineering and Mechanics*, 30(1), 99-117.
- [60] Valenta, R., Šejnoha, M., & Zeman, J. (2010). Macroscopic constitutive law for mastic asphalt mixtures from multiscale modeling. *International Journal for Multiscale Computational Engineering*, 8(1), 131-149.
-

-
- [61] Vorel, J., Zeman, J., Šejnoha, M., & Tomková, B. (2013). Homogenization of plain weave composites with imperfect microstructure: Part II—Analysis of real-world materials. *International Journal for Multiscale Computational Engineering*, 11(5), 443-462.
- [62] Zhuang, X., Wang, Q., & Zhu, H. (2015). A 3D computational homogenization model for porous material and parameters identification. *Computational Materials Science*, 96, 536-548.
- [63] Milani, G., & Lourenço, P. B. (2010). Monte Carlo homogenized limit analysis model for randomly assembled blocks in-plane loaded. *Computational Mechanics*, 46(6), 827-849.
- [64] Milani, G., & Lourenço, P. B. (2010). A simplified homogenized limit analysis model for randomly assembled blocks out-of-plane loaded. *Computers & Structures*, 88(11-12), 690-717.
- [65] Cecchi, A., & Sab, K. (2009). Discrete and continuous models for in plane loaded random elastic brickwork. *European Journal of Mechanics-A/Solids*, 28, 610-625.
- [66] Cecchi, A., & Sab, K. (2009). A homogenized Love–Kirchhoff model for out-of-plane loaded random 2D lattices: Application to “quasi-periodic” brickwork panels. *International Journal of Solids and Structures*, 46, 2907-2919.
- [67] Baraldi, D., & Cecchi, (2017). Discrete model for the collapse behavior of unreinforced random masonry walls. In *Key Engineering Materials* (Vol. 747, pp. 3-10). Trans Tech Publications Ltd.
- [68] Casolo, S., & Milani, G. (2013). Simplified out-of-plane modelling of three-leaf masonry walls accounting for the material texture. *Construction and Building Materials*, 40, 330-351.

MESH GENERATOR FOR MASONRY PANELS

Despite their obvious limitations, macroscale models do not require an accurate description of masonry, not even the actual arrangement of its blocks. Conversely, approaches which separately account for each masonry constituent – such as micro-, mesoscale, and homogenization-based approaches – indeed request the correct representation of the masonry bond, also from a geometrical point of view. In fact, both the creation of the actual masonry geometry for meshing purposes and the generation of a finite element mesh for a suitable representation of that geometry are two issues on their own, and have been seldom addressed in the past. One possible solution may be represented by the use of commercial computer-aided design software such as AutoCAD or Rhinoceros: the image representing the investigated masonry geometry is imported into the workspace, then the boundaries of the units are manually drawn using the available tools in the software. The resulting geometry is then exported in a suitable format in finite element software where the mesh is created. Another solution is the use of finite-element mesh generator, for instance the free software Gmsh: while it directly aims at generating a finite element mesh, the actual masonry geometry must first be reconstructed using the tools made available by the software, which makes the procedure long and cumbersome. It is then evident the need for a simple but straightforward procedure for creating a finite element mesh for a masonry bond directly from the image depicting the geometry. This chapter presents two similar but separate procedures that enable the creation of 2D and 3D finite element meshes; the latter is also extended for the creation of a 3D finite element mesh of a multi-leaf wall. Specifically, Section 3.1 describes the “pixel strategy” that enables the creation of a 2D finite element mesh from the rasterized sketch of a masonry panel with a generic bond, implemented in a MATLAB function. Section 3.2 is devoted to presenting the “voxel strategy” that instead allows the generation of a 3D finite element mesh, again from the rasterized sketch of a masonry panel. Section 3.3 introduces the so-called “coarsing strategy” aiming

at reducing the number of finite element in both the 2D and 3D finite element meshes in cases where the original rasterized sketch contains a high number of pixels. Finally, Section 3.4 briefly describes the procedure for creating the 3D finite element mesh of a multi-leaf masonry wall.

3.1 2D Mesh Generator

The approach used for the generation of the 2D finite element mesh goes under the name “pixel strategy” because it automatically creates finite elements from the pixels of the picture. The source image must be the rasterized sketch of a masonry panel, which is easily obtained in MATLAB [1] by using the Image Processing Toolbox functions available in the software library. This rasterized sketch must either be a black-and-white or greyscale image, in which units and mortar are each characterized by distinct colors; a black-and-white rasterization is in fact preferred. The creation of the FE mesh occurs through a MATLAB function. The user simply needs to input the actual dimensions of the considered panel. The function converts the picture into an $M \times N \times 3$ array, where M and N are the number of pixels along the vertical and horizontal directions of the image, and the 3 “transversal” layers each contain one entry of the pixel’s RGB triplet. Namely, the Red, Green, and Blue values of the triplet are listed in the first, second, and third layer, respectively. Then, a simple $M \times N$ matrix containing only the Red values of the triplet is extracted from the bigger array. Afterwards, each pixel is treated as the centroid of a single finite element, and is provided with XY coordinates determined from the input global dimensions (Fig. 3.1). These coordinates are evaluated according to a reference system whose origin is located at the centroid of the considered masonry element. This procedure enables the creation of planar finite elements, whose shape is generally a regular rectangular. The XY coordinates of each element’s four nodes are then calculated starting from those of its centroid.

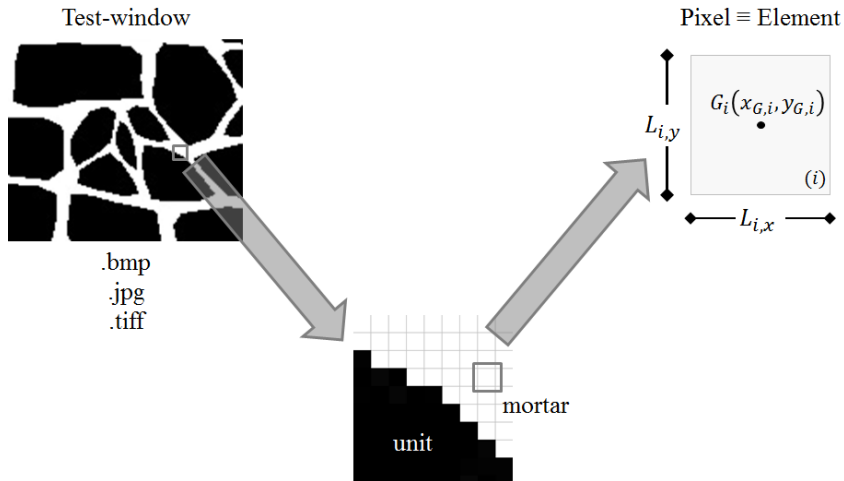


Fig. 3.1. Pixel strategy for the creation of finite elements.

Two distinct matrices are then created: one is named “node matrix” and, for each node, contains its XY coordinates and ID number - ordered from top to bottom first, and from left to right second; the other is named “element matrix” and, for each element, contains its ID number, the ID numbers of its four nodes (listed in a counterclockwise sense starting from the top-left corner), the XY coordinates of its centroid, and eventually its “material flag”. This indicates whether the element pertains to a mortar joint or a unit, depending on the Red value of its RGB triplet. Furthermore, a third matrix is created, named “macro element matrix”: through functions made available in the Image Processing Toolbox, an ID number is assigned to each masonry unit (“macro element”). The macro element representing mortar is given an ID number equal to zero. Then, the ID numbers of the elements belonging to each macro element are extracted, and the “element matrix” is updated so that each finite element is also provided with the ID number of its related macro element. Eventually, the “macro element matrix” is created, which for each macro element (excluding mortar) lists its ID number and the XY coordinates of its centroid. An example of the FE mesh resulting from the procedure - visualized through the patch function - is presented in Fig. 3.2 for a sample masonry element, compared to the original black-and-white rasterized source image.

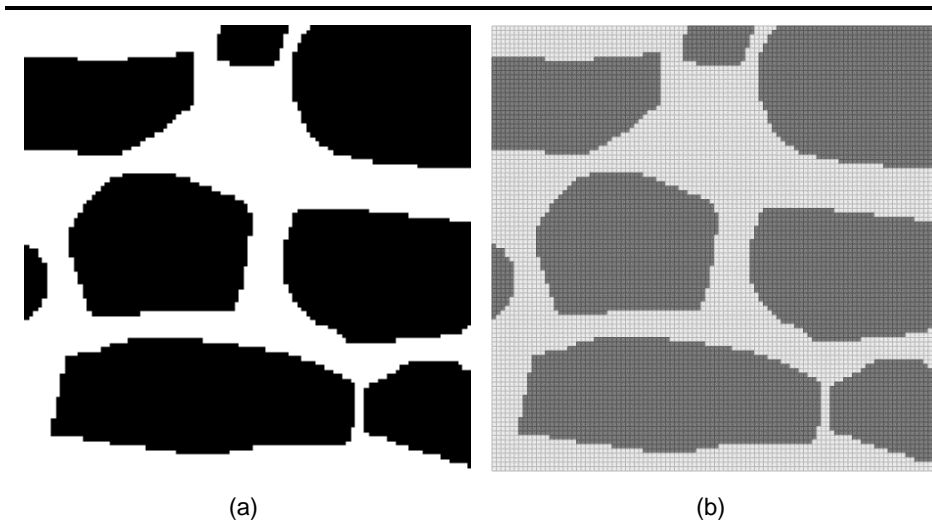


Fig. 3.2. (a) Black-and-white rasterized sketch of a sample masonry element; (b) 2D discretization.

3.2 3D Mesh Generator

Like the previous case, the 3D finite element mesh is created in MATLAB from the rasterized image file of a masonry bond. However, the approach used here goes under the name “voxel approach” because it automatically generates finite elements from voxels, entities that are the 3D equivalent of 2D pixels. This approach is partially inspired by a strategy for modelling historical masonry buildings presented by Castellazzi and co-workers in [2]. The strategy consists in three steps: first, the geometrical domain – conceived as a cloud of points – is created in a semi-automatic way (for example via a photogrammetric survey); then, a FE mesh consisting of 3D brick elements is generated through structural discretization starting from the aforementioned cloud of points; eventually, a suitable characterization of FE mesh and the connection between adjacent structural macro-elements is assumed.

As previously mentioned, the procedure for creating the 3D mesh starts from obtaining the rasterized sketch of the considered masonry bond, for instance by using the Image Processing Toolbox functions available in MATLAB. This sketch represents the source image for the procedure and must be either greyscale or black-and-white so that units and mortar are uniquely identified by distinct colors. The source image is then imported into the MATLAB function purposefully written for the creation of the 3D mesh; the user must also input the real dimensions of the considered masonry element, the number of finite elements

desired in the transversal direction, and the transversal configuration of the considered masonry element. The latter feature is a novelty of this procedure and enables the user to choose between a simple transversal extrusion of the in-plane configuration, and a more complex transversal configuration where the masonry units are provided with an ellipsoidal shape. In this case, the in-plane configuration represents the mid-plane of the 3D mesh; the ellipsoidal shape is obtained by conveniently reducing the mid-plane surface of the units so that their 3D configuration resembles either a full ellipsoid or a truncated one.

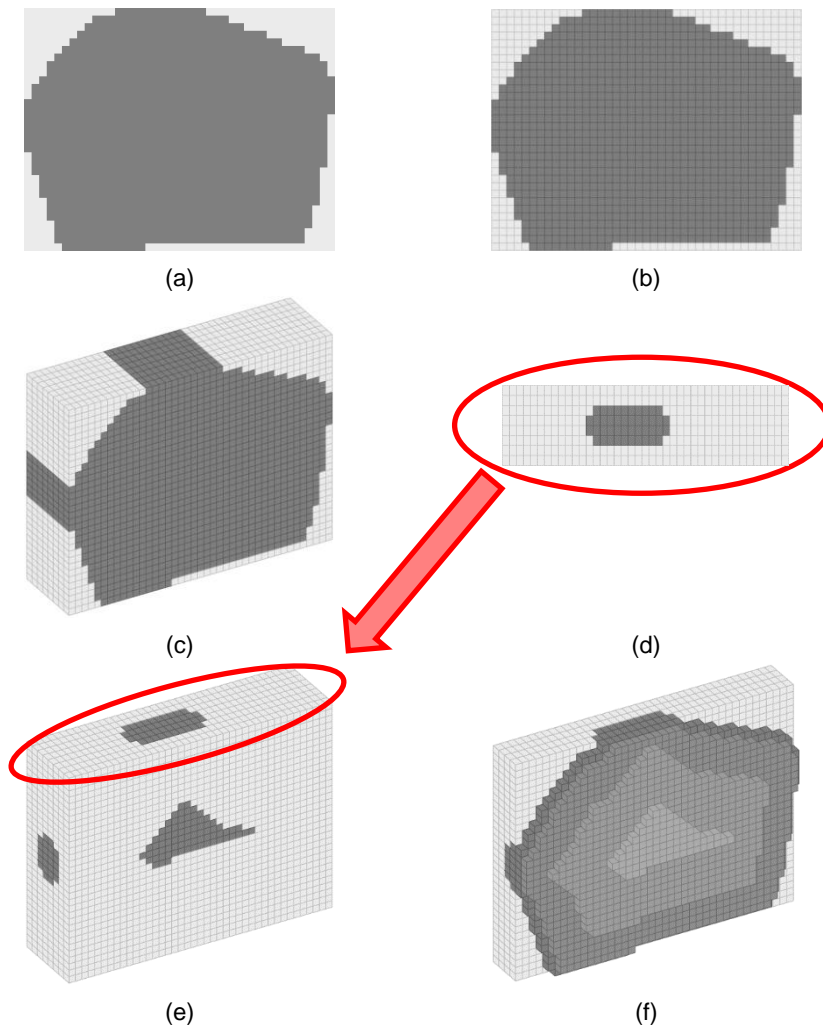


Fig. 3.3. (a) Sample image of a stone embedded in mortar; (b) mid-plane of the 3D FE mesh; (c) 3D FE mesh with extruded stone; (d) aerial view of the 3D FE mesh with ellipsoidal stone; (e) 3D FE mesh with ellipsoidal stone; (f) section of 3D FE mesh with ellipsoidal stone.

Fig. 3.3 shows an example of the aforementioned feature: specifically, Fig. 3.3a shows the greyscale rasterized sketch of a stone embedded in mortar; Fig. 3.3b shows the mid-plane of the 3D finite element mesh obtained for the stone; Fig. 3.3c shows the 3D finite element mesh obtained considering the stone extruded along the transversal direction; Fig. 3.3d-e show the 3D finite element mesh obtained considering an ellipsoidal stone; finally, Fig. 3.3f shows a section of this version of the 3D finite element mesh, where inner layers of FEs pertaining to the ellipsoidal stone are denoted with different colors.

The MATLAB function converts the source image into an $M \times N \times 3$ array, where M and N are the number of pixels along the vertical and horizontal directions of the image, and the 3 layers each contain one entry of the pixel's RGB triplet. Namely, the Red, Green, and Blue values of the triplet are listed in the first, second, and third layer, respectively. Then, a simple $M \times N$ matrix containing only the Red values of the triplet is extracted from the bigger array. Afterwards, an $M \times N \times O$ array is constructed, where O is the number of transversal finite elements; each $M \times N$ layer represents the configuration related to that specific finite element layer, which depends on the chosen transversal configuration. Each single element of the $M \times N \times O$ array corresponds to a voxel, which is treated as the centroid of a single finite element and is provided with XYZ coordinates that are determined from the input global dimensions (as shown in Fig. 3.4). These coordinates are evaluated according to a reference system whose origin is located at the centroid of the considered masonry element, where X and Y represent the horizontal and vertical axes, respectively, while Z is the transversal direction. This procedure enables the generation of solid brick-shaped finite elements. The XYZ coordinates of each element's eight nodes are then calculated starting from those of its centroid.

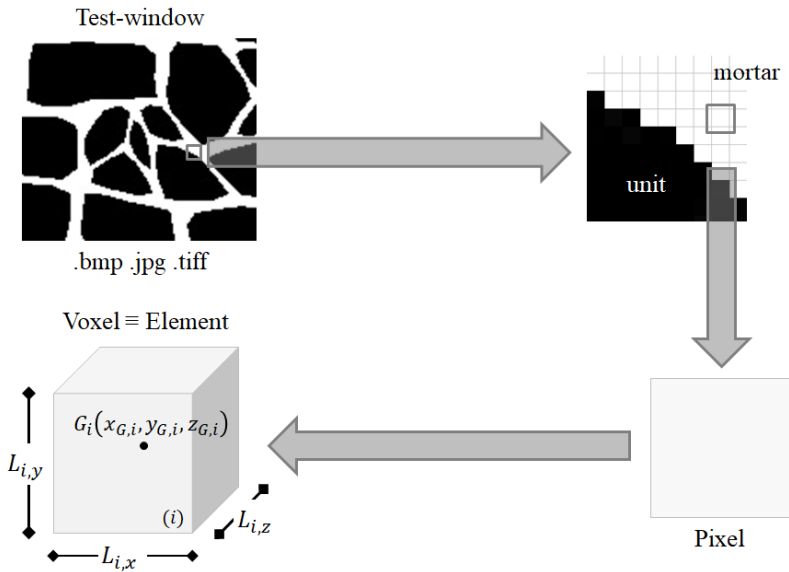
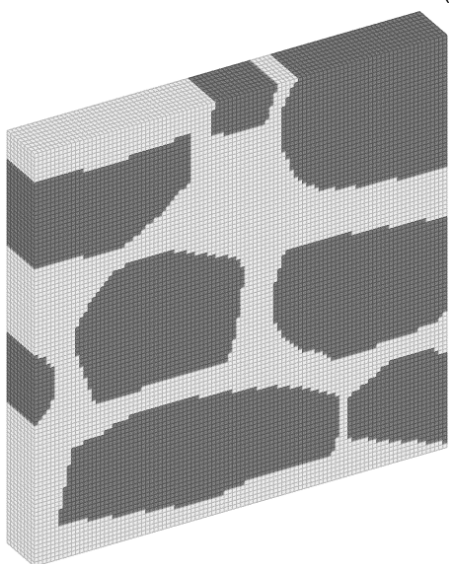


Fig. 3.4. Voxel strategy for creating the 3D finite element mesh.

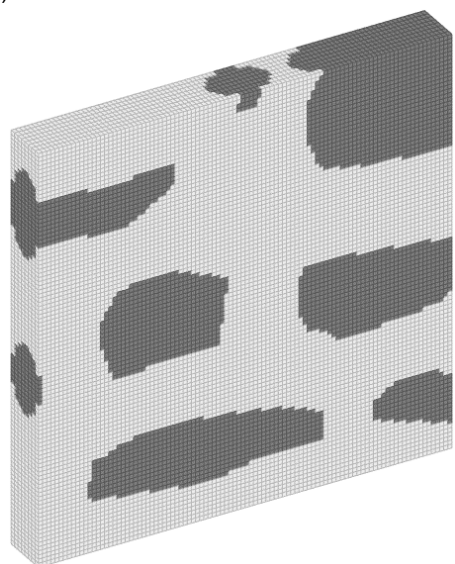
Analogously to the procedure for the 2D mesh, a subscript is included aiming at the identification of the masonry units (“macro element”): through functions made available in the Image Processing Toolbox library, each masonry unit is given an ID number, and the XYZ coordinates of its centroid are determined as well. Three distinct matrices are then created: the first is named “node matrix” and, for each node of the mesh, contains its XYZ coordinates and ID number – ordered in a top-to-bottom fashion that starts from the front-top-left corner and ends in the rear-bottom-right corner. The second is named “matrix element” and, for each finite element of the mesh, contains its ID number, the ID number of its eight nodes (listed in a counterclockwise sense starting from the front-top-left node), the XYZ coordinates of its centroid, its “material flag” that indicates whether it pertains to mortar or to a masonry unit (depending on the Red value of the original pixel’s RGB triplet), and the ID number of its related masonry unit (in case of mortar elements, this ID number is set to zero). The third and final matrix is named “macro element matrix” and, for each masonry unit, lists its ID number and its centroid’s XYZ coordinates. An example of the 3D finite element mesh resulting from this procedure – visualized through the patch function in MATLAB – is presented in Fig. 3.5 for the same sample masonry element shown earlier, for both the “extruded” and “ellipsoidal” cases.



(a)



(b)



(c)

Fig. 3.5. (a) Black-and-white rasterized sketch of the sample masonry element; (b) 3D discretization with extruded transversal configuration; (c) 3D discretization with ellipsoidal units.

3.3 Coarsing Strategy

A further subscript is included in both MATLAB functions that sets a procedure to decrease the number of finite elements according to a “coarsing strategy” whose ultimate goal is to reduce the computational effort needed for the subsequent numerical analyses. In the original $M \times N$ matrix representing the in-plane configuration, this subscript condensates a square consisting of $n \times n$ entries ($n = 2 \div 5$) into a single entry of a new $M_r \times N_r$ matrix (see Fig. 3.6), where M_r and N_r are the reduced number of pixels (which have increased dimensions) along the vertical and horizontal directions, respectively.

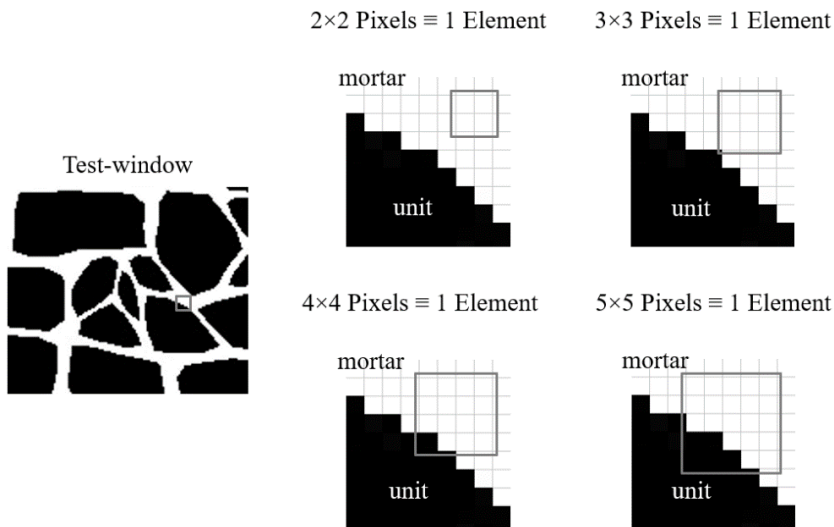


Fig. 3.6. Coarsing strategy for reducing the mesh size.

The physical nature of these new pixels is determined by a threshold representing the overall number of mortar pixels in the original configuration: if the number is lower than the selected threshold, the new pixel is treated as a unit pixel, otherwise it becomes a mortar pixel. An example of the result in terms of increase of the mesh size is shown in Fig. 3.7 for the four considered coarse cases, applied to the same sample masonry element; in this case, the coarser meshes represent the mid-plane configuration of the overall 3D finite element mesh. It can be easily noted that, as the mesh becomes coarser, its accuracy in representing the original geometrical layout decreases.

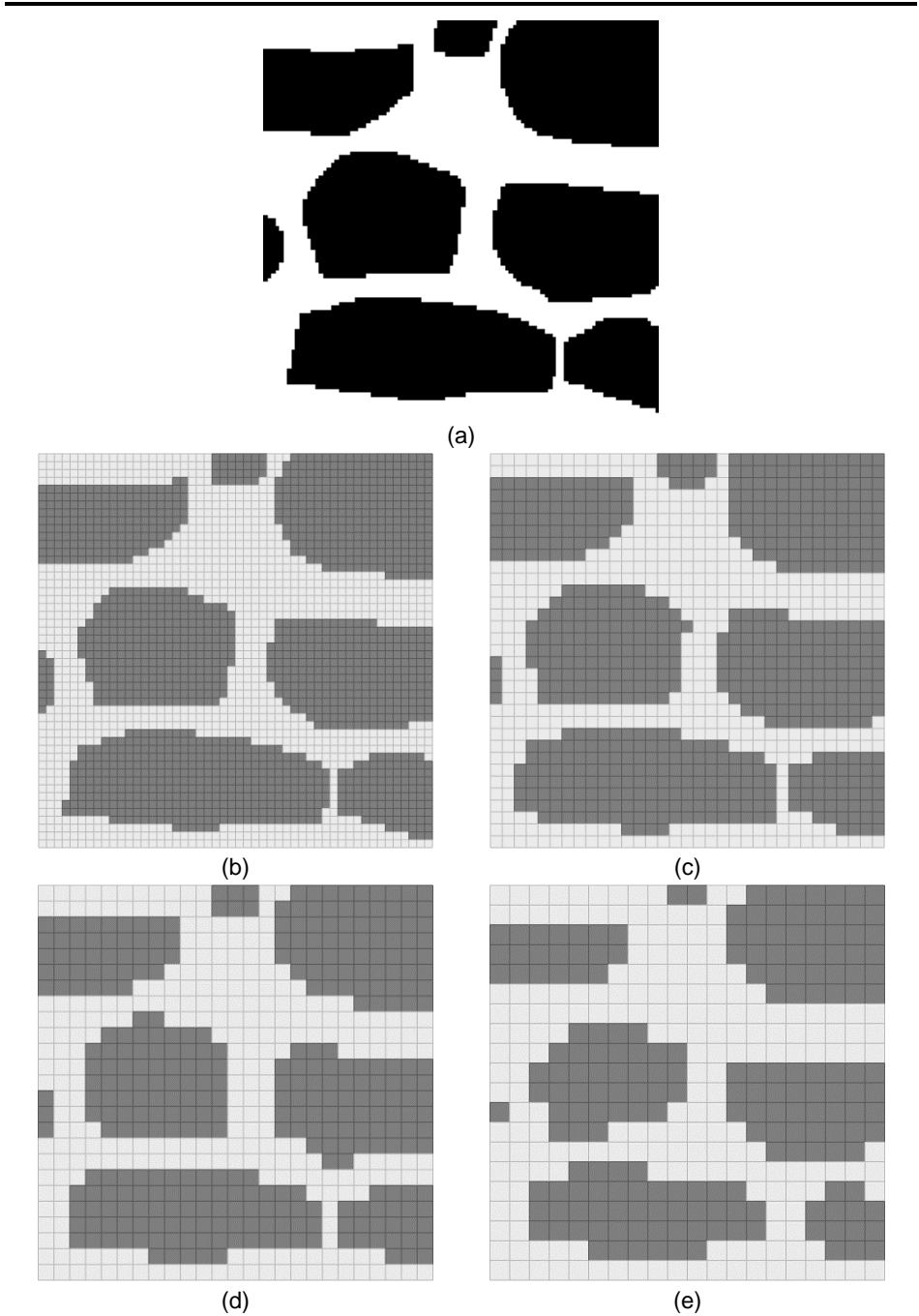


Fig. 3.7. (a) Black-and-white rasterized sketch of the sample masonry element; (b) 2D discretization with a 2×2 coarsing strategy; (c) 2D discretization with a 3×3 coarsing strategy; (d) 2D discretization with a 4×4 coarsing strategy; (e) 2D discretization with a 5×5 coarsing strategy.

3.4 3D Mesh Generator for Multi-Leaf Masonry Walls

A further MATLAB function enables the creation of a 3D finite element mesh for a multi-leaf wall. The procedure is basically the same as the one for the generation of the 3D finite element mesh, only with different inputs: the user must choose the number of wythes for the considered multi-leaf wall, and is allowed to select a separate source image for each wythe. Moreover, the choice of the transversal configuration is still enabled for each wythe, as well as the coarsing strategy. In this case, the user must select a single coarsing strategy to be shared by all the wythes. Once these setups are chosen, the procedure runs in the same way as for the single-leaf 3D finite element mesh. An example of the final result is shown in Fig. 3.8 for a three-leaf wall in which the outer wythes are generated from the same source image of Fig. 3.2a.

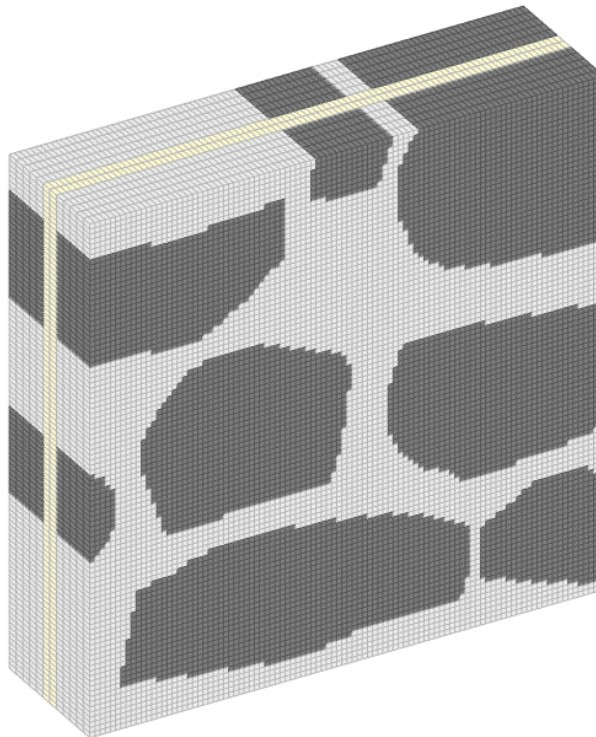


Fig. 3.8. 3D finite element mesh for a three-leaf wall.

3.5 References

- [1] MATLAB Release 2018b, The MathWorks, Inc., Natick, Massachusetts, United States.
- [2] Castellazzi, G., D'Altri, A. M., de Miranda, S., & Ubertini, F. (2017). An innovative numerical modeling strategy for the structural analysis of historical monumental buildings. *Engineering Structures*, 132, 229-248.

2D HOMOGENIZED LIMIT ANALYSIS OF NON-PERIODIC MASONRY

This chapter presents an application of homogenized limit analysis for non-periodic masonry that aims at deriving in-plane homogenized failure surfaces for this specific type of material. This procedure is implemented into a MATLAB function that contains an upper bound limit analysis problem combined with a homogenization approach, written as a linear programming problem in standard form. In-plane homogenized failure surfaces for masonry REV's that are extracted from a larger non-periodic masonry panel. The choice of a REV that can be deemed statistically representative of the considered masonry panel is partially based on the "test-window" method introduced by Cluni & Gusella [1]. On the other hand, the determination of the mean homogenized failure surface for each REV loosely follows the approach by Milani & Lourenço [2]. The homogenized failure surfaces are obtained for in-plane load conditions in the tension-tension range only.

Section 4.1 is devoted to describing in detail the mathematical formulation of the in-plane upper bound limit analysis problem as conceived for this application. Section 4.2 presents the results in terms of in-plane homogenized failure surfaces and selected deformed shapes at collapse for six case studies of real masonry buildings, all characterized by a non-periodic bond but displaying various degrees of irregularity (rubble, quasi-periodic, quasi-regular). In particular, the suitable choice of a REV for non-periodic masonry elements is extensively discussed in Section 4.2.1. Finally, Section 4.3 offers conclusive remarks on the results presented in the previous section by drawing comparisons among the six case studies.

4.1 Problem Formulation

This section presents the mathematical formulation behind the problem that aims at deriving in-plane homogenized failure surfaces for non-periodic masonry walls. Here, an upper bound limit analysis problem is combined with a homogenized approach and is formulated as a standard form linear programming problem in MATLAB [3] that is also subjected to some equality constraints coming from the mathematical formulation, and employs a finite element discretization.

The use of linear programming and FEM for formulating an upper bound limit analysis problem is first introduced by Sloan [4]. However, in the formulation here proposed the discretization of the masonry test-window adopts rigid, rectangular 2D elements, also considered to be without rotation rate ($\dot{\phi} = 0$) in order to handle more elements. This allows a huge reduction of the number of unknowns in the problem, thus making the 2D mesh resulting from the pixel strategy particularly suitable for use.

The hypothesis of rigid elements without rotation rate means that any element is uniquely and fully described by the velocity field of its centroid $\{\dot{u}_x, \dot{u}_y\}$. Recalling the classical formula for the displacement rate field in the homogenization theory [5], the two components can be expressed as:

$$\dot{u}_x = \dot{u}_{x,per} + \dot{E}_{xx}x_G + \dot{E}_{xy}y_G \quad (4.1)$$

$$\dot{u}_y = \dot{u}_{y,per} + \dot{E}_{xy}x_G + \dot{E}_{yy}y_G \quad (4.2)$$

where $\dot{u}_{x,per}$ and $\dot{u}_{y,per}$ are the periodic velocities of the element, whereas \dot{E}_{xx} , \dot{E}_{yy} , and \dot{E}_{xy} are the components of the average strain rate tensor (with \dot{E}_{yx} equal to \dot{E}_{xy} for symmetry). In the following subsections, the complete formulation of the homogenization-limit analysis problem is presented (called “full approach”); eventually, a reduced formulation named “master-slave approach” is described, which aims at reducing the computational time requested for the solution of the problem.

4.1.1 Velocity Jumps and Plastic Flow Constraints

Since all the elements are rigid, plastic dissipation can only occur across their mutual interfaces; this is expressed as a discontinuity in the displacement rate

field. A formulation devoted to addressing such feature is presented by Sloan & Kleeman in a classic work [6]; other formulations are offered by Ferris & Tin-Loi [7] and Krabbenhoft and co-workers [8]. This simplification allows for a dramatic reduction of the number of unknowns in the problem. Because of the pixel strategy used for the creation of the mesh, each element has its four sides oriented according to the local reference system by default. Therefore, the tangential and normal velocity jumps for horizontal and vertical interfaces (see Fig. 4.1 and Fig. 4.2) are trivially evaluated according to Eqs. (4.3), (4.4) and (4.5), (4.6), respectively:

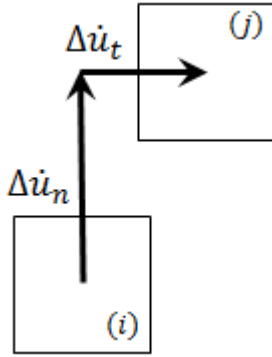


Fig. 4.1. Velocity jumps for a generic horizontal interface.

$$\Delta \dot{u}_n \equiv \Delta \dot{u}_y = \dot{u}_{y,per}^j - \dot{u}_{y,per}^i + \dot{E}_{yy}(y_G^j - y_G^i) \quad (4.3)$$

$$\Delta \dot{u}_t \equiv \Delta \dot{u}_x = \dot{u}_{x,per}^j - \dot{u}_{x,per}^i + \dot{E}_{xy}(y_G^j - y_G^i) \quad (4.4)$$

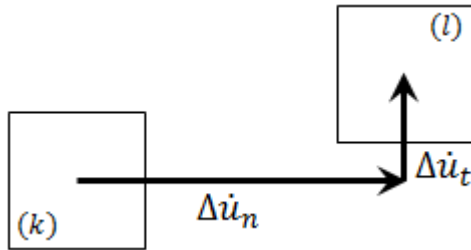


Fig. 4.2. Velocity jumps for a generic vertical interface.

$$\Delta \dot{u}_t \equiv \Delta \dot{u}_y = \dot{u}_{y,per}^l - \dot{u}_{y,per}^k + \dot{E}_{xy}(x_G^l - x_G^k) \quad (4.5)$$

$$\Delta \dot{u}_n \equiv \Delta \dot{u}_x = \dot{u}_{x,per}^l - \dot{u}_{x,per}^k + \dot{E}_{xx}(x_G^l - x_G^k) \quad (4.6)$$

As shown in [6], a kinematically admissible velocity field must satisfy constraints given by an associated flow rule. For the purposes of the numerical applications that follow, a Mohr-Coulomb failure criterion with a tension cut-off is employed. The related bounding yield surface can simply be expressed in terms of normal stress σ_n and tangential stress τ as:

$$|\tau| \leq c - \sigma_n \tan \phi \wedge \sigma_n \leq f_t \quad (4.7)$$

Therefore, the bounding yield surface for the Mohr-Coulomb criterion employing the tension cut-off (Fig. 4.3) consists of three straight lines whose expressions are all linear both in τ and σ_n with the general form $A_n^q \sigma_n + A_t^q \tau - C_I^q = 0$:

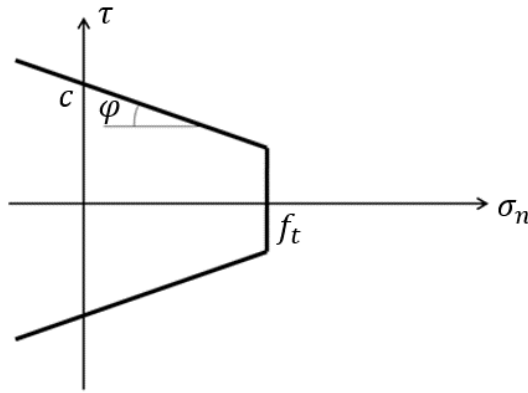


Fig. 4.3. Mohr-Coulomb criterion + tension cut-off.

$$F(\tau, \sigma_n) = \begin{cases} \tau + \sigma_n \tan \phi - c \\ -\tau + \sigma_n \tan \phi - c \\ \sigma_n - f_t \end{cases} = 0 \quad (4.8)$$

where ϕ is the friction angle, c the cohesion, and f_t the tensile strength assigned to the interfaces. It is trivial to notice that distinct parameters can in general be used for different interfaces (namely, unit-unit, mortar-unit, and mortar-mortar interfaces).

Since the interfaces can only be either horizontal or vertical, these expressions do not need to be modified in any case as τ and σ_n are themselves sufficient to describe the stress state at the interfaces. For an associated flow rule the velocity jumps can be simply expressed as:

$$\Delta \dot{u}_n = \sum_{q=1}^3 \lambda_l^q \frac{\partial F_q}{\partial \sigma_n} = \sum_{q=1}^3 \lambda_l^q A_n^q = \lambda_l^1 \tan \phi + \lambda_l^2 \tan \phi + \lambda_l^3 \quad (4.9)$$

$$\Delta \dot{u}_t = \sum_{q=1}^3 \lambda_l^q \frac{\partial F_q}{\partial \tau} = \sum_{q=1}^3 \lambda_l^q A_t^q = \lambda_l^1 - \lambda_l^2 \quad (4.10)$$

where both $\Delta \dot{u}_n$ and $\Delta \dot{u}_t$ can be either $\Delta \dot{u}_x$ or $\Delta \dot{u}_y$, depending on the considered interface. The MATLAB script employs a function containing an algorithm that easily detects which type of interface is currently considered (i.e. horizontal or vertical) and assigns the correct expression for both $\Delta \dot{u}_n$ and $\Delta \dot{u}_t$. In any case, the two expressions for these quantities - coming from the velocity jumps and the plastic flow constraints - are put equal to each other. For instance, considering a single vertical interface l between elements i and j , their combinations become:

$$\Delta \dot{u}_n = \dot{u}_{x,per}^j - \dot{u}_{x,per}^i + \dot{E}_{xx}(x_G^j - x_G^i) = \sum_{q=1}^3 \lambda_l^q A_n^q \quad (4.11)$$

$$\Delta \dot{u}_t = \dot{u}_{y,per}^j - \dot{u}_{y,per}^i + \dot{E}_{xy}(x_G^j - x_G^i) = \sum_{q=1}^3 \lambda_l^q A_t^q \quad (4.12)$$

The overall constraints can be then written as:

$$\dot{u}_{x,per}^j - \dot{u}_{x,per}^i - \sum_{q=1}^3 \lambda_l^q A_n^q + \dot{E}_{xx}(x_G^j - x_G^i) = 0 \quad (4.13)$$

$$\dot{u}_{y,per}^j - \dot{u}_{y,per}^i - \sum_{q=1}^3 \lambda_l^q A_t^q + \dot{E}_{xy}(x_G^j - x_G^i) = 0 \quad (4.14)$$

Using a matrix formulation to compact Eqs. (4.13) and (4.14), these become:

$$\begin{bmatrix} 1 & -1 & 0 & 0 \\ 0 & 0 & 1 & -1 \end{bmatrix} \begin{bmatrix} \dot{u}_{x,per}^j \\ \dot{u}_{x,per}^i \\ \dot{u}_{y,per}^j \\ \dot{u}_{y,per}^i \end{bmatrix} + \begin{bmatrix} -\tan \phi & -\tan \phi & -1 \\ -1 & 1 & 0 \end{bmatrix} \begin{bmatrix} \lambda_l^1 \\ \lambda_l^2 \\ \lambda_l^3 \end{bmatrix} + \quad (4.15)$$

$$+ \begin{bmatrix} (x_G^j - x_G^i) & 0 & 0 \\ 0 & 0 & (x_G^j - x_G^i) \end{bmatrix} \begin{bmatrix} \dot{E}_{xx} \\ \dot{E}_{yy} \\ \dot{E}_{xy} \end{bmatrix} = \begin{bmatrix} 0 \\ 0 \end{bmatrix}$$

This matrix formulation can be written even more compactly:

$$A_{11}^{eq,ij} \dot{\mathbf{u}}_{per}^{ij} + A_{12}^{eq,ij} \dot{\lambda}_I + A_{13}^{eq,ij} \dot{\mathbf{E}} = \mathbf{0} \quad (4.16)$$

From Eq. (4.16) it is trivial to observe that the unknown variables of the linear programming problem are the periodic velocity field of the two adjoining elements i and j (collected in the vector $\dot{\mathbf{u}}_{per}^{ij}$), the plastic multiplier rates of interface I ($\dot{\lambda}_I$), and the components of the average strain rate tensor ($\dot{\mathbf{E}}$). For the overall problem, some simple assemblage operations are performed and the constraint in its global form becomes:

$$A_{11}^{eq} \dot{\mathbf{u}}_{per} + A_{12}^{eq} \dot{\lambda}_{I,ass} + A_{13}^{eq} \dot{\mathbf{E}} = \mathbf{0} \quad (4.17)$$

4.1.2 Periodicity Boundary Conditions

To ensure consistency with the homogenization approach, the linear programming problem must also include constraints related to the periodicity of the velocity field at the boundaries. Specifically, elements on the same line at the opposite sides of the test-window (Fig. 4.4) must share the same periodic velocities.

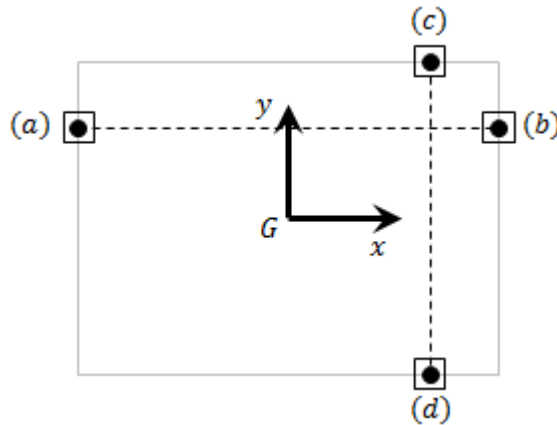


Fig. 4.4. Periodicity boundary conditions.

$$\dot{u}_{x,per}^a = \dot{u}_{x,per}^b \Rightarrow \dot{u}_{x,per}^a - \dot{u}_{x,per}^b = 0 \quad (4.18)$$

$$\dot{u}_{y,per}^a = \dot{u}_{y,per}^b \Rightarrow \dot{u}_{y,per}^a - \dot{u}_{y,per}^b = 0 \quad (4.19)$$

$$\dot{u}_{x,per}^c = \dot{u}_{x,per}^d \Rightarrow \dot{u}_{x,per}^c - \dot{u}_{x,per}^d = 0 \quad (4.20)$$

$$\dot{u}_{y,per}^c = \dot{u}_{y,per}^d \Rightarrow \dot{u}_{y,per}^c - \dot{u}_{y,per}^d = 0 \quad (4.21)$$

The global compact formulation of this constrain is trivially:

$$A_{21}^{eq} \dot{\mathbf{u}}_{per} = \mathbf{0} \quad (4.22)$$

4.1.3 Normalization of Dissipated External Power

A macroscopic tensile load condition for the test-window is defined through two angles, as shown in Fig. 4.5.

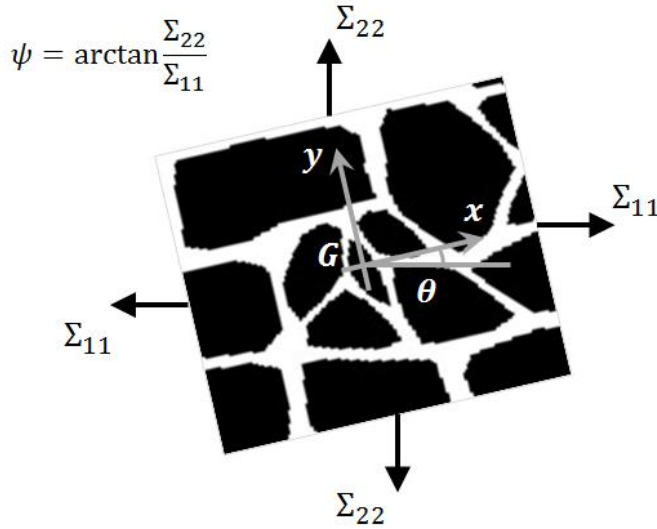


Fig. 4.5. Angles defining the tensile in-plane load condition.

Angle ψ is named “loading angle” and represents the arctangent of the ratio between the principal macroscopic stresses Σ_{22} and Σ_{11} ; specifically, it varies between 0° (uniaxial horizontal tension) and 90° (uniaxial vertical tension), with any value within the range expressing a biaxial tensile load condition. On the

other hand, angle θ represents the inclination of the principal directions with respect to the local reference system. When θ is different from zero, the principal macroscopic stresses can be split in two components that are normal and tangential to their boundaries, thus marking the appearance of shear macroscopic stresses as well. The expressions of the macroscopic stresses in terms of ψ and θ are:

$$\Sigma_{xx} = \frac{1}{2} [\cos \psi (1 + \cos 2\theta) + \sin \psi (1 - \cos 2\theta)] \quad (4.23)$$

$$\Sigma_{yy} = \frac{1}{2} [\cos \psi (1 - \cos 2\theta) + \sin \psi (1 + \cos 2\theta)] \quad (4.24)$$

$$\Sigma_{xy} = \frac{1}{2} (\cos \psi - \sin \psi) \cos 2\theta \tan 2\theta \quad (4.25)$$

The dissipated external power is then simply given as the summation of the products between the macroscopic stresses and the average strain rate tensor components, which are associated by duality.

$$P^{ext} = \Sigma_{xx} \dot{E}_{xx} + \Sigma_{yy} \dot{E}_{yy} + \Sigma_{xy} \dot{E}_{xy} \quad (4.26)$$

In the framework of limit analysis, it is renowned that the collapse load – despite being unique – is indeed associated to infinite collapse mechanisms; the physical meaning of such occurrence is that the motion of the collapse mechanism is unrestricted. One simple and popular way to identify a single collapse mechanism is to enforce a normalization of the dissipated external power, equaling it to 1 [5]:

$$P^{ext} = \Sigma_{xx} \dot{E}_{xx} + \Sigma_{yy} \dot{E}_{yy} + \Sigma_{xy} \dot{E}_{xy} = 1 \quad (4.27)$$

In this way, the motion of the collapse mechanism is indeed restricted; similarly, it can be stated that the actual collapse mechanism is the one satisfying the normalization condition. Eventually, this becomes a further constraint for the linear programming problem in the form:

$$A_{33}^{eq} \dot{E} = 1 \quad (4.28)$$

4.1.4 Power Dissipation in Velocity Discontinuities

The expression for power dissipated across a velocity discontinuity whose length is L can be written as:

$$P^{int} = \int_L (\sigma_n \Delta \dot{u}_n + \tau \Delta \dot{u}_t) dL \quad (4.29)$$

Substituting Eqs. (4.9) and (4.10), this becomes:

$$\int_L \left(\sigma_n \sum_{q=1}^3 \dot{\lambda}_I^q A_n^q + \tau \sum_{q=1}^3 \dot{\lambda}_I^q A_t^q \right) dL = \int_L \sum_{q=1}^3 \dot{\lambda}_I^q (\sigma_n A_n^q + \tau A_t^q) dL \quad (4.30)$$

The dissipated internal power can then be written as:

$$P^{int} = L \sum_{q=1}^3 \dot{\lambda}_I^q C_I^q \quad (4.31)$$

In matrix formulation this becomes:

$$P^{int} = \mathbf{C}_I^T \dot{\boldsymbol{\lambda}}_I \quad (4.32)$$

For the global problem the assembled final expression is:

$$P^{int} = \mathbf{C}_{I,ass}^T \dot{\boldsymbol{\lambda}}_{I,ass} \quad (4.33)$$

4.1.5 Assembly and Solution of the Linear Programming Problem

The homogenized limit analysis problem is then formulated as a linear programming problem, in which the equality constraints are given by Eqs. (4.17), (4.22), and (4.28), whereas the objective function to be minimized is the dissipated internal power as expressed in Eq. (4.33). This problem must also be formulated in a standard form, which allows a smoother solution of the computational problem. The standard form requires that each variable is greater or equal to zero. In the present problem, this implies a slight modification of the actual variables, namely the elements' velocity field and the average strain rate

tensor components. In fact, both must be expressed as the difference of two nonnegative quantities:

$$\dot{u}_{i,per}^E = \dot{u}_{i,per}^{E,+} - \dot{u}_{i,per}^{E,-} \quad i = x, y \quad (4.34)$$

$$\dot{E}_{ij} = \dot{E}_{ij}^+ - \dot{E}_{ij}^- \quad i, j = x, y \quad (4.35)$$

Eventually, the proper standard form for this linear programming problem is:

$$\text{Minimize} \quad \mathbf{C}^T \mathbf{X} \quad (4.36)$$

$$\text{Subject to} \quad \mathbf{A}\mathbf{X} = \mathbf{B} \quad (4.37)$$

$$\mathbf{X} \geq \mathbf{0} \quad (4.38)$$

where

$$A = \begin{bmatrix} A_{11}^{eq} & -A_{11}^{eq} & A_{12}^{eq} & A_{13}^{eq} & -A_{13}^{eq} \\ A_{21}^{eq} & -A_{21}^{eq} & 0 & 0 & 0 \\ 0 & 0 & 0 & A_{33}^{eq} & -A_{33}^{eq} \end{bmatrix} \quad (4.39)$$

$$X = \begin{bmatrix} \dot{u}_{per}^+ \\ \dot{u}_{per}^- \\ \dot{\lambda}_{I,ass} \\ \dot{E}^+ \\ \dot{E}^- \end{bmatrix} \quad (4.40)$$

$$B = \begin{bmatrix} 0 \\ 0 \\ 1 \end{bmatrix} \quad (4.41)$$

$$C = \begin{bmatrix} 0 \\ 0 \\ C_{I,ass} \\ 0 \\ 0 \end{bmatrix} \quad (4.42)$$

Some remarks must be done regarding the total number of variables. For a mesh consisting of $M \times N$ finite elements, where M and N are the number of elements along the vertical and horizontal directions, respectively, the number of interfaces is equal to $2 \cdot M \cdot N - (M + N)$. The total number of variables is given by the following formula:

$$\begin{aligned} & 4 \cdot M \cdot N + 3 \cdot [2 \cdot M \cdot N - (M + N)] + 6 = \\ & = 10 \cdot M \cdot N + 6 - 3 \cdot (M + N) \end{aligned} \quad (4.43)$$

In the initial formula, the first addendum expresses the number of periodic velocities (4 for each element, 2 per direction considering the standard substitution), the second expresses the number of interface plastic multiplier rates, and the third expresses the number of components of the average strain rate tensor (also doubled because of the standard substitution). This means that, for the medium-sized picture of a masonry test-window with 300 pixels on each side, and considering that one pixel corresponds to one finite element, the total number of variables is 898206, which is extremely large and leads to very long computational times. Therefore, a strategy aimed at the reduction of the number

of variables must certainly be sought: here, the simplification is implemented by using a master-slave approach.

4.1.6 Master-Slave Approach

The master-slave approach is based on the trivial consideration that in masonry walls, under specific conditions, failure occurs due to cracks opening within mortar joints and not across units. Specifically, this outcome is observed when masonry walls fail under tensile load conditions, as shown in a classical paper by Page [9] and later by Backes [10]. This is even truer when mortar presents weaker mechanical properties than the units: it is confirmed by experimental tests performed by Page, where the ratio between the mean compressive strengths of mortar and bricks is about 1:3 [9], and further corroborated by the results of shear tests performed by Borri and co-workers shown in [11]. In historical masonry structures, mortar often experiences degradation due to ageing and exposure to weather conditions, which further reduce its mechanical properties. Fig. 4.6 shows an explicative picture of the aforementioned type of failure for masonry walls: it represents the façade of a stone masonry church heavily damaged during the Central Italy seismic event of August 24th, 2016. It can be easily observed how several cracks opened on the façade, all following patterns that are solely contained within mortar joints.

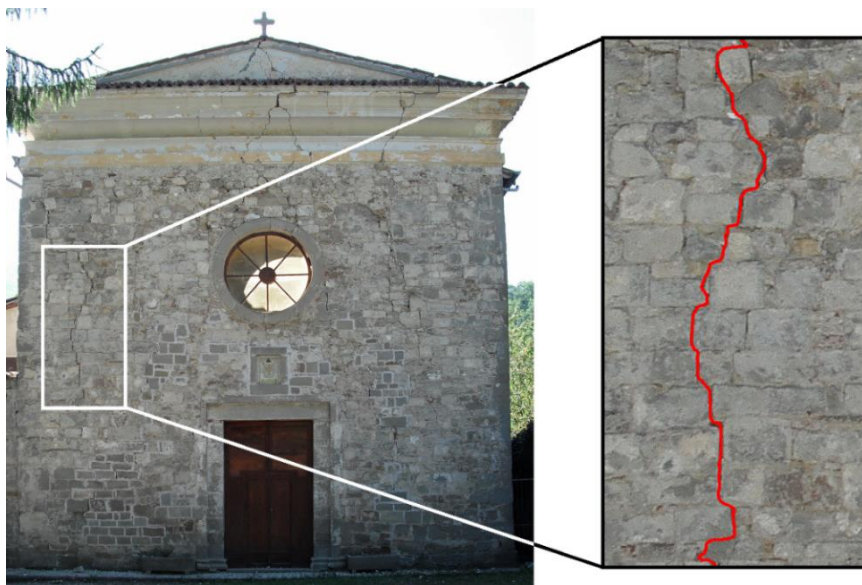


Fig. 4.6. Crack patterns within mortar joints in a stone masonry church (Arquata del Tronto, Ascoli Piceno, Italy).

Subsequently, the full approach can be simplified by solidifying each unit into a single macro finite element that governs the kinematics of all its related finite elements. In fact, the fundamental relation of this master-slave approach is the imposed equality between the velocity field of one macro finite element (the *master* element) and the velocity field of each of its finite elements (the *slave* element). For a generic master element ME and a generic slave element E , the equalities are:

$$\dot{u}_x^E = \dot{u}_x^{ME} = \dot{u}_{x,per}^{ME} + \dot{E}_{xx}x_G^{ME} + \dot{E}_{xy}y_G^{ME} \quad (4.44)$$

$$\dot{u}_y^E = \dot{u}_y^{ME} = \dot{u}_{y,per}^{ME} + \dot{E}_{xy}x_G^{ME} + \dot{E}_{yy}y_G^{ME} \quad (4.45)$$

This relation is not directly used in the new formulation of the homogenized limit analysis problem; instead, it is employed in the post-processing phase to reconstruct the full velocity field for all elements. Nonetheless, this approach generally leads to a substantial reduction in the total number of unknowns. In particular, the variables directly related to the slave elements (i.e. their periodic velocity field and the plastic multiplier rates of unit-unit interfaces) are removed from the solution vector expressed by Eq. (4.40).

In the linear programming problem representing the master-slave approach, the equality constraint related to velocity jumps and plastic flow for two adjacent mortar elements is still expressed by Eq. (4.16). In case one of the two adjacent elements is a slave element, Eqs. (4.13) and (4.14) are updated: the periodic velocity field and centroid coordinates of the slave element are replaced by those of its related master element according to Eqs. (4.44) and (4.45). Conversely, the plastic multiplier rates are still evaluated for the mortar-mortar and the unit-mortar interfaces singularly. The substitution according to Eqs. (4.44) and (4.45) is also performed for the periodicity boundary conditions. The condition related to the normalization of dissipated external power undergoes no changes, whereas the power dissipation in velocity discontinuities is once again limited to the mortar-mortar and unit-mortar interfaces.

4.1.7 Construction of the Homogenized Failure Surfaces

The post-processing phase of the MATLAB script allows the construction of homogenized failure surfaces for the chosen test-window. First, it must be noted that the upper bound limit analysis problem as expressed by Eqs. (4.36)-(4.38) is in fact a slight modification of the kinematic theorem. Actually, the kinematic limit multiplier χ is the minimum among those computed for each kinematically

admissible collapse mechanism. It is usually expressed as the ratio between the dissipated internal and external powers:

$$\mu_k = \frac{P^{int}}{P^{ext}} \quad (4.46)$$

However, the normalization of the dissipated external power introduced by Eq. (4.27) means that the denominator is equal to 1. It follows that:

$$\mu_k = P^{int} = \mathbf{C}_{I,ass}^T \dot{\lambda}_{I,ass} \quad (4.47)$$

$$\chi = \min(\mu_k) = \min(\mathbf{C}_{I,ass}^T \dot{\lambda}_{I,ass}) \quad (4.48)$$

This trivially implies that the minimization of the dissipated internal power, which is the ultimate goal of the linear programming problem here developed, directly results in the determination of the kinematic limit multiplier.

The homogenized failure surface is constructed as follows: after selecting a value for angles ψ and θ , the linear programming problem is solved and the kinematic limit multiplier χ for that specific load condition is obtained. The collapse loads are then calculated by multiplying χ to the initial macroscopic stresses $[\Sigma_{xx} \ \Sigma_{yy} \ \Sigma_{xy}]$. Globally, 11 different values of ψ are investigated, ranging from 0° to 90° with a sampling step of 9° , for 3 distinct values of θ (0° , 22.5° , and 45°). This would result in a 3D homogenized failure surface, but that is actually split in three different diagrams representing the 2D projection for each θ and whose axes are Σ_{xx} and Σ_{yy} . In fact, each pair of collapse loads $\chi\Sigma_{xx}$ and $\chi\Sigma_{yy}$ represents a pair of coordinates in the aforementioned diagram. The homogenized failure surfaces are then piecewise linear, consisting of the segments linking each adjacent pair of collapse loads. Eventually, it must be remarked that it is also possible to plot the failure mode for a specific load condition with the MATLAB command *patch*, reconstructing the position of each finite element from the other quantities coming from the solution of the linear programming problem (namely, the periodic velocity field and the components of the average strain rate tensor) and using Eqs. (4.1) and (4.2).

4.2 Case Studies

Six case studies are investigated in terms of in-plane homogenized failure surfaces, all representing actual masonry structures with non-periodic bonds but each displaying a different rate of irregularity. Specifically, these case studies range from rubble masonry (case study 1) to quasi-periodic masonry (2-4) and eventually to quasi-regular masonry (5-6). The difference between quasi-periodic and quasi-regular is the following: in the former case, the presence of bed joints is clearly visible, although there is no periodicity in terms of head joints and also the height of the units varies within the considered panel. Conversely, in the latter case the units present the same height despite having different lengths and a non-periodic arrangement, thus strongly resembling stretcher bond masonry. All the case studies are selected from a wider range presented in [12] and [13].

No experimental tests on the mechanical properties of the considered masonry types are available; therefore, for each case the same sets of properties are used, which are consistent with those available in literature [14][15]. For the full approach, the unit-unit interfaces are supposed to be infinitely resistant. Conversely, for both approaches the mortar-unit and mortar-mortar interfaces employ a single set of mechanical parameters (cohesion, friction angle, and tensile strength) that is reported in Table 4.1.

Table 4.1

Mechanical properties for the material employed in all case studies.

Cohesion [MPa]	Friction angle [°]	Tensile strength [MPa]
0.15	30	0.1

4.2.1 Strategy for the Identification of the Statistical REV

Four square test-windows of the same dimensions are extracted clockwise from the picture of the chosen masonry panel. In the following subsections, each test-window is denoted with a specific color that is also used for its corresponding homogenized failure surface; the colors are listed in Table 4.2. Also, four tentative sizes of growing dimensions are a priori identified for each test-window, which are listed in Table 4.3. These sizes correspond to different number of pixels for each case, since the pictures of the masonry walls of the six case studies differ in resolution. The actual dimensions are inferred from the masonry geometrical characteristics listed in [12] and [13] for each case. It must be noted that, for these case studies, the coarsing strategy has not been exploited.

Table 4.2

Legend expressing the colors of the extracted test-windows for each case study.

Test-window	Color
A	Blue
B	Red
C	Black
D	Green

Table 4.3

Test-window sizes and corresponding number of pixels for each case study.

Size	Area [cm ²]	Pixels					
		Case study 1	Case study 2	Case study 3	Case study 4	Case study 5	Case study 6
Small	70×70	100×100	108×108	117×117	91×91	103×103	95×95
Medium	100×100	143×143	154×154	167×167	130×130	147×147	135×135
Large	130×130	186×186	200×200	217×217	169×169	191×191	176×176
Huge	160×160	229×229	246×246	267×267	208×208	235×235	217×217

The homogenized failure surfaces are derived for all the test-windows of the same size, along with their envelope and the mean homogenized failure surface for the investigated size. The actual kinematic limit multiplier is evaluated for all the 11 pairs Σ_{xx}, Σ_{yy} constituting each of the four homogenized failure surfaces. From these, the mean limit multiplier $\bar{\chi}$ and the sample standard deviation σ are calculated, as well as the coefficient of variation σ^* (which is the ratio between σ and $\bar{\chi}$) expressed as a percentage. When all the 11 coefficients of variation for a test-window size are smaller than a selected threshold, then that very test-window size is deemed to be representative of the entire panel, thus becoming the sought statistical REV. Conversely, if at least one σ^* is greater than the threshold, the test-window size is enlarged and the analyses are repeated until the above condition is respected. It is trivial to remark that not every test-window size is investigated: once the threshold is successfully attained, the analyses are stopped. Two distinct thresholds are used in the following for the six case studies: specifically, the threshold for case studies 1-4 is equal to 25%, whereas for the last two cases is equal to 12.5%. This seems an arbitrary choice, but it is actually based on a simple observation: in case studies 1-4 the units' geometry varies in height as well as in length, while for the cases 5-6 they vary only in length. Then, since in the latter cases the units display uniform dimensions in height, the overall variation in terms of geometry is much less than in the former cases where also the height randomly varies, so it makes perfectly sense to reduce the threshold for cases 5-6.

4.2.2 Case Study 1: Rubble Masonry Building in Casola in Lunigiana, Tuscany

The first case study is represented by a residential masonry building located in Casola in Lunigiana, in the Province of Massa and Carrara, Tuscany, Italy. The three-story structure directly faces the street with a linteled entrance and is built with large, smoothed ashlar, which are also placed in the corners (Fig. 4.7a). A portion of one of its masonry walls is sketched in Fig. 4.7b, and its black-and-white rasterization is pictured in Fig. 4.7c. The ashlars are actually river pebbles of different geometry that are arranged without a clear regular pattern; in addition, tapered blocks and stone chips are scattered throughout the wall. It can then be stated that this is a shining example of rubble masonry. The test-windows for this case study are depicted in Fig. 4.8.

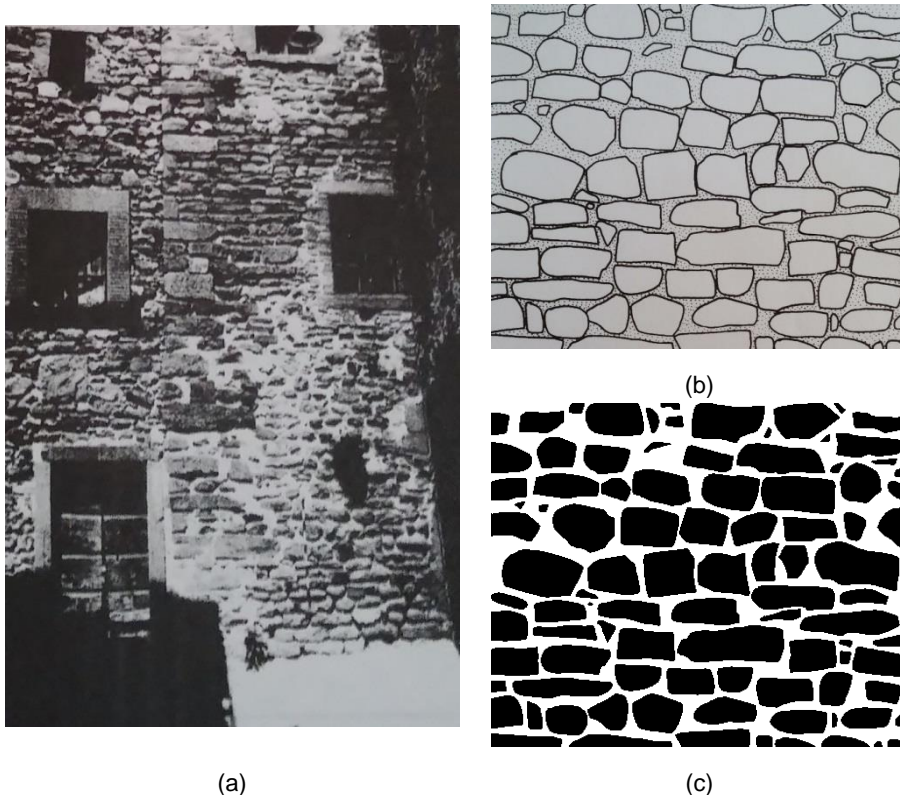


Fig. 4.7. (a) Masonry type for case study 1 [12]; (b) sketch of one of its masonry panels; (c) black-and-white rasterization of the sketch.

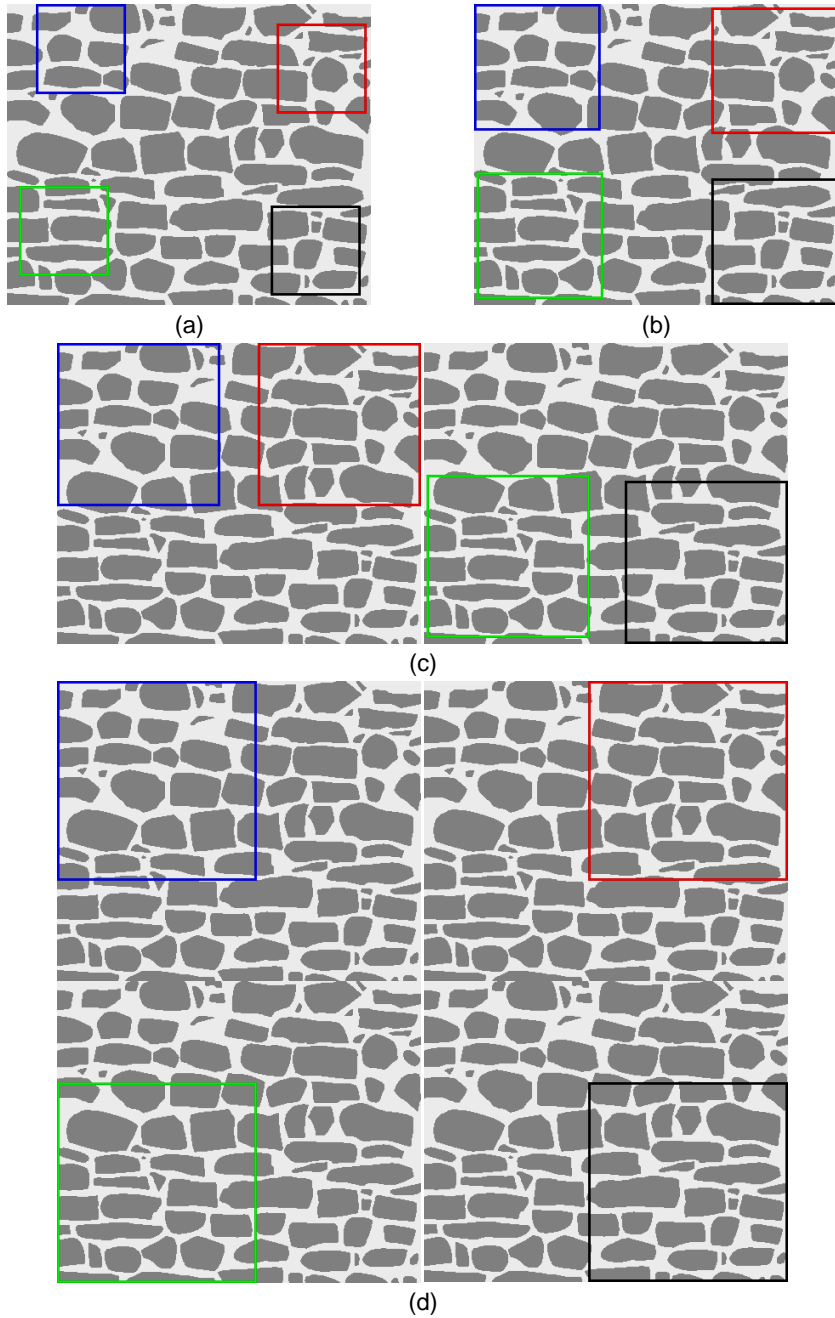


Fig. 4.8. Test-windows extracted for case study 1: (a) small size; (b) medium size; (c) large size; (d) huge size.

Fig. 4.9, Fig. 4.10, and Fig. 4.11 show the homogenized failure surfaces for the small, medium, and large test-windows, respectively, along with the resulting envelopes and the means. Regarding the latter, the results coming from the test-windows of large size satisfy the imposed threshold in terms of coefficient of variation, and so that can be considered the actual dimension of the REV for this specific masonry type.

The related data are reported in Table 4.4, for growing values of the loading angle. In this regard, it is trivial to notice how the higher degree of isotropy due to the presence of rubble masonry is well reflected by the shape of the homogenized mean failure surface for θ equal to 0° (i.e. absence of shear). In fact, the typical plateau that is related to the orthotropy is not present here. Analogous results are obtained for θ equal to 22.5° , while for θ equal to 45° the shape of the mean surface clearly displays a true isotropic behavior. In terms of deviation from the mean values, the scatter is not very large. It must be noted that when θ is equal to 0° , the mean limit multiplier for uniaxial vertical tension ($\psi = 90^\circ$) is lower - about $2/3$ - than the one for uniaxial horizontal tension ($\psi = 0^\circ$).

The reason is evident when considering the related failure modes, which are shown in Fig. 4.12 for the horizontal and vertical tension, respectively. In the first image, all the test-windows show that the random arrangement of ashlar does not allow the opening of true vertical cracks. Conversely, in the second image it is possible to observe a few clear horizontal cracks (especially in test-window A), meaning that the overall response for that load condition is slightly weaker than for the other one.

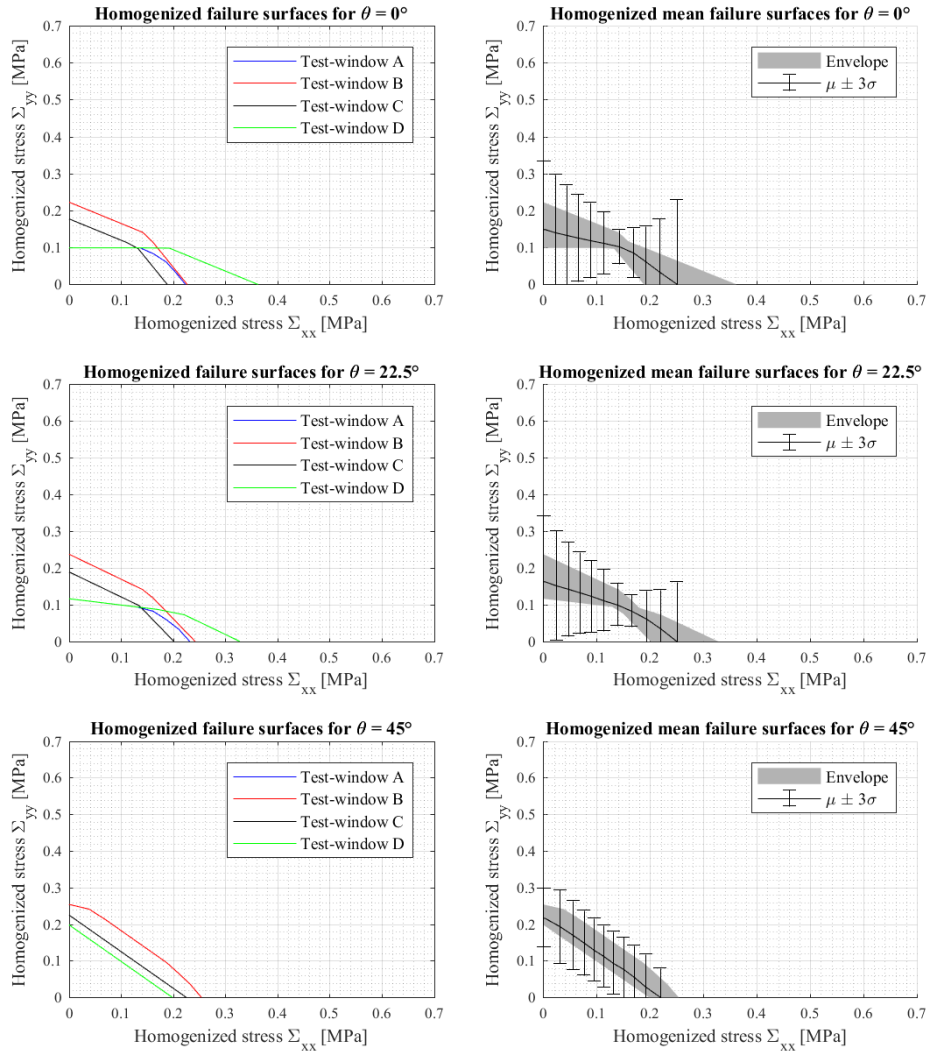


Fig. 4.9. Homogenized failure surfaces, means and envelopes for the small test-window size of case study 1.

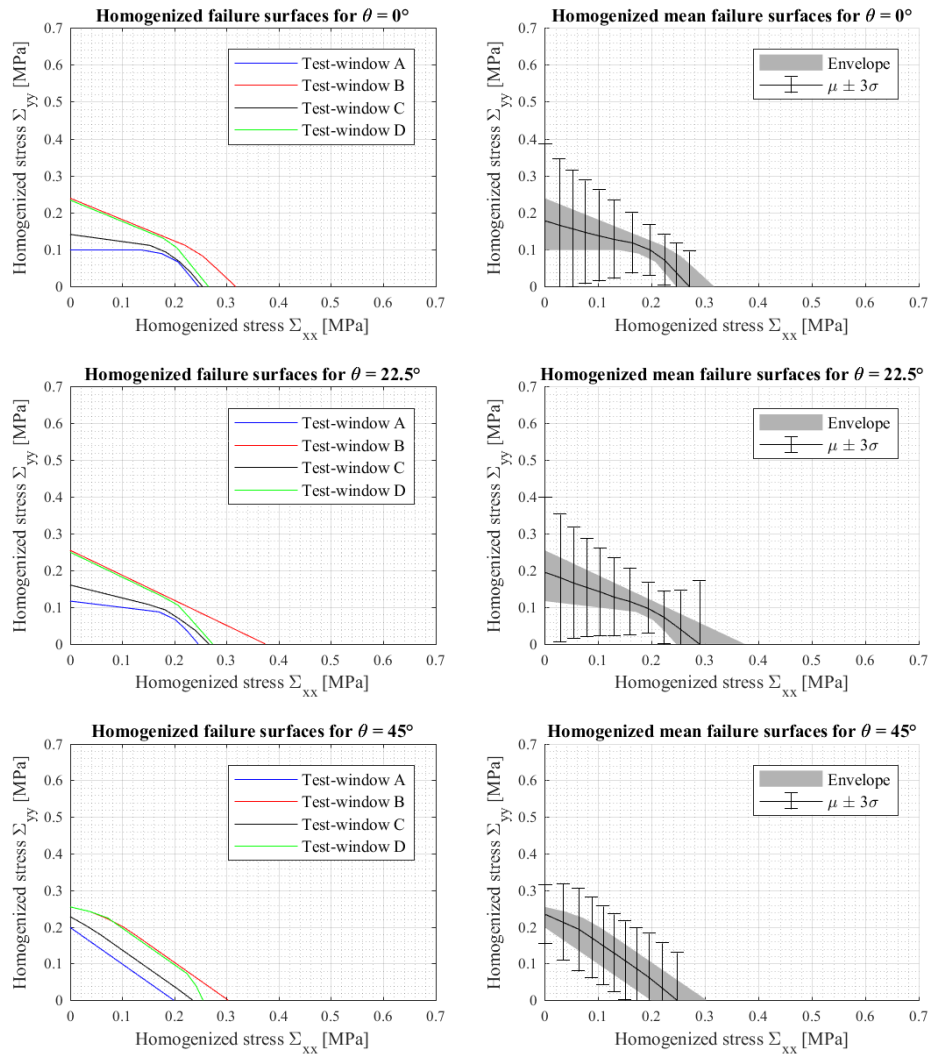


Fig. 4.10. Homogenized failure surfaces, means and envelopes for the medium test-window size of case study 1.

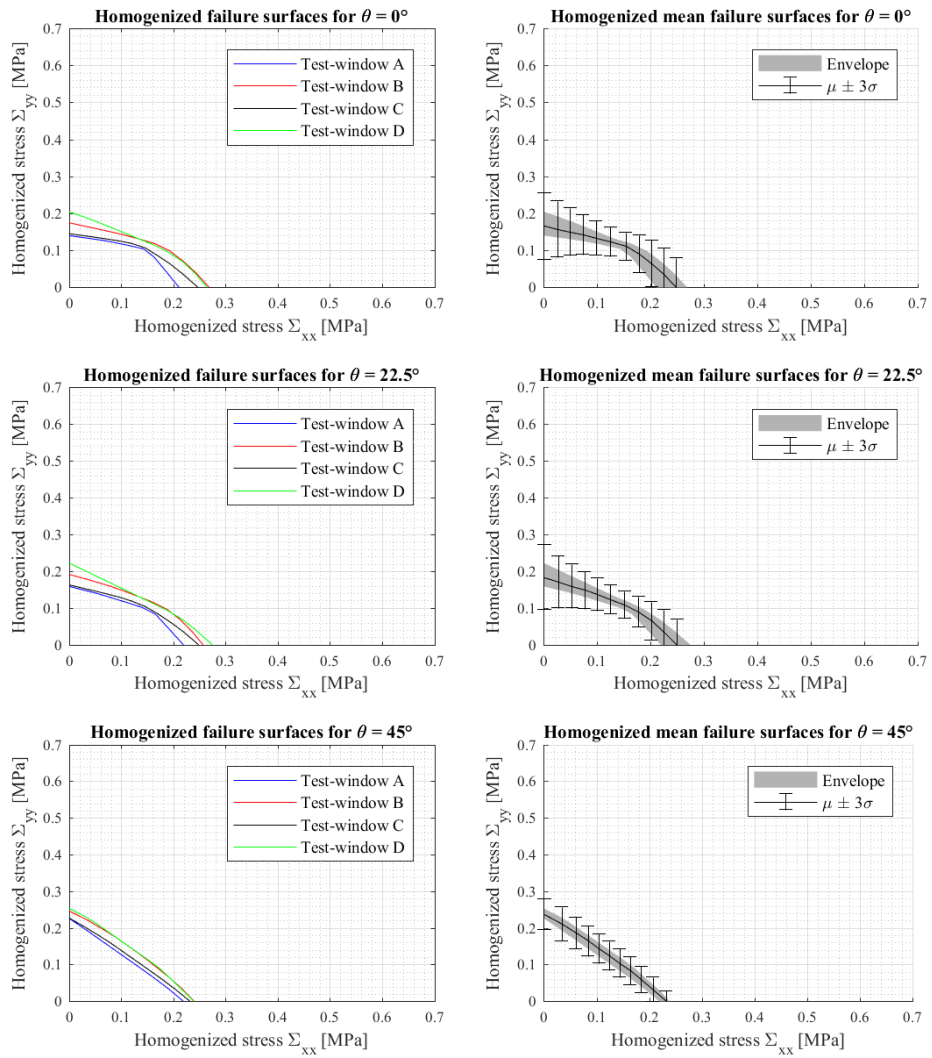


Fig. 4.11. Homogenized failure surfaces, means and envelopes for the large test-window size of case study 1.

Table 4.4

Mean limit multipliers, standard deviations and coefficient of variations for the large test-window size of case study 1.

θ	$\psi =$	0°	9°	18°	27°	36°	45°	54°	63°	72°	81°	90°
0°	$\bar{\chi}$	0.248	0.227	0.212	0.2	0.189	0.175	0.166	0.16	0.158	0.16	0.166
	σ	0.026	0.024	0.021	0.017	0.012	0.013	0.015	0.018	0.021	0.025	0.03
	σ^*	10.7%	10.5%	9.8%	8.4%	6.5%	7.5%	9.2%	11.2%	13.5%	15.8%	18%
22.5°	$\bar{\chi}$	0.249	0.227	0.211	0.198	0.186	0.175	0.169	0.167	0.168	0.173	0.184
	σ	0.023	0.02	0.017	0.014	0.012	0.013	0.015	0.017	0.02	0.024	0.029
	σ^*	9.3%	8.8%	8.2%	6.9%	6.5%	7.5%	8.7%	10.1%	11.7%	13.7%	16%
45°	$\bar{\chi}$	0.232	0.209	0.194	0.183	0.177	0.175	0.178	0.185	0.196	0.214	0.238
	σ	0.01	0.011	0.012	0.013	0.013	0.013	0.013	0.014	0.014	0.015	0.014
	σ^*	4.1%	5.2%	6.1%	7%	7.3%	7.5%	7.5%	7.5%	7.4%	7.1%	5.8%

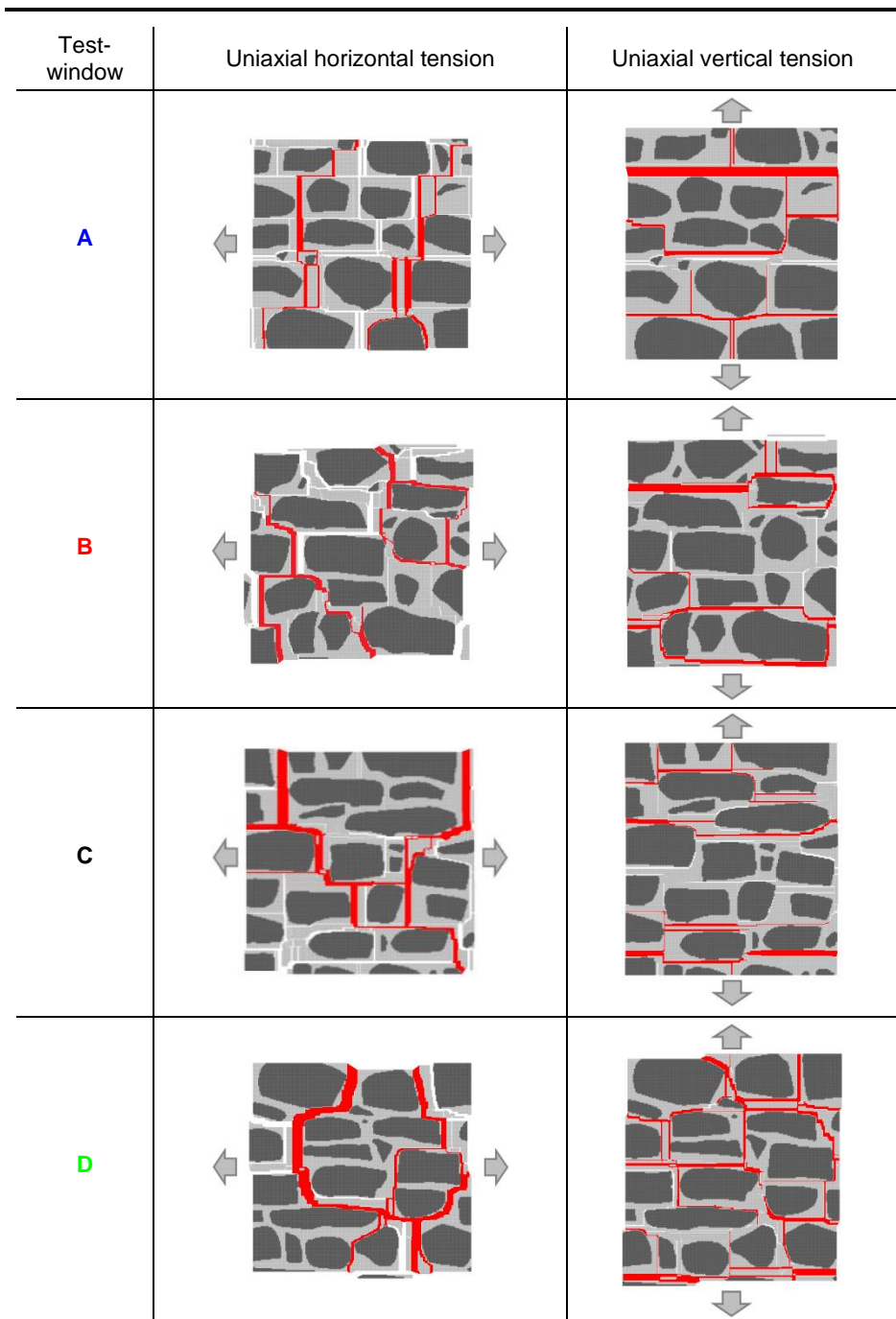


Fig. 4.12. Failure modes for the large test-window size of case study 1 when $\theta = 0^\circ$.

For this case study only, a thorough comparison is performed between the full and master-slave approaches. For the small, medium, and large sizes of the four test-windows, Table 4.5 lists the number of unknown variables and the computational time needed for extracting the homogenized failure surfaces.

Table 4.5

Comparison in terms of number of unknown variables and computational times for case study 1 between the two formulations (full and master-slave approaches).

Test-window	Entity	Approach	Test-window size		
			Small	Medium	Large
A	N° of unknowns	Full	99406	203638	344850
		Master-slave	39300	80708	132336
	Computational time	Full	12m	56m 3s	5h 33m 11s
		Master-slave	6m 45s	24m 50s	2h 19m 23s
B	N° of unknowns	Full	99406	203638	344850
		Master-slave	42626	77708	121783
	Computational time	Full	16m 22s	1h 29m 15s	4h 39m 2s
		Master-slave	8m 23s	36m 31s	1h 48m
C	N° of unknowns	Full	99406	203638	344850
		Master-slave	36335	81781	128257
	Computational time	Full	12m 19s	1h 27m 39s	4h 54m 52s
		Master-slave	5m 39s	37m 49s	2h 2m 12s
D	N° of unknowns	Full	99406	203638	344850
		Master-slave	34550	71613	110034
	Computational time	Full	10m 1s	1h 2m	3h 48m 36s
		Master-slave	4m 16s	26m 4s	1h 28m 13s

It is easy to observe that, for all the considered test-windows, the number of unknown variables for the master-slave approach is always reduced and, on average, is equal to 37.5% of that for the full approach. Similarly, the computational times experience a dramatic reduction: since the number of unknowns for the full approach is equal for different test-windows of the same size, their computational times exclusively depend on the geometry of each considered test-window, where geometry means arrangement of units and mean thickness of the mortar joints. However, when the master-slave approach is employed, the reduction in terms of computational times directly depends on the actual number of unknown variables to be calculated in the linear programming problem. The computational time required by the master-slave approach to derive the homogenized failure surfaces is on average almost 44% of that needed by the full approach. Moreover, there are no differences in terms of

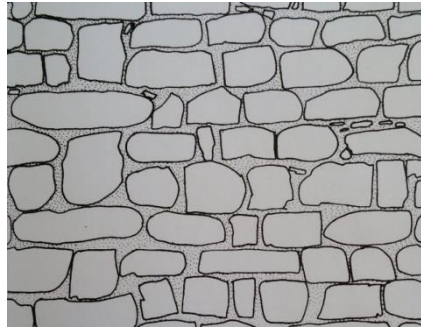
homogenized failure surfaces for the considered 12 test-windows, which are here omitted for sake of brevity. This confirms the initial hypothesis that, for mortar weaker than the units, failure in masonry panels due to tensile loads is usually bound to occur within mortar joints and not across units.

4.2.3 Case Study 2: Quasi-Periodic Masonry Ruin in Codiponte, Tuscany

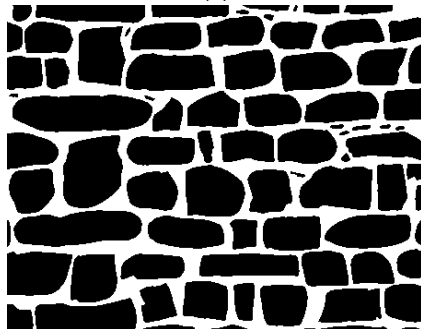
The second case study is represented by the ruin of an abandoned residential masonry building located in the small hamlet of Codiponte, which is part of the municipality of Casola in Lunigiana. This ruin represents the south wall of a now derelict two-story structure (Fig. 4.13a). A portion of this wall is sketched in Fig. 4.13b, and its black-and-white rasterization is pictured in Fig. 4.13c. The ashlar blocks are roughly cut and have distinct dimensions, also showing some tapered blocks and occasional stone chips. Despite the presence of a few blocks spreading over two masonry layers, the bed joints are clearly visible in the wall; hence the masonry is actually quasi-periodic in this case. The test-windows for this case study are depicted in Fig. 4.14.



(a)



(b)



(c)

Fig. 4.13. (a) Masonry type for case study 2 [12]; (b) sketch of the considered masonry panel; (c) black-and-white rasterization of the sketch.

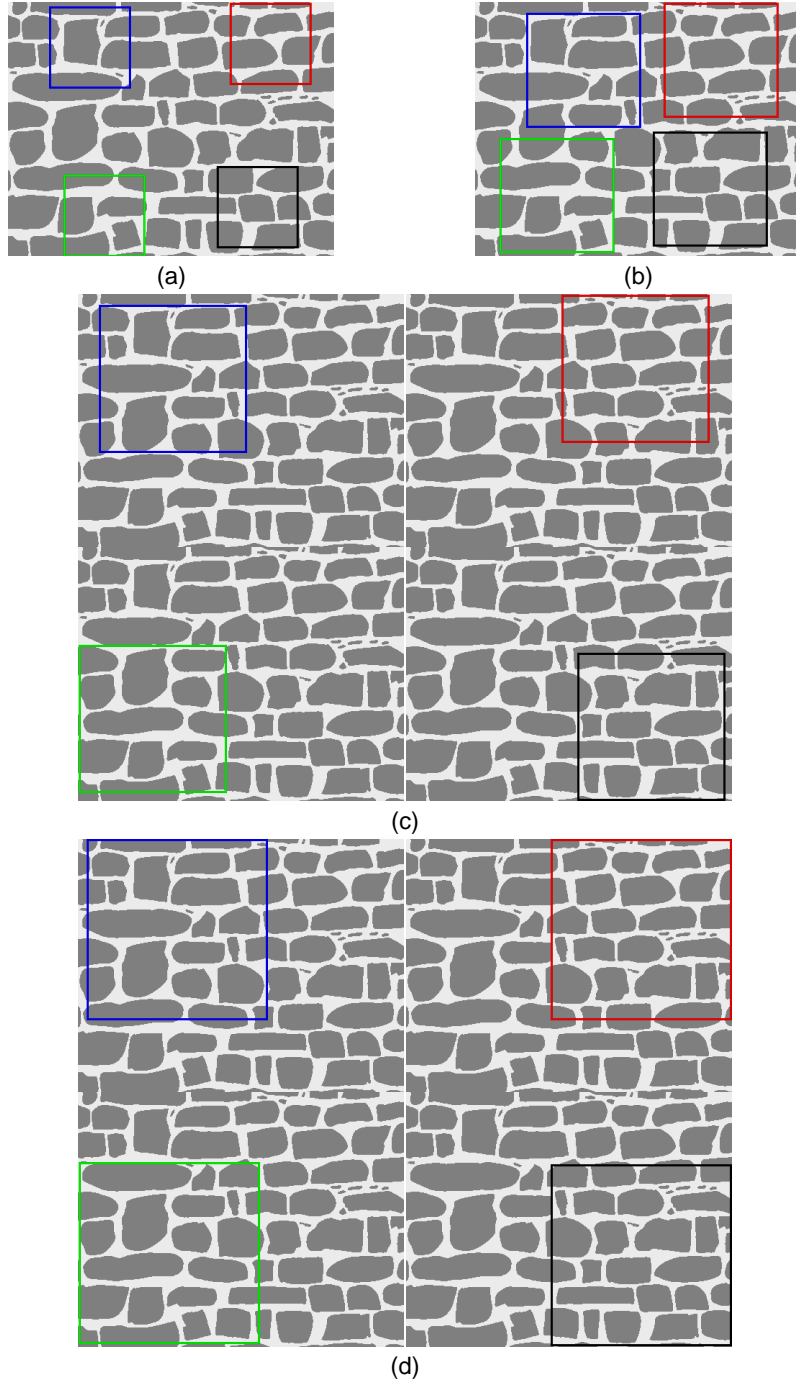


Fig. 4.14. Test-windows extracted for case study 2: (a) small size; (b) medium size; (c) large size; (d) huge size.

Fig. 4.15 to Fig. 4.18 show the homogenized failure surfaces for all the test-windows, along with the resulting envelopes and the means. Regarding the latter, the results coming from the test-windows of huge size satisfy the imposed threshold in terms of coefficient of variation, and so that can be considered the actual dimension of the REV for this specific masonry type.

The related data are reported in Table 4.6, for growing values of the loading angle. Despite bed joints are more clearly visible in this type of masonry, the shape of the homogenized mean failure surface for the huge test-windows when θ equal to 0° is still not fully orthotropic, due to the presence of vertical blocks and stone chips. No differences are observed for θ equal to 22.5° , and once again for θ equal to 45° the shape of the mean surface evidently displays a true isotropic behavior. In terms of deviation from the mean values, the scatter is slightly larger than the previous case. However, when θ is equal to 0° the ratio between the mean limit multipliers for uniaxial vertical and horizontal tension is still about $2/3$. This is due to the presence of vertical blocks and also to the non-uniform vertical dimensions of the masonry courses.

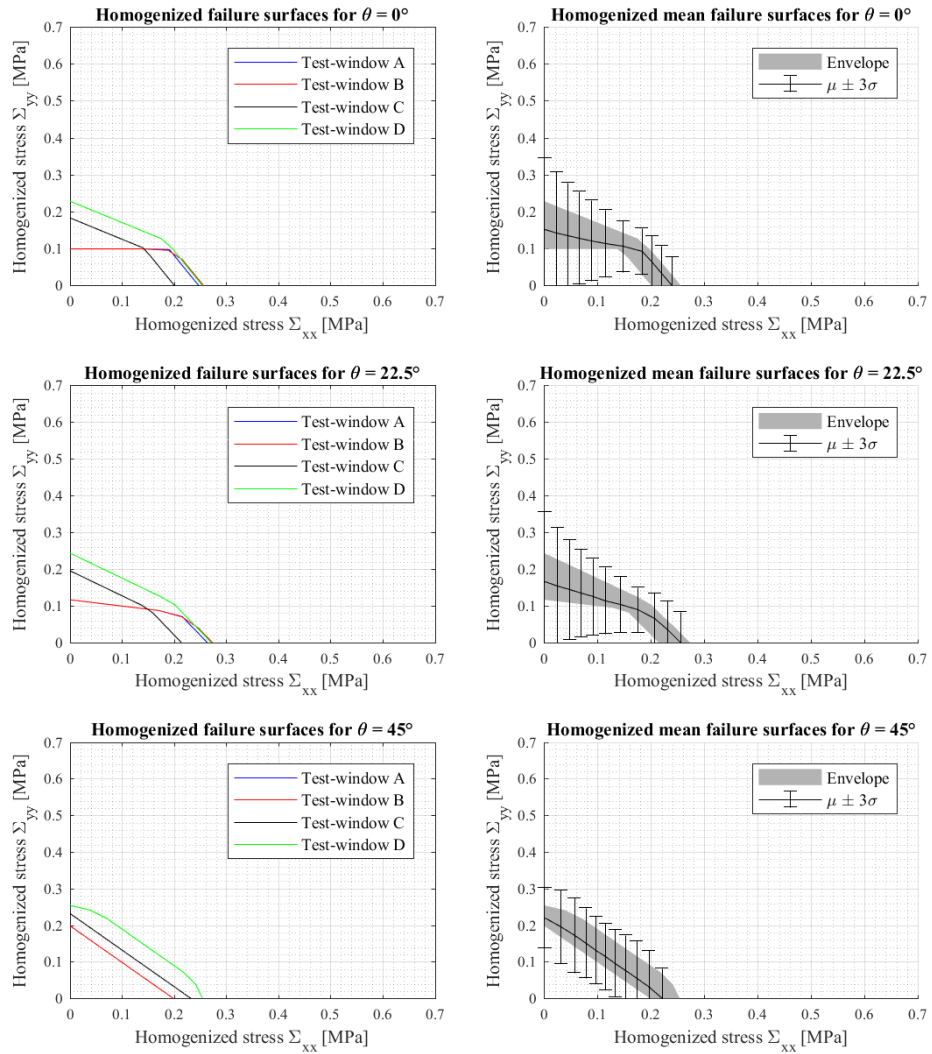


Fig. 4.15. Homogenized failure surfaces, means and envelopes for the small test-window size of case study 2.

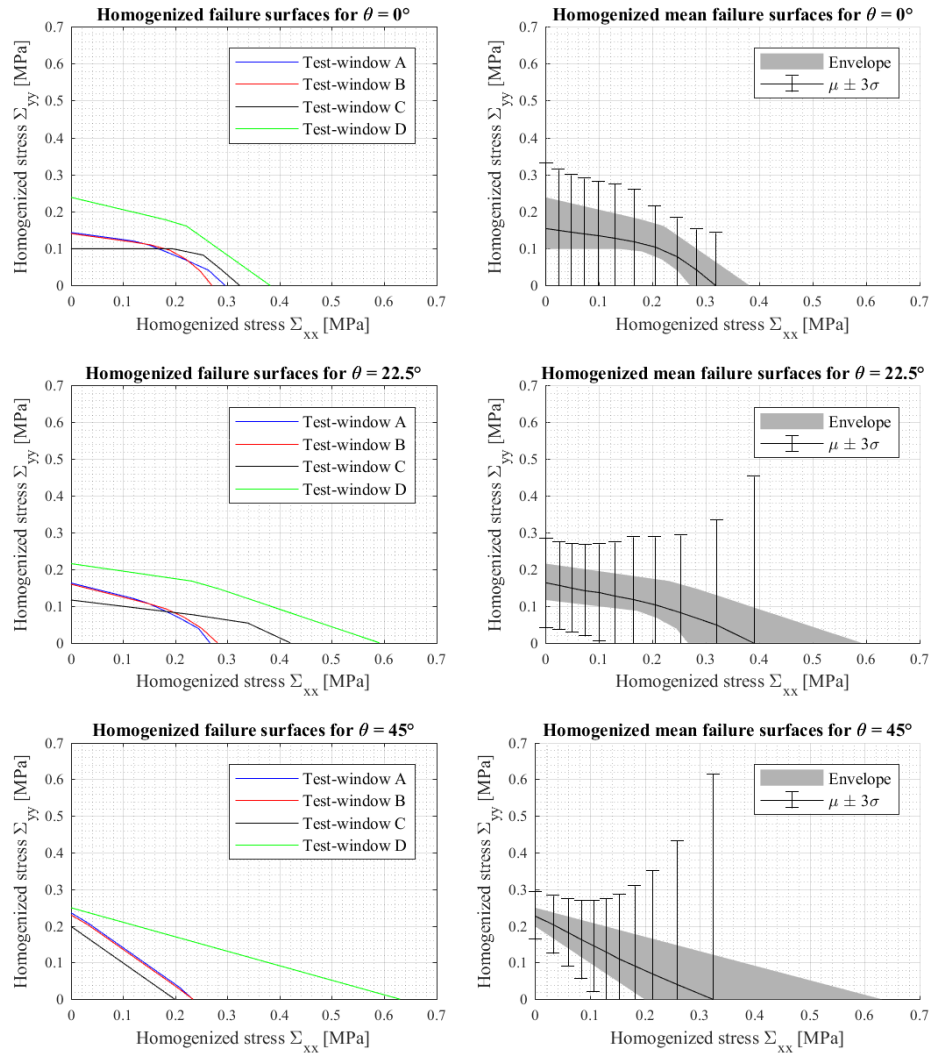


Fig. 4.16. Homogenized failure surfaces, means and envelopes for the medium test-window size of case study 2.

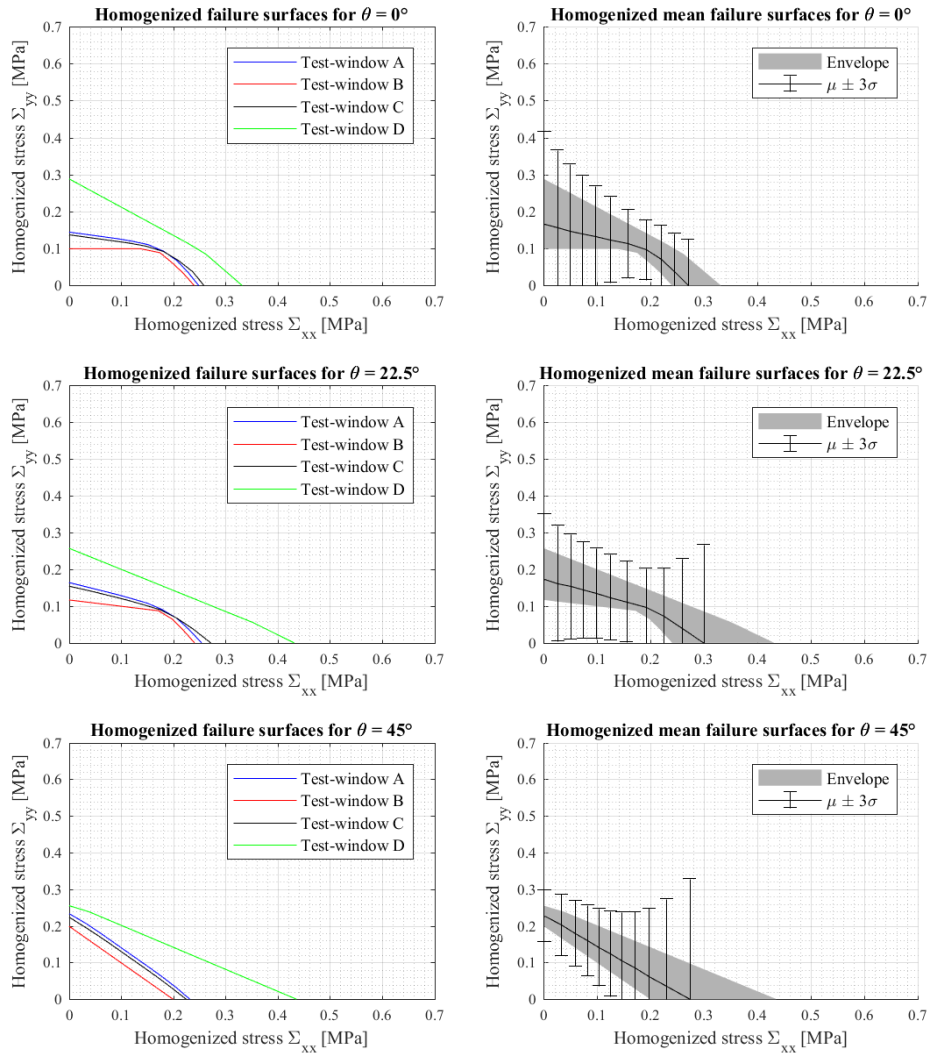


Fig. 4.17. Homogenized failure surfaces, means and envelopes for the large test-window size of case study 2.

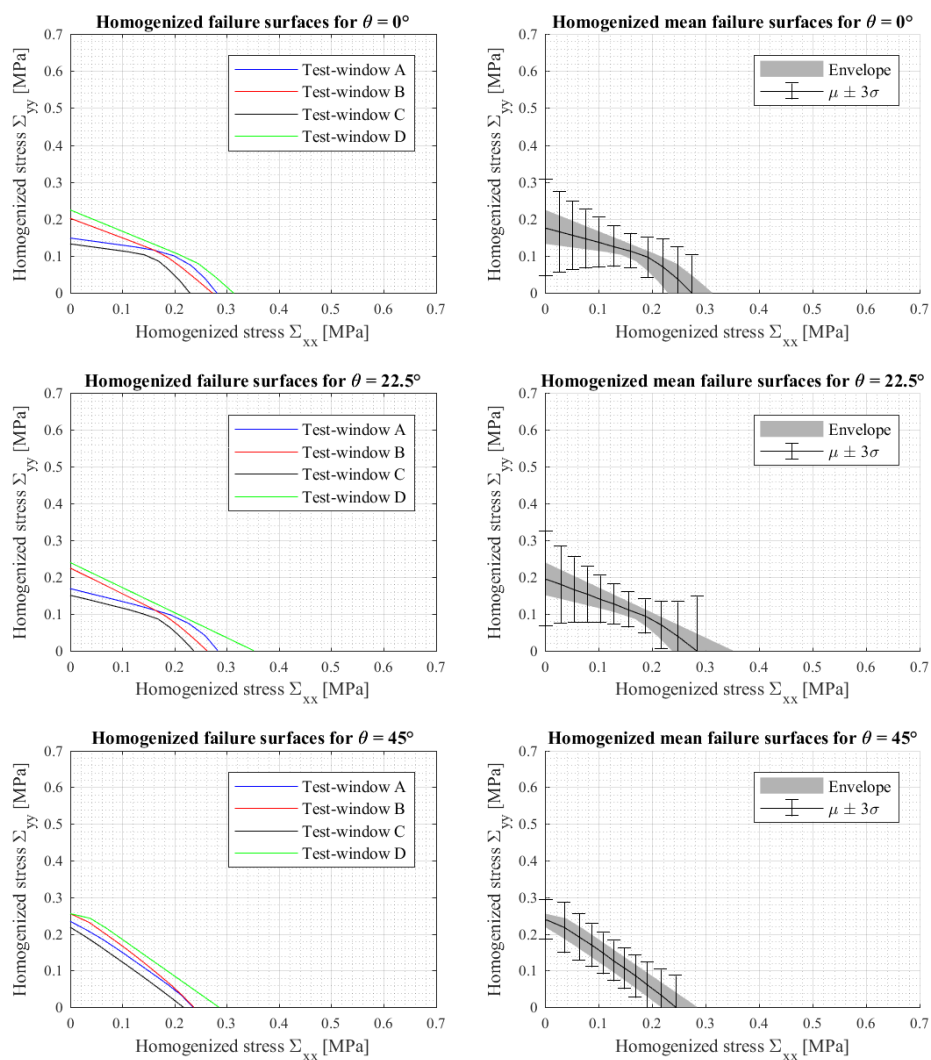


Fig. 4.18. Homogenized failure surfaces, means and envelopes for the huge test-window size of case study 2.

Table 4.6

Mean limit multipliers, standard deviations and coefficient of variations for the huge test-window size of case study 2.

θ	$\psi =$	0°	9°	18°	27°	36°	45°	54°	63°	72°	81°	90°
0°	$\bar{\chi}$	0.274	0.25	0.231	0.214	0.196	0.181	0.17	0.165	0.165	0.165	0.177
	σ	0.035	0.029	0.025	0.018	0.015	0.018	0.022	0.026	0.031	0.036	0.043
	σ^*	12.6%	11.6%	10.9%	8.4%	7.8%	10.1%	13.1%	15.9%	18.7%	21.5%	24.5%
22.5°	$\bar{\chi}$	0.283	0.251	0.227	0.209	0.192	0.181	0.174	0.172	0.175	0.183	0.196
	σ	0.049	0.031	0.022	0.016	0.016	0.018	0.022	0.025	0.029	0.035	0.043
	σ^*	17.4%	12.5%	9.5%	7.4%	8.4%	10.1%	12.4%	14.6%	16.8%	19.2%	21.9%
45°	$\bar{\chi}$	0.244	0.218	0.2	0.189	0.182	0.181	0.183	0.19	0.203	0.221	0.241
	σ	0.029	0.023	0.021	0.019	0.018	0.018	0.019	0.02	0.021	0.023	0.018
	σ^*	11.9%	10.7%	10.3%	10.2%	10.1%	10.1%	10.2%	10.3%	10.4%	10.4%	7.4%

4.2.4 Case Study 3: Quasi-Periodic Masonry Parish Church in Filattiera, Tuscany

The third case study is represented by a Romanesque masonry parish church located in the small hamlet of Sorano, which is part of the municipality of Filattiera, in the Province of Massa and Carrara, Tuscany, Italy. This parish church is dedicated to Saint Stephen and presents three naves, each terminating with an apse (Fig. 4.19a). A portion of one of its masonry walls is sketched in Fig. 4.19b, and its black-and-white rasterization is pictured in Fig. 4.19c. The ashlar blocks are river pebbles of different dimensions, which are joined together with thick mortar joints. The bed joints are again clearly visible in the wall, but unlike the last case study there are no vertical elements; hence this masonry is again considered quasi-periodic. The test-windows for this case study are depicted in Fig. 4.20.

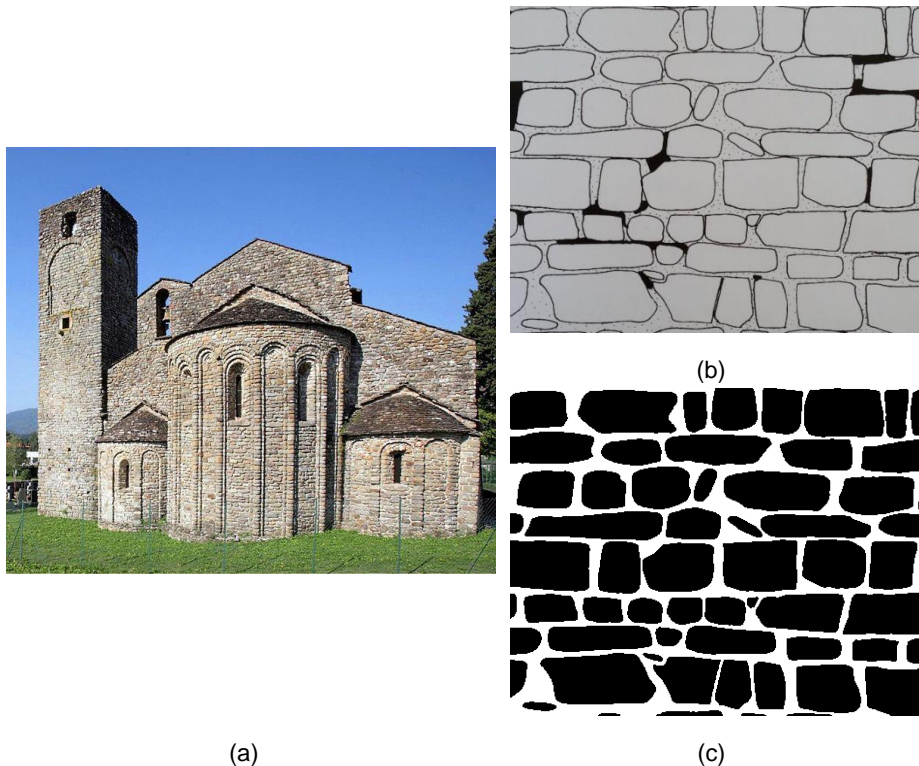


Fig. 4.19. (a) Masonry type for case study 3 ^[source]; (b) sketch of the considered masonry panel; (c) black-and-white rasterization of the sketch.

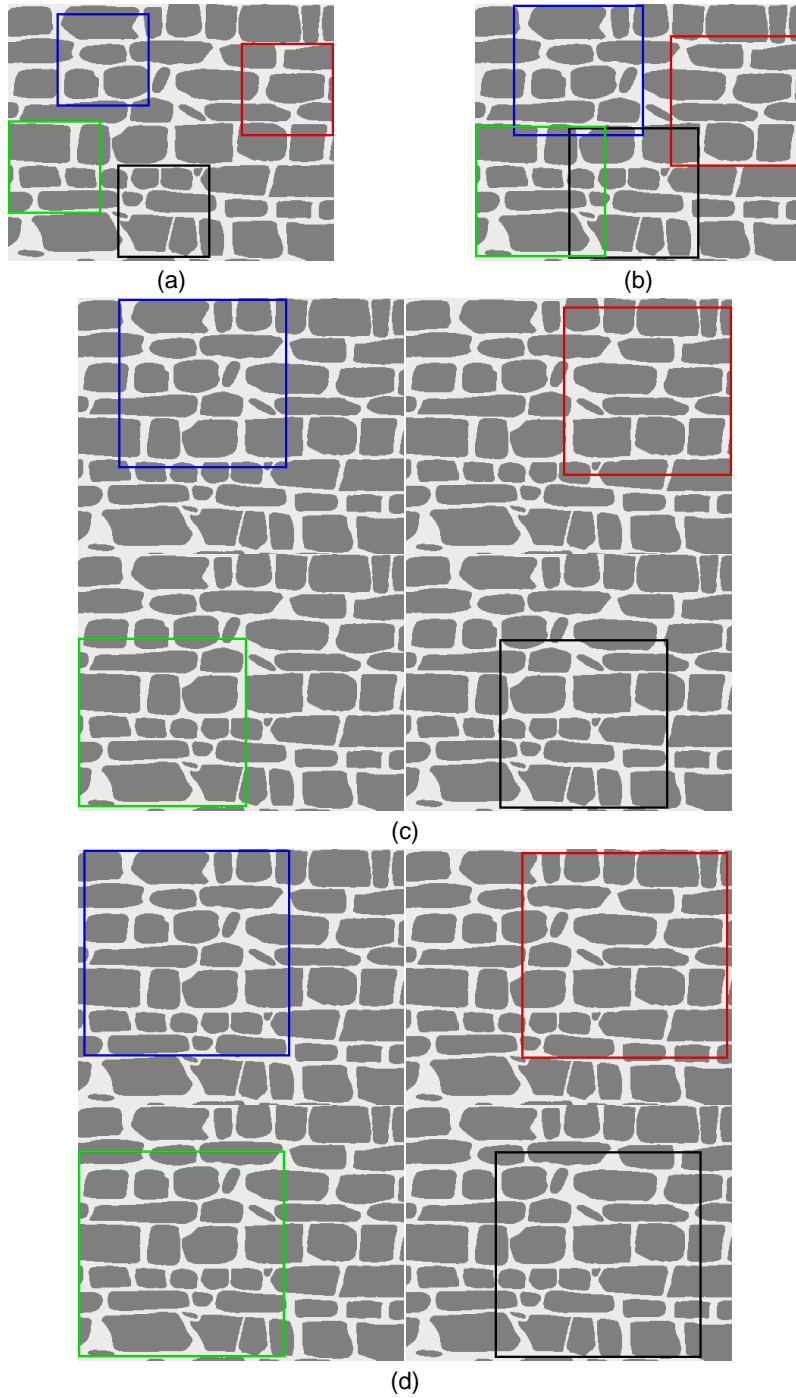


Fig. 4.20. Test-windows extracted for case study 3: (a) small size; (b) medium size; (c) large size; (d) huge size.

Fig. 4.21 to Fig. 4.24 show the homogenized failure surfaces for all the test-windows, along with the resulting envelopes and the means. Regarding the latter, the results coming from the test-windows of huge size satisfy the imposed threshold in terms of coefficient of variation, and so that can be considered the actual dimension of the REV for this specific masonry type.

The related data are reported in Table 4.7, for growing values of the loading angle. The shape of the homogenized mean failure surface for the huge test-windows when θ equal to 0° suggests a quasi-orthotropic behavior of this type of masonry. In fact, unlike the previous case, there are no vertical blocks within the masonry bulk; therefore, despite a general dissimilarity in terms of units' geometry, the behavior is still consistent with that of a periodic masonry type. In terms of deviation from the mean values, the scatter is not very large except for the uniaxial vertical tension. Moreover, when θ is equal to 0° , the mean limit multiplier for uniaxial vertical tension is about 40% of the one for uniaxial horizontal tension, with this ratio being lower than the previous two cases.

The reason is evident when considering the related failure modes, which are shown in Fig. 4.25 for horizontal and vertical tension, respectively. In particular, the failure modes for the latter load condition are remarkably different than those for the former; here, the formation of horizontal cracks is very evident for the uniaxial vertical tension, as no vertical blocks are inserted into the masonry bulk.

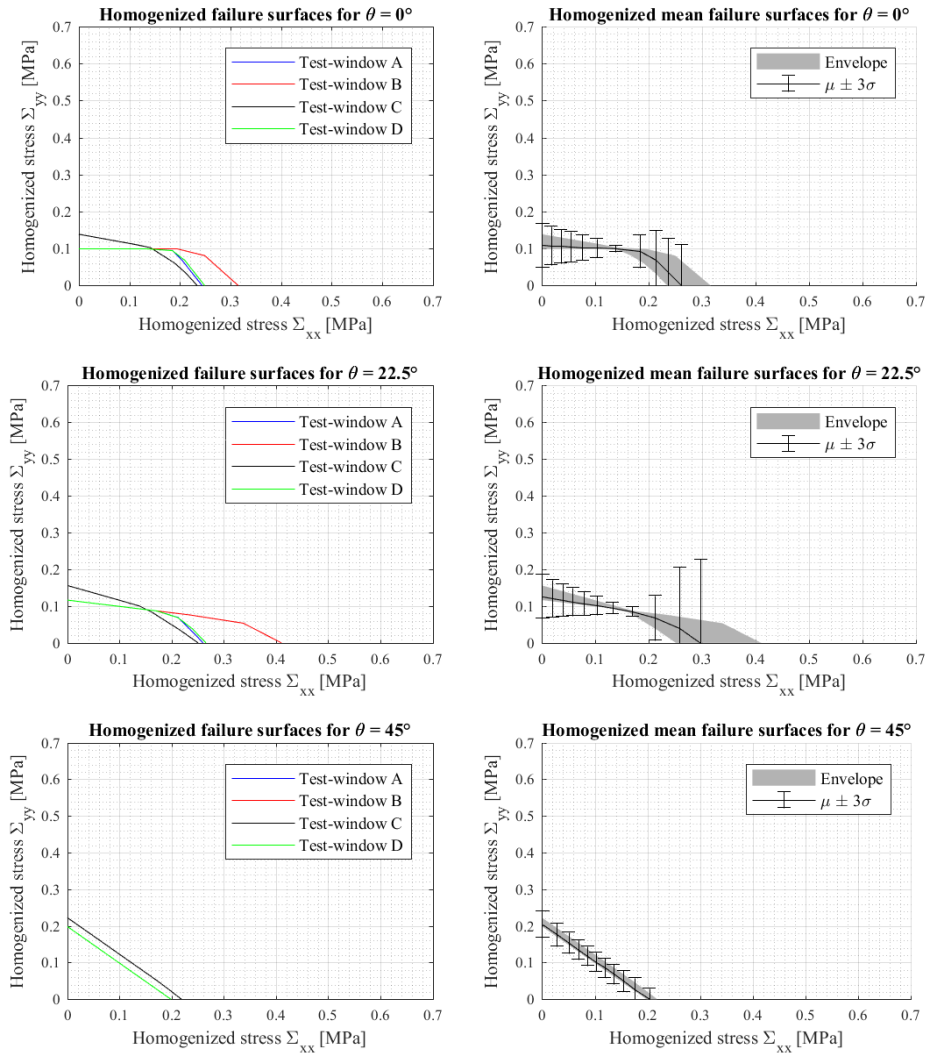


Fig. 4.21. Homogenized failure surfaces, means and envelopes for the small test-window size of case study 3.

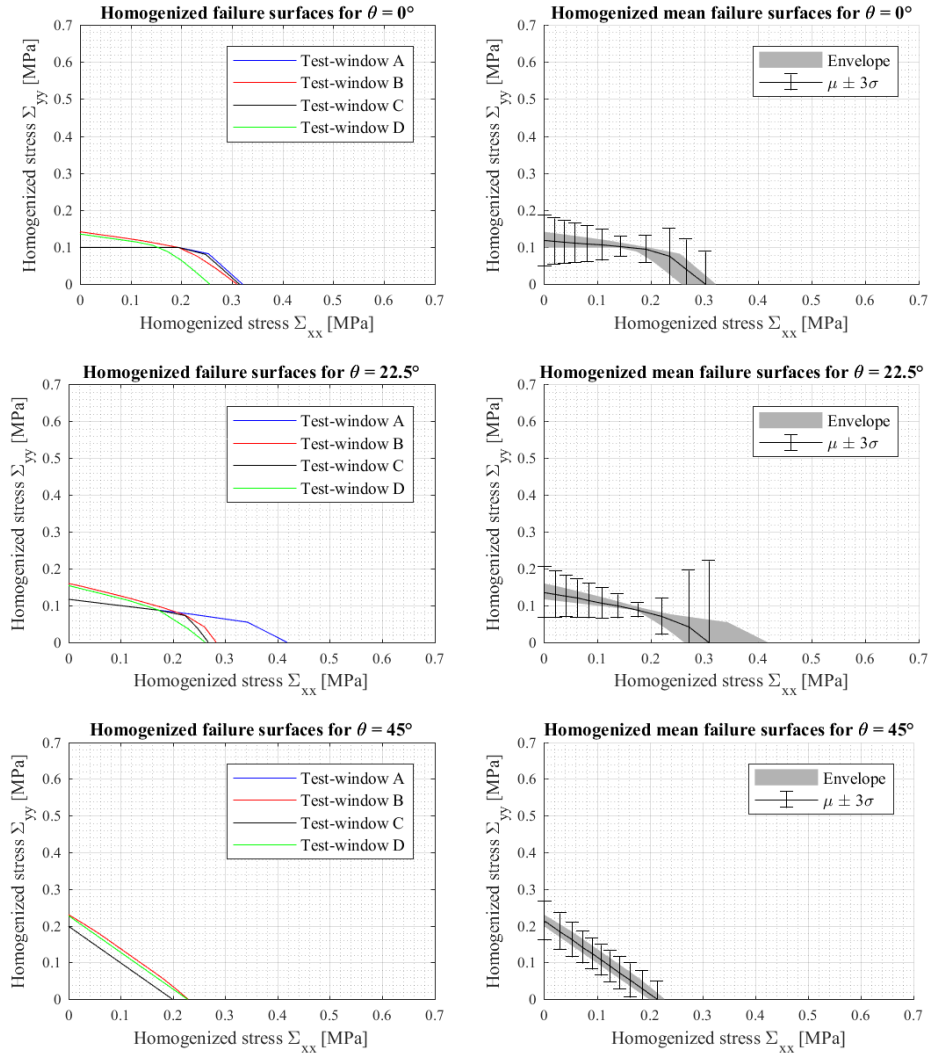


Fig. 4.22. Homogenized failure surfaces, means and envelopes for the medium test-window size of case study 3.

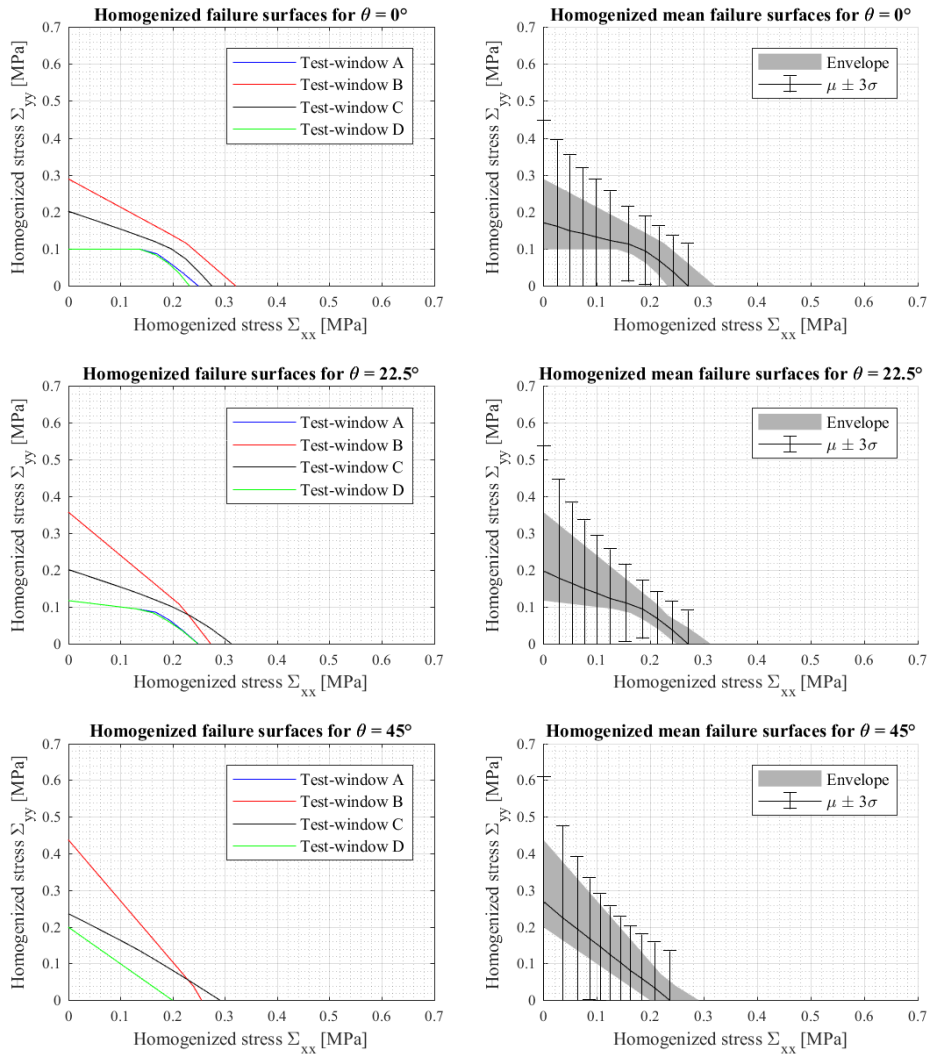


Fig. 4.23. Homogenized failure surfaces, means and envelopes for the large test-window size of case study 3.

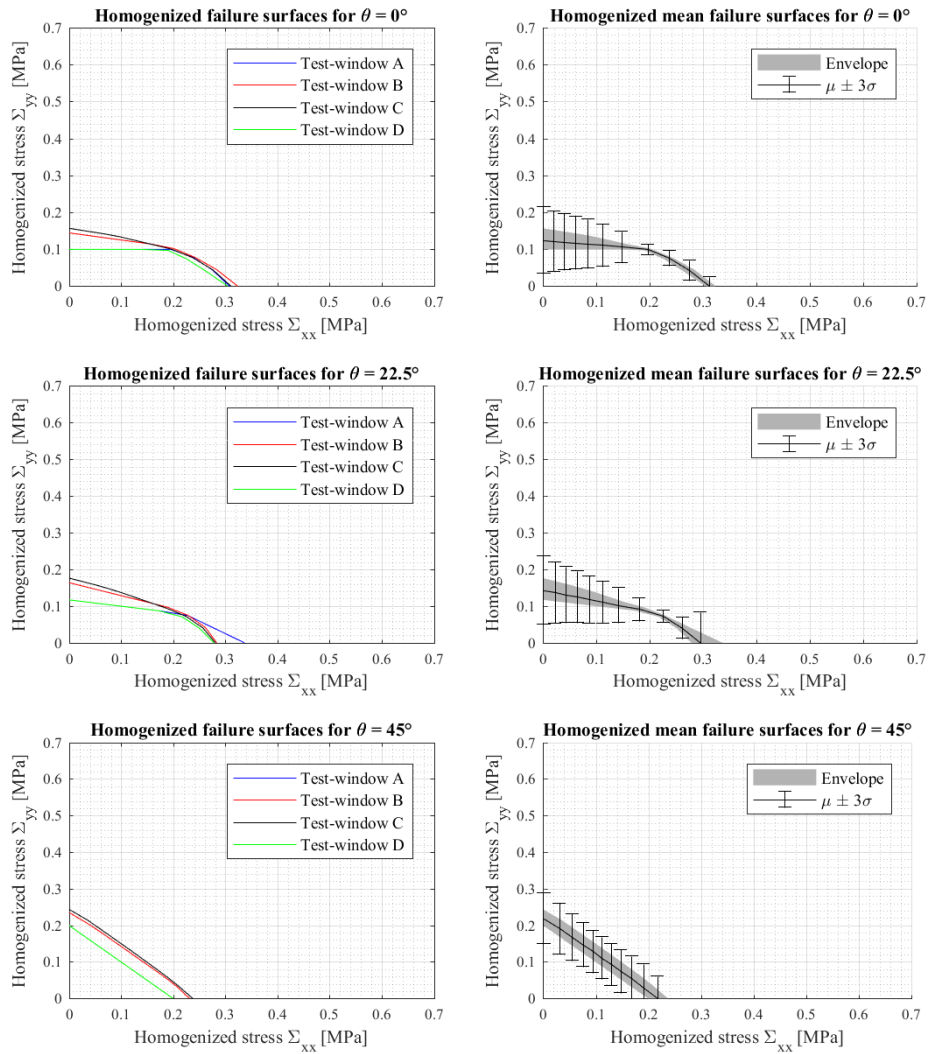


Fig. 4.24. Homogenized failure surfaces, means and envelopes for the huge test-window size of case study 3.

Table 4.7

Mean limit multipliers, standard deviations and coefficient of variations for the huge test-window size of case study 3.

θ	$\psi =$	0°	9°	18°	27°	36°	45°	54°	63°	72°	81°	90°
0°	$\bar{\chi}$	0.312	0.277	0.248	0.219	0.182	0.157	0.142	0.132	0.126	0.124	0.125
	σ	0.008	0.009	0.007	0.005	0.014	0.019	0.022	0.024	0.025	0.027	0.03
	σ^*	2.7%	3.3%	2.8%	2.2%	7.7%	12.1%	15.5%	18.1%	20.1%	22%	23.8%
22.5°	$\bar{\chi}$	0.294	0.263	0.236	0.201	0.174	0.157	0.147	0.141	0.138	0.139	0.143
	σ	0.028	0.01	0.006	0.011	0.016	0.019	0.021	0.024	0.026	0.028	0.031
	σ^*	9.5%	3.7%	2.4%	5.2%	9.1%	12.1%	14.6%	16.8%	18.5%	20.1%	21.7%
45°	$\bar{\chi}$	0.217	0.193	0.176	0.165	0.159	0.157	0.159	0.165	0.177	0.194	0.219
	σ	0.02	0.021	0.021	0.02	0.019	0.019	0.019	0.02	0.021	0.023	0.023
	σ^*	9.3%	11.1%	11.8%	11.9%	12%	12.1%	12.1%	12.1%	12.1%	11.9%	10.6%

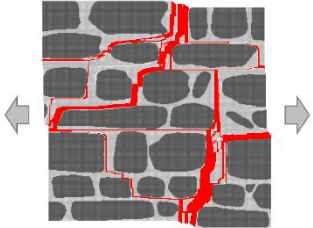
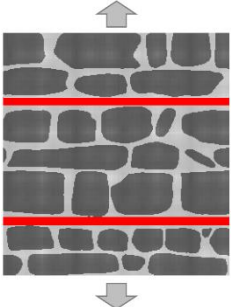
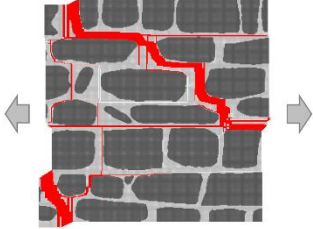
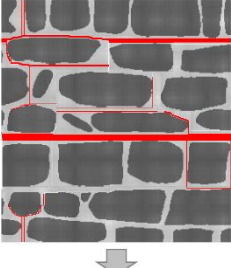
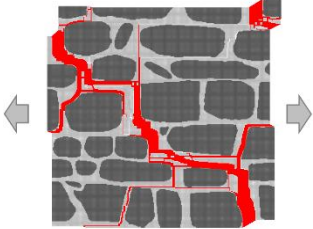
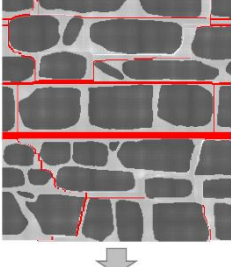
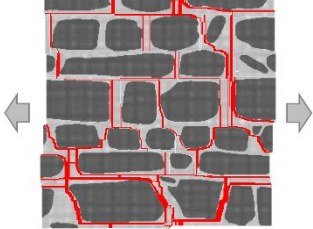
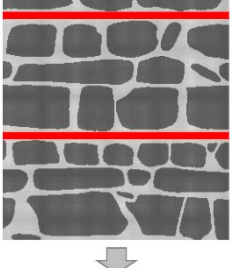
Test-window	Uniaxial horizontal tension	Uniaxial vertical tension
A		
B		
C		
D		

Fig. 4.25. Failure modes for the huge test-window size of case study 3 when $\theta = 0^\circ$

4.2.5 Case Study 4: Quasi-Periodic Masonry Tower Ruins in Mulazzo, Tuscany

The fourth case study is represented by the ruins of a masonry tower located in Mulazzo, in the Province of Massa and Carrara, Tuscany, Italy. The tower presents a hexagonal shape and was the *mastio* of a larger castle (Fig. 4.26a). A portion of one of its walls is sketched in Fig. 4.26b, and its black-and-white rasterization is pictured in Fig. 4.26c. The ashlar blocks are roughly cut and have distinct dimensions, although their height is more uniform. Some stone chips are also occasionally present. Once more, the bed joints are clearly visible in the wall, and as in the last case study there are no vertical elements; hence this masonry is once again considered quasi-periodic. The test-windows for this case study are depicted in Fig. 4.27.

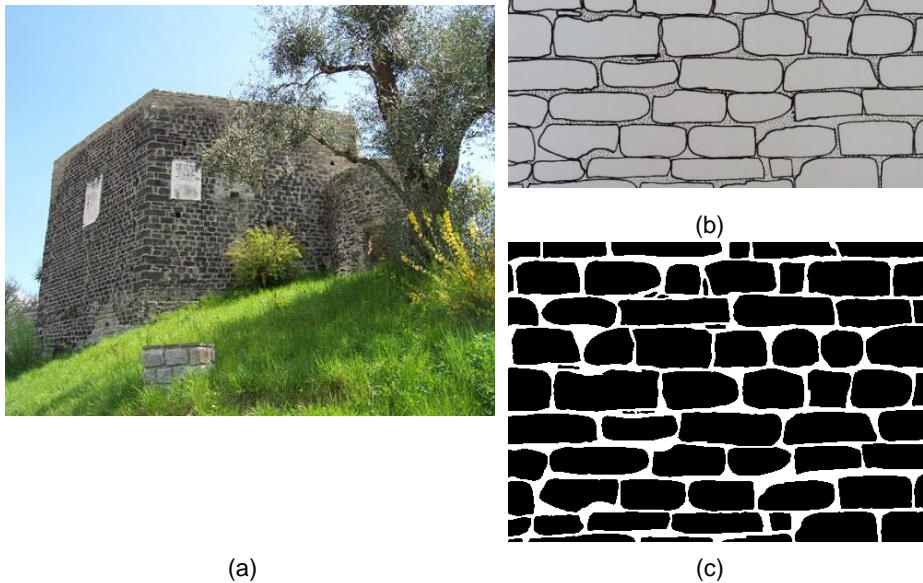


Fig. 4.26. (a) Masonry type for case study 4 ^[source]; (b) sketch of the considered masonry panel; (c) black-and-white rasterization of the sketch.

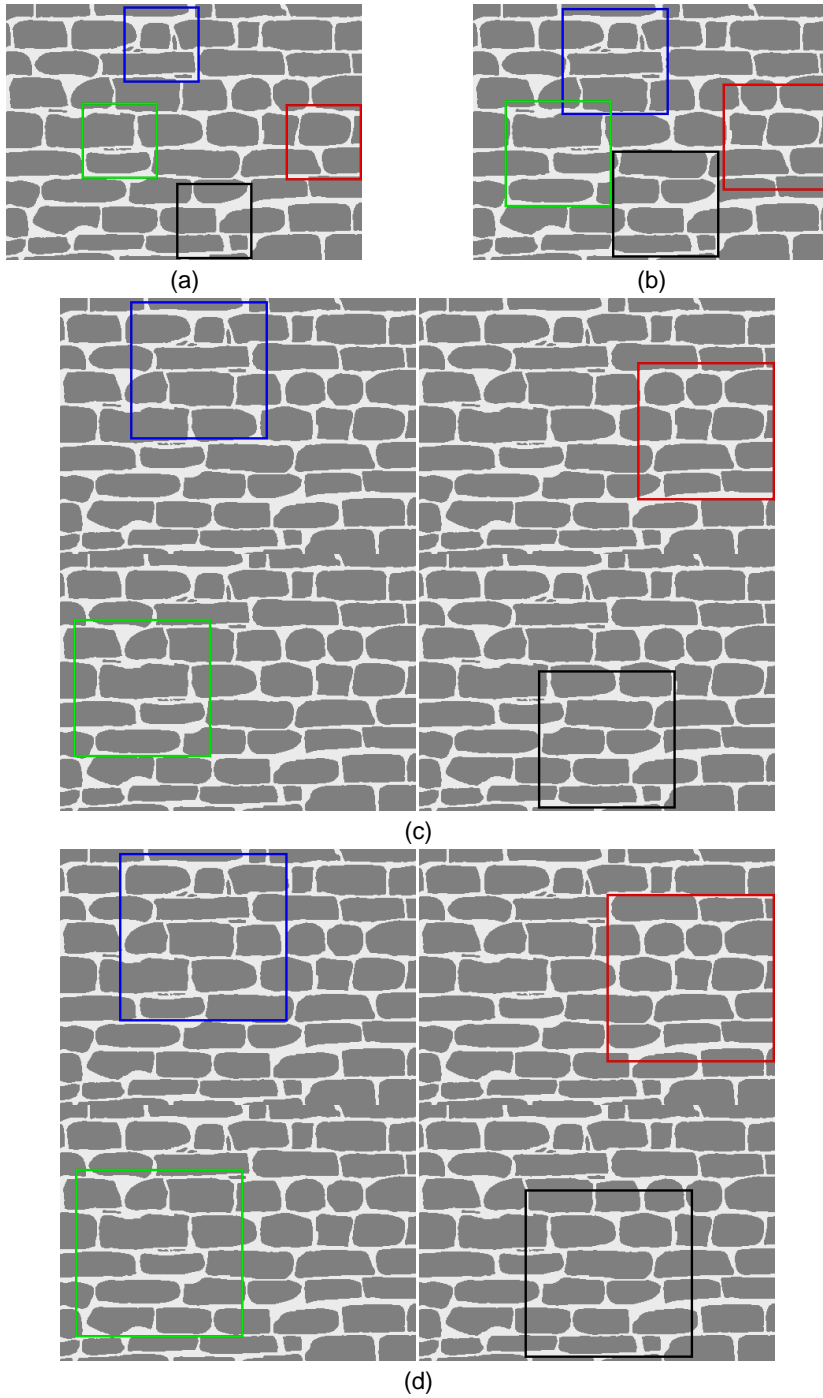


Fig. 4.27. Test-windows extracted for case study 4: (a) small size; (b) medium size; (c) large size; (d) huge size.

Fig. 4.28 to Fig. 4.31 show the homogenized failure surfaces for all the test-windows, along with the resulting envelopes and the means. Regarding the latter, the results coming from the test-windows of huge size satisfy the imposed threshold in terms of coefficient of variation, and so that can be considered the actual dimension of the REV for this specific masonry type.

The related data are reported in Table 4.8, for growing values of the loading angle. The shape of the homogenized mean failure surface for the huge test-windows when θ equal to 0° suggests an almost complete orthotropic behavior of this type of masonry, even more evident than the previous case. In terms of deviation from the mean values, the scatter is not very large except for the uniaxial horizontal tension. Moreover, when θ is equal to 0° , the mean limit multiplier for uniaxial vertical tension is 37% of the one for uniaxial horizontal tension, a ratio slightly lower than the previous case but originating from the same causes (absence of vertical blocks).

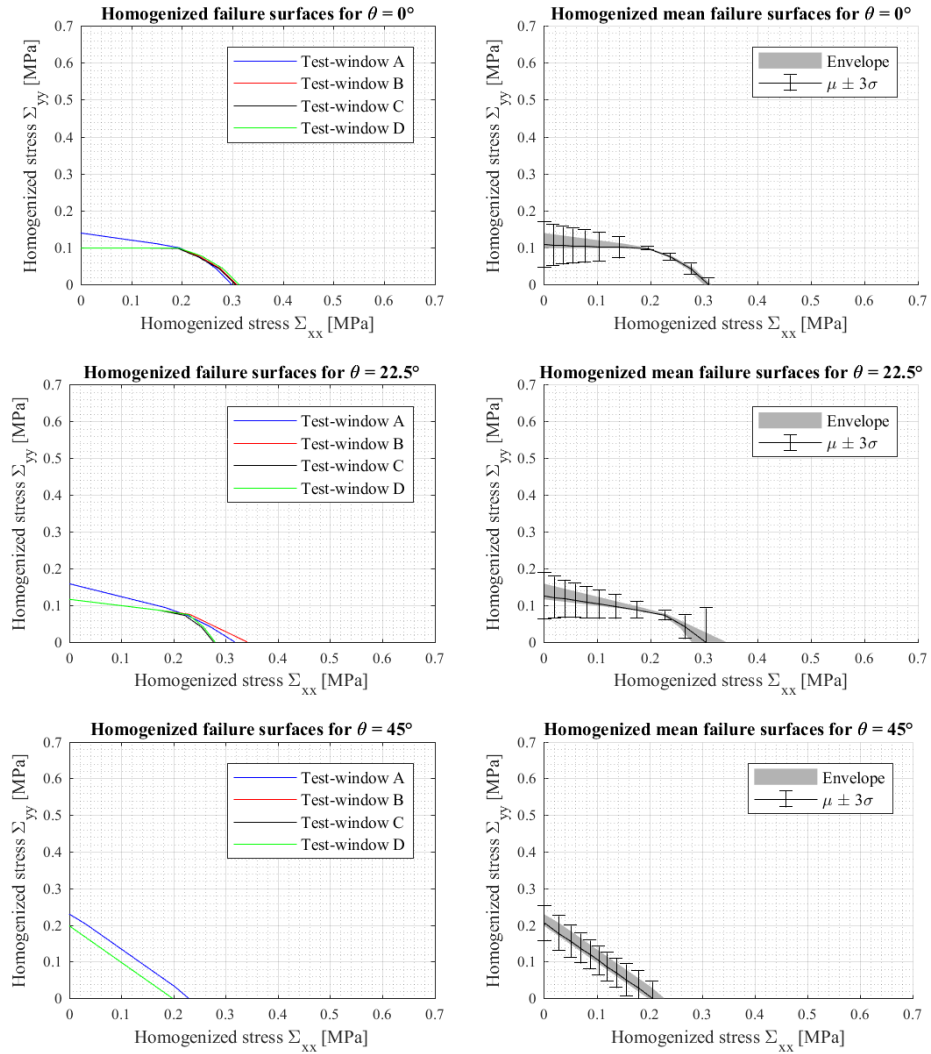


Fig. 4.28. Homogenized failure surfaces, means and envelopes for the small test-window size of case study 4.

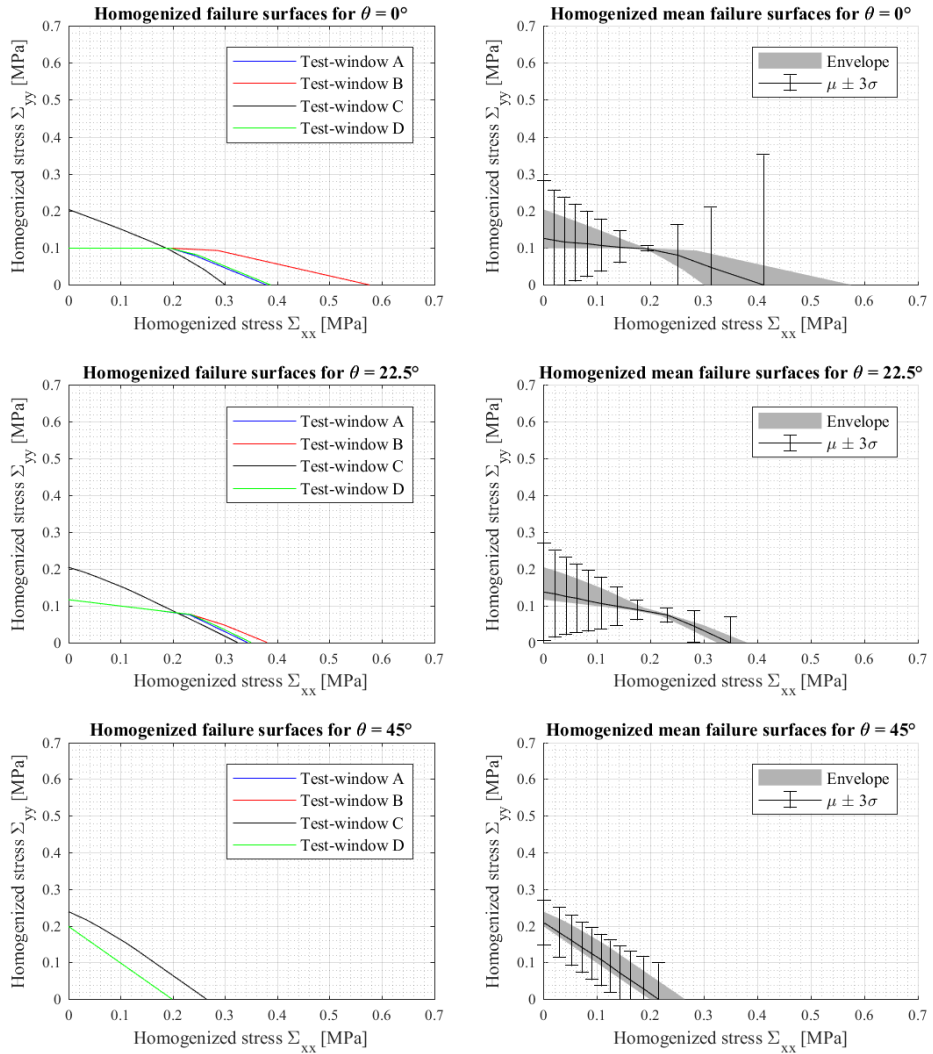


Fig. 4.29. Homogenized failure surfaces, means and envelopes for the medium test-window size of case study 4.

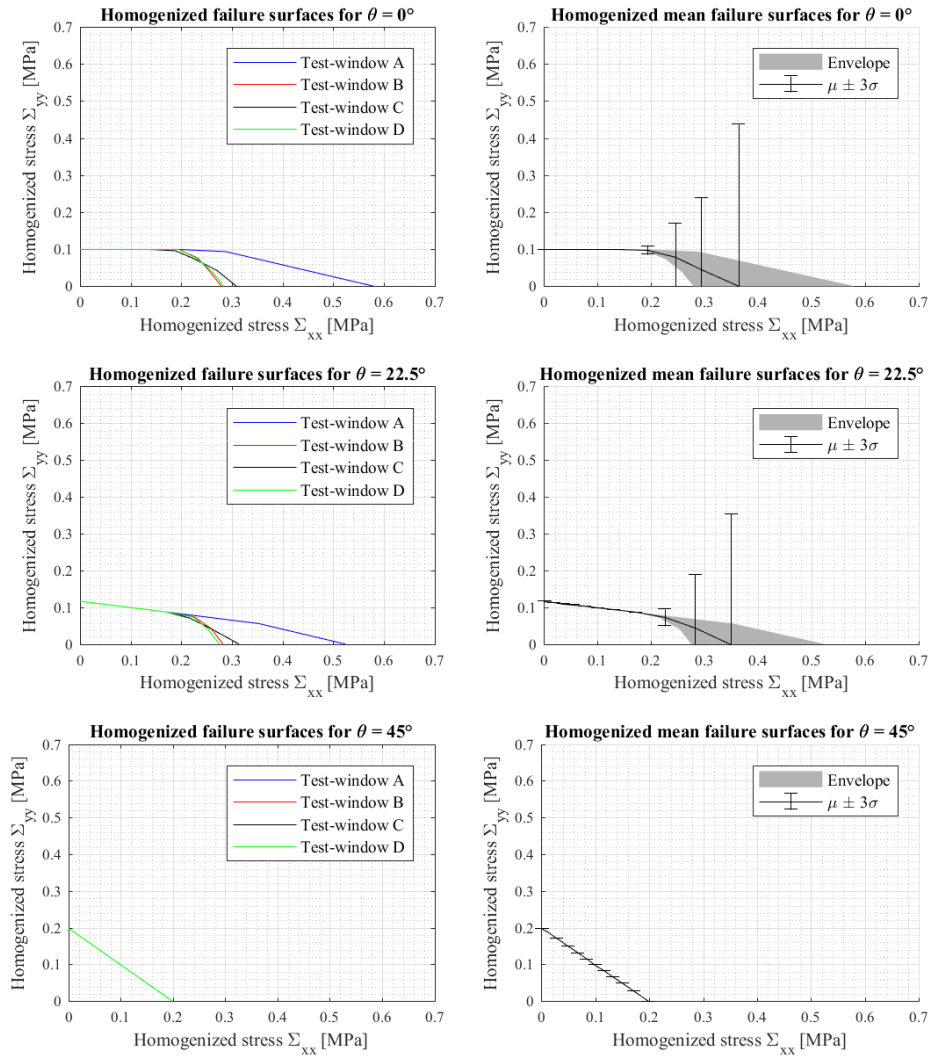


Fig. 4.30. Homogenized failure surfaces, means and envelopes for the large test-window size of case study 4.

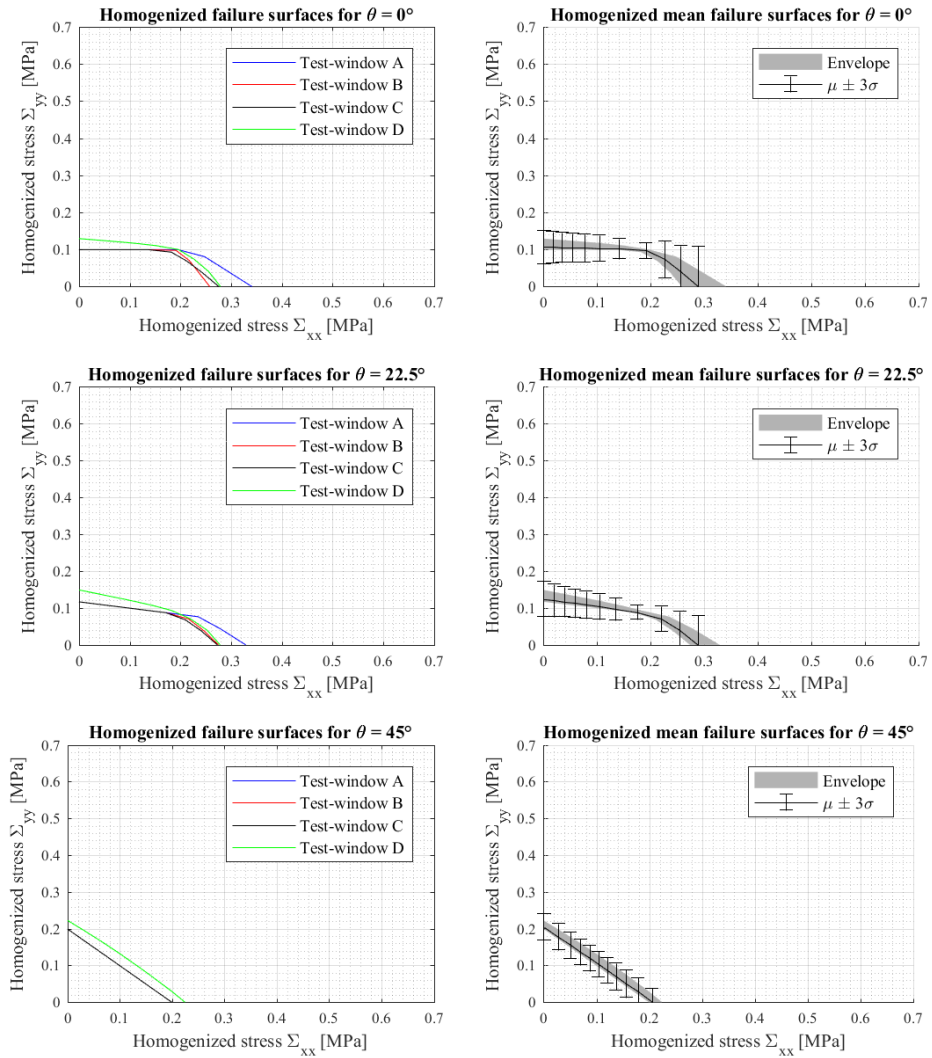


Fig. 4.31. Homogenized failure surfaces, means and envelopes for the huge test-window size of case study 4.

Table 4.8

Mean limit multipliers, standard deviations and coefficient of variations for the huge test-window size of case study 4.

θ	$\psi =$	0°	9°	18°	27°	36°	45°	54°	63°	72°	81°	90°
0°	$\bar{\chi}$	0.289	0.259	0.238	0.215	0.174	0.147	0.129	0.118	0.111	0.108	0.107
	σ	0.036	0.023	0.017	0.007	0.009	0.012	0.012	0.013	0.013	0.014	0.015
	σ^*	12.6%	9.1%	7%	3.4%	5.3%	7.9%	9.6%	10.9%	12%	13%	13.9%
22.5°	$\bar{\chi}$	0.289	0.257	0.231	0.195	0.166	0.147	0.134	0.127	0.123	0.122	0.125
	σ	0.027	0.017	0.011	0.006	0.01	0.012	0.012	0.013	0.014	0.015	0.016
	σ^*	9.3%	6.5%	4.9%	3.3%	6.2%	7.9%	9.2%	10.2%	11.1%	12%	12.9%
45°	$\bar{\chi}$	0.205	0.18	0.164	0.154	0.148	0.147	0.148	0.154	0.164	0.18	0.205
	σ	0.013	0.013	0.012	0.012	0.012	0.012	0.012	0.012	0.012	0.012	0.012
	σ^*	6.2%	7.2%	7.6%	7.8%	7.9%	7.9%	7.9%	7.7%	7.3%	6.6%	5.7%

4.2.6 Case Study 5: Quasi-Regular Masonry Parish Church in San Secondo Parmense, Emilia Romagna

The fifth case study is represented by a Romanesque masonry parish church located in San Secondo Parmense, in the Province of Parma, Emilia Romagna, Italy. This parish church is dedicated to Saint Genesio and, similarly to the third case, presents three naves each terminating with an apse (Fig. 4.32a). A portion of one of its masonry walls is sketched in Fig. 4.32b, and its black-and-white rasterization is pictured in Fig. 4.32c. Unlike all the previous cases, the church consists of bricks presenting the same height but different lengths; some are also truncated or damaged. They are arranged rather regularly, hence the masonry is considered quasi-regular in this case. The test-windows for this case study are depicted in Fig. 4.33.

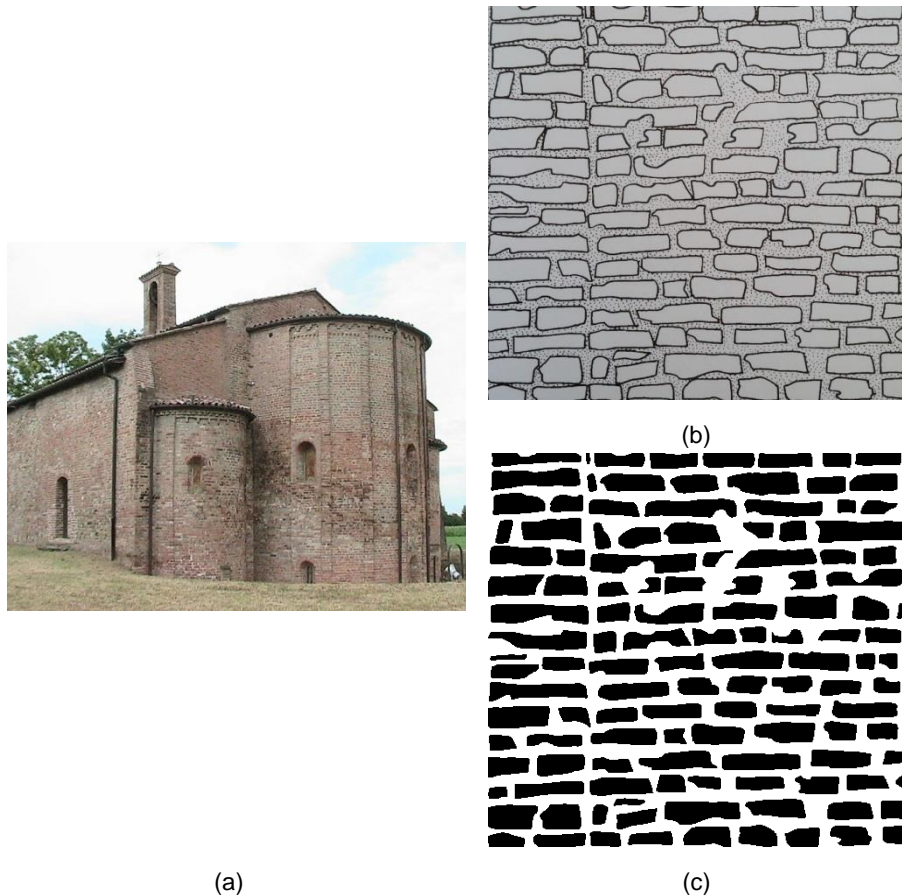


Fig. 4.32. (a) Masonry type for case study 5 ^[source]; (b) sketch of one of its masonry panels; (c) black-and-white rasterization of the sketch.

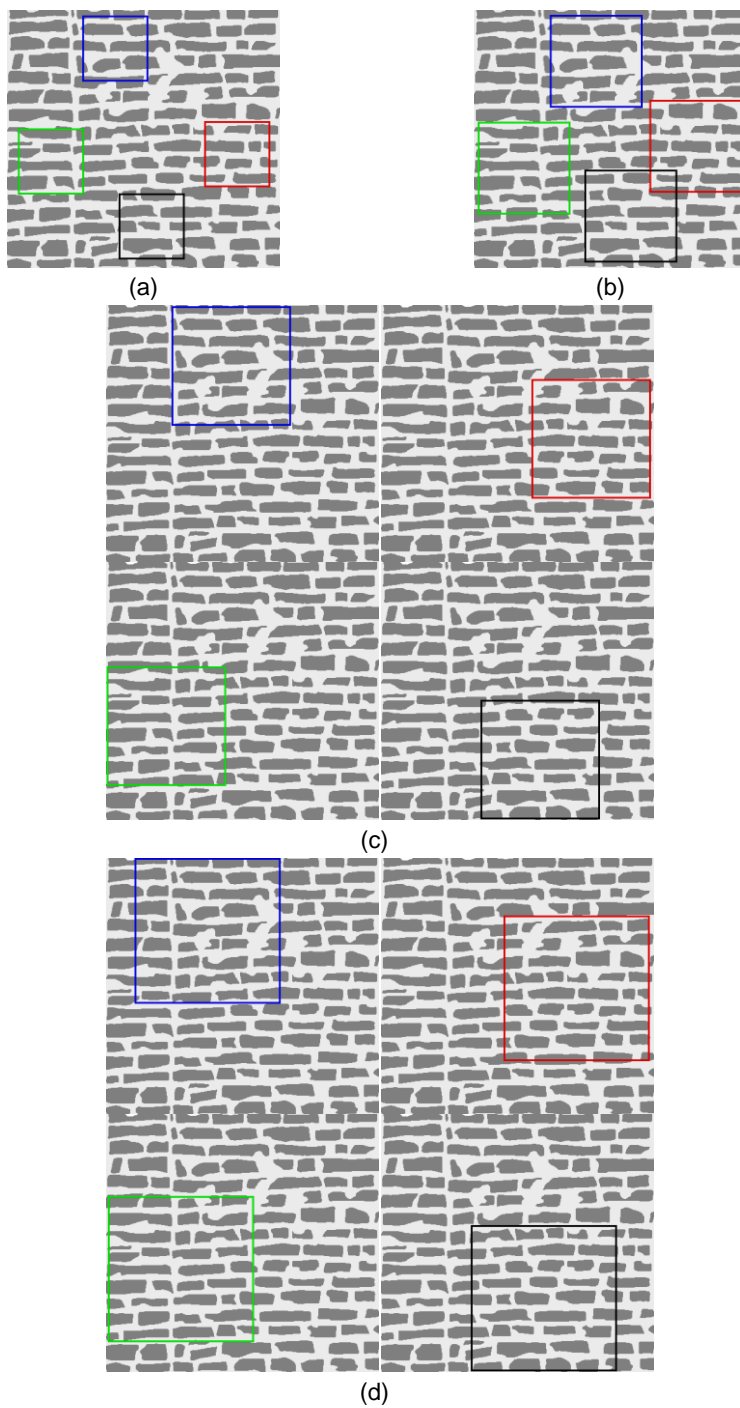


Fig. 4.33. Test-windows extracted for case study 5: (a) small size; (b) medium size; (c) large size; (d) huge size.

Fig. 4.34 and Fig. 4.35 show the homogenized failure surfaces small and medium test-windows, respectively, along with the resulting envelopes and the means. Regarding the latter, the results coming from the test-windows of medium size already satisfy the imposed threshold in terms of coefficient of variation, and so that can be considered the actual dimension of the REV for this specific masonry type.

The related data are reported in Table 4.9, for growing values of the loading angle. The shape of the homogenized mean failure surface for the huge test-windows when θ equal to 0° shows a true orthotropic behavior of this type of masonry: unlike the previous two cases, here the plateau associated to orthotropy is fully visible. It must be noted that the four homogenized failure surfaces for θ equal to 45° all coincide with their mean. In terms of deviation from the mean values, the scatter is not very large, and is limited for small values of ψ . In all the other cases, the four homogenized failure surfaces perfectly overlap with their mean. Moreover, when θ is equal to 0° , the mean limit multiplier for uniaxial vertical tension is again about 37% of the one for uniaxial horizontal tension, similarly to the last case.

The related failure modes, which are shown in Fig. 4.36 for horizontal and vertical tension, respectively, show analogies to those for the case study 3. Horizontal cracks are once again observed for the uniaxial vertical tension, since vertical blocks are absent in the masonry bulk.

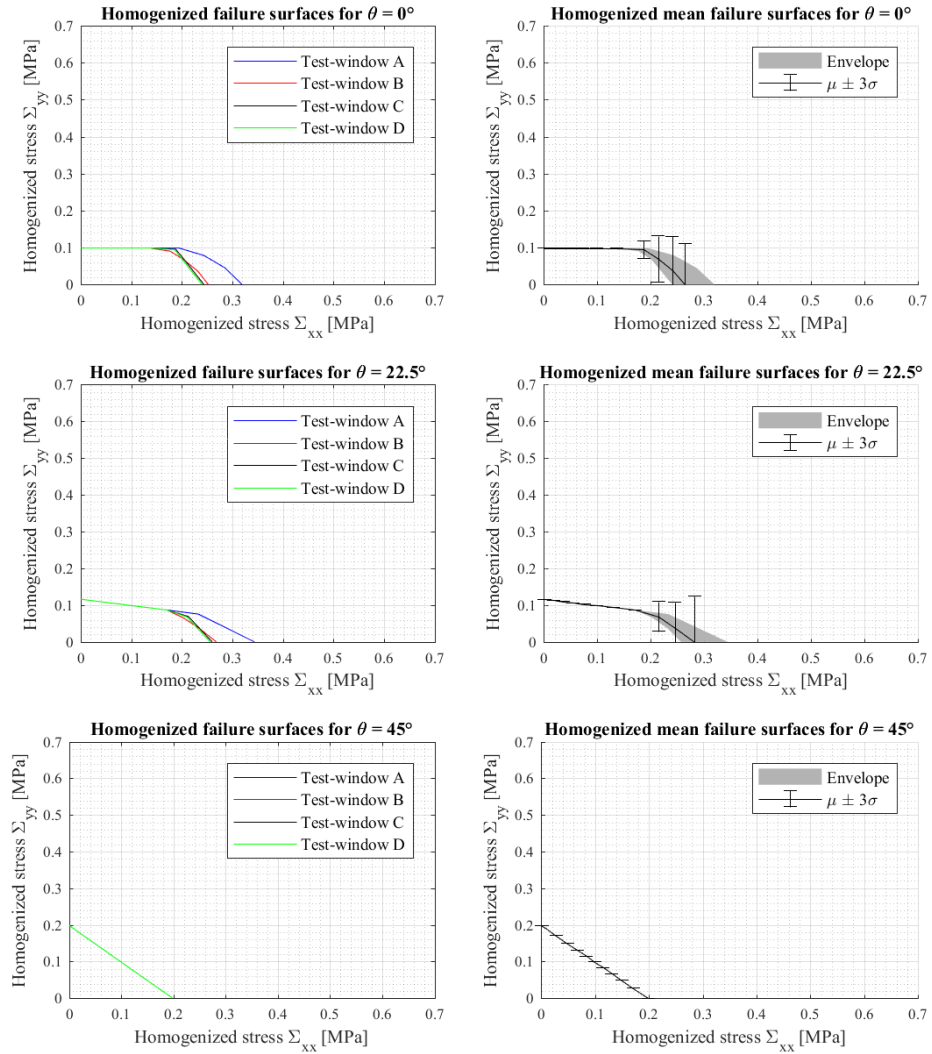


Fig. 4.34. Homogenized failure surfaces, means and envelopes for the small test-window size of case study 5.

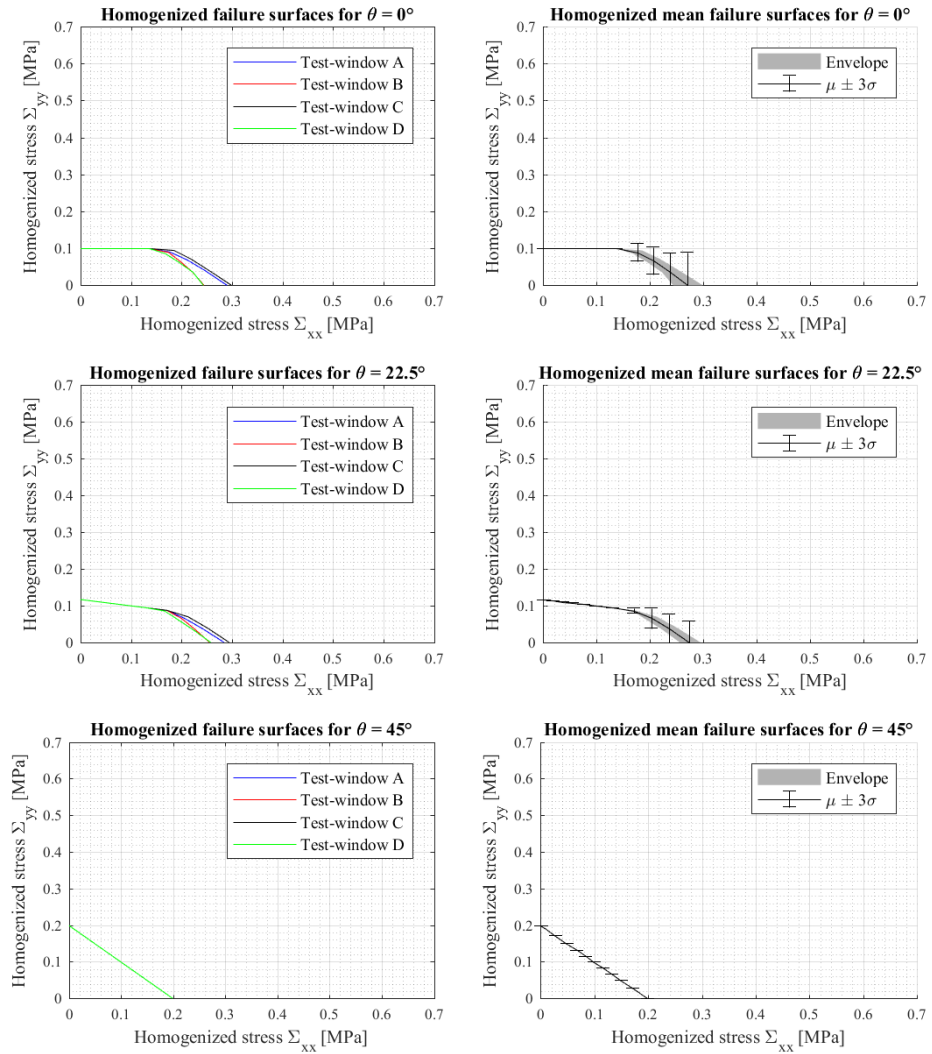


Fig. 4.35. Homogenized failure surfaces, means and envelopes for the medium test-window size of case study 5.

Table 4.9

Mean limit multipliers, standard deviations and coefficient of variations for the medium test-window size of case study 5.

θ	$\psi =$	0°	9°	18°	27°	36°	45°	54°	63°	72°	81°	90°
0°	$\bar{\chi}$	0.269	0.24	0.216	0.192	0.169	0.14	0.123	0.111	0.104	0.101	0.099
	σ	0.03	0.017	0.012	0.008	0	0	0	0	0	0	0
	σ^*	11%	7%	5.6%	4%	0%	0%	0%	0%	0%	0%	0%
22.5°	$\bar{\chi}$	0.273	0.238	0.213	0.191	0.16	0.14	0.128	0.12	0.116	0.115	0.116
	σ	0.019	0.013	0.009	0.002	0	0	0	0	0	0	0
	σ^*	7.1%	5.5%	4.4%	1.1%	0%	0%	0%	0%	0%	0%	0%
45°	$\bar{\chi}$	0.199	0.174	0.158	0.148	0.142	0.14	0.142	0.148	0.158	0.174	0.199
	σ	0	0	0	0	0	0	0	0	0	0	0
	σ^*	0%	0%	0%	0%	0%	0%	0%	0%	0%	0%	0%

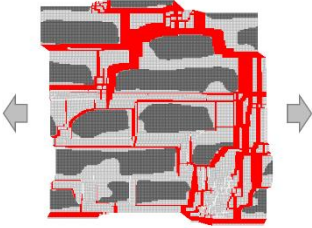
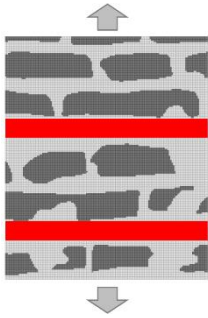
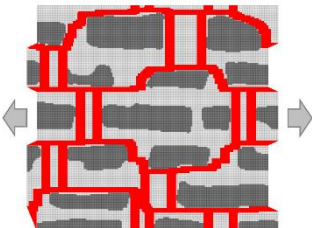
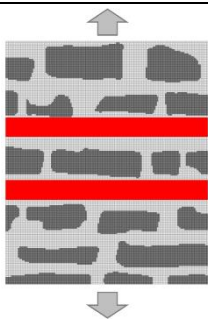
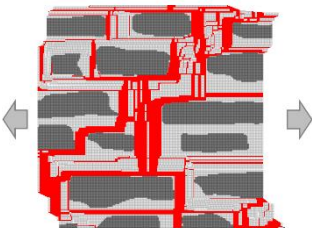
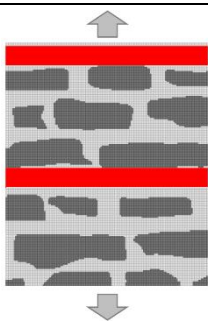
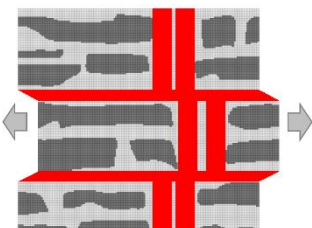
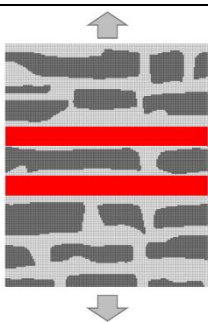
Test-window	Uniaxial horizontal tension	Uniaxial vertical tension
A		
B		
C		
D		

Fig. 4.36. Failure modes for the medium test-window size of case study 5 when $\theta = 0^\circ$.

4.2.7 Case Study 6: Quasi-Regular Masonry Grand Corridor in Sabbioneta, Lombardy

The sixth and final case study is represented by a masonry grand corridor located in Sabbioneta, in the Province of Mantua, Lombardy, Italy. This arched grand corridor, now named *Galleria degli Antichi* (“Gallery of the Ancient”), is 27 m long and used to host ancient marbles and hunting trophies owned by the Duke of Sabbioneta (Fig. 4.37a). A portion of one of its masonry walls is sketched in Fig. 4.37b, and its black-and-white rasterization is pictured in Fig. 4.37c. As in the previous case, the grand corridor consists of bricks presenting the same height and comparable lengths, with smaller brick heads occasionally inserted into the wall. Since they are arranged almost regularly, this masonry is also considered quasi-regular. The test-windows for this case study are depicted in Fig. 4.38.

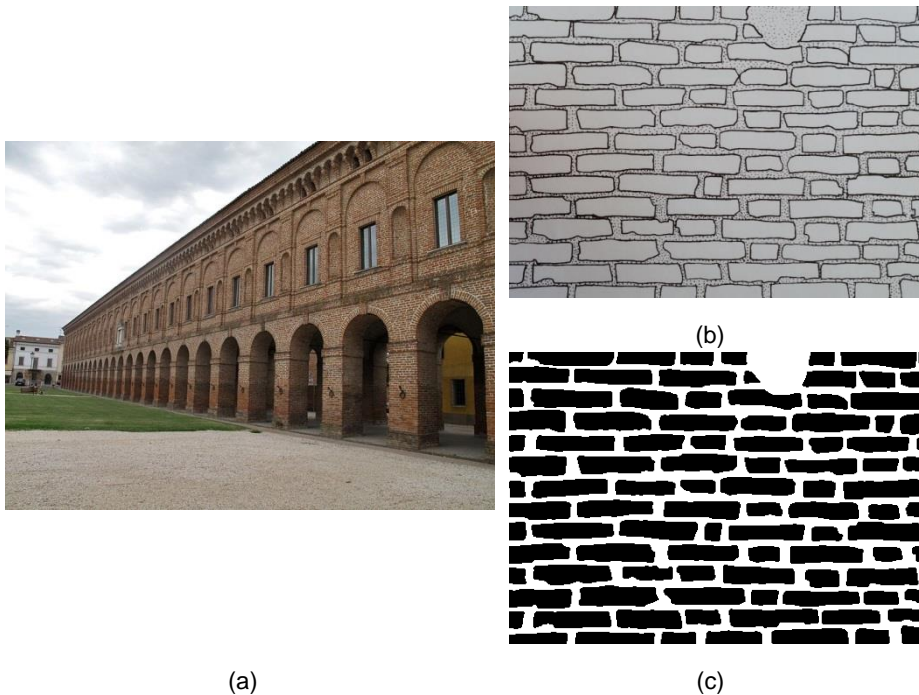


Fig. 4.37. (a) Masonry type for case study 6 ^[source]; (b) sketch of the considered masonry panel; (c) black-and-white rasterization of the sketch.

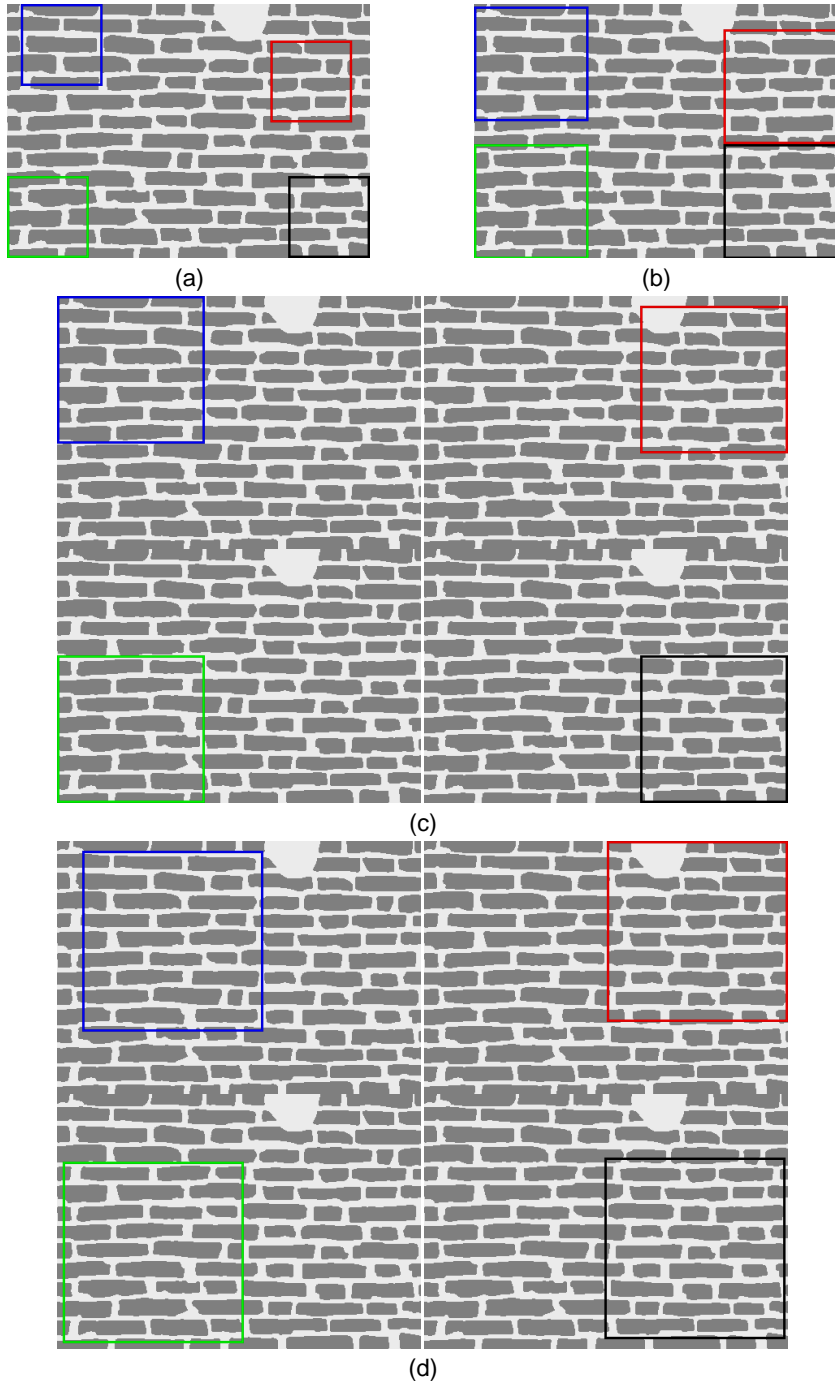


Fig. 4.38. Test-windows extracted for case study 6: (a) small size; (b) medium size; (c) large size; (d) huge size.

Fig. 4.39, Fig. 4.40, and Fig. 4.41 show the homogenized failure surfaces small, medium, and large test-windows, respectively, along with the resulting envelopes and the means. Regarding the latter, the results coming from the test-windows of large size satisfy the imposed threshold in terms of coefficient of variation, and so that can be considered the actual dimension of the REV for this specific masonry type.

The related data are reported in Table 4.10, for growing values of the loading angle. The shape of the homogenized mean failure surface for the huge test-windows when θ equal to 0° again shows a true orthotropic behavior of this type of masonry, similarly to the previous case. In terms of deviation from the mean values, the scatter is not very large, and is limited for small values of ψ as in the previous case. When θ is equal to 0° , the mean limit multiplier for uniaxial vertical tension is about 27% of the one for uniaxial horizontal tension, the lowest value among all six cases.

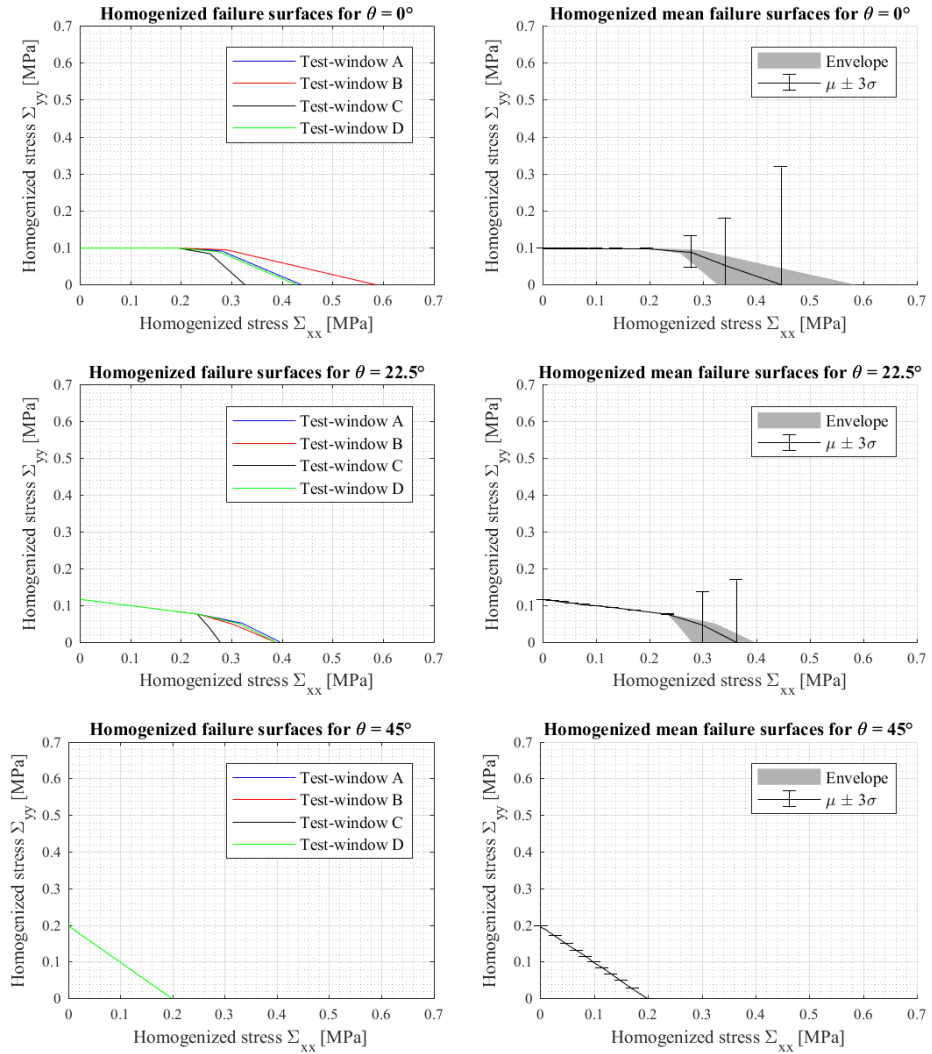


Fig. 4.39. Homogenized failure surfaces, means and envelopes for the small test-window size of case study 6.

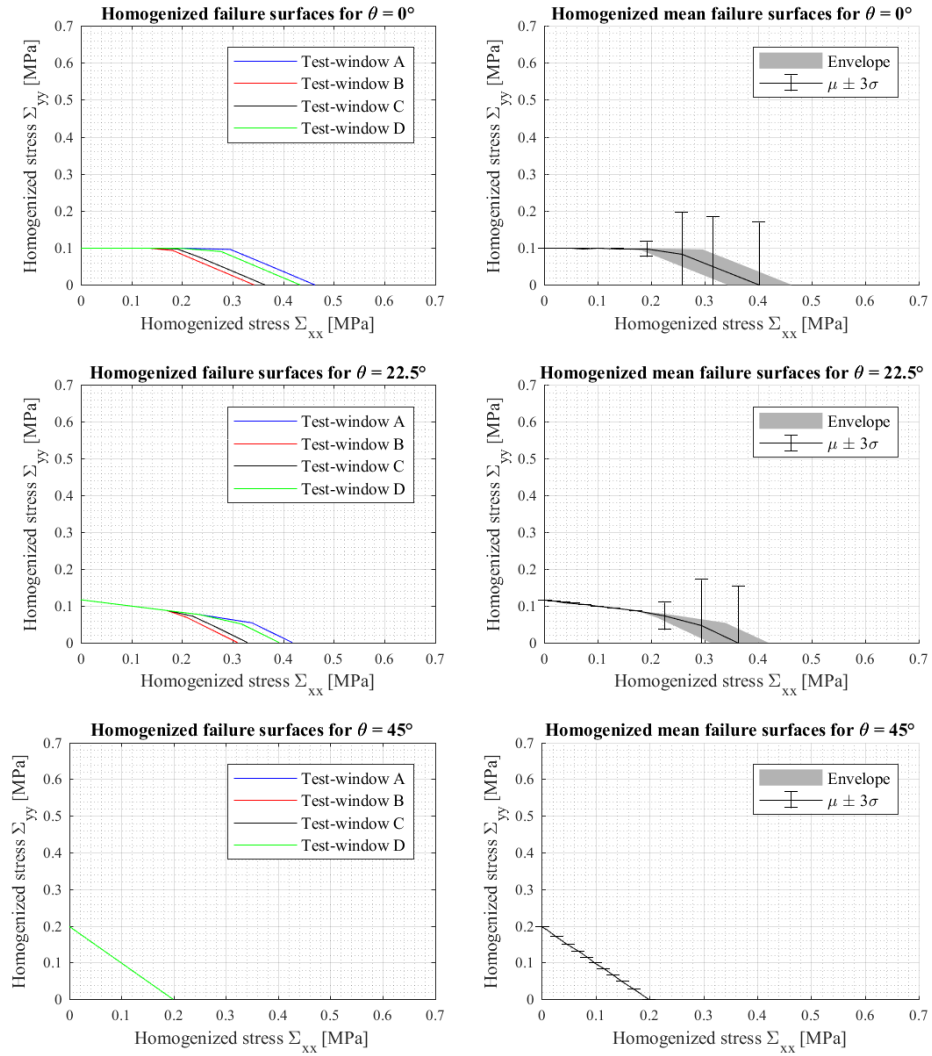


Fig. 4.40. Homogenized failure surfaces, means and envelopes for the medium test-window size of case study 6.

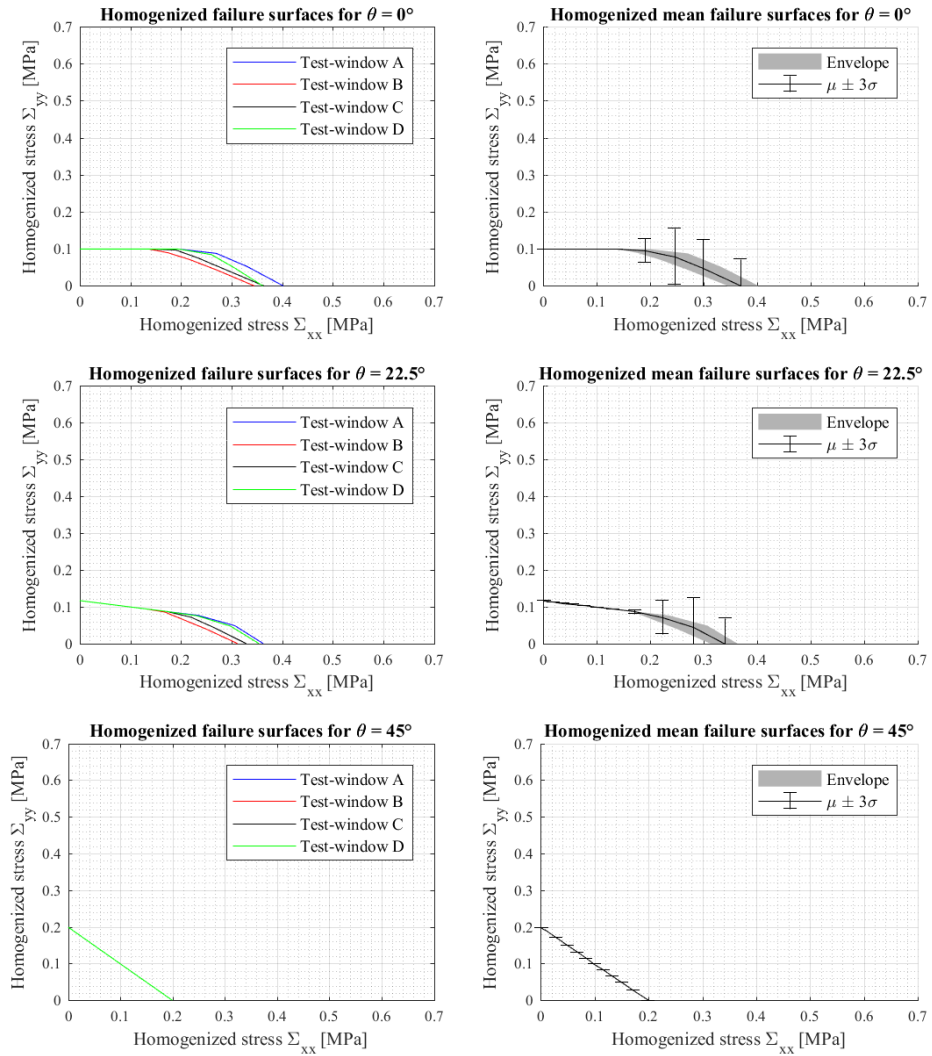


Fig. 4.41. Homogenized failure surfaces, means and envelopes for the large test-window size of case study 6.

Table 4.10

Mean limit multipliers, standard deviations and coefficient of variations for the large test-window size of case study 6.

θ	$\psi =$	0°	9°	18°	27°	36°	45°	54°	63°	72°	81°	90°
0°	$\bar{\chi}$	0.368	0.302	0.258	0.212	0.169	0.141	0.123	0.112	0.105	0.101	0.099
	σ	0.024	0.026	0.025	0.011	0	0	0	0	0	0	0
	σ^*	6.6%	8.7%	9.8%	5%	0%	0%	0%	0%	0%	0%	0%
22.5°	$\bar{\chi}$	0.339	0.284	0.234	0.191	0.16	0.141	0.128	0.12	0.116	0.115	0.117
	σ	0.023	0.027	0.015	0.002	0	0	0	0	0	0	0
	σ^*	6.9%	9.5%	6.5%	0.9%	0%	0%	0%	0%	0%	0%	0%
45°	$\bar{\chi}$	0.199	0.174	0.158	0.148	0.142	0.141	0.142	0.148	0.158	0.174	0.199
	σ	0	0	0	0	0	0	0	0	0	0	0
	σ^*	0%	0%	0%	0%	0%	0%	0%	0%	0%	0%	0%

4.3 Conclusions

Fig. 4.42a-c contain the comparison of the mean homogenized failure surfaces for the statistical REVs of the considered six case studies when θ equal to 0° , 22.5° , and 45° , respectively. From the first picture, it is possible to observe how the first two case studies offer the highest resistance to uniaxial vertical tension, which compensates the lower resistance to uniaxial horizontal tension with respect to the other cases. This is a clear sign of the greater degree of isotropy that characterizes the behavior of these masonry types, as previously remarked. On the other hand case studies 3-6, which progressively lose randomness in terms of units' arrangement and geometry, show higher resistance to uniaxial horizontal tension but display a much lower resistance to uniaxial vertical tension. Their overall behavior is indeed marked by a clearly visible orthotropy. As angle θ increases, the behavior of all six case studies tends to be more and more isotropic: this is evident from the third picture, where the only difference is in terms of dimensions of the mean homogenized failure surfaces (namely, those for the first two cases is slightly larger than the others).

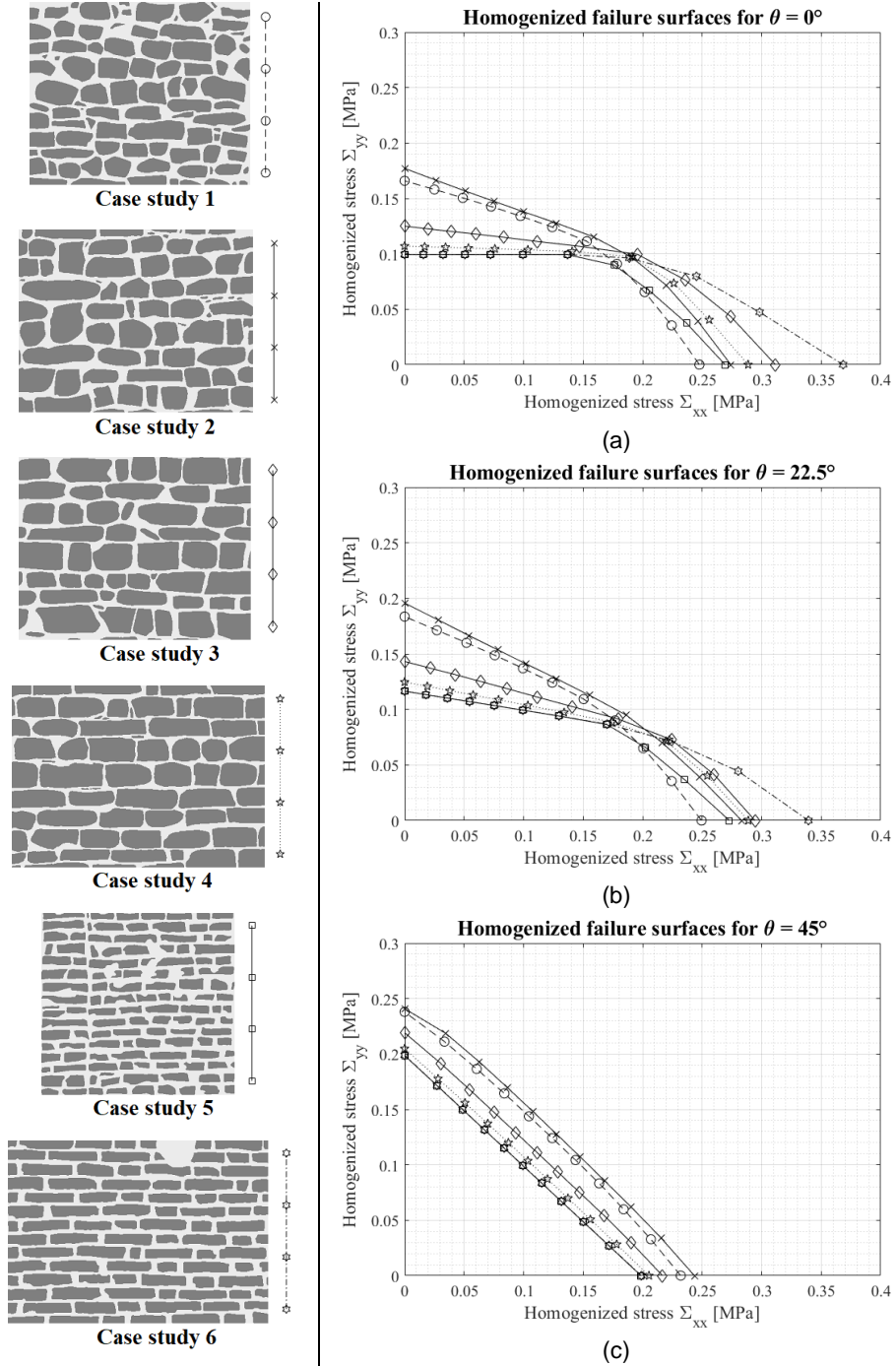


Fig. 4.42. Comparison of the mean homogenized failure surfaces among the six case studies: (a) $\theta = 0^\circ$; (b) $\theta = 22.5^\circ$; (c) $\theta = 45^\circ$.

4.4 References

- [1] Cluni, F., & Gusella, V. (2004). Homogenization of non-periodic masonry structures. *International Journal of Solids and Structures*, 41(7), 1911-1923.
- [2] Milani, G., & Lourenço, P. B. (2010). Monte Carlo homogenized limit analysis model for randomly assembled blocks in-plane loaded. *Computational Mechanics*, 46(6), 827-849.
- [3] MATLAB Release 2018b, The MathWorks, Inc., Natick, Massachusetts, United States.
- [4] Sloan, S. W. (1989). Upper bound limit analysis using finite elements and linear programming. *International Journal for Numerical and Analytical Methods in Geomechanics*, 13(3), 263-282.
- [5] Milani, G., Lourenço, P. B., & Tralli, A. (2006). Homogenised limit analysis of masonry walls, Part I: Failure surfaces. *Computers & structures*, 84(3-4), 166-180.
- [6] Sloan, S. W., & Kleeman, P. W. (1995). Upper bound limit analysis using discontinuous velocity fields. *Computer Methods in Applied Mechanics and Engineering*, 127(1-4), 293-314.
- [7] Ferris, M. C., & Tin-Loi, F. (2001). Limit analysis of frictional block assemblies as a mathematical program with complementarity constraints. *International Journal of Mechanical Sciences*, 43(1), 209-224.
- [8] Krabbenhoft, K., Lyamin, A. V., Hjjaj, M., & Sloan, S. W. (2005). A new discontinuous upper bound limit analysis formulation. *International Journal for Numerical Methods in Engineering*, 63(7), 1069-1088.
- [9] Page, A. W. (1982, May). An experimental investigation of the biaxial strength of brick masonry. In *Proceedings of the Sixth International Brick Masonry Conference (Rome)* (pp. 3-15).
- [10] Backes, H. P. (1985, February). Tensile strength of masonry. In *Proceedings of the 7th International Brick Masonry Conference (Melbourne)* (pp. 779-790).
- [11] Como, M. (2013). *Statics of historic masonry constructions* (Vol. 1). Berlin: Springer.
- [12] Ministero per i Beni Culturali e Ambientali. Atlante dei tipi costruttivi murari Italia Settentrionale, Schedatura tecniche murarie: Area n° 8, Lunigiana.

-
- [13] Ministero per i Beni Culturali e Ambientali. Atlante dei tipi costruttivi murari Italia Settentrionale, Schedatura tecniche murarie: Area n° 13, Valli di Parma e Reggio.
- [14] van der Pluijm, R., Rutten, H., & Ceelen, M. (2000, June). Shear behaviour of bed joints. In *Proceedings of the Twelfth International Brick/Block Masonry Conference (Madrid)* (Vol. 3, pp. 1849-1862).
- [15] van der Pluijm, R. (1992, June). Material properties of masonry and its components under tension and shear. In *Proceedings of the 6th Canadian Masonry Symposium (Saskatoon)* (pp. 675-686).

3D HOMOGENIZED LIMIT ANALYSIS OF SINGLE-LEAF NON-PERIODIC MASONRY

This literature review presented in Section 2.3.2 highlights the absence of a full 3D model combining limit analysis and homogenization. This chapter presents a homogenized limit analysis model that is capable of tackling the out-of-plane collapse behavior of masonry single-leaf walls as well as their in-plane collapse behavior. A Kirchhoff-Love plate model is used for representing the kinematic field of the considered wall, and a MATLAB script is employed for the derivation of both in- and out-of-plane homogenized failure surfaces, as well as the extraction of the deformed configurations at collapse (“failure modes”).

This chapter is organized as follows: Section 5.1 is devoted to describing in detail the mathematical formulation of the upper bound limit analysis problem as conceived for its extension to the out-of-plane case. Section 5.2 provides the numerical validation of the proposed methodology, involving two periodic masonry bonds (namely, running bond masonry and English bond masonry). The results obtained in terms of out-of-plane homogenized failure surfaces are compared against those derived by other authors for the same periodic bonds using different approaches. Section 5.3 presents the results in terms of out-of-plane homogenized failure surfaces and selected deformed shapes at collapse for the six case studies of real masonry buildings previously investigated in Section 4.2. Finally, Section 5.4 offers conclusive remarks on the results presented in the previous section by drawing comparisons among the six case studies.

5.1 Problem Formulation

This section presents the mathematical formulation behind the problem that aims at deriving out-of-plane homogenized failure surfaces for single-leaf masonry walls. Like the 2D application presented in the previous chapter, an upper bound limit analysis problem is here combined with a homogenized approach and is formulated as a standard form linear programming problem in MATLAB [1] that is also subjected to some equality constraints coming from the mathematical formulation. For the purposes of this problem, the out-of-plane behavior of the masonry wall is assessed introducing a Kirchhoff-Love plate model into the displacement rate field; moreover, any investigated masonry wall must be discretized into a mesh consisting of rigid, regular parallelepiped 3D elements bereft of rotation rate ($\dot{\phi} = 0$). This enables to handle a higher number of elements and entails an overall reduction of the problem unknowns; also, this makes the 3D mesh resulting from the voxel strategy particularly suitable for use.

Considering the elements as rigid and devoid of rotation rate, the kinematics of each element is hence completely determined by the displacement rate field of its centroid $\{\dot{u}_x, \dot{u}_y, \dot{u}_z\}$, where axis Z represents the transversal direction. Since a Kirchhoff-Love plate model is here used for a full representation of each element's kinematics, the three components are expressed as:

$$\dot{u}_x = \dot{u}_{x,per} + \dot{E}_{xx}x_G + \dot{E}_{xy}y_G + \dot{\chi}_{xx}z_Gx_G + 0.5\dot{\chi}_{xy}z_Gy_G \quad (5.1)$$

$$\dot{u}_y = \dot{u}_{y,per} + \dot{E}_{xy}x_G + \dot{E}_{yy}y_G + \dot{\chi}_{yy}z_Gy_G + 0.5\dot{\chi}_{xy}z_Gx_G \quad (5.2)$$

$$\dot{u}_z = \dot{u}_{z,per} - 0.5\dot{\chi}_{xx}x_G^2 - 0.5\dot{\chi}_{yy}y_G^2 - 0.5\dot{\chi}_{xy}x_Gy_G \quad (5.3)$$

where $\{x_G, y_G, z_G\}$ are the coordinates of the element's centroid with respect to a reference system located at the center of the investigated masonry wall, $\{\dot{u}_{x,per}, \dot{u}_{y,per}, \dot{u}_{z,per}\}$ are the periodic velocities of the element, $\{\dot{E}_{xx}, \dot{E}_{xy}, \dot{E}_{yy}\}$ the components of the average strain rate tensor (with \dot{E}_{yx} equal to \dot{E}_{xy} for symmetry), and $\{\dot{\chi}_{xx}, \dot{\chi}_{xy}, \dot{\chi}_{yy}\}$ the components of the average curvature rate tensor (again, with $\dot{\chi}_{yx}$ equal to $\dot{\chi}_{xy}$ for symmetry). The choice of such kinematics is compatible with the hypothesis of a Kirchhoff-Love plate model; the requirements of $\dot{\chi}_{xx} = -\frac{\partial^2 \dot{u}_z}{\partial x^2}$, $\dot{\chi}_{yy} = -\frac{\partial^2 \dot{u}_z}{\partial y^2}$, and $\dot{\chi}_{xy} = -2\frac{\partial^2 \dot{u}_z}{\partial x \partial y}$ are all satisfied.

5.1.1 Velocity Jumps and Plastic Flow Constraints

The hypothesis of rigid elements means that plastic dissipation is possible only across their mutual interfaces, which also implies a reduction in terms of unknowns. Moreover, the use of regular parallelepiped elements entails that their six sides are already oriented according to the reference system chosen for the masonry wall. The problem is further simplified even more by introducing three accessory hypotheses:

- no dissipation occurs across interfaces that are orthogonal to the Z axis;
- no shear dissipation occurs along the Z axis of all the other interfaces;
- no condition is enforced with respect to the elements' velocity along the Z direction.

Therefore, the only active interfaces are those orthogonal to the X or Y axis, and the shear component along the Z axis is neglected. Each active interface can then only experience tangential and normal velocity jumps, which are evaluated according to Eqs. (5.4), (5.5) or (5.6), (5.7) depending on the considered interface (see Fig. 5.1 and Fig. 5.2):

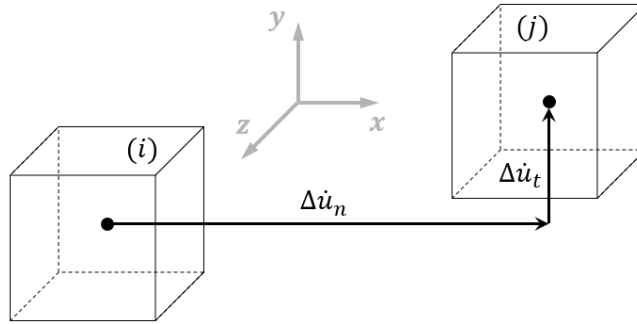


Fig. 5.1. Velocity jumps for a generic interface normal to axis X.

$$\Delta \dot{u}_n \equiv \Delta \dot{u}_x = \dot{u}_{x,per}^j - \dot{u}_{x,per}^i + \dot{E}_{xx}(x_G^j - x_G^i) + \dot{\chi}_{xx}(z_G^j x_G^j - z_G^i x_G^i) \quad (5.4)$$

$$\Delta \dot{u}_t \equiv \Delta \dot{u}_y = \dot{u}_{y,per}^j - \dot{u}_{y,per}^i + \dot{E}_{xy}(x_G^j - x_G^i) + 0.5 \dot{\chi}_{xy}(z_G^j x_G^j - z_G^i x_G^i) \quad (5.5)$$

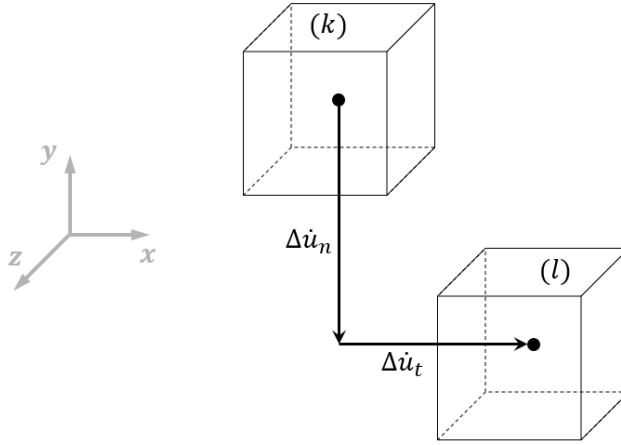


Fig. 5.2. Velocity jumps for a generic interface normal to axis Y.

$$\Delta \dot{u}_n \equiv \Delta \dot{u}_y = \dot{u}_{y,per}^l - \dot{u}_{y,per}^k + \dot{E}_{yy}(y_G^l - y_G^k) + \dot{\chi}_{yy}(z_G^l y_G^l - z_G^k y_G^k) \quad (5.6)$$

$$\Delta \dot{u}_t \equiv \Delta \dot{u}_x = \dot{u}_{x,per}^l - \dot{u}_{x,per}^k + \dot{E}_{xy}(y_G^l - y_G^k) + 0.5 \dot{\chi}_{xy}(z_G^l y_G^l - z_G^k y_G^k) \quad (5.7)$$

As shown in [2], a kinematically admissible velocity field must satisfy constraints given by an associated flow rule. For instance, if a Mohr-Coulomb failure criterion with tension and compression cutoffs is employed, its bounding yield surface is expressed in terms of normal stress σ_n and tangential stress τ as:

$$|\tau| \leq c - \sigma_n \tan \phi \wedge \sigma_n \leq f_t \wedge \sigma_n \geq -f_c \quad (5.8)$$

Four straight lines are then needed to describe the bounding yield surface for this failure criterion (Fig. 5.3), and their expressions are linear both in τ and σ_n :

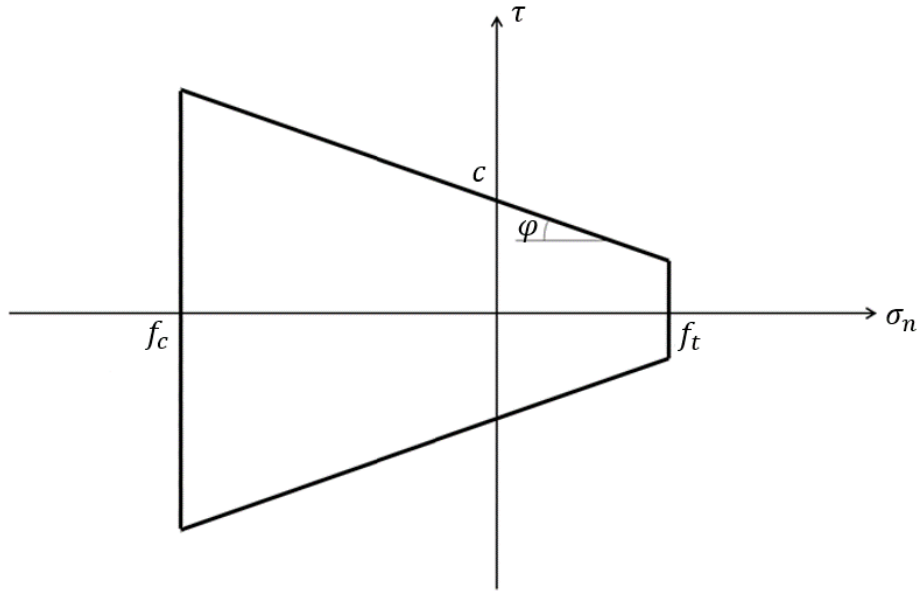


Fig. 5.3. Mohr-Coulomb failure criterion with tension and compression cutoffs.

$$F(\tau, \sigma_n) = \begin{cases} \tau + \sigma_n \tan \phi - c \\ -\tau + \sigma_n \tan \phi - c \\ \sigma_n - f_t \\ -\sigma_n - f_c \end{cases} = 0 \quad (5.9)$$

in which ϕ is the friction angle, c the cohesion, f_c the compressive strength, and f_t the tensile strength of the active interfaces. It must be noted that the bounding yield surface must always be expressed with the general form $A_n^q \sigma_n + A_t^q \tau - C_l^q = 0$ regardless of the chosen failure criterion.

Since the expressions of Eq. (5.9) are already oriented along the reference system chosen for the masonry panel, they are not subject to any modification. Therefore, when considering an associated flow rule, the velocity jumps are simply expressed as:

$$\Delta \dot{u}_n = \sum_{q=1}^4 \lambda_l^q \frac{\partial F_q}{\partial \sigma_n} = \sum_{q=1}^4 \lambda_l^q A_n^q = \lambda_l^1 \tan \phi + \lambda_l^2 \tan \phi + \lambda_l^3 - \lambda_l^4 \quad (5.10)$$

$$\Delta \dot{u}_t = \sum_{q=1}^4 \lambda_l^q \frac{\partial F_q}{\partial \tau} = \sum_{q=1}^4 \lambda_l^q A_t^q = \lambda_l^1 - \lambda_l^2 \quad (5.11)$$

where the velocity jumps $\Delta\dot{u}_n$ and $\Delta\dot{u}_t$ coincide with either $\Delta\dot{u}_x$ or $\Delta\dot{u}_y$, depending on the considered active interface. A custom-built algorithm is implemented in the MATLAB script aiming at identifying which type of interface is considered, which then assigns the correct expression for both $\Delta\dot{u}_n$ and $\Delta\dot{u}_t$. Afterwards, Eqs. (5.10) and (5.11) are equaled to Eqs. (5.4) and (5.5) or (5.6) and (5.7). For instance, considering a single interface I between elements i and j and normal to axis X , their combinations become:

$$\dot{u}_{x,per}^j - \dot{u}_{x,per}^i - \sum_{q=1}^4 \lambda_I^q A_n^q + \dot{E}_{xx}(x_G^j - x_G^i) + \dot{\chi}_{xx}(z_G^j x_G^j - z_G^i x_G^i) = 0 \quad (5.12)$$

$$\dot{u}_{y,per}^j - \dot{u}_{y,per}^i - \sum_{q=1}^4 \lambda_I^q A_t^q + \dot{E}_{xy}(x_G^j - x_G^i) + 0.5\dot{\chi}_{xy}(z_G^j x_G^j - z_G^i x_G^i) = 0 \quad (5.13)$$

Using a matrix formulation to compact Eqs. (5.12) and (5.13), these become:

$$\begin{bmatrix} 1 & -1 & 0 & 0 \\ 0 & 0 & 1 & -1 \end{bmatrix} \begin{bmatrix} \dot{u}_{x,per}^j \\ \dot{u}_{x,per}^i \\ \dot{u}_{y,per}^j \\ \dot{u}_{y,per}^i \end{bmatrix} + \begin{bmatrix} -\tan\phi & -\tan\phi & -1 & 1 \\ -1 & 1 & 0 & 0 \end{bmatrix} \begin{bmatrix} \lambda_I^1 \\ \lambda_I^2 \\ \lambda_I^3 \\ \lambda_I^4 \end{bmatrix} + \begin{bmatrix} \dot{E}_{xx} \\ \dot{E}_{yy} \\ \dot{E}_{xy} \\ \dot{\chi}_{xx} \\ \dot{\chi}_{yy} \\ \dot{\chi}_{xy} \end{bmatrix} = \begin{bmatrix} 0 \\ 0 \end{bmatrix} \quad (5.14)$$

This matrix formulation can be written even more compactly:

$$\mathbf{A}_{11}^{eq,ij} \dot{\mathbf{u}}_{per}^{ij} + \mathbf{A}_{13}^{eq,ij} \dot{\lambda}_I + \mathbf{A}_{14}^{eq,ij} \dot{\mathbf{D}} = \mathbf{0} \quad (5.15)$$

From Eq. (5.15) it is clear that the periodic velocity field of the two adjoining elements i and j (collected in the vector $\dot{\mathbf{u}}_{per}^{ij}$), the plastic multiplier rates of interface I ($\dot{\lambda}_I$), and the components of the average strain and curvature rate tensors (both collected in the vector $\dot{\mathbf{D}}$) are among the unknown variables of the linear programming problem. It must be noted that these are not the only unknown variables of the overall problem, as some more are introduced in the

following section. After some simple assemblage operations, the constraint in its global form becomes:

$$A_{11}^{eq} \dot{\mathbf{u}}_{per} + A_{13}^{eq} \dot{\lambda}_{I,ass} + A_{14}^{eq} \dot{\mathbf{D}} = \mathbf{0} \quad (5.16)$$

5.1.2 Master-Slave Relations for Unit Elements

The kinematic field of the finite elements that pertain to a masonry unit is governed by master-slave relations that link the kinematic field of a single finite element (“slave element”, superscript S) and that of the masonry unit to which it belongs (“master element”, superscript M), as shown in Fig. 5.4. In this case, this is enforced to enable the rotation of a generic masonry unit, since the single elements cannot rotate; the kinematics of unit finite elements is expressed in such a way that their interfaces are not considered in the overall solution, mirroring what happens in real case studies where failure within masonry units is unlikely to occur. The master-slave relations are expressed according to Eqs. (5.17) to (5.19):

$$\dot{u}_x^S = \dot{u}_x^M + \dot{\theta}_{yy}^M (z_G^S - z_G^M) \quad (5.17)$$

$$\dot{u}_y^S = \dot{u}_y^M - \dot{\theta}_{xx}^M (z_G^S - z_G^M) \quad (5.18)$$

$$\dot{u}_z^S = \dot{u}_z^M + \dot{\theta}_{xx}^M (y_G^S - y_G^M) - \dot{\theta}_{yy}^M (x_G^S - x_G^M) \quad (5.19)$$

\dot{u}_x^M , \dot{u}_y^M , and \dot{u}_z^M are the components of the displacement rate field of a single masonry unit, which acts as the master macroelement, and they are expressed according to Eqs. (5.1) to (5.3). x_G^M , y_G^M , and z_G^M are the coordinates of the centroid of the considered masonry unit, which are automatically calculated by the MATLAB script. \dot{u}_x^S , \dot{u}_y^S , and \dot{u}_z^S are the components of the displacement rate field of a generic finite element - in this case, the slave element - that belongs to the considered masonry unit; they are also expressed according to Eqs. (5.1) to (5.3). The quantities $\dot{\theta}_{xx}^M$ and $\dot{\theta}_{yy}^M$ represent the rotations about the X and Y axes of the master macroelement, respectively, so that its kinematics is enriched enabling macroscopic rotations that are representative of the deformed shape associated to an out-of-plane load condition. It must be remarked that the finite elements do not actually rotate, but the general deformed shape of a masonry unit is indeed able to simulate rotations in a “pixed” way.

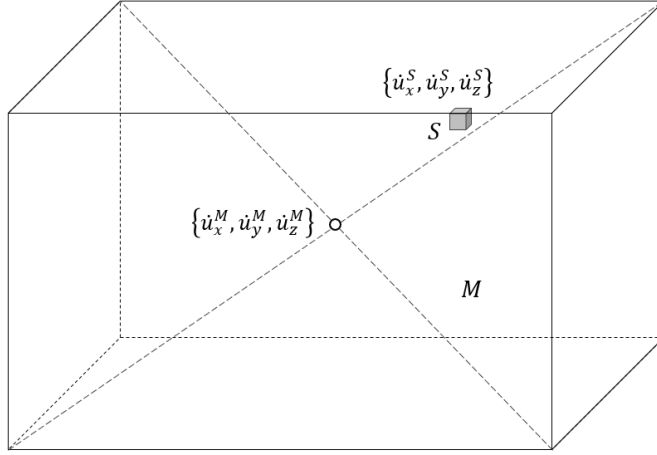


Fig. 5.4. Graphical representation of a masonry unit (M) and a unit finite element (S).

The expansions of Eqs. (5.17) to (5.19) lead to the following expressions:

$$\begin{aligned} \dot{u}_{x,per}^S - \dot{u}_{x,per}^M + \dot{\theta}_{yy}^M(z_G^M - z_G^S) + \dot{E}_{xx}(x_G^S - x_G^M) + \dot{E}_{xy}(y_G^S - y_G^M) + \\ + \dot{\chi}_{xx}(z_G^S x_G^S - z_G^M x_G^M) + 0.5 \dot{\chi}_{xy}(z_G^S y_G^S - z_G^M y_G^M) = 0 \end{aligned} \quad (5.20)$$

$$\begin{aligned} \dot{u}_{y,per}^S - \dot{u}_{y,per}^M + \dot{\theta}_{xx}^M(z_G^S - z_G^M) + \dot{E}_{xy}(x_G^S - x_G^M) + \dot{E}_{yy}(y_G^S - y_G^M) + \\ + \dot{\chi}_{yy}(z_G^S y_G^S - z_G^M y_G^M) + 0.5 \dot{\chi}_{xy}(z_G^S x_G^S - z_G^M x_G^M) = 0 \end{aligned} \quad (5.21)$$

$$\begin{aligned} \dot{u}_{z,per}^S - \dot{u}_{z,per}^M + \dot{\theta}_{xx}^M(y_G^M - y_G^S) + \dot{\theta}_{yy}^M(x_G^S - x_G^M) + \\ + 0.5 \dot{\chi}_{xx}[(x_G^M)^2 - (x_G^S)^2] + 0.5 \dot{\chi}_{yy}[(y_G^M)^2 - (y_G^S)^2] + \\ + 0.5 \dot{\chi}_{xy}(x_G^M y_G^M - x_G^S y_G^S) = 0 \end{aligned} \quad (5.22)$$

These can also be written in a matrix formulation, which is here omitted for sake of brevity. The global compact formulation of the constraints coming from the master-slave relations is:

$$\mathbf{A}_{21}^{eq} \dot{\mathbf{u}}_{per} + \mathbf{A}_{22}^{eq} \dot{\mathbf{R}} + \mathbf{A}_{24}^{eq} \dot{\mathbf{D}} = \mathbf{0} \quad (5.23)$$

Eq. (5.23) gives the remaining set of unknown variables of the linear programming problem, represented by vector $\dot{\mathbf{R}}$ that includes the periodic velocity fields and macroscopic rotations of all the masonry units of the considered masonry panel.

5.1.3 Periodicity Boundary Conditions

The homogenization approach requires the inclusion of periodicity constraints applied to the velocity field at the boundaries of the investigated panel. These must be enforced on elements lying at the external boundaries of the panel that are orthogonal to axes X and Y ; the elements here involved are located at the opposite sides of each of those boundaries (Fig. 5.5).

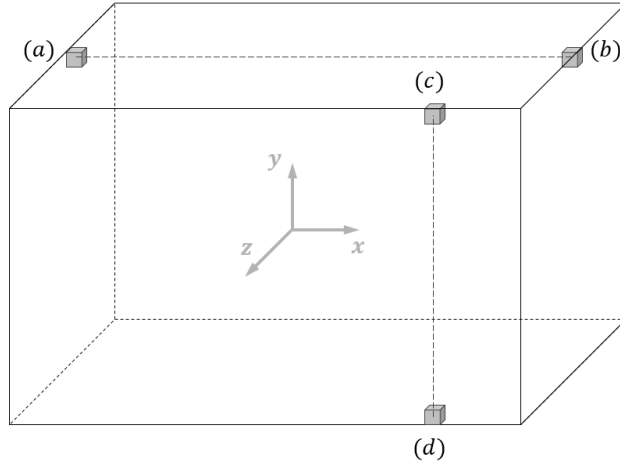


Fig. 5.5. Periodicity boundary conditions.

$$\dot{u}_{x,per}^a = \dot{u}_{x,per}^b \Rightarrow \dot{u}_{x,per}^a - \dot{u}_{x,per}^b = 0 \quad (5.24)$$

$$\dot{u}_{y,per}^a = \dot{u}_{y,per}^b \Rightarrow \dot{u}_{y,per}^a - \dot{u}_{y,per}^b = 0 \quad (5.25)$$

$$\dot{u}_{z,per}^a = \dot{u}_{z,per}^b \Rightarrow \dot{u}_{z,per}^a - \dot{u}_{z,per}^b = 0 \quad (5.26)$$

The same applies for the generic couple of elements c and d . The global compact formulation of this constraint is:

$$A_{31}^{eq} \dot{\mathbf{u}}_{per} = \mathbf{0} \quad (5.27)$$

5.1.4 Normalization of Dissipated External Power

Two sets of out-of-plane load conditions are defined through two separate “loading angles”, as shown in Fig. 5.6.

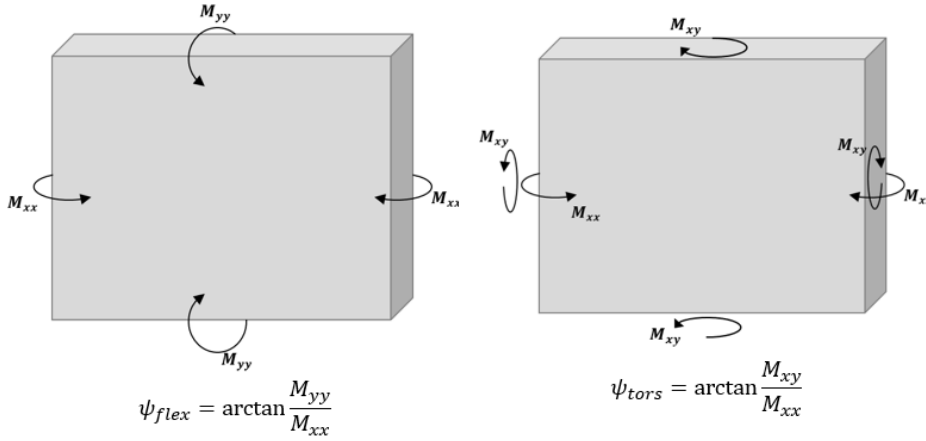


Fig. 5.6. Angles defining the out-of-plane load condition.

Angle ψ_{flex} is named “flexural loading angle”: it represents the arctangent of the ratio between the macroscopic horizontal and vertical bending moments M_{yy} and M_{xx} , and varies between 0 and 2π . Similarly, angle ψ_{tors} is named “torsional loading angle”: it represents the arctangent of the ratio between the macroscopic torsional moment and the vertical bending moments M_{xy} and M_{xx} , again ranging between 0 and 2π . Also, an in-plane load condition is included and defined in the same way as shown in Section 4.1.3.

Overall, the dissipated external power is expressed as the summation of the products between the macroscopic stresses and bending moments and their associated average strain and curvature rate tensors components. Eventually, the dissipated external power is normalized and equaled to 1 to enforce a restriction in terms of all the possible collapse mechanisms that are associated to the collapse load, which is unique:

$$p^{ext} = \Sigma_{xx}\dot{E}_{xx} + \Sigma_{yy}\dot{E}_{yy} + \Sigma_{xy}\dot{E}_{xy} + M_{xx}\dot{\chi}_{xx} + M_{yy}\dot{\chi}_{yy} + M_{xy}\dot{\chi}_{xy} = 1 \quad (5.28)$$

In the end, Eq. (5.28) represents another constraint for the linear programming problem, concisely expressed in the form:

$$A_{44}^{eq}\dot{D} = 1 \quad (5.29)$$

5.1.5 Power Dissipation in Velocity Discontinuities

The expression for power dissipated across a velocity discontinuity whose area is A can be written as:

$$P^{int} = \int_A (\sigma_n \Delta \dot{u}_n + \tau \Delta \dot{u}_t) dA \quad (5.30)$$

Substituting Eqs. (5.10) and (5.11), this becomes:

$$\int_A \left(\sigma_n \sum_{q=1}^4 \lambda_I^q A_n^q + \tau \sum_{q=1}^4 \lambda_I^q A_t^q \right) dA = \int_A \sum_{q=1}^4 \lambda_I^q (\sigma_n A_n^q + \tau A_t^q) dA \quad (5.31)$$

The dissipated internal power can then be written as:

$$P^{int} = A \sum_{q=1}^4 \lambda_I^q C_I^q \quad (5.32)$$

For the global problem the assembled final expression in matrix form is:

$$P^{int} = \mathbf{C}_{I,ass}^T \boldsymbol{\lambda}_{I,ass} \quad (5.33)$$

5.1.6 Assembly and Solution of the Linear Programming Problem

The homogenized limit analysis problem is eventually formulated as a linear programming problem. The objective function that ought to be minimized is the dissipated internal power as expressed in Eq. (5.33), and the equality constraints are given by Eqs. (5.16), (5.23), (5.27), and (5.29). For a smoother solution, this computational problem is formulated in a standard form, which requires that each unknown variable of the problem is greater or equal to zero. In particular, for this specific problem the following unknowns must be modified: the elements' periodic velocity field, the masonry units' periodic velocity field and macroscopic rotations, and the components of average strain and curvature rate tensors. All of them are expressed as the difference of two nonnegative quantities to satisfy the requirements of the standard form:

$$\dot{u}_{i,per}^S = \dot{u}_{i,per}^{S,+} - \dot{u}_{i,per}^{S,-} \quad i = x, y \quad (5.34)$$

$$\dot{u}_{i,per}^M = \dot{u}_{i,per}^{M,+} - \dot{u}_{i,per}^{M,-} \quad i = x, y \quad (5.35)$$

$$\dot{\theta}_{ii}^M = \dot{\theta}_{ii}^{M,+} - \dot{\theta}_{ii}^{M,-} \quad i = x, y \quad (5.36)$$

$$\dot{E}_{ij} = \dot{E}_{ij}^+ - \dot{E}_{ij}^- \quad i, j = x, y \quad (5.37)$$

$$\dot{\chi}_{ij} = \dot{\chi}_{ij}^+ - \dot{\chi}_{ij}^- \quad i, j = x, y \quad (5.38)$$

The standard form for this linear programming problem is:

$$\text{Minimize} \quad \mathbf{C}^T \mathbf{X} \quad (5.39)$$

$$\text{Subject to} \quad \mathbf{A}\mathbf{X} = \mathbf{B} \quad (5.40)$$

$$\mathbf{X} \geq \mathbf{0} \quad (5.41)$$

where

$$A = \begin{bmatrix} A_{11}^{eq} & -A_{11}^{eq} & 0 & 0 & A_{13}^{eq} & A_{14}^{eq} & -A_{14}^{eq} \\ A_{21}^{eq} & -A_{21}^{eq} & A_{22}^{eq} & -A_{22}^{eq} & 0 & A_{24}^{eq} & -A_{24}^{eq} \\ A_{31}^{eq} & -A_{31}^{eq} & 0 & 0 & 0 & 0 & 0 \\ 0 & 0 & 0 & 0 & 0 & A_{44}^{eq} & -A_{44}^{eq} \end{bmatrix} \quad (5.42)$$

$$X = \begin{bmatrix} \dot{u}_{per}^+ \\ \dot{u}_{per}^- \\ \dot{R}^+ \\ \dot{R}^- \\ \dot{\lambda}_{I,ass} \\ \dot{D}^+ \\ \dot{D}^- \end{bmatrix} \quad (5.43)$$

$$B = \begin{bmatrix} 0 \\ 0 \\ 0 \\ 1 \end{bmatrix} \quad (5.44)$$

$$C = \begin{bmatrix} 0 \\ 0 \\ 0 \\ 0 \\ C_{I,ass} \\ 0 \\ 0 \end{bmatrix} \quad (5.45)$$

5.1.7 Construction of the Out-of-Plane Homogenized Failure Surfaces

The MATLAB script includes a final part where the construction of the two out-of-plane homogenized failure surfaces for the chosen single-leaf wall is actually performed. In the framework of the upper bound theorem of limit analysis, the kinematic limit multiplier χ is the minimum among those computed for each kinematically admissible collapse mechanism, and may be expressed as the ratio between the dissipated internal and external powers:

$$\mu_k = \frac{p^{int}}{p^{ext}} \quad (5.46)$$

Introducing the normalization of the dissipated external power of Eq. (5.28) implies that the denominator is equal to 1, which means that:

$$\mu_k = P^{int} = \mathbf{C}_{I,ass}^T \dot{\lambda}_{I,ass} \quad (5.47)$$

$$\chi = \min(\mu_k) = \min(\mathbf{C}_{I,ass}^T \dot{\lambda}_{I,ass}) \quad (5.48)$$

Hence, the kinematic load multiplier is directly determined by the minimization of the dissipated internal power, which is correctly the objective of the linear programming problem here developed.

The flexural and torsional out-of-plane homogenized failure surfaces are constructed as follows: after selecting a value for the loading angles ψ_{flex} (or ψ_{tors}), the linear programming problem is solved and the kinematic limit multiplier χ for that specific out-of-plane load condition is obtained. The collapse bending (or torsional) moments are then calculated by multiplying χ to the initial macroscopic moments $[M_{xx} \ M_{yy}]$ (or $[M_{xx} \ M_{xy}]$ for the torsional failure surface). Globally, 41 different values of ψ_{flex} (or ψ_{tors}) are investigated, ranging from 0 to 2π with a sampling step of $\pi/20$. Each pair of collapse moments χM_{xx} and χM_{yy} (or χM_{xy}) represents a pair of coordinates in the resulting out-of-plane homogenized failure surface, which is then piecewise linear and consists of the segments linking each adjacent pair of collapse moments. An analogous procedure is employed for extracting the in-plane homogenized failure surfaces. The post-processing phase also enables to plot the failure mode for a specific in- and out-of-plane load condition with the MATLAB command *patch*: the position of each finite element is reconstructed using the solution values of the remaining variables of the linear programming problem (namely, those included in vectors $\dot{\mathbf{u}}_{per}$, $\dot{\mathbf{R}}$, and $\dot{\mathbf{D}}$) and using Eqs. (5.1) to (5.3) and (5.17) to (5.19).

5.2 Numerical Validation

In this section, the proposed approach is validated by drawing comparisons with three distinct models used in works available in literature to describe the in- and out-of-plane behavior of masonry at collapse. In particular, the results concerning homogenized failure surfaces are critically discussed to assess the reliability of the present approach in correctly representing the out-of-plane collapse behavior of common masonry bonds, with attention given to the in-plane collapse behavior as well.

In the first example, a running bond masonry test-window is investigated in terms of homogenized in- and out-of-plane failure surfaces. The results are then compared to those obtained by Milani and Taliervo in two distinct works, one devoted to the in-plane behavior [3], the other to the out-of-plane one [4]. As previously mentioned in Section 2.3.1, they use the so-called “Method of Cells” as a homogenizing approach, which is typical of problem involving fiber-reinforced composites. Relevant failure modes in bending and torsion are also presented and discussed.

In the second example, an English bond masonry test-window is investigated only in terms of homogenized out-of-plane failure surfaces. The results are then compared to those obtained by Cecchi and Milani [5]; as already discussed in Section 2.3.2, the authors do not use a rigorous homogenization approach, instead they enforce the equivalence between a 3D system of blocks connected by interfaces and a 2D Reissner-Mindlin plate through a kinematic identification. Also in this case, relevant failure modes in bending and torsion are presented and discussed.

5.2.1 Running Bond Masonry REV

The first case study deals with a running bond masonry REV that consists of standard Italian bricks ($25 \times 12 \times 5.5 \text{ cm}^3$) and mortar joints whose thickness is 1 cm; the in-plane layout is shown in Fig. 5.7a. Two meshes are used for validating the proposed model: one is extremely refined, consisting of about 260000 elements and displaying 48 elements over the thickness (Mesh 1, Fig. 5.7b), the other is extremely coarse, consisting of about 17000 elements and displaying 12 elements over the thickness (Mesh 2, Fig. 5.7c).

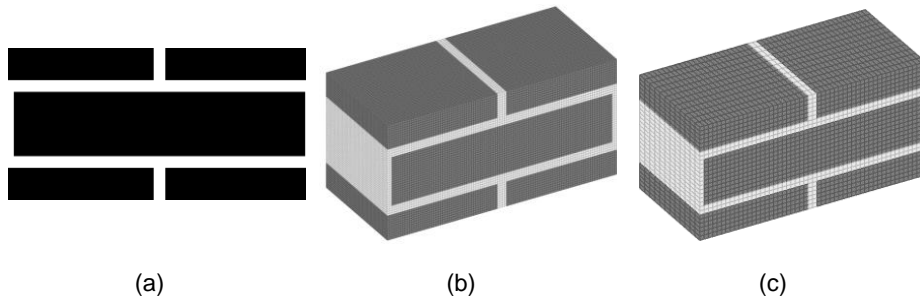


Fig. 5.7. (a) In-plane layout of the running bond masonry REV; (b) Mesh 1; (c) Mesh 2.

For the validation in terms of in-plane homogenized failure surfaces, a Mohr-Coulomb failure criterion with cut-offs in tension and compression is used. The mechanical properties of the interfaces are the same as those used in [3] and are listed in Table 5.1, with the tensile and compressive strength f_t and f_c evaluated according to the formulas there reported.

Table 5.1

Mechanical properties for the material employed in comparison with in-plane Milani-Taliercio.

Cohesion c [MPa]	Friction angle ϕ [°]	Tensile strength f_t [MPa]	Compressive strength f_c [MPa]
0.1	36	$\frac{2c \cos \phi}{1 + \sin \phi}$	$\frac{2c \cos \phi}{1 - \sin \phi}$

Fig. 5.8 and Fig. 5.9 show the comparison between the in-plane homogenized failure surfaces obtained by Milani and Taliercio in [3] and those resulting from the present model for Mesh 1; in particular, Fig. 5.8a-c show the failure surfaces in the tension-tension range for three different values of angle θ (which represents the inclination of the principal directions with respect to the reference system of the REV), whereas Fig. 5.9a-c show the failure surfaces in the compression-compression range.

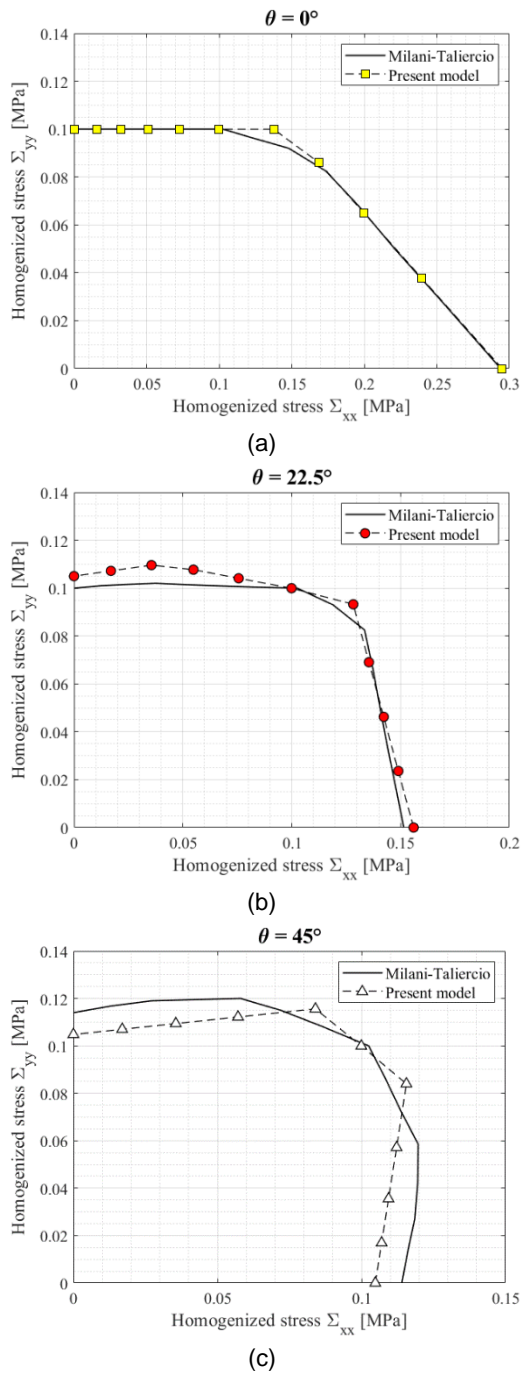
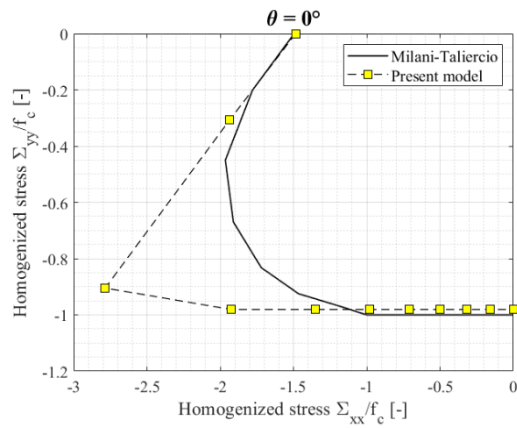
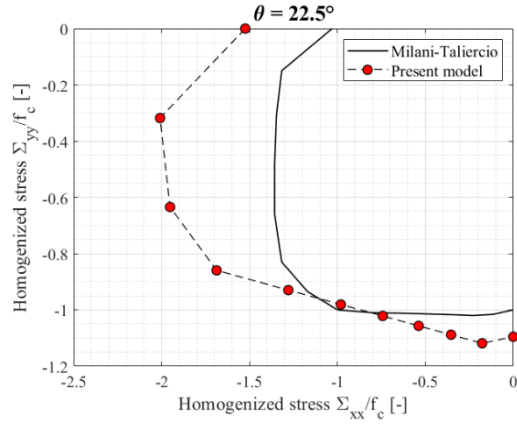


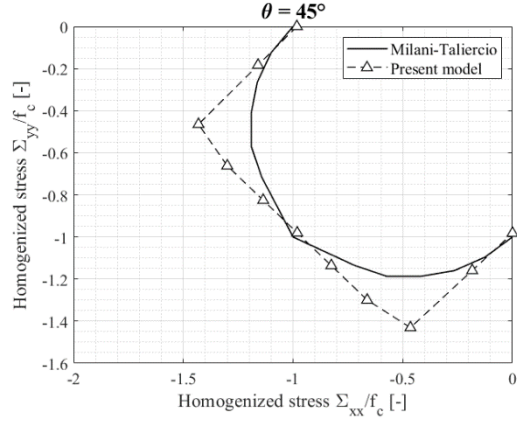
Fig. 5.8. Comparison of in-plane homogenized failure surfaces in the tension-tension range, for different values of angle θ .



(a)



(b)



(c)

Fig. 5.9. Comparison of in-plane homogenized failure surfaces in the compression-compression range, for different values of angle θ .

As far as the tension-tension range is concerned, the results obtained from the present model are thoroughly consistent with those obtained by Milani and Taliercio, despite some minor differences for the case of θ equal to 45° . Conversely, the results in the compression-compression range show some slightly more marked discrepancies, which are rather evident for the case with θ equal to 22.5° : these may be due to the different homogenization approach employed in the present model. It must be noted that, regardless of the value assumed by θ , the shape of the failure surfaces in the compression-compression range is more similar to those obtained by Milani and co-workers [6] (see also Fig. 2.7), albeit for different material properties. In fact, that work considers mortar joints reduced to interfaces, which more closely resembles the assumption of the present model (i.e. dissipation only occurs at the interfaces between adjacent elements). Nonetheless, the homogenized collapse stresses for uniaxial macroscopic loads are almost always coincident for any value of θ . Four failure modes are also shown in Fig. 5.10 for relevant load conditions applied to Mesh 1.

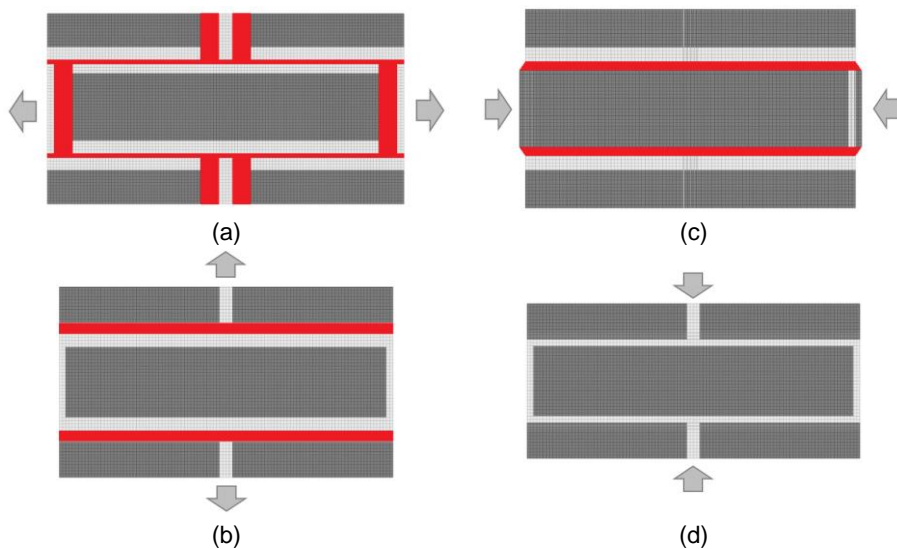
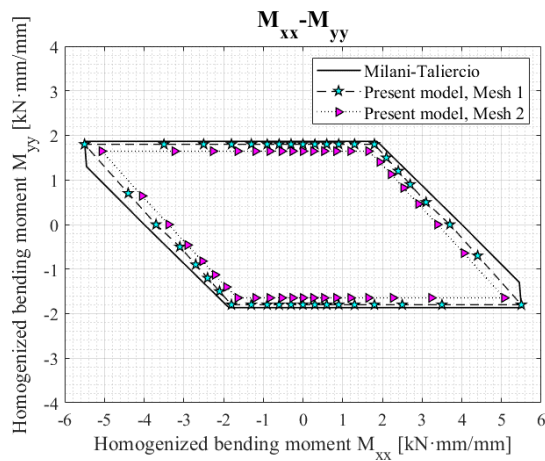


Fig. 5.10. Failure modes for in-plane load conditions on Mesh 1: (a) uniaxial horizontal tension; (b) uniaxial vertical tension; (c) uniaxial horizontal compression; (d) uniaxial vertical compression.

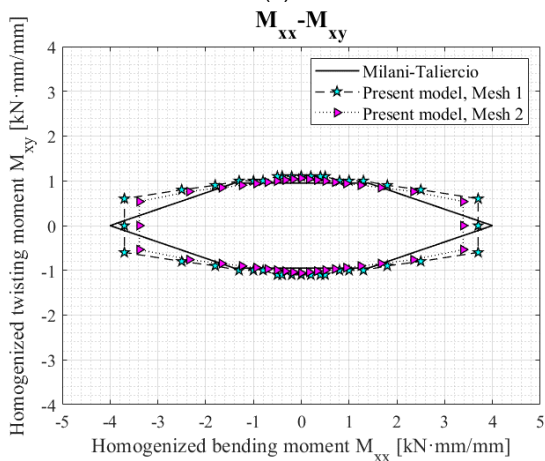
As it can be seen, splitting occurs in both bed and head joints for uniaxial horizontal tension, whereas for uniaxial vertical tension it only takes place in bed joints; crushing occurs for both uniaxial horizontal and vertical compression, with the former also displaying some splitting in bed joints. Therefore, these results

are consistent with the expected deformed configurations at collapse for the four considered cases.

For the validation in terms of out-of-plane homogenized failure surfaces, a simple Mohr-Coulomb failure criterion is used; the values of cohesion c and friction angle ϕ are 0.132 MPa and 27° , respectively, to be consistent with the values used in [4]. Fig. 5.11 shows the comparison between the out-of-plane homogenized failure surfaces obtained by Milani and Taliercio and those resulting from the present model for both Mesh 1 and Mesh 2; the latter is included to investigate the influence of the mesh size on the results.



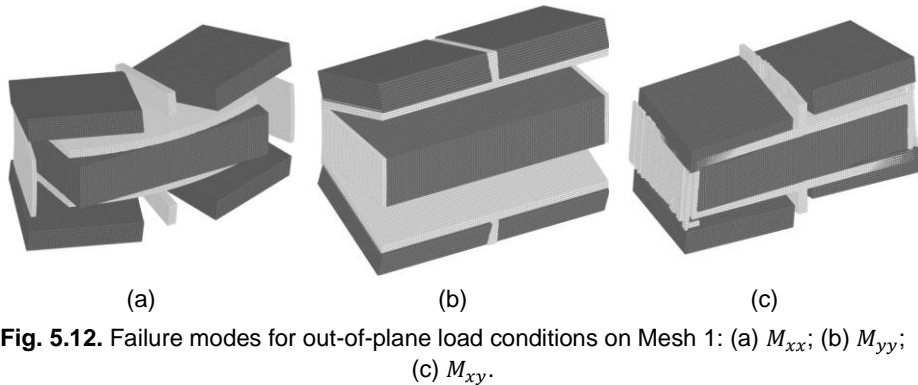
(a)



(b)

Fig. 5.11. Comparison of out-of-plane homogenized failure surfaces with Milani-Taliercio: (a) M_{xx} - M_{yy} plane; (b) M_{xx} - M_{xy} plane.

The results coming from the present model display a satisfying correspondence to those obtained by Milani and Taliercio; only the shape of the out-of-plane homogenized failure surface in the M_{xx} - M_{xy} plane is slightly different, but this may depend on the different kinematics of the two models. The use of coarser Mesh 2 does not affect the results in a significant way, producing only a small reduction of the out-of-plane failure surfaces. Three failure modes are also shown in Fig. 5.12 for relevant out-of-plane load conditions applied to Mesh 1.



As expected, the failure mode coming from the application of vertical overturning bending moment M_{xx} presents vertical cracks in the head joints, whereas the failure mode coming from the application of horizontal overturning bending moment M_{yy} presents horizontal cracks across the bed joints. The failure mode coming from the application of the twisting moment M_{xy} is also consistent with the expectations, displaying cracks corresponding to a clear torsional deformed shape.

5.2.2 English Bond Masonry REV

The second case study deals with an English bond masonry REV that also consists of standard Italian bricks ($25 \times 12 \times 5.5 \text{ cm}^3$) and mortar joints whose thickness is 1 cm. Its finite element mesh counts about 35000 elements (25 over the thickness), and is shown in Fig. 5.13; it must be noted that the chosen REV is not exactly the same as the cell used by Cecchi and Milani in [5], but it has been selected in order to ensure a rigorous application of homogenization. Also for this case study, a Mohr-Coulomb failure criterion is used; the mechanical properties for the interfaces are listed in Table 5.2 and are the same as those used in the work by Cecchi and Milani.

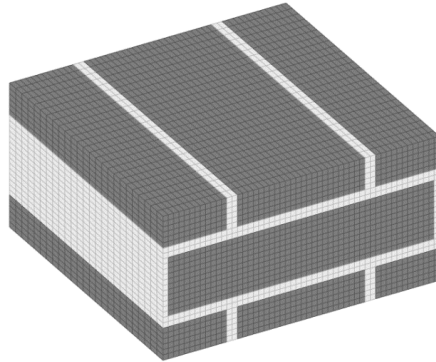
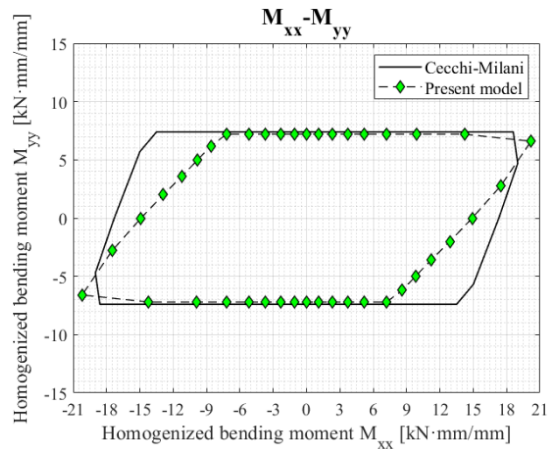


Fig. 5.13. English bond masonry REV used for validation against data from Cecchi-Milani.

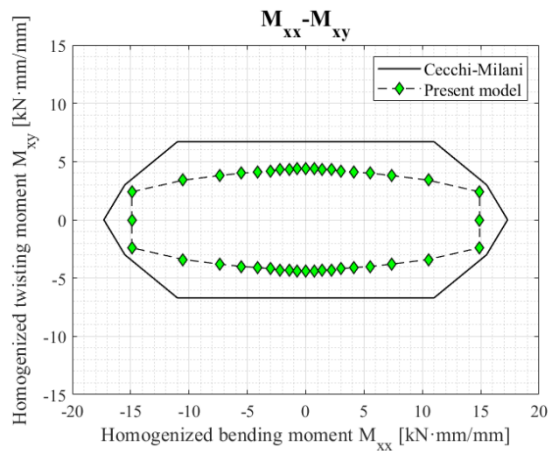
Table 5.2

Mechanical properties for the material employed in comparison with Cecchi-Milani.

Cohesion c [MPa]	Friction angle ϕ [°]	Tensile strength f_t [MPa]
0.132	27	$\frac{c}{\tan \phi}$



(a)



(b)

Fig. 5.14. Comparison of out-of-plane homogenized failure surfaces with Cecchi-Milani: (a) M_{xx} - M_{yy} plane; (b) M_{xx} - M_{xy} plane.

Fig. 5.14 shows the comparison between the out-of-plane homogenized failure surfaces obtained by Cecchi and Milani and those resulting from the present model. For the M_{xx} - M_{yy} plane, a satisfying overall correspondence is noted, despite a difference in terms of inclination of the lateral boundaries of the failure surface; it is highly possible that this discrepancy comes from the difference in terms of approach used for the evaluation of the out-of-plane failure surfaces between the two models. For the M_{xx} - M_{xy} plane, the failure surface coming from this model is smaller than the one obtained by Cecchi and Milani; this can also be due to the different approaches used in the two applications. In fact, the work by the aforementioned authors does not consider the actual thickness of mortar

joints; instead, since their cell just consists of masonry units, dissipation can only occur across the surfaces shared by adjoining units. Furthermore, their approach also enables dissipation to occur along the out-of-plane direction: this has an impact on the results obtained when the macroscopic torsional moment M_{xy} is significant, since in this case the dissipation between the two central blocks in correspondence of the mortar joint at the cell's midplane becomes relevant.

In order to accurately assess how the results in the M_{xx} - M_{xy} plane are affected by the differences between the two approaches, the upper bound limit analysis problem presented in this work is suitably modified to include dissipation along the out-of-plane direction for those interfaces that are located in correspondence of the midplane mortar joint. Moreover, a second finite element mesh is created in which the mortar joints are extremely thin, aiming at mirroring more closely the cell's configuration of Cecchi and Milani (Fig. 5.15a): this consists of about 240000 elements, 51 over the thickness. To account for the dissipation also in the out-of-plane direction, it is necessary to express the Mohr-Coulomb failure criterion with a 3D surface in the σ_n - τ_1 - τ_2 plane, which in principle is a cone. However, since linear programming requires the bounding yield surfaces to have linear expressions in their variables, a piecewise linear approximation of the failure criterion is needed in the τ_1 - τ_2 plane. Fig. 5.15b shows the very refined one used by Cecchi and Milani; to keep the swiftness of the present model, two rougher approximations are instead used in this modified upper bound limit analysis problem, namely a box-shaped approximation of the surface (Model A, Fig. 5.15c) and one that circumscribes the actual surface (Model B, Fig. 5.15d).

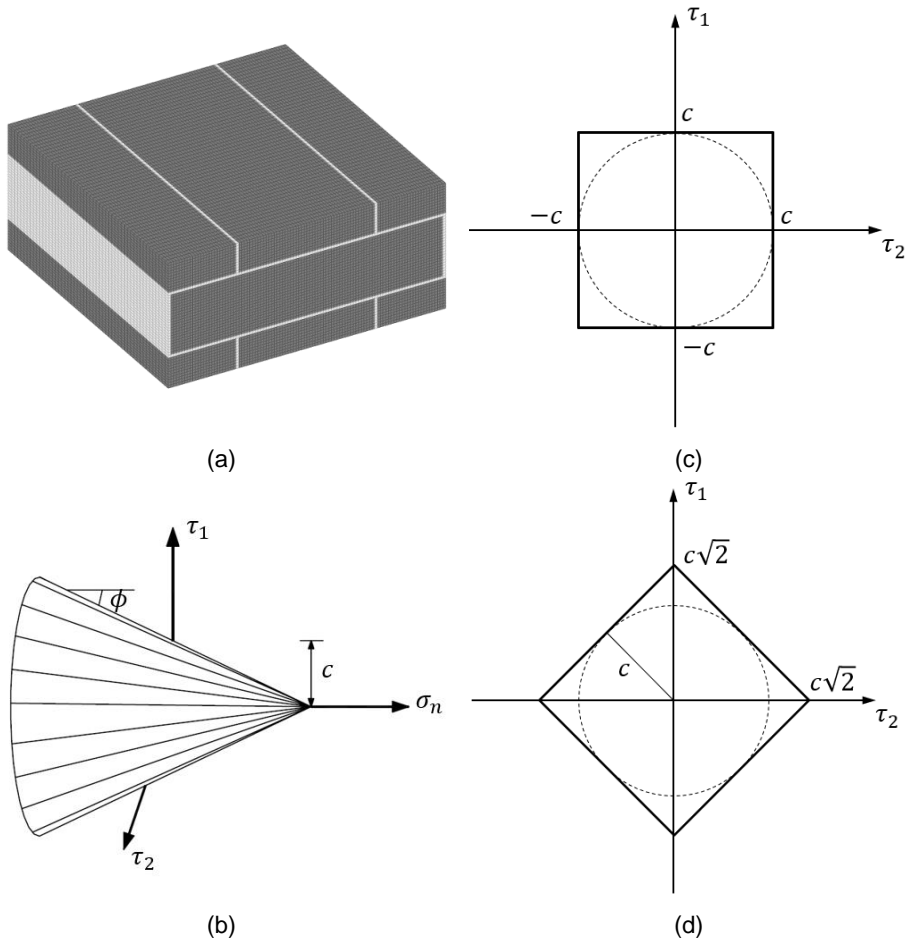
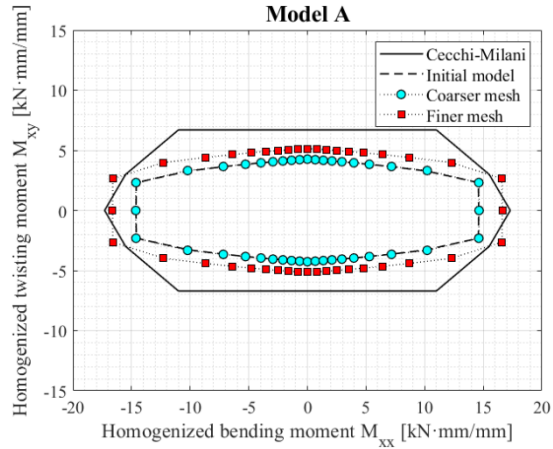


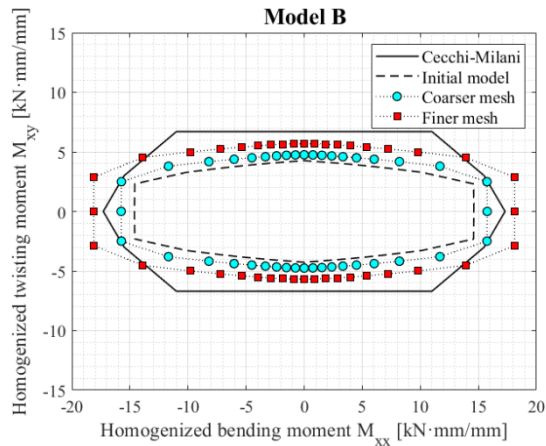
Fig. 5.15. (a) Finer mesh for the English bond masonry REV; (b) piecewise linear approximation for the 3D Mohr-Coulomb failure criterion used by Cecchi-Milani; (c) Model A, box-shaped approximation in the τ_1 - τ_2 plane; (d) Model B, circumscribing approximation in the τ_1 - τ_2 plane.

Fig. 5.16a and Fig. 5.16b show the out-of-plane homogenized failure surfaces in the M_{xx} - M_{xy} plane for Model A and Model B, respectively, compared against the results obtained by Cecchi and Milani and against those coming from the approach originally used in this work. It can be noted that the finer mesh better matches the original results for both models, especially for Model B - even though it still slightly underestimates the boundaries of the homogenized failure surfaces in correspondence of M_{xy} . To this regard, it must be recalled that the REV used in the present work is different than the cell used by Cecchi and Milani, which displays three pairs of central blocks instead of just one as in this case. Finally, it must be remarked that the out-of-plane homogenized failure surfaces

in the M_{xx} - M_{yy} plane do not show meaningful differences among the various cases and finite element meshes, hence they are here omitted for sake of conciseness.



(a)



(b)

Fig. 5.16. Comparison of different out-of-plane homogenized failure surfaces in the M_{xx} - M_{xy} plane: (a) Model A; (b) Model B.

Eventually, three failure modes are extracted for the coarser mesh in relation to the initial model of Fig. 5.14, and they are shown in Fig. 5.17 for relevant out-of-plane load conditions.

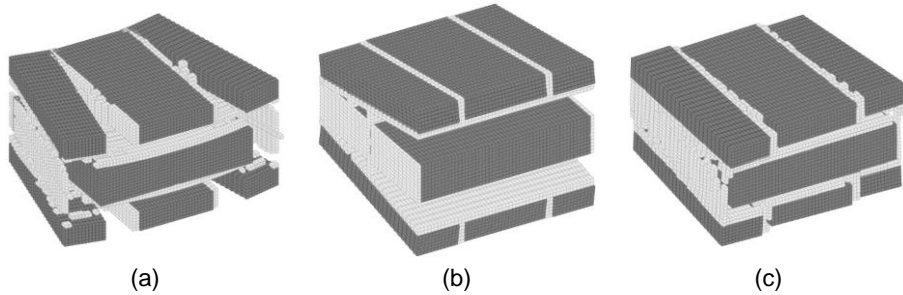


Fig. 5.17. Failure modes for out-of-plane load conditions on English bond masonry REV: (a) M_{xx} ; (b) M_{yy} ; (c) M_{xy} .

Similarly to the running bond masonry case, the three resulting deformed configurations for the selected out-of-plane load conditions are consistent with the expectations, thus confirming the reliability of the initial model. The failure modes for M_{xy} related to Model A and B and for the coarser mesh are here omitted for sake of brevity, since they display no relevant differences to those shown in Fig. 5.17.

5.3 Case Studies

The six case studies that are investigated in terms of out-of-plane homogenized failure surfaces are the same previously considered for the in-plane homogenized failure surfaces in Chapter 4.2 (Fig. 5.18), which are here recapped:

- Case study 1, a rubble masonry building in Casola in Lunigiana, Tuscany.
- Case study 2, a quasi-periodic masonry ruin in Codiponte, Tuscany.
- Case study 3, a quasi-periodic masonry parish church in Filattiera, Tuscany.
- Case study 4, quasi-periodic masonry tower ruins in Mulazzo, Tuscany.
- Case study 5, a quasi-regular masonry parish church in San Secondo Parmense, Emilia-Romagna.
- Case study 6, a quasi-regular masonry grand corridor in Sabbioneta, Lombardy.

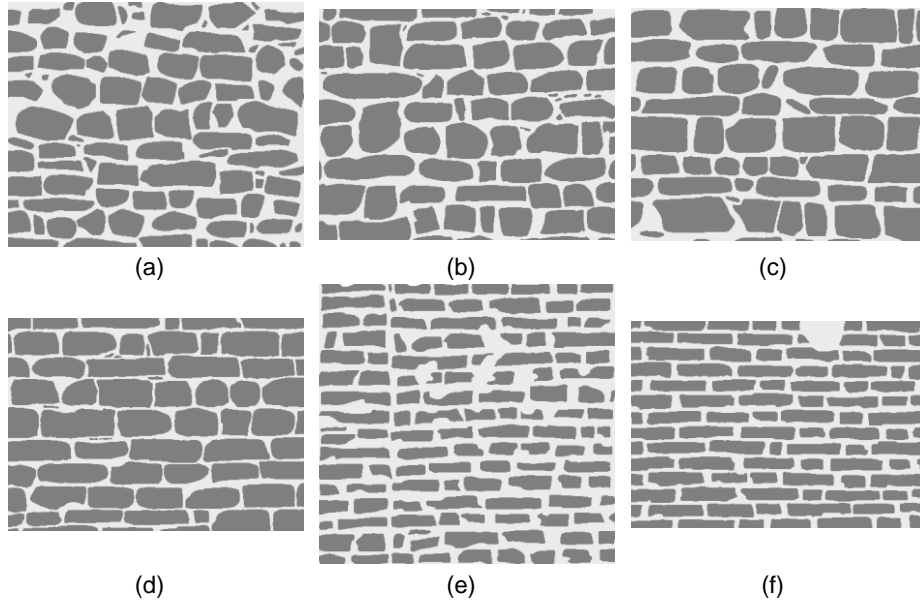


Fig. 5.18. (a) case study 1; (b) case study 2; (c) case study 3; (d) case study 4; (e) case study 5; (f) case study 6.

For the out-of-plane homogenized failure surfaces of all the six case studies, a Mohr-Coulomb failure criterion with cutoffs in tension and compression is selected. All the six case studies share the same set of mechanical parameters (cohesion, friction angle, tensile strength, and compressive strength) that are listed in Table 5.3:

Table 5.3

Mechanical properties for the material employed in all case studies.

Cohesion [MPa]	Friction angle [°]	Tensile strength [MPa]	Compressive strength [MPa]
0.15	30	0.1	1.5

5.3.1 Case Study 1: Rubble Masonry Building in Casola in Lunigiana, Tuscany

The four considered test-windows are those depicted in Fig. 4.8c and their dimensions are $130 \times 130 \times 40$ cm³; the transversal configuration of their masonry units is ellipsoidal (see Chapter 3.2), since it is consistent with that of river pebbles (which are present in this case) and employs 16 finite elements over the thickness.

The flexural and torsional out-of-plane homogenized failure surfaces for the four test-windows are depicted in Fig. 5.19, along with their envelope and mean: all

the moment values are normalized by $0.5 \cdot t^2 \cdot f_t$. It can be noted that test-windows A and D display smaller out-of-plane failure surfaces with respect to the other two: this is because they contain some clearly visible bed joints (actually, pseudo bed joints), despite consisting of rubble masonry. In fact, test-windows B and C show a normalized value of M_{yy} that is greater than 1: again, this is due to the more marked randomness in the arrangement of their masonry units. Nonetheless, the shape of both out-of-plane failure surfaces for the four test-windows reflects the high rate of randomness of this case study. Fig. 5.20 shows the deformed shapes at collapse (“failure modes”) of the four test-windows of this case study coming from the single application of M_{xx} , M_{yy} , and M_{xy} . All these failure modes are consistent with what is expected to occur under the application of the aforementioned moments. In particular, it can be noted how the application of M_{xx} causes widespread cracks in all four test-windows; moreover, the application of M_{yy} to test-window C does not induce a single horizontal crack across one of the pseudo bed joints but again it generates widespread cracking patterns. This confirms the resulting flexural out-of-plane homogenized failure surface for this test-window, which is the largest of the four and shows the biggest normalized collapse value of M_{yy} (which is greater than 1, also).

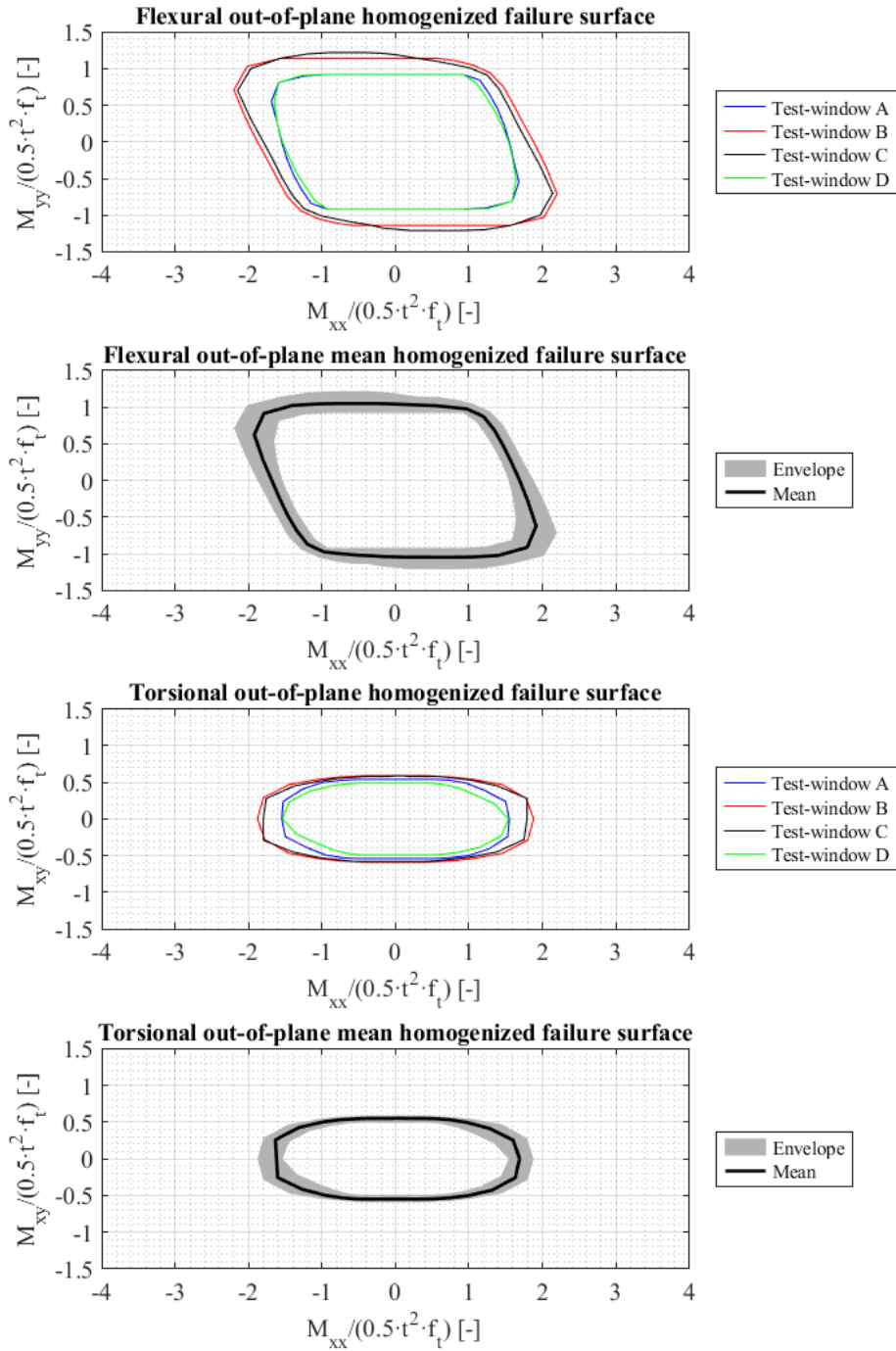


Fig. 5.19. Out-of-plane homogenized failure surfaces for case study 1.

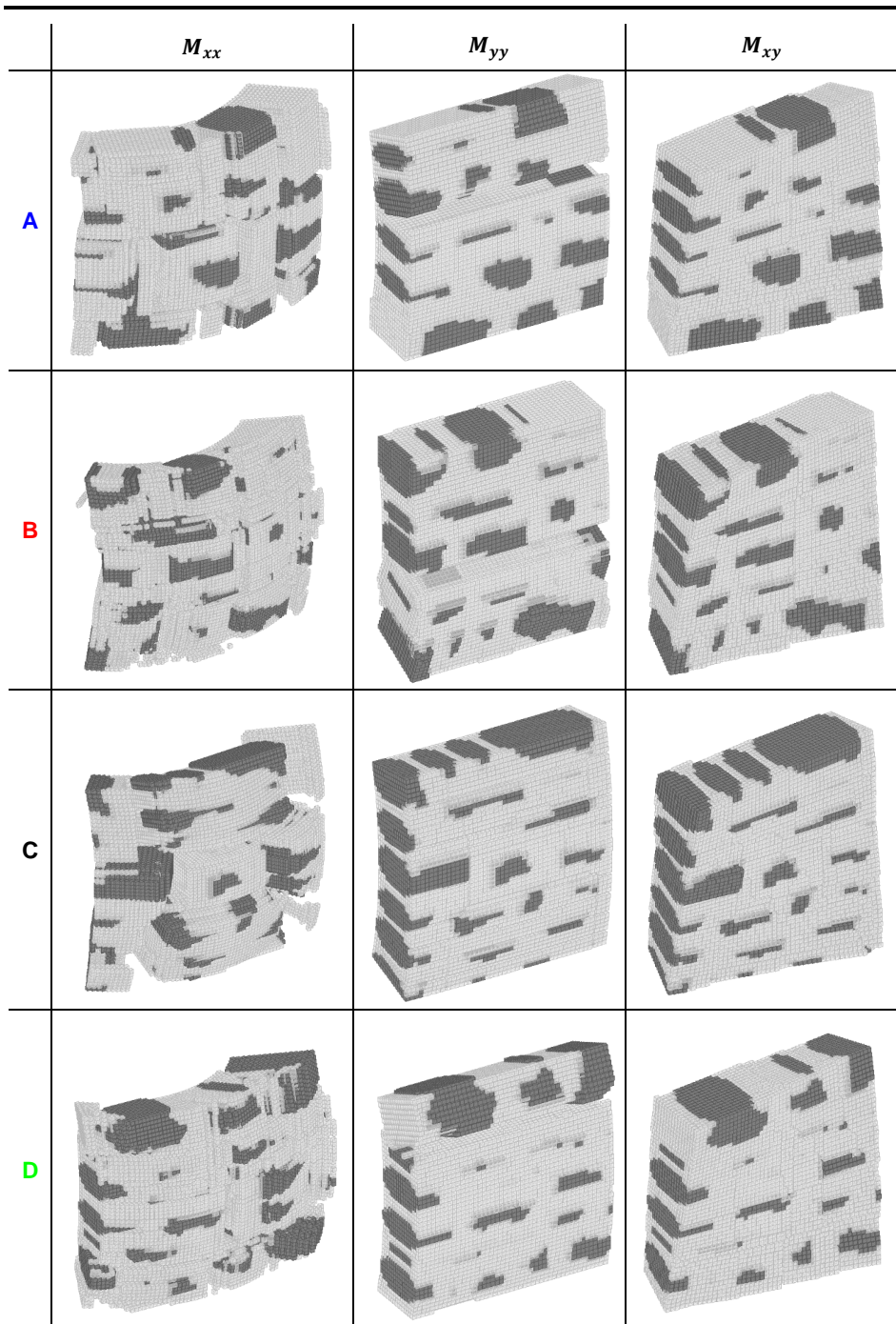


Fig. 5.20. Failure modes under M_{xx} , M_{yy} , and M_{xy} for the four test-windows of case study 1.

5.3.2 Case Study 2: Quasi-Periodic Masonry Ruin in Codiponte, Tuscany

The four considered test-windows are those depicted in Fig. 4.14d and their dimensions are $160 \times 160 \times 40$ cm³; the transversal configuration of their masonry units is ellipsoidal to ensure consistency with the in-plane shape of the ashlar in this case, and employs 16 finite elements over the thickness.

The flexural and torsional out-of-plane homogenized failure surfaces for the four test-windows are depicted in Fig. 5.21, along with their envelope and mean: all the moment values are normalized by $0.5 \cdot t^2 \cdot f_t$. Unlike the previous case, the shape of the flexural out-of-plane homogenized failure surfaces is very similar for all the four test-windows, with no differences whatsoever in the normalized collapse value of M_{yy} . Conversely, more marked differences among the four test-windows can be observed in the torsional out-of-plane homogenized failure surfaces. Fig. 5.22 shows the failure modes of the four test-windows of this case study: all are consistent with what is expected to occur under the application of M_{xx} , M_{yy} , and M_{xy} .

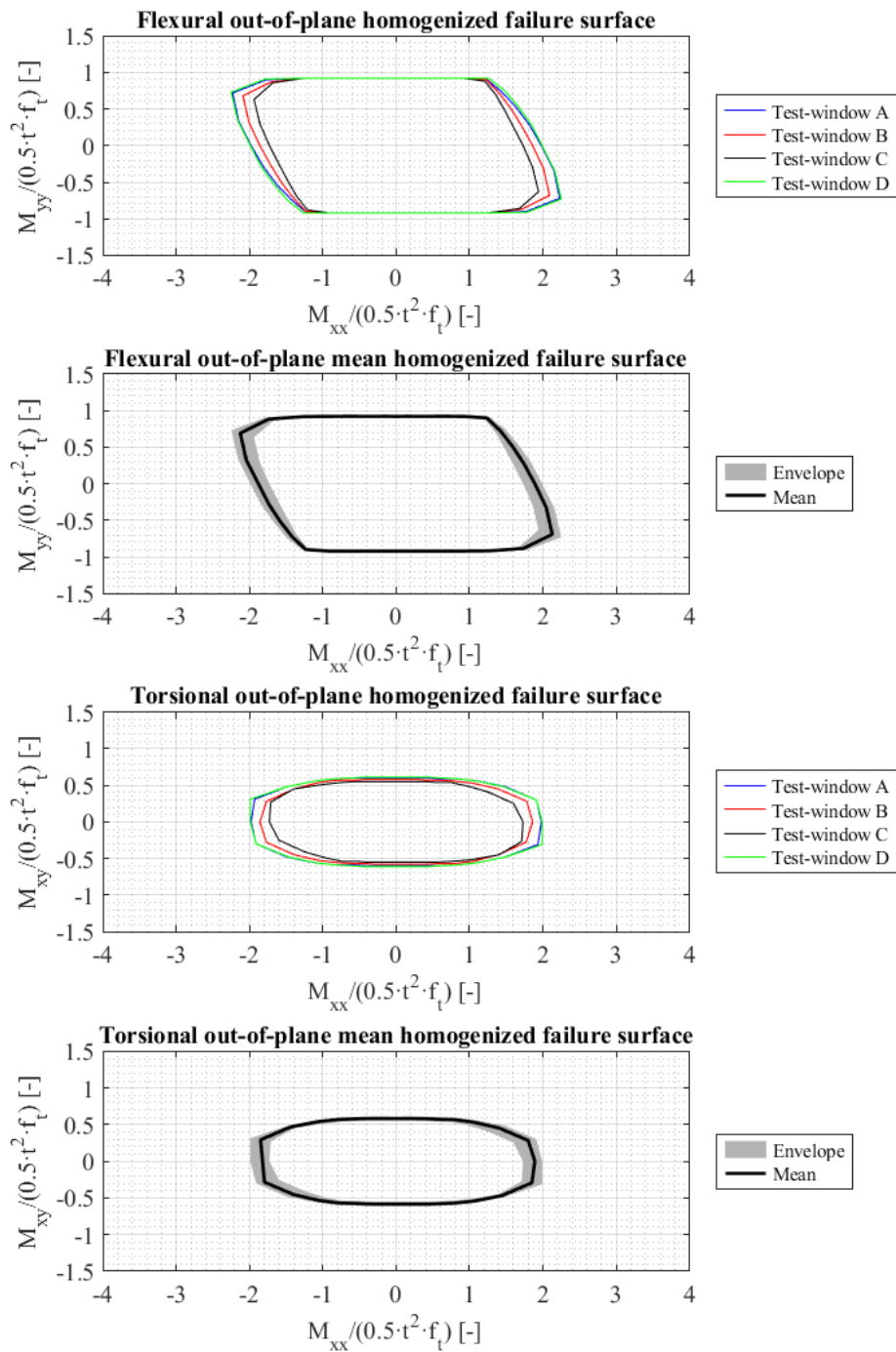


Fig. 5.21. Out-of-plane homogenized failure surfaces for case study 2.

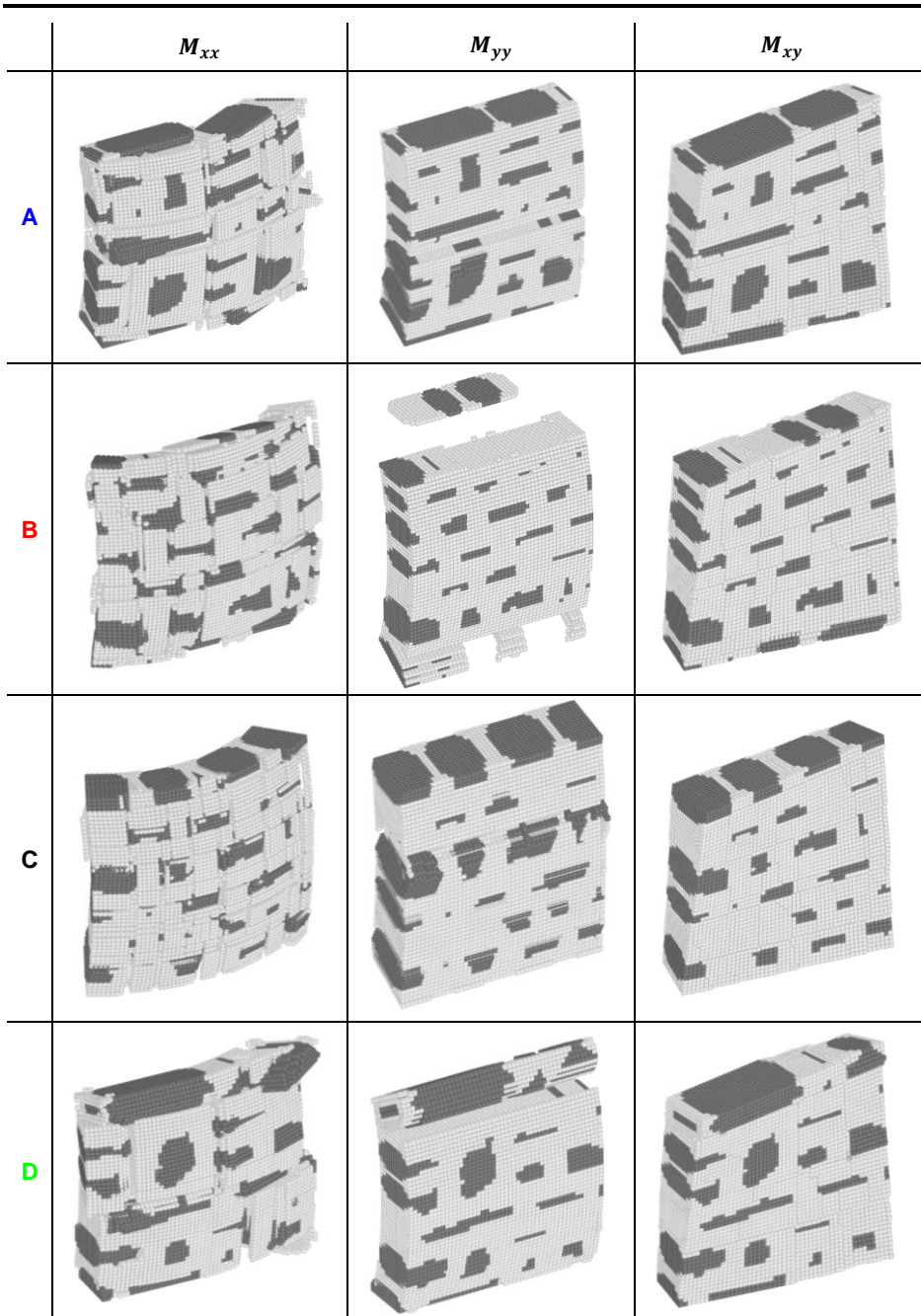


Fig. 5.22. Failure modes under M_{xx} , M_{yy} , and M_{xy} for the four test-windows of case study 2.

5.3.3 Case Study 3: Quasi-Periodic Masonry Parish Church in Filattiera, Tuscany

The four considered test-windows are those depicted in Fig. 4.20d and their dimensions are $160 \times 160 \times 40 \text{ cm}^3$; the transversal configuration of their masonry units is again ellipsoidal, and employs 16 finite elements over the thickness.

The flexural and torsional out-of-plane homogenized failure surfaces for the four test-windows are depicted in Fig. 5.23, along with their envelope and mean: all the moment values are normalized by $0.5 \cdot t^2 \cdot f_t$. As in the previous case, the shape of the flexural out-of-plane homogenized failure surfaces is very similar for all the four test-windows, whereas the torsional out-of-plane homogenized failure surfaces display noticeable differences. Fig. 5.24 shows the failure modes of the four test-windows of this case study: once again, all are consistent with what is expected to occur under the application of M_{xx} , M_{yy} , and M_{xy} .

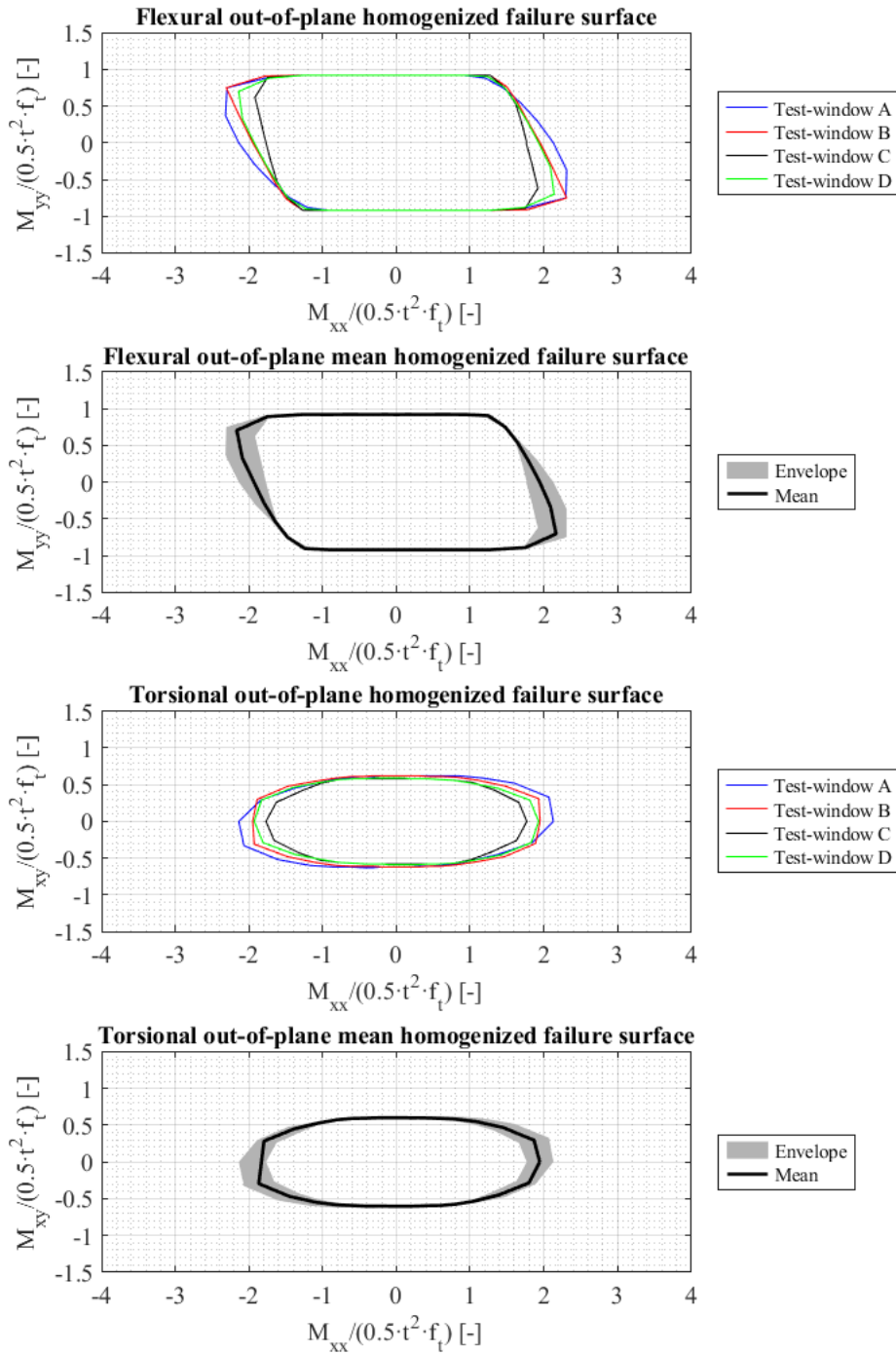


Fig. 5.23. Out-of-plane homogenized failure surfaces for case study 3.

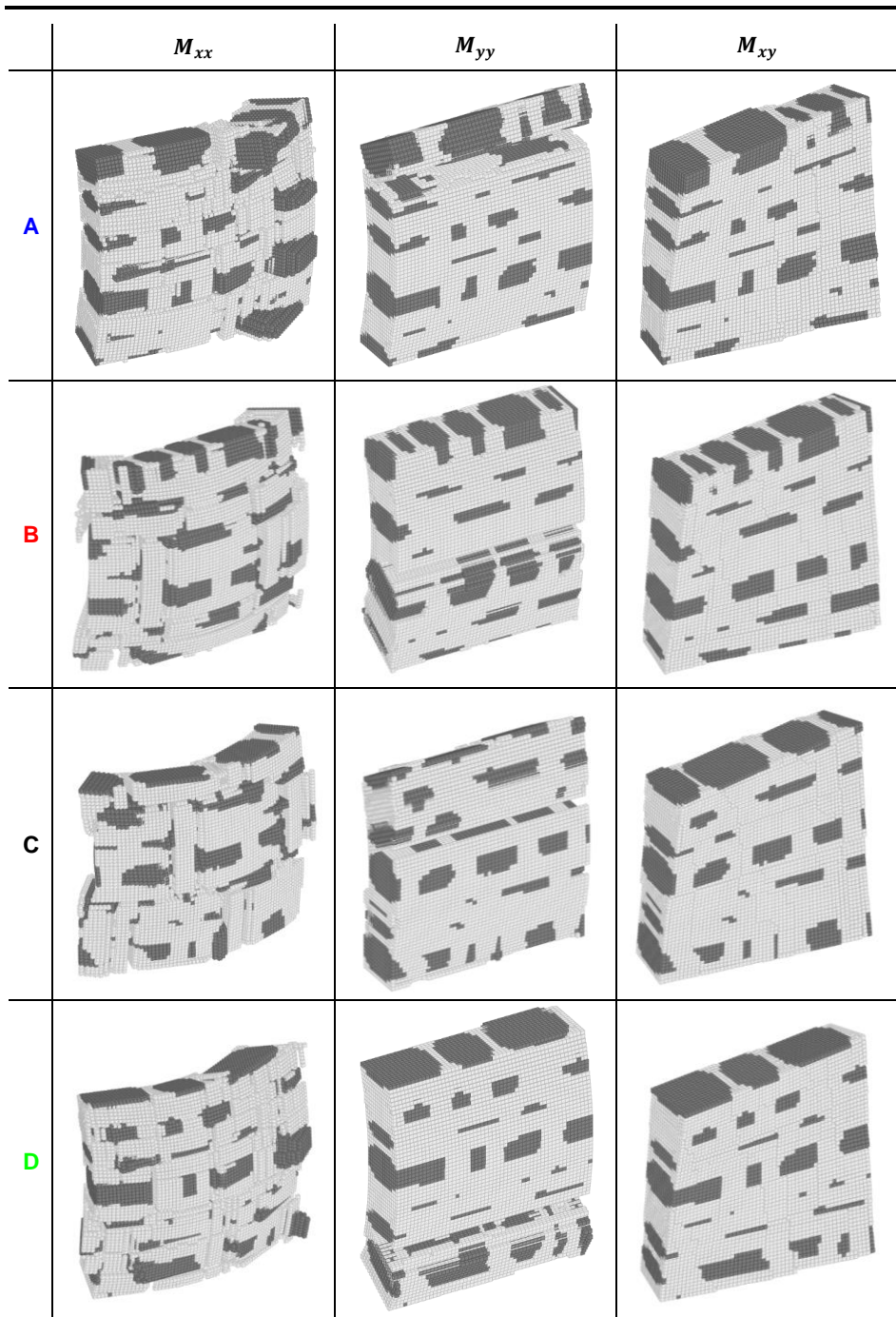


Fig. 5.24. Failure modes under M_{xx} , M_{yy} , and M_{xy} for the four test-windows of case study 3.

5.3.4 Case Study 4: Quasi-Periodic Masonry Tower Ruins in Mulazzo, Tuscany

The four considered test-windows are those depicted in Fig. 4.27d and their dimensions are $160 \times 160 \times 40$ cm³; the transversal configuration of their masonry units is again ellipsoidal, and employs 16 finite elements over the thickness.

The flexural and torsional out-of-plane homogenized failure surfaces for the four test-windows are depicted in Fig. 5.25, along with their envelope and mean: all the moment values are normalized by $0.5 \cdot t^2 \cdot f_t$. In this case, both the flexural and torsional out-of-plane homogenized failure surfaces almost coincide for three of the four test-windows: only test-window A displays larger homogenized failure surfaces, probably due to the presence of stone chips within some of its bed joints. Fig. 5.26 shows the failure modes of the four test-windows of this case study: once again, all are consistent with what is expected to occur under the application of M_{xx} , M_{yy} , and M_{xy} .

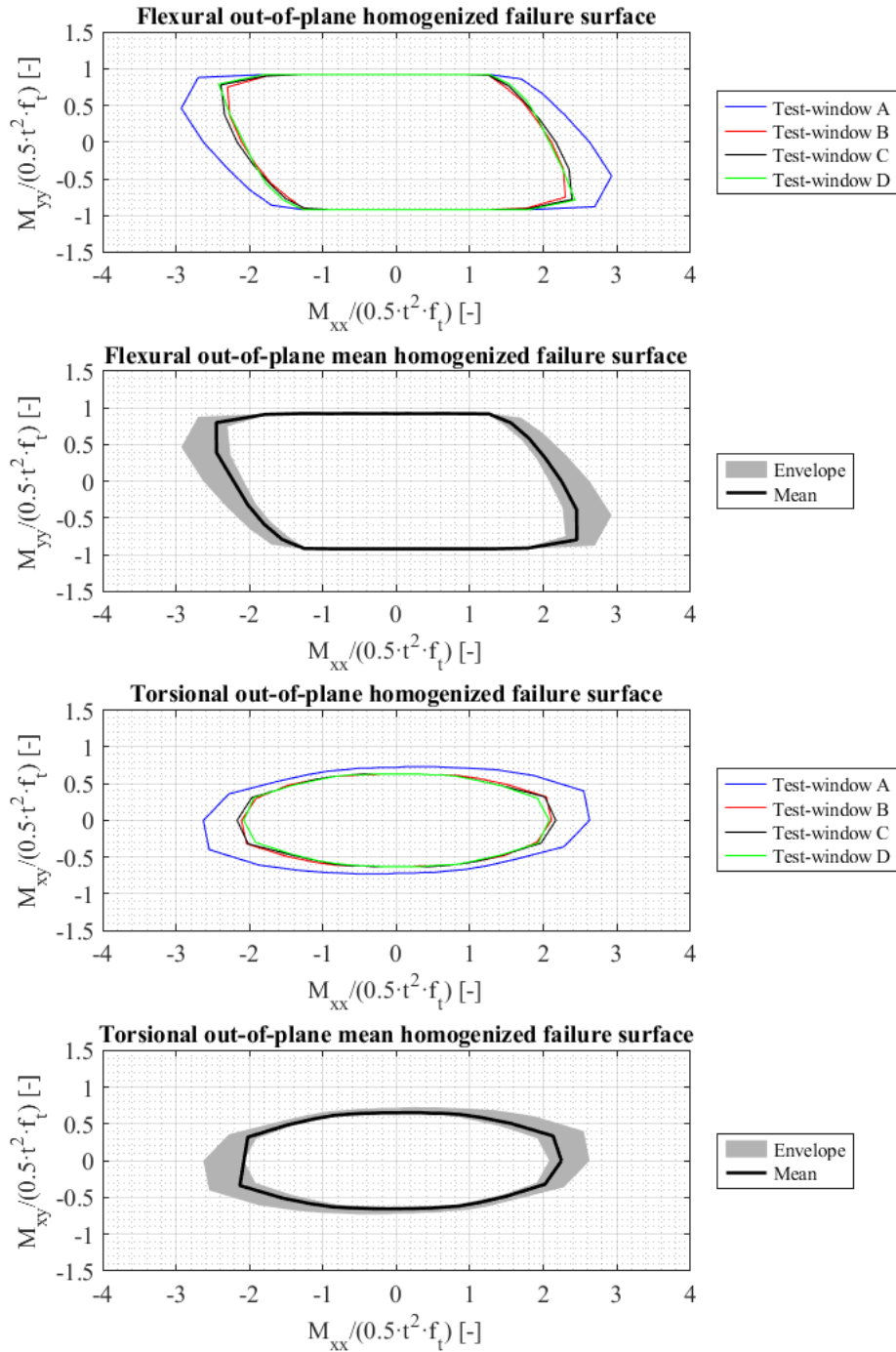


Fig. 5.25. Out-of-plane homogenized failure surfaces for case study 4.

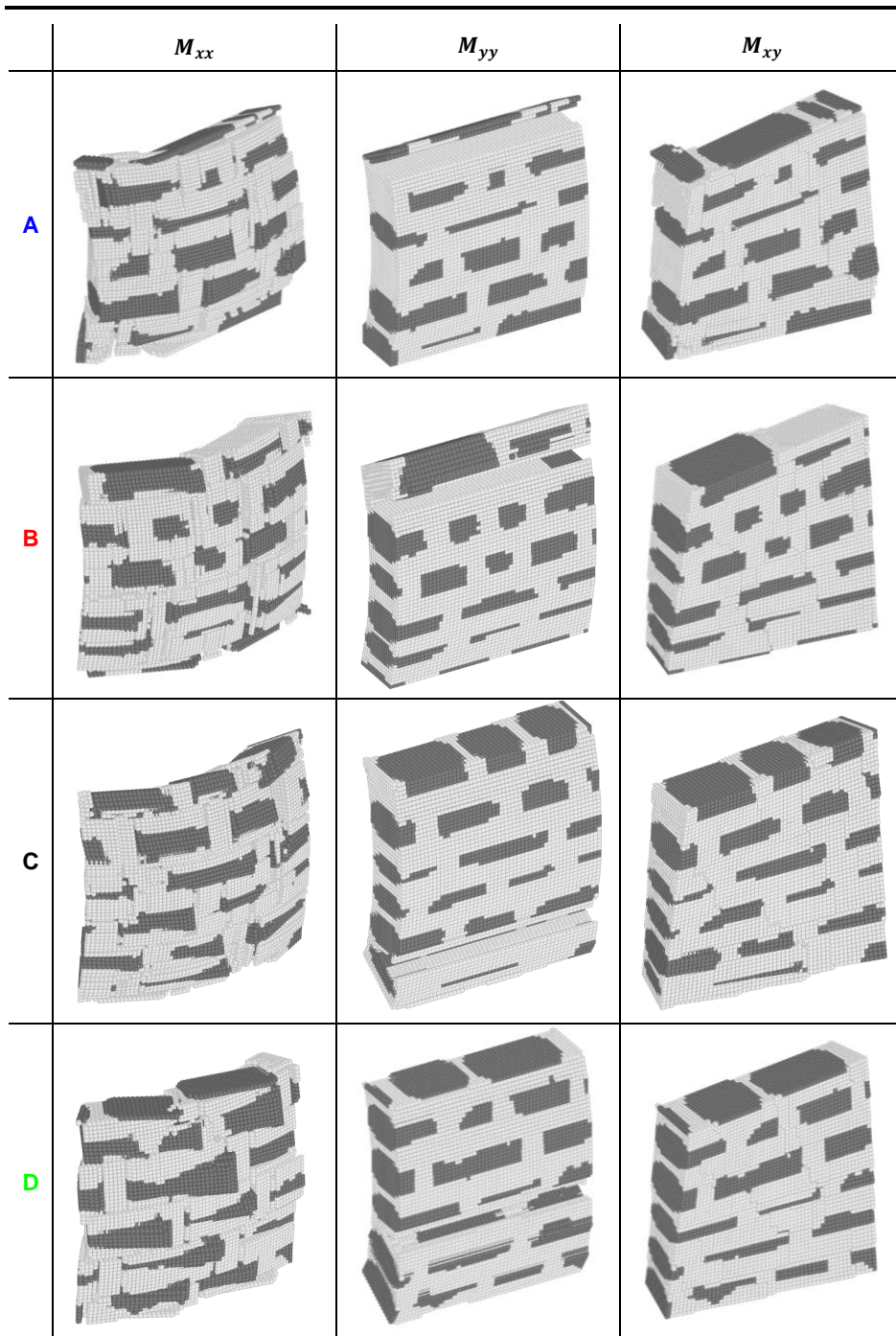


Fig. 5.26. Failure modes under M_{xx} , M_{yy} , and M_{xy} for the four test-windows of case study 4.

5.3.5 Case Study 5: Quasi-Regular Masonry Parish Church in San Secondo Parmense, Emilia Romagna

The four considered test-windows are those depicted in Fig. 4.33b and their dimensions are $100 \times 100 \times 15 \text{ cm}^3$; the transversal configuration of their masonry units is simply the extrusion of their brick-like in-plane configuration, and employs 10 finite elements over the thickness.

The flexural and torsional out-of-plane homogenized failure surfaces for the four test-windows are depicted in Fig. 5.27, along with their envelope and mean: all the moment values are normalized by $0.5 \cdot t^2 \cdot f_t$. This case is particularly interesting due to the peculiar behavior of test-window D: it is the only test-window containing part of the continuous head joint, which greatly affects its out-of-plane behavior. In fact, both its out-of-plane homogenized failure surfaces are considerably different than those of the other three test-windows and display a sensibly small normalized collapse value of M_{xx} , which is due to the presence of the continuous head joint. Fig. 5.28 shows the failure modes of the four test-windows of this case study: they are all consistent with what is expected to occur under the application of M_{xx} , M_{yy} , and M_{xy} . In particular, it can be observed how the presence of the continuous head joint affects the failure modes of test-window D for M_{xx} and M_{xy} : in both cases the test-window displays a continuous vertical crack in correspondence of the aforementioned head joint, which is extremely marked for M_{xx} where the test-window actually splits.

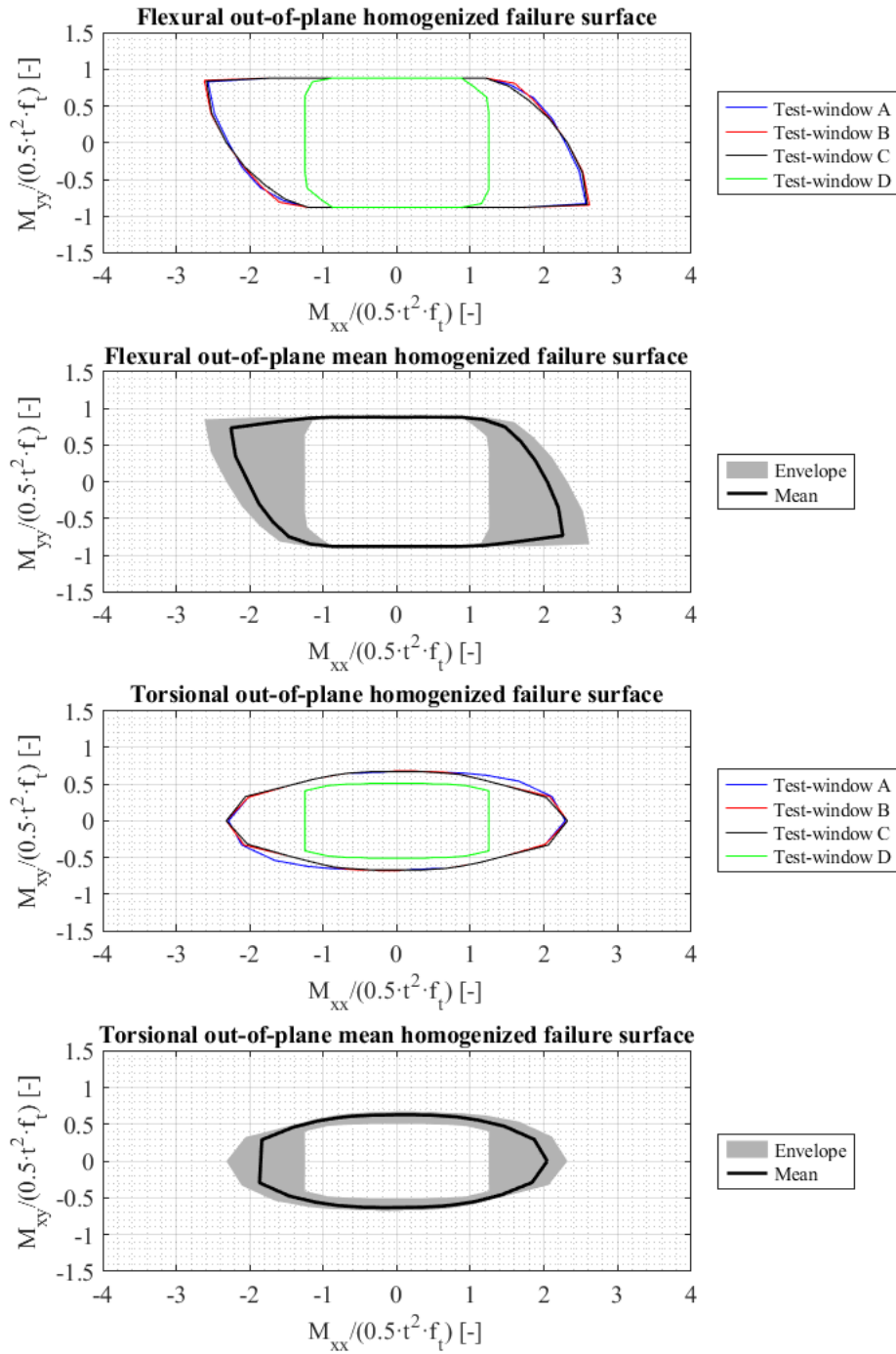


Fig. 5.27. Out-of-plane homogenized failure surfaces for case study 5.

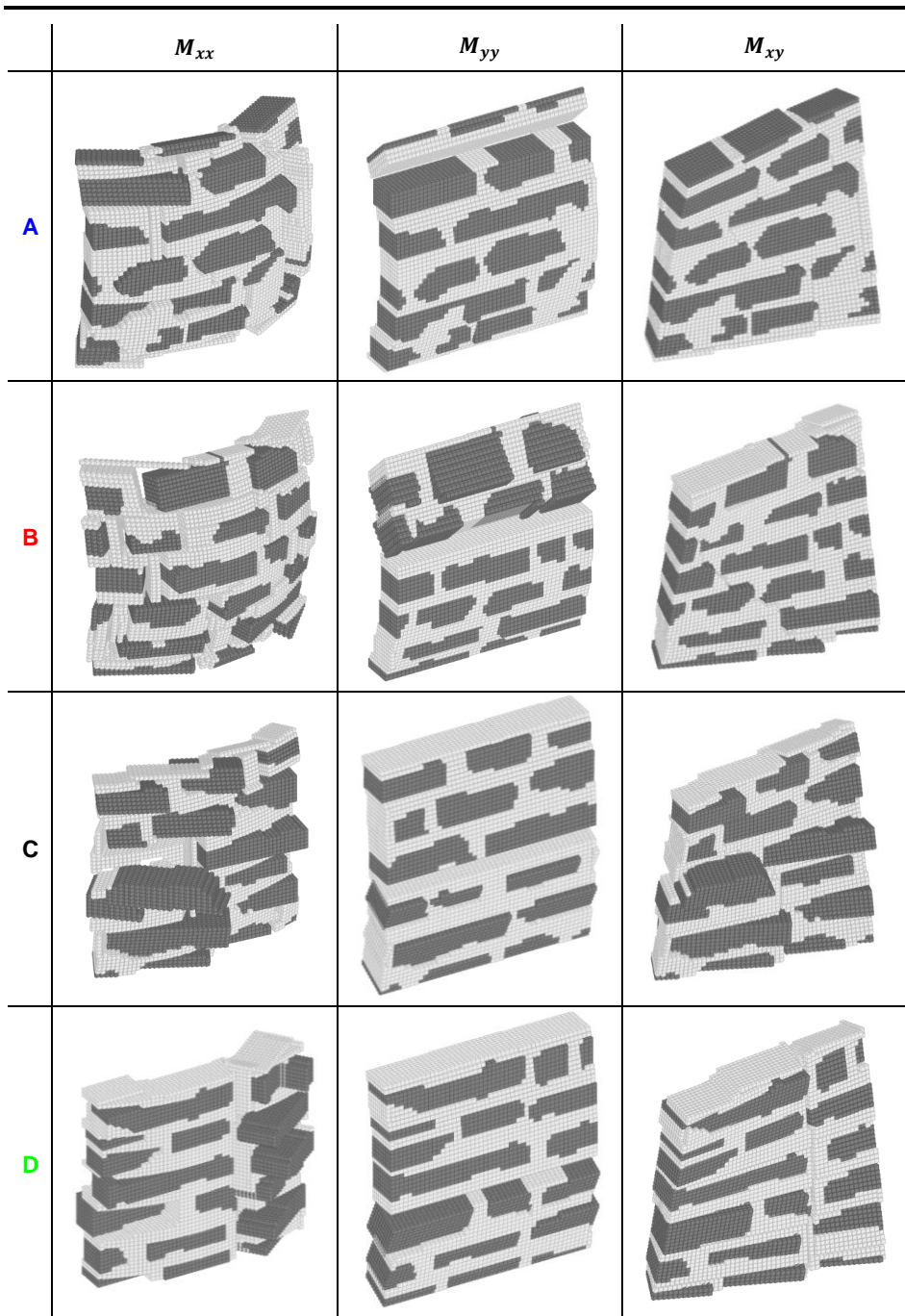


Fig. 5.28. Failure modes under M_{xx} , M_{yy} , and M_{xy} for the four test-windows of case study 5.

5.3.6 Case Study 6: Quasi-Regular Masonry Grand Corridor in Sabbioneta, Lombardy

The four considered test-windows are those depicted in Fig. 4.38c and their dimensions are 130×130×15 cm³; the transversal configuration of their masonry units is again the mere extrusion of their in-plane configuration, and employs 10 finite elements over the thickness.

The flexural and torsional out-of-plane homogenized failure surfaces for the four test-windows are depicted in Fig. 5.29, along with their envelope and mean: all the moment values are normalized by $0.5 \cdot t^2 \cdot f_t$. Both the flexural and torsional out-of-plane homogenized failure surfaces for the four test-windows present an elongated shape that is usually associated to a running bond masonry, which means that the out-of-plane behavior of this case is the closest to that of periodic masonry among the six cases. The out-of-plane homogenized failure surfaces of test-window B are actually slightly smaller than those of the other three test-windows, and this is due to the presence of a mortar spot in its top-left corner. Fig. 5.30 shows the failure modes of the four test-windows of this case study: once again, all are consistent with what is expected to occur under the application of M_{xx} , M_{yy} , and M_{xy} .

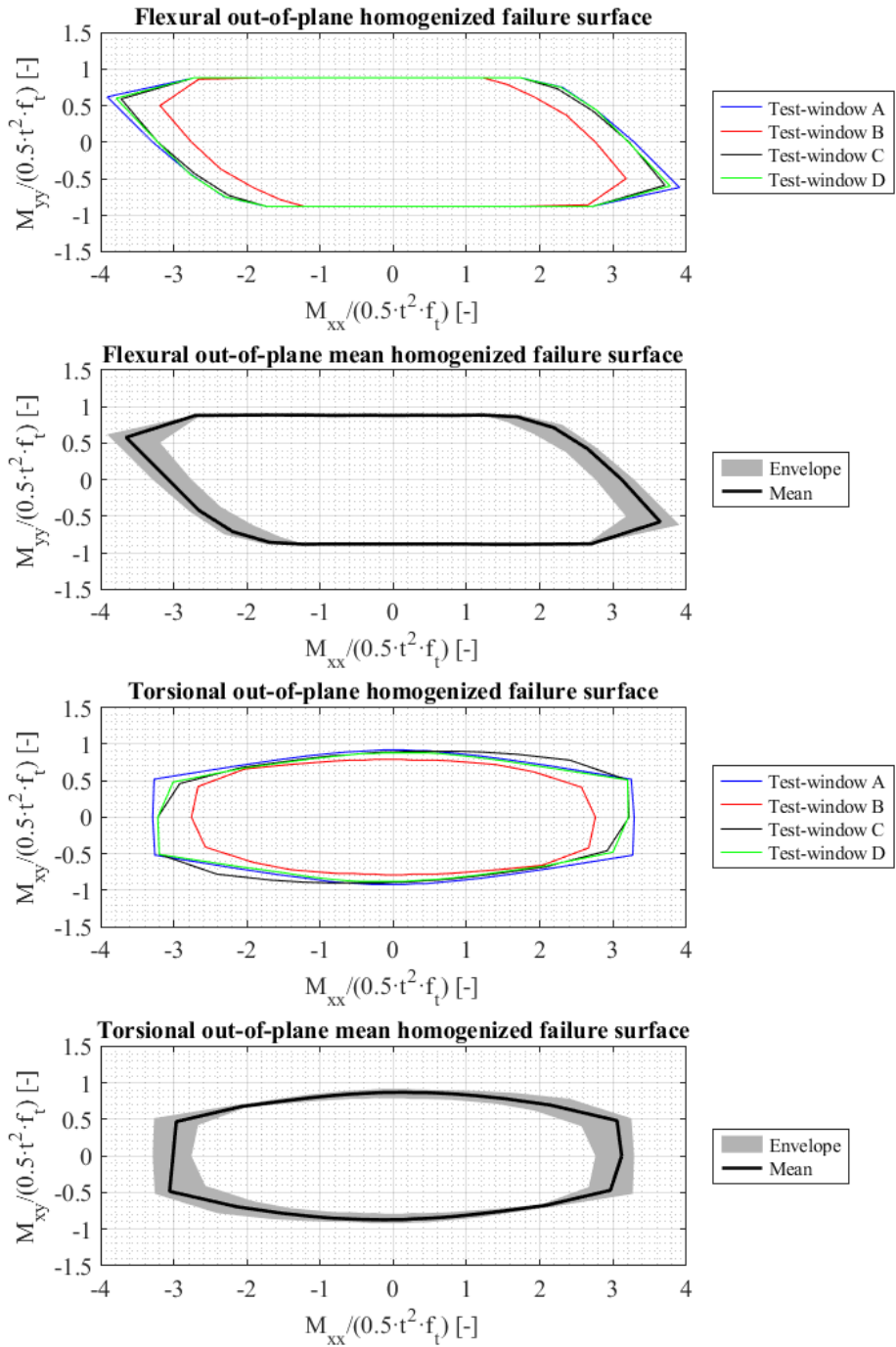


Fig. 5.29. Out-of-plane homogenized failure surfaces for case study 6.

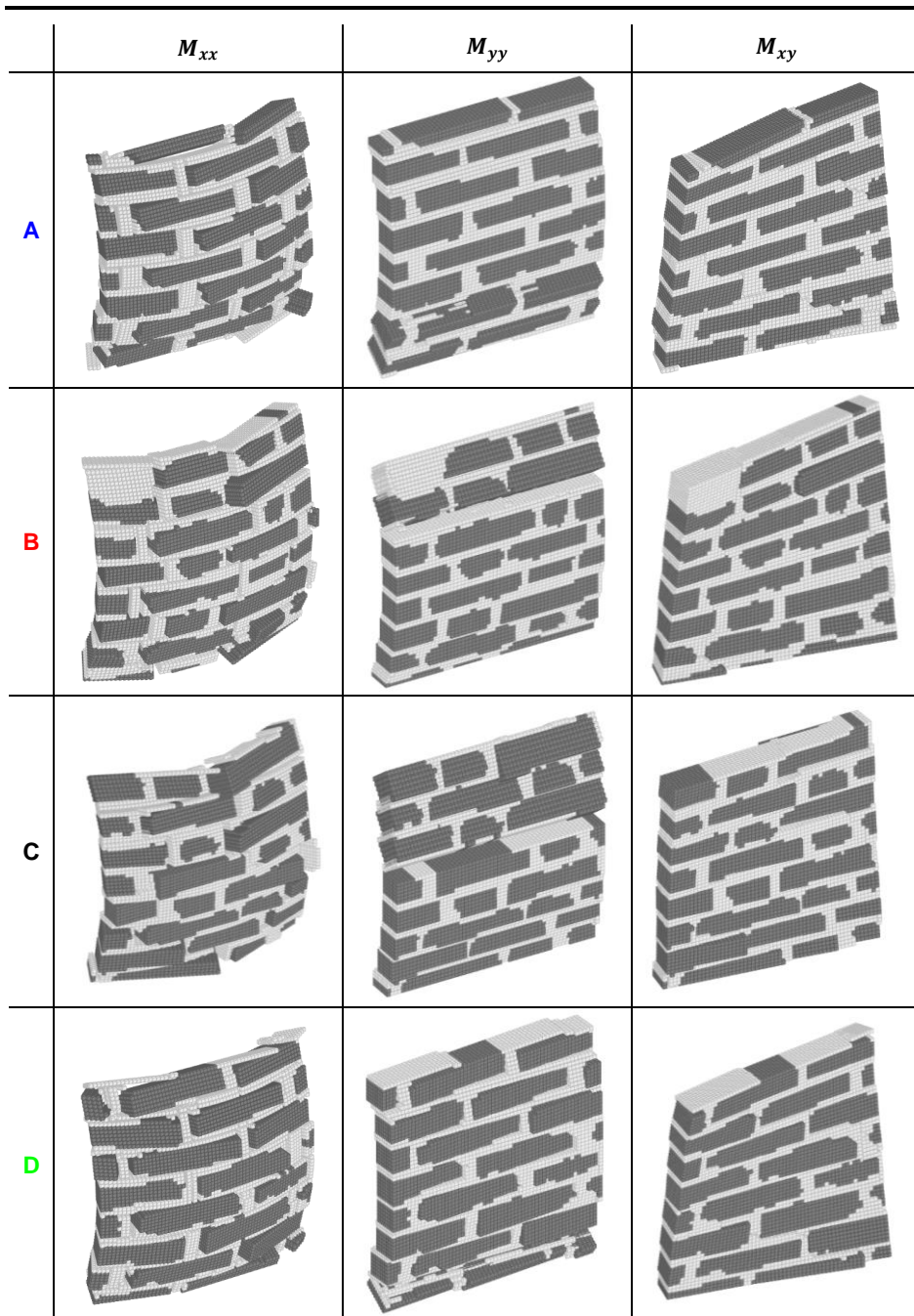


Fig. 5.30. Failure modes under M_{xx} , M_{yy} , and M_{xy} for the four test-windows of case study 6.

5.4 Conclusions

Fig. 5.31 contains the comparison of the out-of-plane mean homogenized failure surfaces for the test-windows of the considered six case studies; all the moment values are normalized by $0.5 \cdot t^2 \cdot f_t$. In both the flexural and torsional out-of-plane homogenized failure surfaces, it is possible to observe how the quasi-regular sixth case study offers the highest normalized collapse value for M_{xx} and M_{xy} . As previously observed, the shape of both failure surfaces closely resembles that usually obtained for a running bond masonry (see Section 5.2.1). Although the fifth case study is itself quasi-regular, its out-of-plane mean homogenized failure surfaces are severely affected by the presence of the continuous head joint, so that they are actually reduced with respect to the expectations. This leads to an interesting observation: when considering historical masonry, the test-windows must be randomly extracted from the wall under investigation in order to encompass all the possible geometrical features. As clearly shown by the fifth case study, even though the units' arrangement may be almost regular, the overall out-of-plane behavior is definitely affected by the presence of a feature such as the continuous head joint, and this must be always taken into account. As far as the other four cases are concerned, the quasi-periodic fourth case study offers the highest resistance to M_{xx} and M_{xy} with respect to the other three. Conversely, the rubble first case study offers the lowest resistance to M_{xx} and M_{xy} , but this is partially compensated by its high resistance to M_{yy} , which is usually the out-of-plane load condition mostly relevant when assessing the vulnerability of masonry walls to out-of-plane actions, for instance induced by a seismic event. It can then be remarked how a rubble masonry wall offers a greater resistance to such actions with respect to more periodic bonds, and this helps explaining the fact that historical rubble masonry buildings seem to be spared from collapse more frequently than other masonry structures.

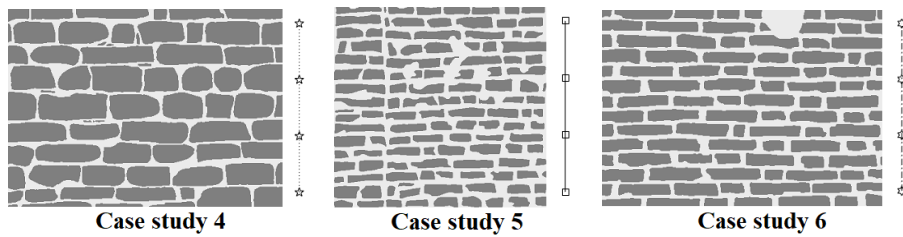
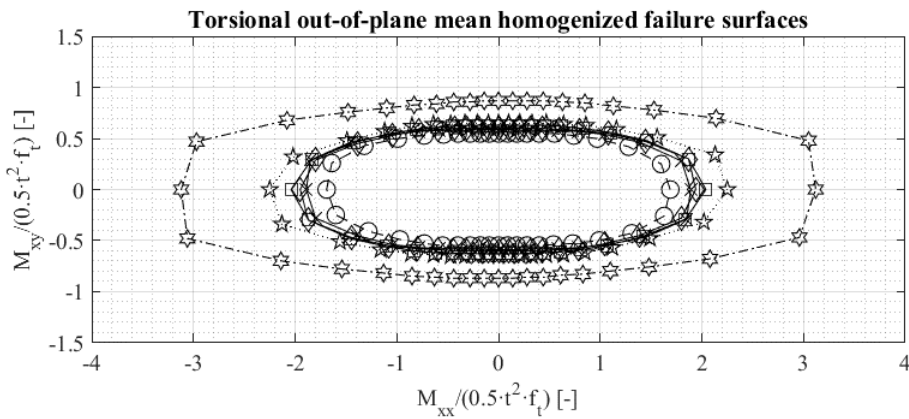
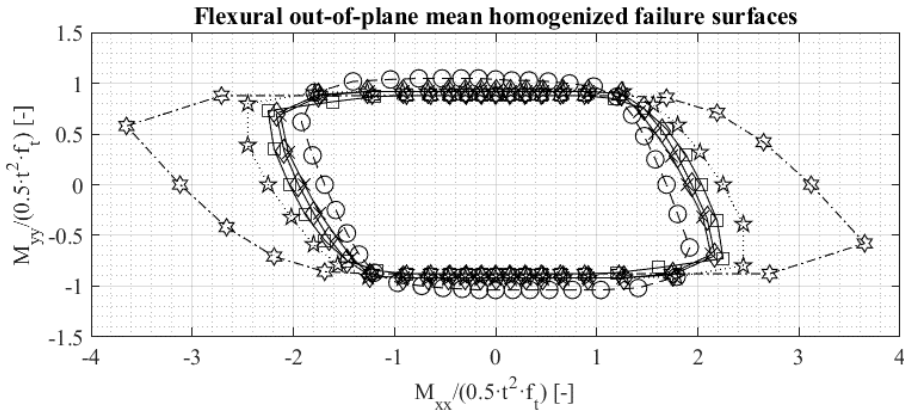
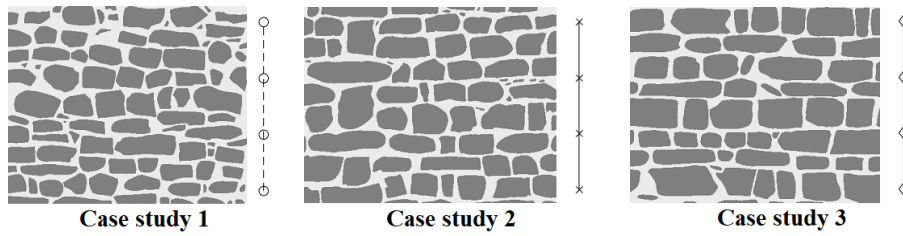


Fig. 5.31. Comparison of the flexural and torsional out-of-plane mean homogenized failure surfaces among the six case studies.

Some concluding remarks are here offered about the choice of a Kirchhoff-Love plate model for expressing the displacement rate field of the finite elements in this out-of-plane formulation. In fact, the Reissner-Mindlin model for thick plates could have been employed for a more accurate representation of the out-of-plane components in the displacement rate field. However, this would have implied the introduction of further unknowns in the overall problem - namely, the components of the average shear strain rate vector. This could have led to an increase of the computational burden for solving the standard-form linear programming problem. A relevant work published by Cecchi and co-workers [7] offers some insight into this issue. There, the authors consider a masonry wall clamped at its base, simply supported at the top, and subjected to a horizontal load distribution that is governed by a load multiplier. The masonry wall is then modeled with both the Kirchhoff-Love and the Reissner-Mindlin plate models, and provided with two different values of the wall's thickness (namely, 30 cm and 60 cm). It is then shown that, for the thinner wall, the discrepancy in terms of collapse load multiplier between the two plate models is negligible; conversely, the difference becomes more marked for the thicker wall. It must be considered that the six case studies presented in Section 5.3 display two different values for the wall's thickness, equal to 40 cm for the first four case studies and to 15 cm for the last two of them. In both cases, there is no doubt that using a Kirchhoff-Love plate model is totally justifiable: this is especially true for the smaller value of thickness here considered, but surely holds also for the other value. Therefore, the Kirchhoff-Love plate model can be deemed as a realistic choice for modeling the out-of-plane behavior of masonry walls when the value of their thickness is reasonably small.

5.5 References

- [1] MATLAB Release 2018b, The MathWorks, Inc., Natick, Massachusetts, United States.
- [2] Sloan, S. W., & Kleeman, P. W. (1995). Upper bound limit analysis using discontinuous velocity fields. *Computer Methods in Applied Mechanics and Engineering*, 127(1-4), 293-314.
- [3] Milani, G., & Taliencio, A. (2015). In-plane failure surfaces for masonry with joints of finite thickness estimated by a method of cells-type approach. *Computers & Structures*, 150, 34-51.

-
- [4] Milani, G., & Taliervo, A. (2016). Limit analysis of transversally loaded masonry walls using an innovative macroscopic strength criterion. *International Journal of Solids and Structures*, 81, 274-293.
- [5] Cecchi, A., & Milani, G. (2008). A kinematic FE limit analysis model for thick English bond masonry walls. *International Journal of Solids and Structures*, 45(5), 1302-1331.
- [6] Milani, G., Lourenço, P. B., & Tralli, A. (2006). Homogenised limit analysis of masonry walls, Part I: Failure surfaces. *Computers & structures*, 84(3-4), 166-180.
- [7] Cecchi, A., Milani, G., & Tralli, A. (2007). A Reissner–Mindlin limit analysis model for out-of-plane loaded running bond masonry walls. *International Journal of Solids and Structures*, 44(5), 1438-1460.

3D HOMOGENIZED LIMIT ANALYSIS OF THREE-LEAF NON-PERIODIC MASONRY

As already hinted at in the introductory section of the previous chapter, the out-of-plane analysis at collapse of single-leaf masonry walls is a very important topic because it directly addresses one of the most vulnerable spots of such walls. However, the architectural heritage of several European countries consists also of multi-leaf walls [1]. This type of masonry walls is structured as follows: two external layers (or wythes) of masonry are erected, leaving an in-between void that is usually thinner than the two outer layers; this is later filled with loose material such as stone chips, or with low quality mortar. Multi-leaf walls are often characterized by a rate of transversal interconnection that is either very poor or wholly absent most of the times; this entails an insufficient resistance against out-of-plane actions.

As shown in Section 2.4.1, almost no papers have dealt with the study of multi-leaf masonry walls so far, due to the complexity that is typical of this kind of walls, therefore it is very difficult to employ micro- or macro-modelling approaches. In general, these walls are characterized by peculiar geometries and units' arrangements that make each of them a unique instance; an extremely refined analytical model at the microscale is then required, which would make any numerical analysis very cumbersome and computationally unfeasible. On the other hand, it is also very difficult to properly investigate the mechanical properties of the masonry constituents in these walls, not to mention the impossibility to run extensive and effective experimental tests, thus ruling out any possibility of defining a reliable macroscale model for such kind of masonry. Eventually, assessing the actual rate of transversal interconnection between adjacent layers represents another delicate issue to be addressed for these walls.

The pairing of homogenization and limit analysis seems to offer once more an acceptable solution to all the aforementioned issues; this is especially true when considering the fact that in many cases it is paramount to only assess the out-of-plane behavior at collapse of these walls in a swift and straightforward way, and limit analysis with a homogenized approach is potentially a very powerful tool in this sense.

Regarding the contents of this chapter, Section 6.1 describes the modifications implemented in the out-of-plane upper bound limit analysis problem with homogenization that are needed to account for the presence of multiple wythes in the non-periodic masonry wall. Section 6.2 presents two case studies, derived from the real single-leaf non-periodic masonry walls previously investigated; namely, a three-leaf rubble masonry wall and a three-leaf quasi-regular masonry wall are considered. For the latter case, the influence of transversal interconnection on the global out-of-plane collapse behavior is also assessed. Section 6.3 offers some concluding remarks on the results found in the previous section.

6.1 Problem Formulation

This section presents the mathematical formulation of the problem that aims at deriving out-of-plane homogenized failure surfaces for multi-leaf masonry walls, which consist of two or more wythes. This requires the definition of a kinematic model that accounts for the presence of these different layers. In fact, the main difference with respect to the single-leaf formulation lies in the definition of separate average strain rate tensors for each wythe; conversely, the average curvature rate tensor is still unique for all the wythes. This modification is enforced to reproduce separate in-plane behaviors for each wythe, as is usually the case in multi-leaf walls where the wythes are not so well connected; the use of a single average curvature rate tensor for all the wythes instead represents a simplification of the out-of-plane behavior, for which the multiple wythes cannot bend differently with respect to each other, therefore removing the possibility of disconnection between the wythes along the out-of-plane direction (in this case, axis Z). Even though multi-leaf walls in general do not behave as a sandwich structures, it is also well known that their inner core usually consists of either loose materials such as stone chips or materials that display poor mechanical properties. Therefore, it is totally reasonable to suppose that there is no actual contact between the outer wythes and the inner core, which justifies the simplifications adopted in the present formulation.

The difference between the single- and multi-leaf formulation is displayed in Fig. 6.1, where the macroscopic quantities involved in each case are highlighted.

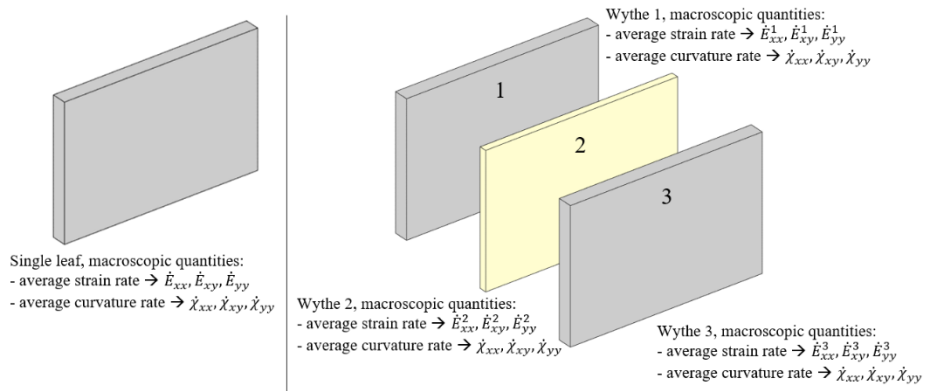


Fig. 6.1. Difference in terms of macroscopic quantities between the single-leaf (left) and multi-leaf case (right).

Since each element of the multi-leaf wall is rigid and bereft of rotation rate, its kinematics is fully determined by the displacement rate field of its centroid $\{\dot{u}_x, \dot{u}_y, \dot{u}_z\}$, where axis Z represents the transversal direction. The use of a Kirchhoff-Love plate model leads to the following expressions for the three components of the displacement rate field, written for each wythe in the general case of a three-leaf masonry wall:

$$\dot{u}_x = \dot{u}_{x,per} + \dot{E}_{xx}^1 x_G + \dot{E}_{xy}^1 y_G + \dot{\chi}_{xx} z_G x_G + 0.5 \dot{\chi}_{xy} z_G y_G \quad (6.1)$$

$$\dot{u}_y = \dot{u}_{y,per} + \dot{E}_{xy}^1 x_G + \dot{E}_{yy}^1 y_G + \dot{\chi}_{yy} z_G y_G + 0.5 \dot{\chi}_{xy} z_G x_G \quad (6.2)$$

$$\dot{u}_z = \dot{u}_{z,per} - 0.5 \dot{\chi}_{xx} x_G^2 - 0.5 \dot{\chi}_{yy} y_G^2 - 0.5 \dot{\chi}_{xy} x_G y_G \quad (6.3)$$

$$\dot{u}_x = \dot{u}_{x,per} + \dot{E}_{xx}^2 x_G + \dot{E}_{xy}^2 y_G + \dot{\chi}_{xx} z_G x_G + 0.5 \dot{\chi}_{xy} z_G y_G \quad (6.4)$$

$$\dot{u}_y = \dot{u}_{y,per} + \dot{E}_{xy}^2 x_G + \dot{E}_{yy}^2 y_G + \dot{\chi}_{yy} z_G y_G + 0.5 \dot{\chi}_{xy} z_G x_G \quad (6.5)$$

$$\dot{u}_z = \dot{u}_{z,per} - 0.5 \dot{\chi}_{xx} x_G^2 - 0.5 \dot{\chi}_{yy} y_G^2 - 0.5 \dot{\chi}_{xy} x_G y_G \quad (6.6)$$

$$\dot{u}_x = \dot{u}_{x,per} + \dot{E}_{xx}^3 x_G + \dot{E}_{xy}^3 y_G + \dot{\chi}_{xx} z_G x_G + 0.5 \dot{\chi}_{xy} z_G y_G \quad (6.7)$$

$$\dot{u}_y = \dot{u}_{y,per} + \dot{E}_{xy}^3 x_G + \dot{E}_{yy}^3 y_G + \dot{\chi}_{yy} z_G y_G + 0.5 \dot{\chi}_{xy} z_G x_G \quad (6.8)$$

$$\dot{u}_z = \dot{u}_{z,per} - 0.5 \dot{\chi}_{xx} x_G^2 - 0.5 \dot{\chi}_{yy} y_G^2 - 0.5 \dot{\chi}_{xy} x_G y_G \quad (6.9)$$

As previously stated, the only changes between Eqs. (5.1) to (5.3) and (6.1) to (6.15) are enforced in the components of the average strain rate tensor, whose number is here equal to 9 $\{\dot{E}_{xx}^1, \dot{E}_{xy}^1, \dot{E}_{yy}^1, \dot{E}_{xx}^2, \dot{E}_{xy}^2, \dot{E}_{yy}^2, \dot{E}_{xx}^3, \dot{E}_{xy}^3, \dot{E}_{yy}^3\}$ instead of the only 3 components originally included in the single-leaf formulation.

Eqs. (5.4) to (5.7) are updated as well to reflect these changes. It must be noted that these equations refer to interfaces that are orthogonal to axes X and Y: the involved adjacent finite elements then do belong to the same layer. Eq. (5.14) is now recalled: it expresses the matrix formulation of the constraints related to the velocity jumps and plastic dissipation, written for interface I between elements i and j and orthogonal to axis X. Supposing that these elements belong to the 1st wythe of a three-leaf wall, the equation is updated as follows:

$$\begin{aligned}
& \begin{bmatrix} 1 & -1 & 0 & 0 \\ 0 & 0 & 1 & -1 \end{bmatrix} \begin{bmatrix} \dot{u}_{x,per}^j \\ \dot{u}_{x,per}^i \\ \dot{u}_{y,per}^j \\ \dot{u}_{y,per}^i \end{bmatrix} + \begin{bmatrix} -\tan \phi & -\tan \phi & -1 & 1 \\ -1 & 1 & 0 & 0 \end{bmatrix} \begin{bmatrix} \lambda_l^1 \\ \lambda_l^2 \\ \lambda_l^3 \\ \lambda_l^4 \end{bmatrix} + \\
& + \begin{bmatrix} (x_G^j - x_G^i) & 0 & 0 & 0 & 0 & 0 & 0 & 0 & 0 & (z_G^j x_G^j - z_G^i x_G^i) & 0 & 0 \\ 0 & 0 & (x_G^j - x_G^i) & 0 & 0 & 0 & 0 & 0 & 0 & 0 & 0.5(z_G^j x_G^j - z_G^i x_G^i) \end{bmatrix} \begin{bmatrix} \dot{E}_{xx}^1 \\ \dot{E}_{yy}^1 \\ \dot{E}_{xy}^1 \\ \dot{E}_{xx}^2 \\ \dot{E}_{yy}^2 \\ \dot{E}_{xy}^2 \\ \dot{E}_{xx}^3 \\ \dot{E}_{yy}^3 \\ \dot{E}_{xy}^3 \\ \dot{\chi}_{xx} \\ \dot{\chi}_{yy} \\ \dot{\chi}_{xy} \end{bmatrix} = \\
& = \begin{bmatrix} 0 \\ 0 \end{bmatrix}
\end{aligned} \tag{6.10}$$

Hence, vector $\mathbf{\dot{D}}$ now contains the components of the average strain rate tensors pertaining to all the wythes, as well as the three independent components of the average curvature rate tensor.

Eqs. (5.20) to (5.22), which are related to the master-slave relations that link the kinematic field of a single finite element and that of the masonry unit to which it belongs, are updated as well:

$$\begin{aligned} \dot{u}_{x,per}^S - \dot{u}_{x,per}^M + \dot{\theta}_{yy}^M(z_G^M - z_G^S) + \dot{E}_{xx}^t(x_G^S - x_G^M) + \dot{E}_{xy}^t(y_G^S - y_G^M) + \\ + \dot{\chi}_{xx}(z_G^S x_G^S - z_G^M x_G^M) + 0.5 \dot{\chi}_{xy}(z_G^S y_G^S - z_G^M y_G^M) = 0 \end{aligned} \quad (6.11)$$

$$\begin{aligned} \dot{u}_{y,per}^S - \dot{u}_{y,per}^M + \dot{\theta}_{xx}^M(z_G^S - z_G^M) + \dot{E}_{xy}^t(x_G^S - x_G^M) + \dot{E}_{yy}^t(y_G^S - y_G^M) + \\ + \dot{\chi}_{yy}(z_G^S y_G^S - z_G^M y_G^M) + 0.5 \dot{\chi}_{xy}(z_G^S x_G^S - z_G^M x_G^M) = 0 \end{aligned} \quad (6.12)$$

$$\begin{aligned} \dot{u}_{z,per}^S - \dot{u}_{z,per}^M + \dot{\theta}_{xx}^M(y_G^M - y_G^S) + \dot{\theta}_{yy}^M(x_G^S - x_G^M) + \\ + 0.5 \dot{\chi}_{xx}[(x_G^M)^2 - (x_G^S)^2] + 0.5 \dot{\chi}_{yy}[(y_G^M)^2 - (y_G^S)^2] + \\ + 0.5 \dot{\chi}_{xy}(x_G^M y_G^M - x_G^S y_G^S) = 0 \end{aligned} \quad (6.13)$$

No modifications are needed by the constraints related to the periodicity of the velocity field at the boundaries. Conversely, Eq. (5.28) - which expresses the normalization of the dissipated external power - needs to be modified as well:

$$\begin{aligned} P^{ext} = \Sigma_{xx} \dot{E}_{xx}^1 + \Sigma_{yy} \dot{E}_{yy}^1 + \Sigma_{xy} \dot{E}_{xy}^1 + (\dots) + \Sigma_{xx} \dot{E}_{xx}^n + \Sigma_{yy} \dot{E}_{yy}^n + \Sigma_{xy} \dot{E}_{xy}^n + \\ + M_{xx} \dot{\chi}_{xx} + M_{yy} \dot{\chi}_{yy} + M_{xy} \dot{\chi}_{xy} = 1 \end{aligned}$$

$$\begin{aligned} P^{ext} = \Sigma_{xx} \sum_{t=1}^n \dot{E}_{xx}^t + \Sigma_{yy} \sum_{t=1}^n \dot{E}_{yy}^t + \Sigma_{xy} \sum_{t=1}^n \dot{E}_{xy}^t + \\ + M_{xx} \dot{\chi}_{xx} + M_{yy} \dot{\chi}_{yy} + M_{xy} \dot{\chi}_{xy} = 1 \end{aligned} \quad (6.14)$$

Eventually, the homogenized limit analysis problem is once more formulated as a linear programming problem. The objective function that ought to be minimized is still the dissipated internal power as expressed in Eq. (5.33), and the equality constraints are still given by Eqs. (5.16), (5.23), (5.27), and (5.29), provided that they include the modifications introduced in Eqs. (6.10) to (6.14). In the usual standard form, the components of the average strain tensors are expressed as:

$$\dot{E}_{ij}^t = \dot{E}_{ij}^{t,+} - \dot{E}_{ij}^{t,-} \quad i, j = x, y \quad (6.15)$$

The standard form for this linear programming problem is:

$$\text{Minimize} \quad \mathbf{C}^T \mathbf{X} \quad (6.16)$$

$$\text{Subject to} \quad \mathbf{A} \mathbf{X} = \mathbf{B} \quad (6.17)$$

$$\mathbf{X} \geq \mathbf{0} \quad (6.18)$$

where

$$A = \begin{bmatrix} A_{11}^{eq} & -A_{11}^{eq} & 0 & 0 & A_{13}^{eq} & A_{14}^{eq} & -A_{14}^{eq} \\ A_{21}^{eq} & -A_{21}^{eq} & A_{22}^{eq} & -A_{22}^{eq} & 0 & A_{24}^{eq} & -A_{24}^{eq} \\ A_{31}^{eq} & -A_{31}^{eq} & 0 & 0 & 0 & 0 & 0 \\ 0 & 0 & 0 & 0 & 0 & A_{44}^{eq} & -A_{44}^{eq} \end{bmatrix} \quad (6.19)$$

$$X = \begin{bmatrix} \dot{u}_{per}^+ \\ \dot{u}_{per}^- \\ \dot{R}^+ \\ \dot{R}^- \\ \dot{\lambda}_{I,ass} \\ \dot{D}^+ \\ \dot{D}^- \end{bmatrix} \quad (6.20)$$

$$B = \begin{bmatrix} 0 \\ 0 \\ 0 \\ 1 \end{bmatrix} \quad (6.21)$$

$$C = \begin{bmatrix} 0 \\ 0 \\ 0 \\ 0 \\ C_{I,ass} \\ 0 \\ 0 \end{bmatrix} \quad (6.22)$$

6.2 Case Studies

Two multi-leaf case studies are investigated in terms of out-of-plane homogenized failure surfaces. The first case study deals with a three-leaf wall whose outer wythes consist of rubble masonry, while the second is represented by a three-leaf wall whose outer wythes consist of quasi-regular masonry. In the latter case, the influence of the transversal interconnection on the out-of-plane collapse behavior is also examined.

Two separate sets of mechanical parameters (cohesion, friction angle, tensile strength, and compressive strength) are employed in these case studies: one set is dedicated to simulate the properties of the outer wythes, where the mechanical parameters are equal to those assumed in Sections 4.2 and 5.3; the

other set is dedicated to simulate the properties of the inner wythe, which is supposed to consist of low quality mortar. Both sets are listed in Table 6.1.

Table 6.1

Mechanical properties for the material employed in all case studies.

Type of interface	Cohesion [MPa]	Friction angle [°]	Tensile strength [MPa]	Compressive strength [MPa]
Outer wythes	0.15	30	0.1	1.5
Mortar inner wythe	0.05	35	0.02	0.5

6.2.1 Case Study 1: Three-Leaf Rubble Masonry Wall

The first case study consists of a three-leaf wall whose outer wythes are rubble masonry walls. Two instances of such wall are created aiming at investigating how the possible presence of different rubble masonry bonds influences the out-of-plane response of a three-leaf wall: specifically, one is named “Instance 1” and considers test-window C of case study 1 (see Fig. 4.8 of Section 4.2.2) as the masonry bond for both outer wythes (Fig. 6.2a), whereas the other is named “Instance 2” and employs the previous masonry bond for a single wythe, considering instead test-window B of the same case study as the masonry bond for the opposite wythe (Fig. 6.2b). In both instances, a 5x5 coarsing strategy is employed to reduce the number of finite elements in the analytical models (Fig. 6.2c and Fig. 6.2d); the outer wythes are supposed to be 40 cm thick and the mortar inner one 15 cm thick. The 3D finite element meshes of the two instances are shown in Fig. 6.3 along with their exploded view: the outer wythes employ 16 finite elements over the thickness, while the mortar inner one employs 6 finite elements over the thickness.

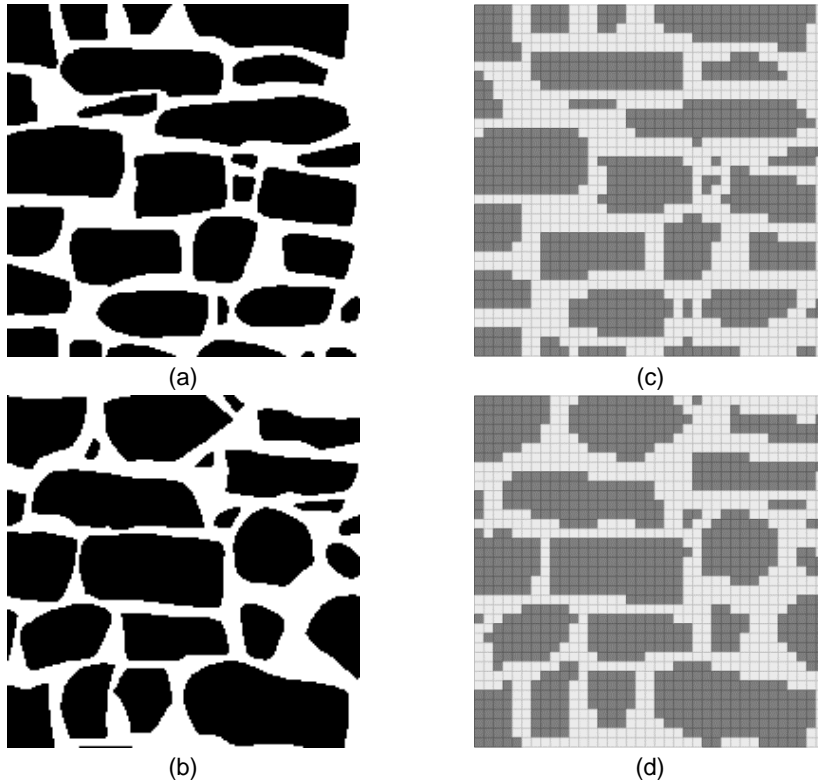


Fig. 6.2. (a) Test-window C of case study 1; (b) test-window B of case study 1; (c) in-plane configuration of both the outer wythes for Instance 1, and of one wythe of Instance 2; (d) in-plane configuration of the other outer wythe of Instance 2.

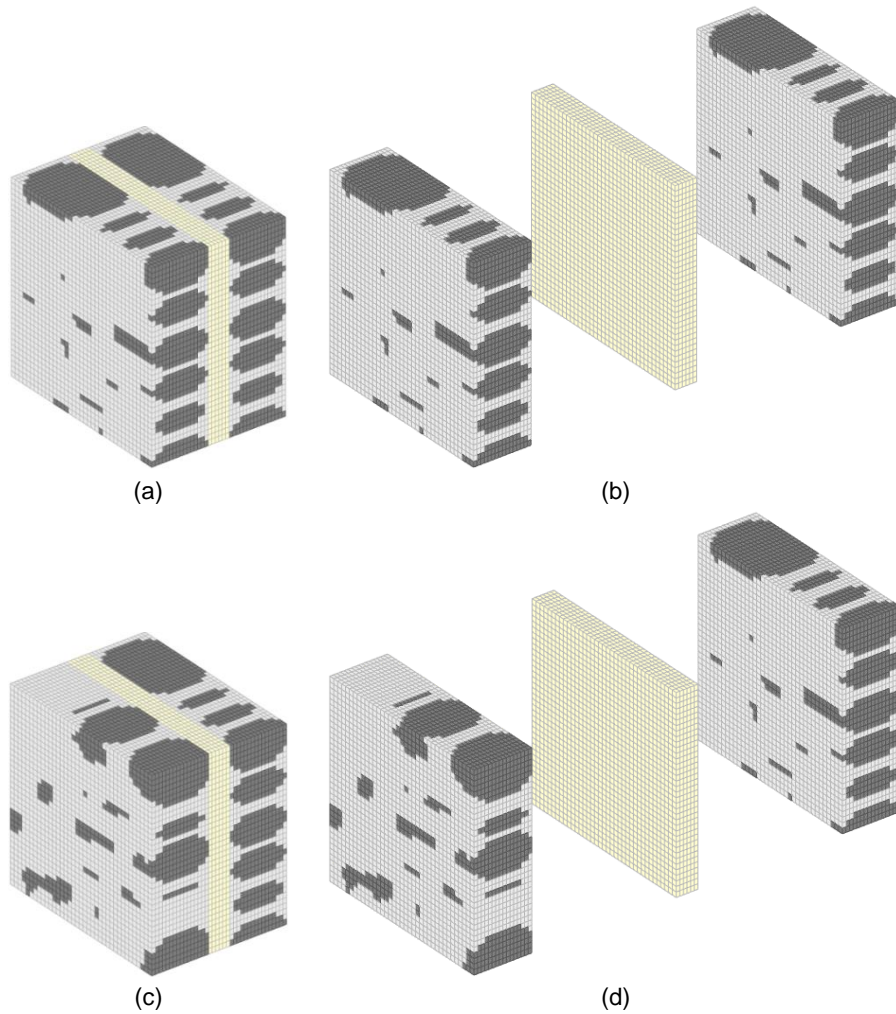


Fig. 6.3. First case study: (a) 3D finite element mesh for Instance 1; (b) exploded view of the 3D finite element mesh for Instance 1; (c) 3D finite element mesh for Instance 2; (d) exploded view of the 3D finite element mesh for Instance 2.

Fig. 6.4 shows the comparison between the two instances in terms of flexural and torsional out-of-plane homogenized failure surfaces. It is possible to observe that Instance 2 (the one with different rubble masonry bonds in the outer wythes) displays larger failure surfaces in both the flexural and torsional cases: this means that, when it comes to rubble masonry three-leaf walls, the presence of different bonds in the outer wythes somehow increases the out-of-plane resistance of the wall, probably due to the combined effect of the two different types of irregularity at the extremities.

The deformed shapes at collapse (“failure modes”) of the two instances of this case study are shown in Fig. 6.5, which come from the single application of M_{xx} , M_{yy} , and M_{xy} . The outcomes of both the out-of-plane homogenized failure surfaces are corroborated: in fact, it is possible to observe how Instance 2 shows less widespread crack patterns for all the applied moments, suggesting a more compact (and, in the end, stiffer) out-of-plane response with respect to Instance 1.

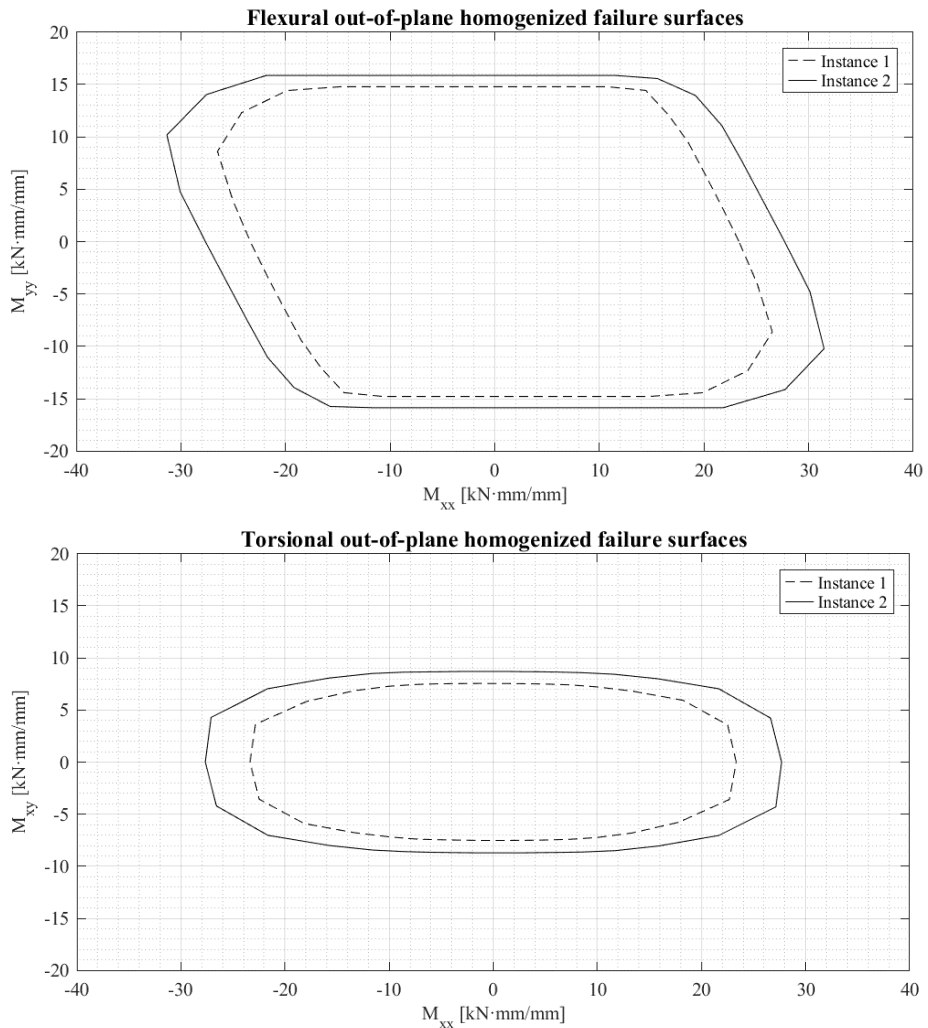


Fig. 6.4. Flexural and torsional out-of-plane homogenized failure surfaces for the two instances of the first case study.

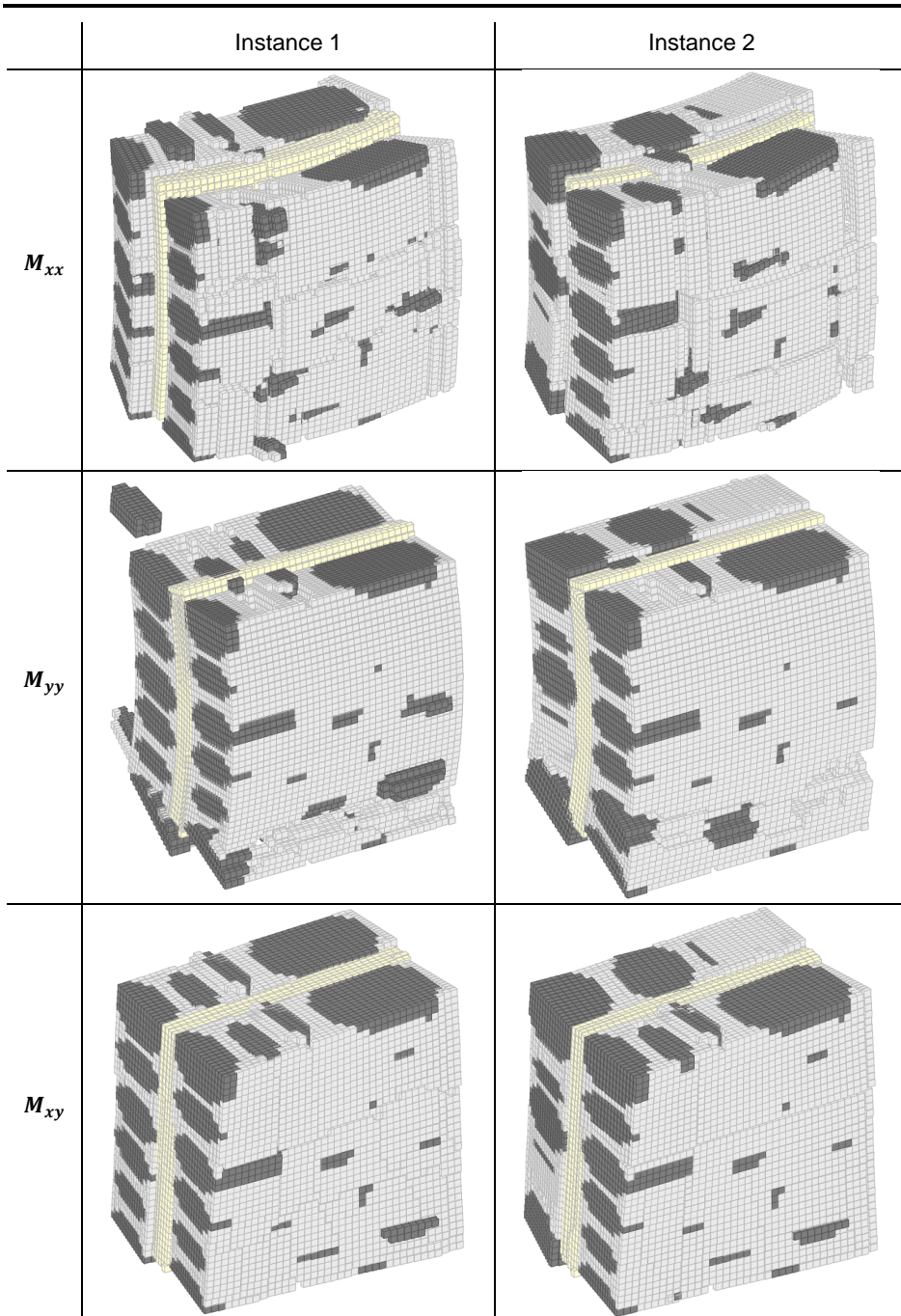


Fig. 6.5. Failure modes under M_{xx} , M_{yy} , and M_{xy} for the two instances of the first case study.

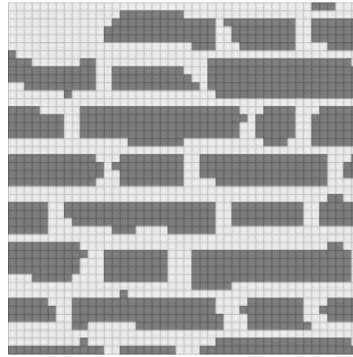
6.2.2 Case Study 2: Three-Leaf Quasi-Regular Masonry Wall

The second case study consists of a three-leaf wall whose outer wythes are quasi-regular masonry walls; also, two numerical applications are here considered. Analogously to the previous case, the first investigates how the possible presence of different quasi-regular masonry bonds influences the out-of-plane response of a three-leaf wall; the second aims at investigating the role of the possible presence of transversal bricks, which ensure interconnection between the outer wythes.

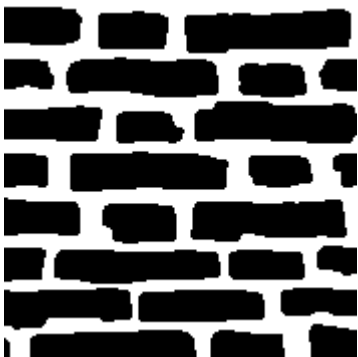
For the first numerical application, two instances of the quasi-regular three-leaf wall are created: specifically, one is named “Instance 1” and considers test-window C of case study 6 (see Fig. 4.38 of Section 4.2.7) as the masonry bond for the outer wythes (Fig. 6.6a), whereas the other is named “Instance 2” and employs the previous masonry bond for a single wythe, considering instead test-window B of the same case study as the masonry bond for the opposite wythe in this case (Fig. 6.6b). In both instances, a 4×4 coarsing strategy is employed to reduce the number of finite elements in the analytical model of the three-leaf wall (Fig. 6.6c and Fig. 6.6d); in this case, the outer wythes are supposed to be 15 cm thick and the inner one 6 cm thick. The 3D finite element meshes of the two instances are shown in Fig. 6.7 along with their exploded view: the outer wythes employ 7 finite elements over the thickness, while the mortar inner one employs 3 finite elements over the thickness.



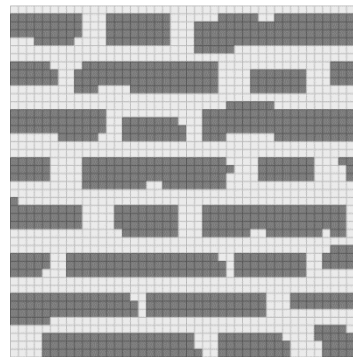
(a)



(c)



(b)



(d)

Fig. 6.6. (a) Test-window C of case study 6; (b) test-window B of case study 6; (c) in-plane configuration of both the outer wythes for Instance 1, and of one wythe of Instance 2; (d) in-plane configuration of the other outer wythe of Instance 2.

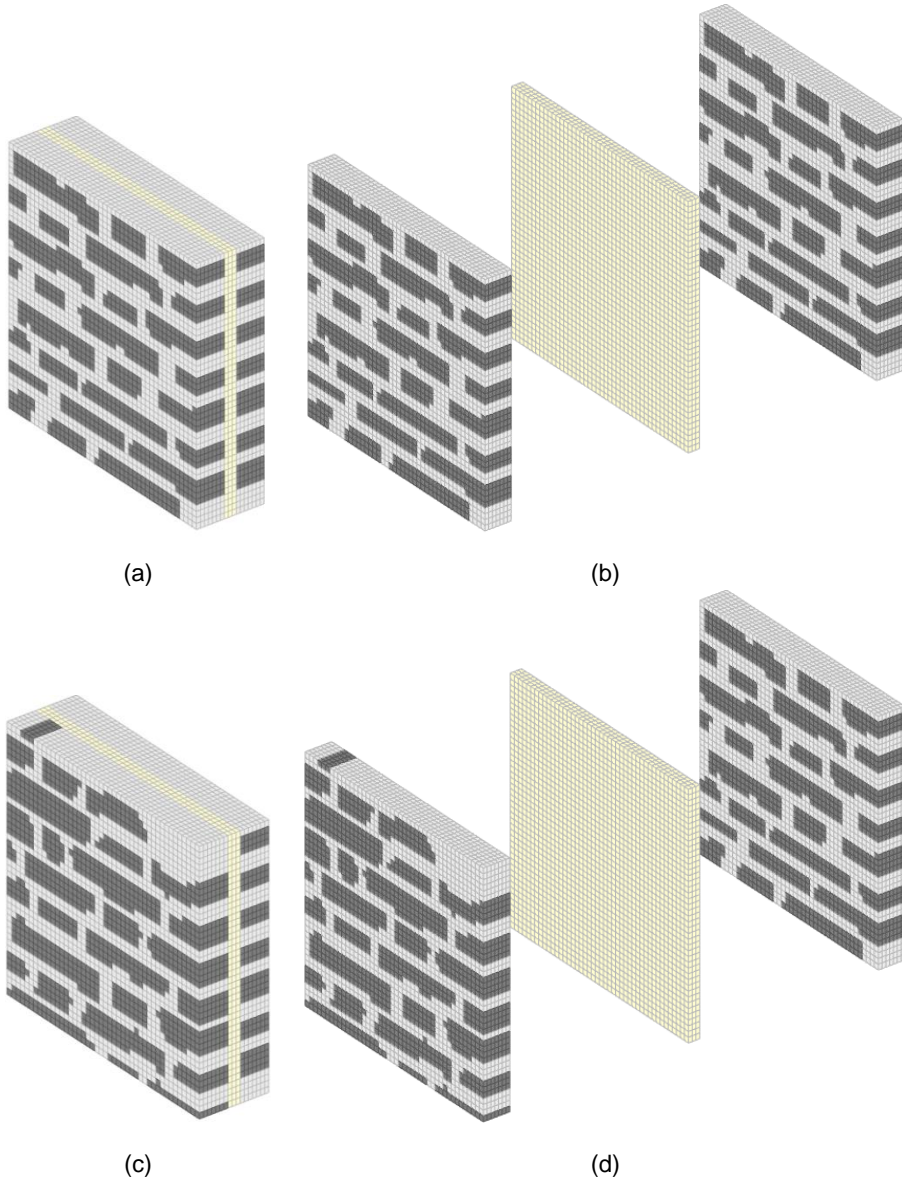


Fig. 6.7. Second case study, first numerical application: (a) 3D finite element mesh for Instance 1; (b) exploded view of the 3D finite element mesh for Instance 1; (c) 3D finite element mesh for Instance 2; (d) exploded view of the 3D finite element mesh for Instance 2.

Fig. 6.8 shows the comparison between the two instances in terms of flexural and torsional out-of-plane homogenized failure surfaces for this first numerical application. Unlike what shown in Section 6.2.1 for the previous case study, it is possible to observe that Instance 2 (the one with different quasi-regular masonry

bonds in the outer wythes) displays smaller failure surfaces in the torsional case. This may imply that, in case of a quasi-regular three-leaf wall, the presence of different bonds in the outer wythes actually decreases the torsional out-of-plane resistance of the wall, but this should be more deeply investigated in further studies regarding multi-leaf walls. Nonetheless, it must be considered that one of the two outer wythes here presents a widespread portion of mortar in one of its corners, which may have an effect in the final torsional response of the three-leaf wall.

The deformed shapes at collapse (“failure modes”) of the two instances of this first numerical application are shown in Fig. 6.9, which come from the single application of M_{xx} , M_{yy} , and M_{xy} . It is very easy to observe that Instance 2 shows more widespread cracks for all the applied moments, which further proves its lower resistance to out-of-plane actions (albeit rather slight).

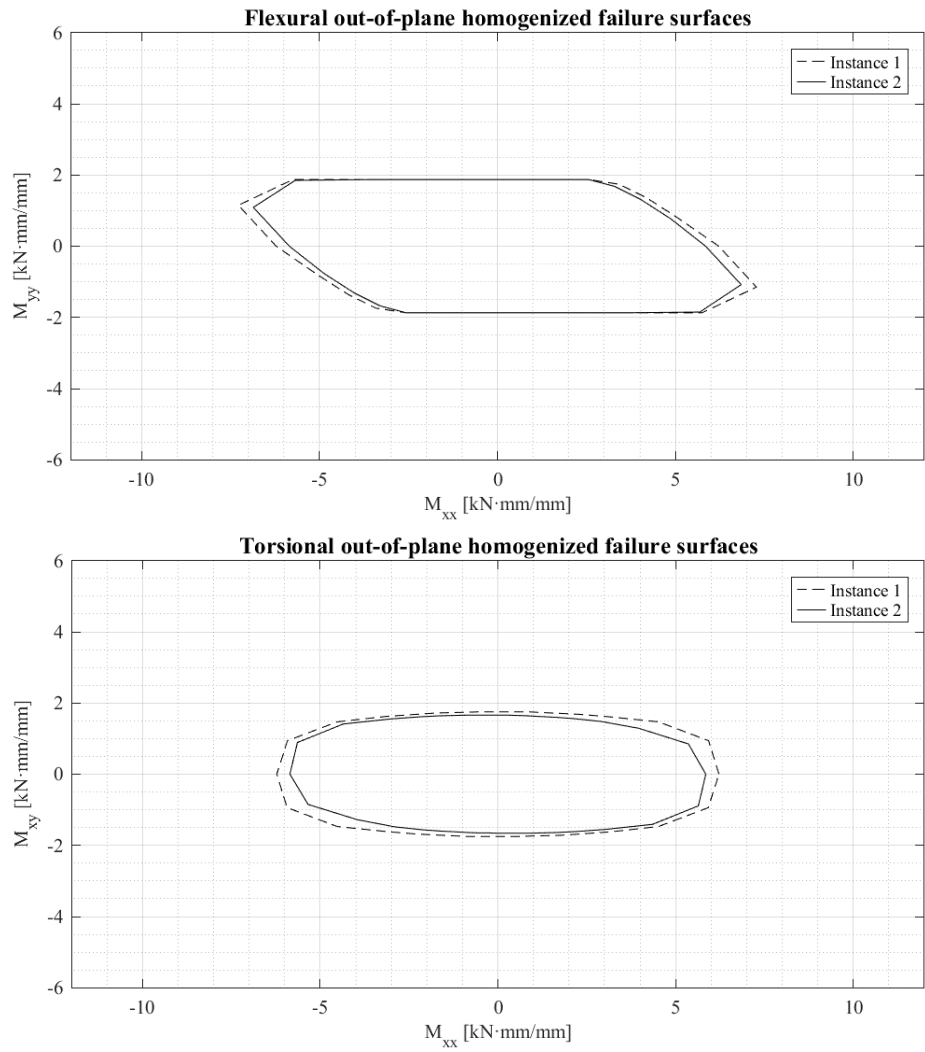


Fig. 6.8. Flexural and torsional out-of-plane homogenized failure surfaces for the two instances of the first numerical application of the second case study.

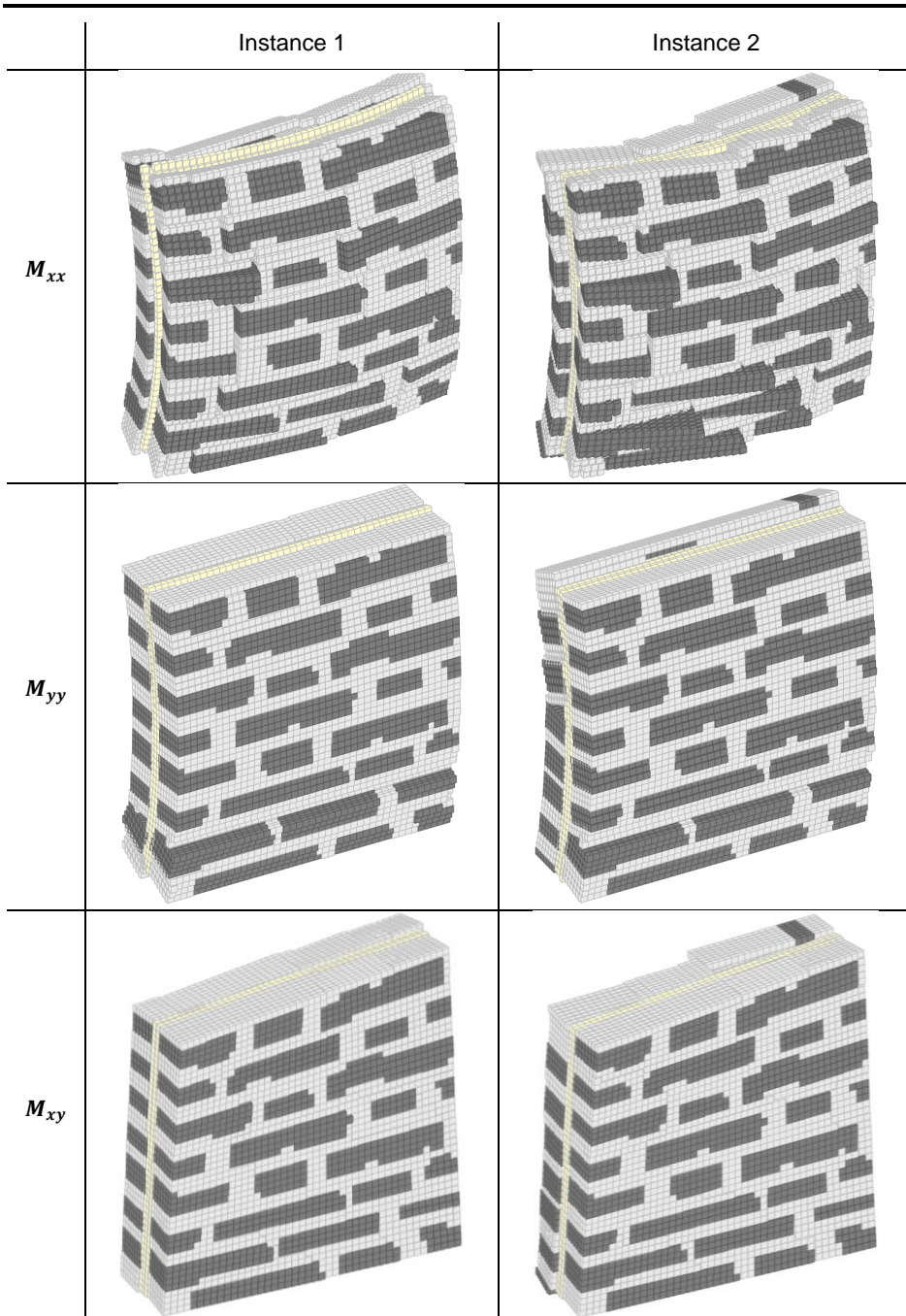


Fig. 6.9. Failure modes under M_{xx} , M_{yy} , and M_{xy} for the two instances of the first numerical application of the second case study.

The second numerical application of this case study considers two other instances of the quasi-regular three-leaf wall. Specifically, one is the Instance 1 coming from the first numerical application, here representing the case where the mutual interaction between the three wythes is supposed to be null (i.e. with the absence of transversal bricks): this mirrors a common case in multi-leaf walls, where the transversal interconnection is very often nonexistent [2]. Conversely, the other instance (here named “Instance 3”) is a slight modification of Instance 1 and assumes the presence of some transversal bricks that span the whole thickness of the three-leaf wall. This is a rarer occurrence in real multi-leaf walls, but it can be observed in some examples where the expertise in erecting this type of wall was state-of-the-art and, likely, heavily influenced by the experience of past seismic events that taught valuable lessons on how to ensure a tight out-of-plane behavior of the walls. The 3D finite element mesh for Instance 3 is shown in Fig. 6.10 along with its exploded view; it is possible to observe that some of the bricks are extended over the whole transversal length of the quasi-regular three-leaf wall. Once more, the outer wythes employ 7 finite elements over the thickness, while the inner one employs 3 finite elements over the thickness.

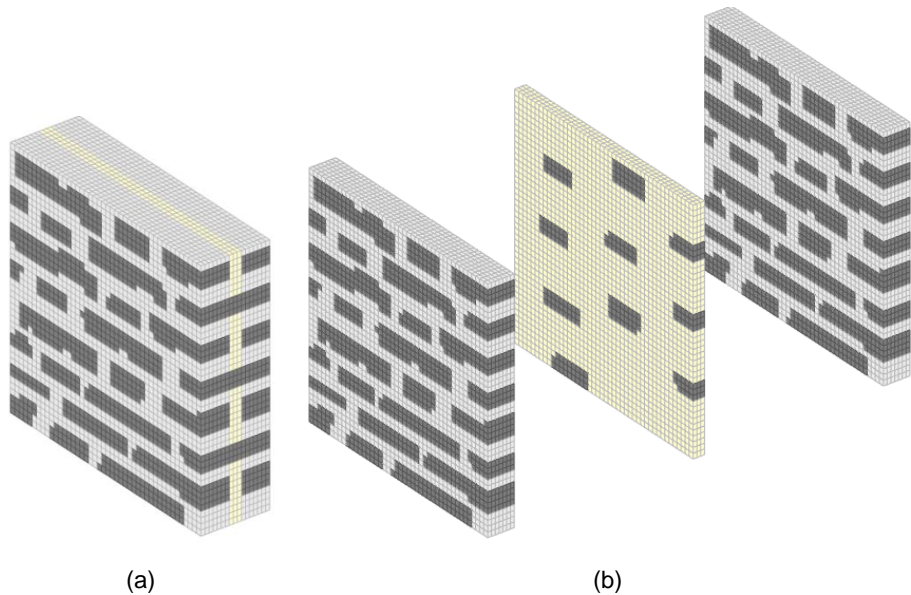


Fig. 6.10. (a) 3D finite element mesh for Instance 3; (b) exploded view of the 3D finite element mesh for Instance 3.

Fig. 6.11 shows the comparison between the two instances in terms of flexural and torsional out-of-plane homogenized failure surfaces for this second

numerical application. It is possible to observe that Instance 3 (the one with the presence of transversal bricks) displays larger failure surfaces: this means that in cases where multi-leaf walls are provided with a good transversal interconnection between the outer wythes, their out-of-plane collapse behavior greatly improves. In this specific case, it is possible to see how the beneficial effect due to the presence of the transversal bricks provides the considered wall with a collapse value of M_{yy} that is doubled with respect to the previous case that presents no transversal interconnection. The collapse value of M_{xx} and M_{xy} increase as well: in fact, a fair transversal interconnection as the one given in this case is enough to stiffen the wall.

This is further confirmed by the deformed shapes at collapse (“failure modes”) of the two instances coming from the single application of M_{xx} , M_{yy} , and M_{xy} , which are shown in Fig. 6.12. In particular, for M_{xx} and M_{xy} it is possible to observe how the presence of transversal bricks gives an overall tightening of the three-leaf wall; moreover, for M_{yy} the failure mode changes completely, since in Instance 1 a single, wide crack appears across a bed joint in the lower part of the three-leaf wall, whereas in Instance 3 the crack pattern is more widespread over the wall.

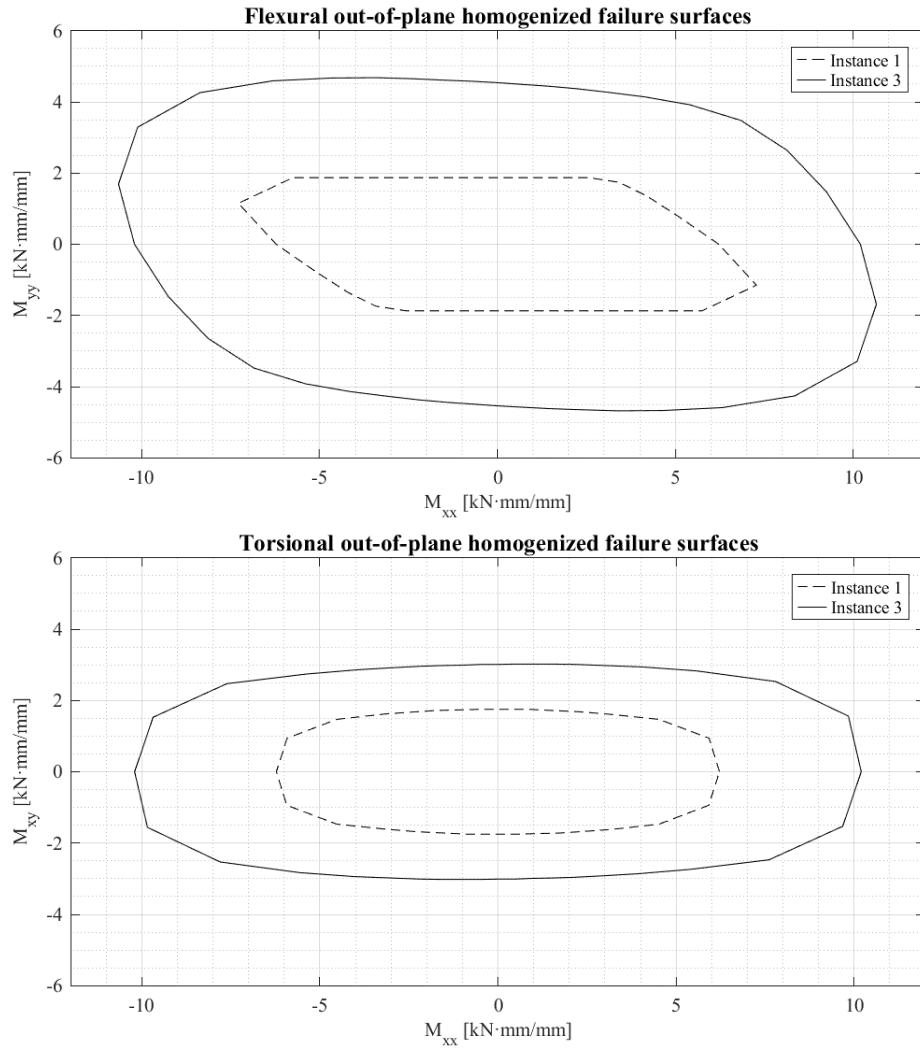


Fig. 6.11. Flexural and torsional out-of-plane homogenized failure surfaces for the two instances of the second numerical application of the second case study.

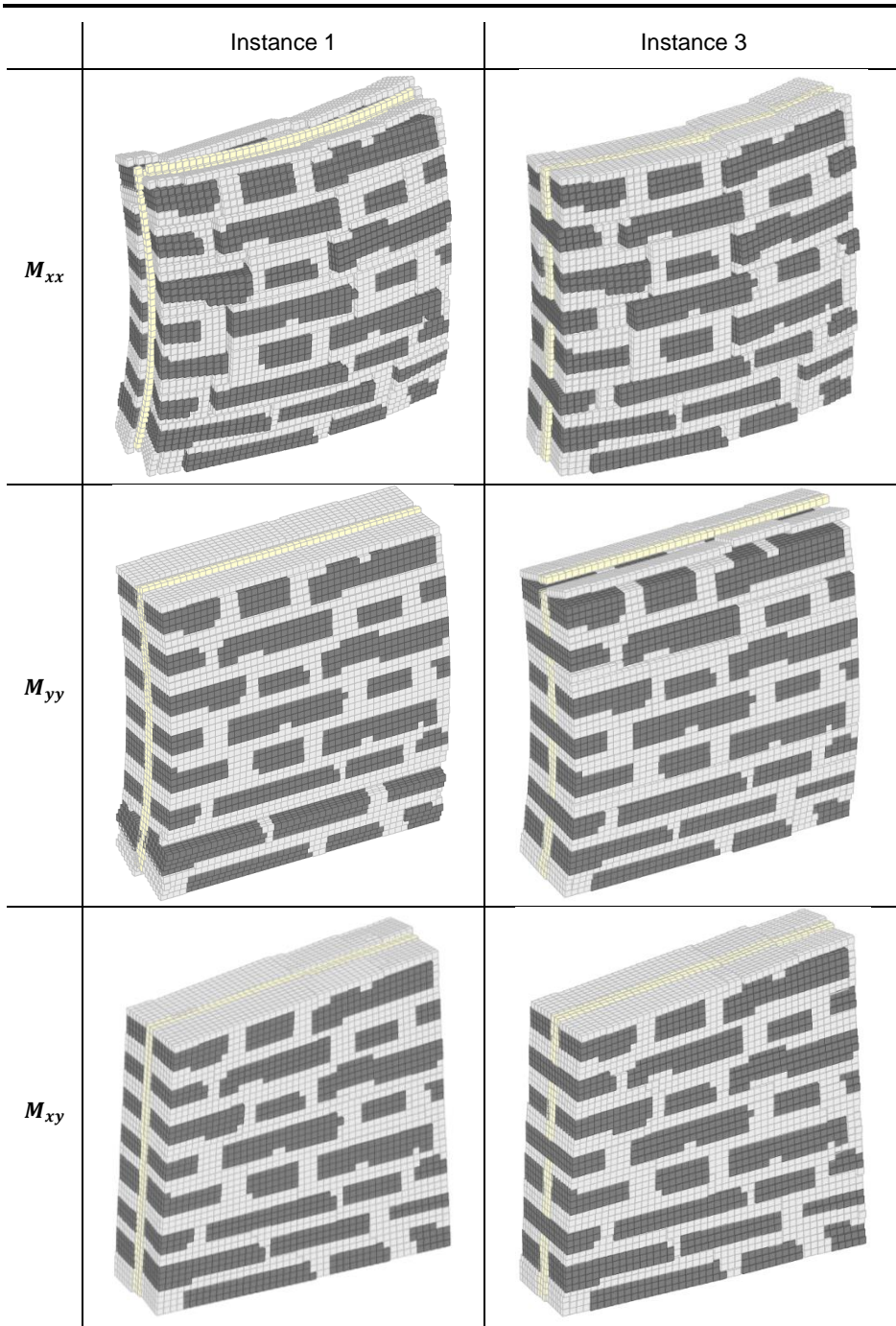


Fig. 6.12. Failure modes under M_{xx} , M_{yy} , and M_{xy} for the two instances of the second numerical application of the second case study.

6.3 Conclusions

This chapter has presented an investigation on two case studies involving three-leaf masonry walls, the first consisting of a rubble masonry wall and the second a quasi-regular wall. For both case studies, the effects due to the possible presence of separate but similar masonry bonds in the outer wythes have been investigated; in the second case study, the influence of the transversal interconnection has also been inquired. The results are very interesting and show that, for a rubble three-leaf masonry wall, the presence of two different wythes increases the out-of-plane response of the wall both under flexural and torsional actions. Conversely, for a quasi-regular three-leaf masonry wall the presence of two different wythes decreases the out-of-plane response of the wall, albeit to a lesser extent than in the previous case. Eventually, the beneficial effects of a good transversal interconnection between the outer wythes - usually brought by the presence of transversal bricks - are confirmed by the numerical results both in terms of out-of-plane homogenized failure surfaces and of deformed shapes at collapse.

6.4 References

- [1] Ramalho, M. A., Taliercio, A., Anzani, A., Binda, L., & Papa, E. (2008). A numerical model for the description of the nonlinear behaviour of multi-leaf masonry walls. *Advances in Engineering Software*, 39(4), 249-257.
- [2] Casolo, S., & Milani, G. (2013). Simplified out-of-plane modelling of three-leaf masonry walls accounting for the material texture. *Construction and Building Materials*, 40, 330-351.

CHAPTER 7

CONCLUSIONS

This concluding chapter is meant to provide the author's thought about possible future developments of work presented in this PhD thesis. Before tackling the contents of the following sections, it must be remarked that all the results reported in previous chapters are purely numerical, albeit the case studies are extracted from real non-periodic masonry buildings. Indeed, a thorough validation of the proposed model against experimental data would surely give support to its overall effectiveness and reliability. However, it must be noted that experimental data in terms of collapse loads for non-periodic masonry are very scarce, and are usually only a small part of broader investigations that go beyond the simple characterization of the experimental collapse behavior of non-periodic masonry (see for instance Gattesco & Boem [1] as well as Gattesco and co-workers [2]). Nonetheless, a modest proposal for an immediate follow-up of this PhD thesis is the execution of an experimental campaign oriented to studying the collapse behavior of non-periodic masonry, whose results can subsequently be used for a validation of the proposed model.

Regarding the contents of this chapter, Section 7.1 presents a proposal regarding the conception of a model solely devoted to the homogenized limit analysis of non-periodic multi-leaf walls, whereas Section 7.2 describes a proposal regarding the creation of a MATLAB app provided with a GUI, whose goal is to undertake all the numerical steps needed for the homogenized limit analysis investigation on non-periodic masonry.

7.1 Comprehensive Study of the Collapse Behavior of Multi-Leaf Walls

The results presented in Chapter 6 concerning the out-of-plane collapse behavior non-periodic multi-leaf walls focus on two case studies that do not correspond to existing buildings. They merely represent an interesting example of the potential provided by the proposed homogenization-limit analysis model. However, as discussed in the introduction of the aforementioned chapter, multi-leaf walls are a common feature of the local architectural heritage in several European countries; many Italian regions also host widespread instances of non-periodic multi-leaf masonry walls, especially in areas rather prone to earthquakes. Considering the high seismic vulnerability of walls built with this construction technique, the correct assessment of their collapse behavior is of utmost importance. Unfortunately, in historical masonry buildings the presence of multi-leaf walls is only revealed after the local or global failure of the structure due to an earthquake, as shown in Fig. 7.1 where two interesting cases are considered. On the left, it is possible to observe the ejection of the external wythe caused by the seismic action; while in this case the building is still standing, this occurrence is often the prelude to the partial or even total collapse of the construction. On the right, it is possible to observe that the inner layer of the multi-leaf wall is basically absent, suggesting a total lack of transversal interconnection between the outer wythes.



Fig. 7.1. Multi-leaf walls in two buildings located in Accumoli (RI), revealed after the collapse of the façade due to the 2016 Central Italy earthquake.

Therefore, one future development of the work presented in this PhD thesis should be the creation of a model solely devoted to studying non-periodic multi-leaf walls, which must consider all their features. Specifically, this development should follow these propositions:

- The basic mathematical formulation of the problem should be the same, or at least very similar, to that proposed in Section 6.1.
- A needed modification of the aforementioned formulation should be devoted to actually represent the multiple wythes of the multi-leaf wall. In fact, choosing the same curvature for all the wythes is a simplification that proves to be useful in many cases; however, the proposed modification should consider each wythe as a single body. This is required to represent real occurrences in multi-leaf walls such as the ejection of the external wythe.
- The actual rate of transversal interconnection should also be featured in the modified formulation. This entails a twofold implementation:
 - One in the MATLAB function for the creation of the 3D finite element mesh: the script should be provided with an automated procedure that recognizes the presence of transversal units, along with their shape and dimensions.
 - One in the equality constraint coming from velocity jumps and plastic dissipation. Namely, the mutual interfaces of adjacent elements belonging to distinct wythes should be able to dissipate also in the out-of-plane direction. This is equivalent in stating that each wythe of the multi-leaf wall is considered as a single Kirchhoff-Love plate, and the wall itself consists of several plates that are assembled together.
- An alternative to the latter proposition could be a more radical modification of the mathematical formulation, considering the multi-leaf wall as a single Reissner-Mindlin plate. In this case, some simplifications in terms of dissipation between adjacent interfaces could also be enforced.

7.2 Development of GUI-Based MATLAB App for Homogenized Limit Analysis of Non-Periodic Masonry

The methodology developed in this PhD thesis is built upon the idea of providing an instrument for assessing the in- and out-of-plane collapse behavior of non-periodic masonry. To this end, a standard-form linear programming problem is devised, which represents the numerical implementation of an upper bound limit analysis problem coupled with a homogenization approach. Among the main innovations of the proposed methodology, the possibility to generate a 2D or 3D finite element mesh from the rasterized sketch of a generic masonry element must surely be highlighted.

It can be noted that all the stages of the proposed methodology are implemented in MATLAB, the most prominent and versatile numerical computing environment available for academic purposes. The latest releases of this software (including R2018b, the one used for the numerical applications of this PhD thesis [3]) contain an App Designer; this is a self-contained program that enables the creation of an app and a related Graphical User Interface (GUI) where all the needed interactive controls are displayed.

The proposed methodology follows a series of steps (the dark grey regions and arrows of Fig. 7.2) that are performed consequentially and logically: first, the 2D or 3D finite element mesh is created from the rasterized sketch of a source image representing a generic (non-periodic) masonry structural element. Then, the resulting mesh is used as a basis for the subsequent in- or out-of-plane homogenized limit analysis, from which the in- or out-of-plane failure surfaces are extracted as well as relevant deformed shapes at collapse (or, failure modes) for single in- or out-of-plane load conditions.

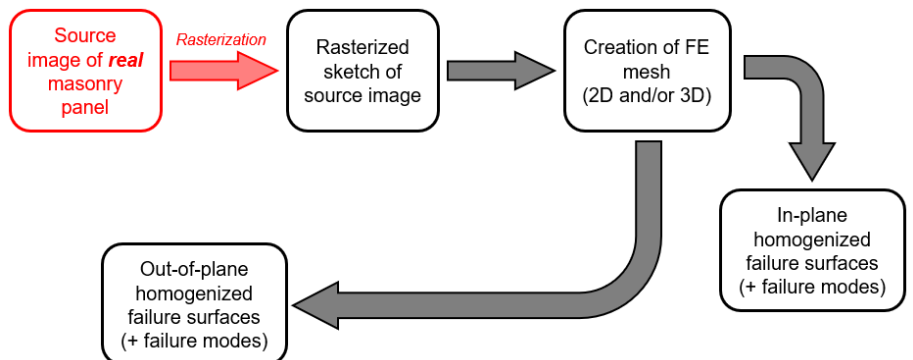


Fig. 7.2. Conceptual workflow of the procedure to develop in the MATLAB app.

The only missing point in the proposed methodology is an initial step consisting of an automated and reliable procedure for the creation of the rasterized sketch from the picture of a *real* generic masonry structural element (the red region and arrow in Fig. 7.2). This initial step is not trivial, since it should employ dedicated tools for the correct identification of units and mortar in the considered masonry element.

Once the automated procedure representing this initial step is originated and successfully validated, it should be possible to implement the whole methodology in a dedicated, GUI-based MATLAB app, which represents another future development of the work presented in this PhD thesis. The proposed GUI should at least include the following features:

- A button for uploading the image of the real masonry structural element.
- A window for displaying the uploaded image.
- A button for starting the rasterization procedure.
- A separate window for displaying the rasterized sketch of the source image.
- A button for creating the finite element mesh, and a menu that enables the selection of a 2D/3D mesh and other requirements (dimensions of the masonry element, parameters for the coarsing strategy, etc.).
- A separate window for displaying the 2D finite element mesh or the in-plane configuration of the 3D finite element mesh.

-
- A cropping tool for selecting the position and dimensions of the test-window directly from the depiction of the 2D/3D finite element mesh.
 - A button for starting the homogenized limit analysis of the considered test-window, and a menu for selecting the in- or out-of-plane case.
 - A separate window for displaying the resulting in- or out-of-plane homogenized failure surfaces.
 - A button for extracting the deformed shapes at collapse, and a menu for selecting the in- or out-of-plane load conditions for which the failure mode should be extracted.

The proposed GUI-based MATLAB app could represent a useful and integrated tool for researchers and scholars needing for a quick assessment of the collapse behavior of non-periodic masonry walls for academic purposes, possibly after the occurrence of a seismic sequence.

7.3 References

- [1] Gattesco, N., & Boem, I. (2017). Out-of-plane behavior of reinforced masonry walls: Experimental and numerical study. *Composites Part B: Engineering*, 128, 39-52.
- [2] Gattesco, N., Amadio, C., & Bedon, C. (2015). Experimental and numerical study on the shear behavior of stone masonry walls strengthened with GFRP reinforced mortar coating and steel-cord reinforced repointing. *Engineering Structures*, 90, 143-157.
- [3] MATLAB Release 2018b, The MathWorks, Inc., Natick, Massachusetts, United States.